Development of Nanodiamond and Raman Spectroscopy Sensing Methods towards the Measurement of Mitochondrial Membrane Potential in Single Cells

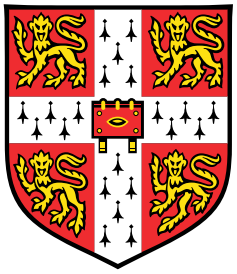

Benjamin John Woodhams

Supervisors: Dr. Sarah E. Bohndiek
Prof. Mete Atatüre

Cavendish Laboratory, Department of Physics and Cancer Research UK
University of Cambridge

This dissertation is submitted for the degree of
Doctor of Philosophy

St. John's College September 2018

Abstract

Name: Benjamin John Woodhams

Thesis title: *Development of Nanodiamond and Raman Spectroscopy Sensing Methods towards the Measurement of Mitochondrial Membrane Potential in Single Cells*

Mitochondrial membrane potential ($\Delta\Psi_m$) in cells is a critical biological parameter that is related to diseases such as cancer through biological processes including metabolism, oxidative stress and apoptosis. Studying $\Delta\Psi_m$ in normal and diseased states is limited by significant challenges associated with the current state-of-the-art methods for measurement, particularly fluorescent dyes, which are often toxic and photobleaching. The aim of this work was to develop electrical and chemical sensing methods to enable sensitive detection of changes in $\Delta\Psi_m$ in single cells. Fluorescent Nitrogen Vacancy Centres (NVCs) in nanodiamond were identified as potential sensors of electric field that could be applied in living cells to directly measure $\Delta\Psi_m$. Furthermore, Raman spectroscopy was identified as a label-free chemical sensing technique that could be used to reveal the location and chemical composition of the mitochondria in cells. To achieve the aim of detecting changes in $\Delta\Psi_m$ using these two methods, complementary NVC and Raman measurements in live cells were needed. Initially, a specialised microscope was designed, built and validated to enable dual measurement of both NVC fluorescence and Raman spectroscopic signals simultaneously. Next, protocols and analysis techniques were developed for live cell Raman microscopy using a commercial reference instrument. An investigation of the impact of nanodiamonds as nanoparticles for biological sensing within live breast cancer cells, including surface modification by oxidation, was then conducted. By developing both techniques together, this project leverages the complementary advantages of long time course measurement, common laser excitation, the observation of nanodiamonds via Raman signal, with live single cell interrogation. The thesis concludes with an outlook on the future development needed to utilise NVCs and Raman spectroscopy in the measurement of cellular $\Delta\Psi_m$. Achieving this goal in future will provide new biological understanding of $\Delta\Psi_m$ in normal and disease states, allowing us to follow over time changes in $\Delta\Psi_m$ in response to biological processes such as apoptosis in single cancer cells.

I would like to dedicate this thesis to my family.

Declaration

This dissertation is the result of my own work and includes nothing which is the outcome of work done in collaboration except as declared in the Preface and specified in the text. It is not substantially the same as any that I have submitted, or, is being concurrently submitted for a degree or diploma or other qualification at the University of Cambridge or any other University or similar institution except as declared in the Preface and specified in the text. I further state that no substantial part of my dissertation has already been submitted, or, is being concurrently submitted for any such degree, diploma or other qualification at the University of Cambridge or any other University or similar institution except as declared in the Preface and specified in the text. This dissertation contains fewer than 60,000 words including appendices, bibliography, footnotes, tables and equations.

Benjamin John Woodhams
September 2018

Acknowledgements

Firstly I would like to thank my primary supervisor, Dr Sarah Bohndiek, who has been of steadfast support during my PhD. Her professionalism, accessibility, patience, wisdom and encouragements are a model for principal investigators, especially during the difficult times of my project. I have learnt much from her. Secondly I would like to thank my second supervisor, Prof Mete Atatüre, whose energy and willingness to collaborate has made this project possible.

More broadly, I would like to thank my collaborators in science, including everyone in my research groups. From these I would like to particularly credit Jakub, Laura A-B, Siri, Alex F, Emma C, Alex G, Gu, Helena, Philippa, Fiona, Dhiren, Jonghee, James J, Rajesh, Judith, Emma B, Liz, Laura M, Hajime, and Jo for their scientific advice and help, both small and large. I would also like to thank my funding bodies, particularly the Oliver Gatty studentship, the Winton fund for sustainability and NanoDTC. I would also like to thank the technical and administrative staff of the physics department.

I would also like to thank my friends for providing joy and peace in the difficult times of my PhD. Apart from those already mentioned above, I am grateful for these things to Pouya, Clara, Rachael, Deryck, Gamal, Alex Q, James C, Chris, David, Prossie, Derk, Vincent, Di, Nard, Yaikhomba, and Jane. I am especially thankful to my (almost-) office-mates, Travis, Sophia, Dale, Lina, and Ayaka, who make coming into the department a pleasure. I would also like to acknowledge the friendship of others such as my undergraduate co-workers and fellow students at school.

Additionally I would like to thank my family. Their self-sacrificial service and support demonstrates a love I could never repay and I would not have got to this point without them. Finally I would like to thank God. May the glory be to Him.

Publications

Peer reviewed publications

[1] Benjamin Woodhams, Laura Ansel-Bollepalli, Jakub Surmacki, Helena Knowles, Laura Maggini, Michael De Volder, Mete Atatüre, and Sarah Bohndiek. "Graphitic and Oxidised High Pressure High Temperature (HPHT) Nanodiamonds Induce Differential Biological Responses in Breast Cancer Cell Lines." Nanoscale, 2018, 26–32.
https://doi.org/10.1039/c8nr02177e

[2] Jakub Surmacki, Benjamin Woodhams, Alexandria Haslehurst, Bruce Ponder, and Sarah Bohndiek. "Raman Micro-Spectroscopy for Accurate Identification of Primary Human Bronchial Epithelial Cells." Scientific Reports 8, no. 1 (2018): 12604.
https://doi.org/10.1038/s41598-018-30407-8

Conference proceedings papers

Benjamin Woodhams, Helena Knowles, Dhiren Kara, Mete Atatüre, and Sarah Bohndiek. "Nanodiamond Preparation and Surface Characterization for Biological Applications." In Progress in Biomedical Optics and Imaging - Proceedings of SPIE, Vol. 10079. San Francisco, CA, USA, 2017. https://doi.org/10.1117/12.2252892.

Table of contents

List of figures

List of tables

Chapter 1

Introduction

The electrical potential across the boundary of a mitochondrion, an intracellular organelle, is a critical biological parameter due to its connections with processes such as cell death. However, current methods to study this are limited by photobleaching and toxicity issues, impeding progress in this area. Potential new methods of cellular metrology are emerging including nanodiamonds and Raman microscopy. This thesis examines the properties of these emerging methods including construction of an instrument to measure them, development of Raman experimental and analytical protocols, and the biological impact of nanodiamonds.

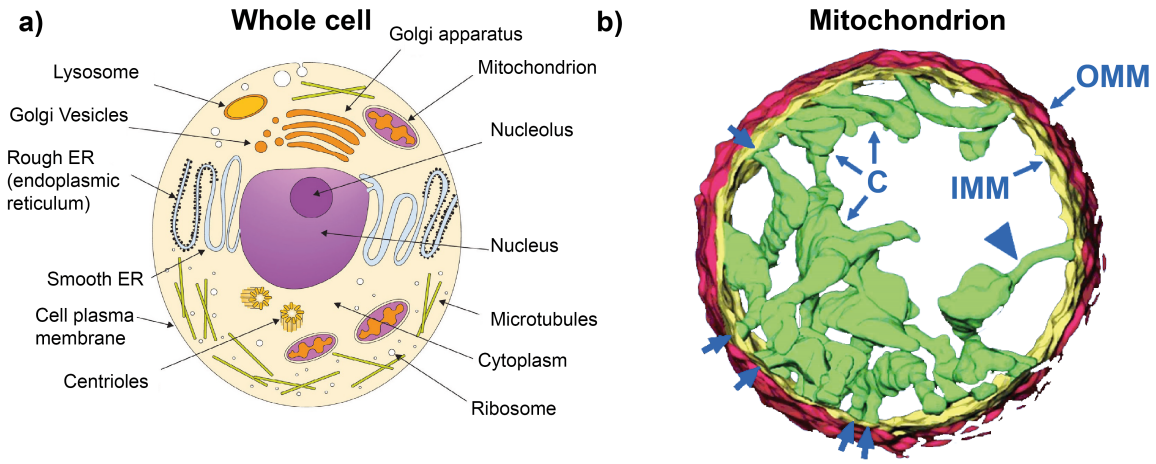

Fig. 1.1 a) A schematic of the organelles inside a typical eukaryotic cell as produced by Ball et al. [3]. b) Electron tomographic image of a mammalian mitochondrion [4]. Outer Mitochondrial Membrane (OMM), Inner Mitochondrial Membrane (IMM) and Cristae (C) are shown, with the blue arrows labelling the tubular regions that connect the cristae to the periphery. The mitochondrial membrane potential is maintained across the IMM.

1.1 Mitochondrial membrane potential

1.1.1 Biological background to mitochondria and Mitochondrial Membrane Potential ($\Delta\Psi_m$)

Mitochondria are a crucial sub-cellular organelle (Figure 1.1a) that are responsible for a wide variety of processes. They are known as the cell's executioner for their role in cell death [29], the energy powerhouse for the their role in releasing energy to the cell [30], and a major source of highly reactive chemicals called Reactive Oxygen Species (ROS) [6]. These key organelles are enclosed by the outer and inner mitochondrial membranes (OMM and IMM, Figure 1.1b, c) that are phospholipid bilayers [4].

The IMM expresses a wide range of ion channels and pumps resulting in the creation of several crucial ion and molecule gradients as well as the maintenance of a membrane potential difference between the inner and outer side of the IMM. This causes a force on charged particles such as protons, given by:

$$\Delta\text{p (proton motive force)} = \Delta\Psi_\text{m} \text{ (Mitochondrial Membrane Potential)} + \Delta\text{pH}$$

[31]. The mitochondrial membrane potential difference is finely tuned and is required for the synthesis of ATP (adenosine tri-phosphate), the cell "energy currency", by oxidative phosphorylation [30]. As a result, $\Delta\Psi_\text{m}$ is considered an established, highly sensitive indicator of the health of the cells providing useful insight on cell metabolism and energy production, the balance of reactive species and cell death [7, 32–34]. In turn, these processes and their dysfunctions are connected with diseases such as cancer [35], establishing $\Delta\Psi_\text{m}$ as a vital object for biological investigation.

1.1.2 Connections of $\Delta\Psi_m$ with important biological processes

$\Delta\Psi_m$ and Metabolic Rate

The metabolic rate of a cell is the rate at which it produces Adenosine Tri-Phosphate (ATP), the energy carrier of the cell, necessary for powering the processes of life [5]. This process mainly happens at mitochondria, resulting in their common description as 'the powerhouse of the cell' [36]. ATP is synthesised at mitochondria via the Electron Transport Chain (ETC, Figure 1.2), in a process called Oxidative Phosphorylation.

In this process, electrons are transferred through membrane complexes (C1-4), and hydrogen ions are pumped across the membrane. In combination with some other ion pumps,

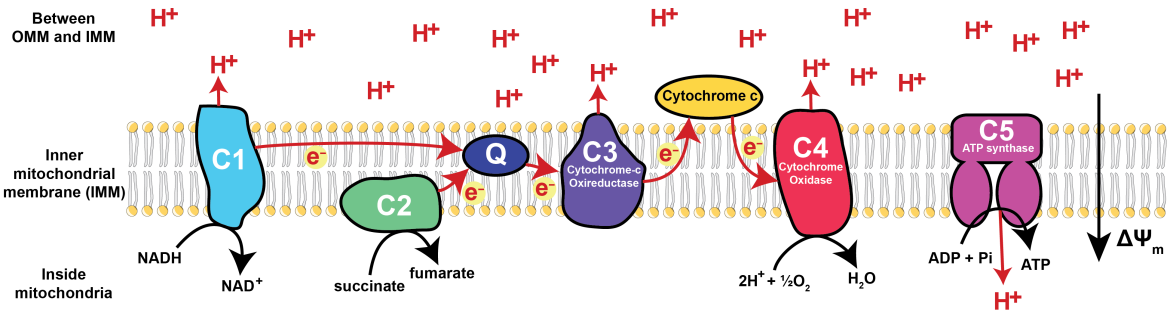

Fig. 1.2 Picture of the Electron Transport Chain from El Bacha et al. [5]. Electrons are passed through the electron transport chain complexes 1-4 (C1-4), including the reduction and oxidation of cytochrome c. Hydrogen ions are pumped across the membrane by these complexes, creating power for ATP synthesis at complex 5 (C5) by forming $\Delta\Psi_m$ and ΔpH. Forming ATP is the metabolic rate of the cell, in a process called oxidative phosphorylation.

a potential is formed across the membrane, providing the energy for complex 5 to form ATP. This Δp typically consists of 80-85% $\Delta\Psi_m$ with 15-20% from ΔpH [37, 36].

As a result, $\Delta\Psi_m$ and metabolic rate are intricately linked. For example, a low membrane polarisation results in insufficient ATP production for the cell [32]. Additionally, a dysfunction of ATP synthase (complex 5) or a lack of ADP can lead to the hyperpolarisation of the mitochondrial membrane ($|\Delta\Psi_m| \uparrow$) [38].

This relationship is also modified in pathological conditions such as cancer. Cancer cells also have been observed to have lower average $\Delta\Psi_m$, thought to be a result of their avoidance of the normal oxidative phosphorylation pathway that is described above [39]. Cancer cells instead tend to use a glycolytic metabolism, a process that is typically used in normal cells that are deficient in oxygen. Cancer cells however, predominantly use this glycolytic process even in the presence of oxygen, known as the Warburg effect [40].

$\Delta\Psi_m$ and Reactive Oxygen Species (ROS)

Reactive oxygen species (ROS) are a group of highly unstable molecules that incorporate oxygen atoms. ROS include chemical species with one unpaired electron, known as free radicals, such as the superoxide anion ($\bullet O_2^-$), and are essential to many biological processes such as cell protection, mitochondrial fission, and mitochondrial removal [41]. They are often produced at the mitochondria, as shown in Figure 1.3. Under normal circumstances ($|\Delta\Psi_m| = 100 - 130$ mV [38]), ROS are slowly produced at Complexes 1 and 3 of the Electron Transport Chain, often going on to form hydrogen peroxide (H_2O_2).

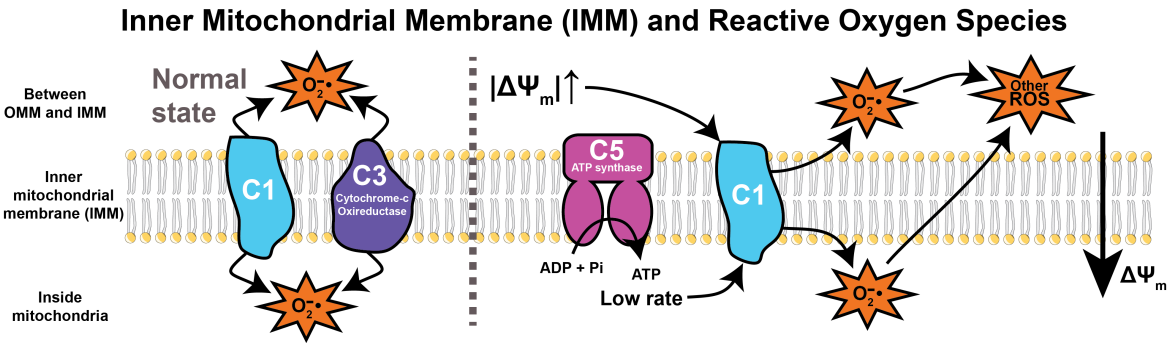

Fig. 1.3 Reactive Oxygen Species (ROS) are highly unstable molecules produced at the cell membrane from oxygen gas. Complex 1 and Complex 3 (C1 and C3) are part of the Electron Transport Chain (Figure 1.2) that slow 'leak' superoxide anions ($\bullet O_2^-$), which may lead to over types of ROS. ROS production is greatly increased if $|\Delta\Psi_m|$ is increased, and if complex 5 is inhibited. Information from [6, 7].

In other circumstances, stressful conditions can can increase ROS levels dramatically [38]. For example, the addition of H_2O_2, irradiation, or therapeutic drugs can raise $|\Delta\Psi_m|$ to $150-200$ mV, leading to an excessive and exponential generation of superoxide free radicals [32, 42]. This occurs especially when metabolic rate does not increase with $|\Delta\Psi_m|$ [6], leading to superoxide production at Complex 1 as the complex transports electrons in the reverse direction to normal [6]. This change may be transient as it is known that ROS will open the mitochondrial Permeability Transition Pore (PTP), thereby reducing $|\Delta\Psi_m|$ [8]. If large amounts of ROS are produced, then the cell may proceed through its programmed death mechanisms, known as apoptosis (see below). For cancer cells, it has been noted that persistently high levels of ROS accelerate their transformation towards heightened malignancy [43].

$\Delta\Psi_m$ and Apoptosis

Apoptosis is the process of programmed, controlled cell death. It is used in multicellular organisms to remove cells that are no longer needed or are dysfunctional, through a process that does not damage the surrounding cells [44]. The pathways of apoptosis are highly sophisticated, with some dependent on extrinsic factors and mediated by cell surface death receptors, while some are intrinsic, focused around the mitochondria [45].

In the intrinsic apoptotic pathway [44], the cell detects internal problems such as stress or DNA damage that cannot be rectified and therefore necessitate the response of cell death. The Bax protein is activated to make pores in the OMM and modify $\Delta\Psi_m$ (as described below). Then, the IMM Permeability Transition Pore (PTP) opening causes the reduction of

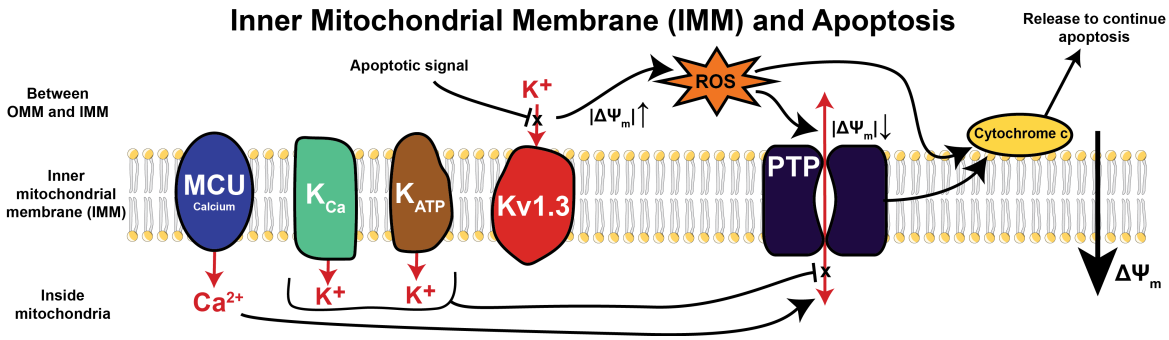

Fig. 1.4 Relationship between $\Delta\Psi_m$, ion channels, and apoptosis. Inhibition of potassium channel Kv1.3 increases $|\Delta\Psi_m|$, generating ROS and leading to cytochrome c detachment for apoptosis activation. Kv1.3 and Mitochondrial Calcium Uniporter (MCU) channel also open the Permeability Transition Pore (PTP), another event that can lead to cytochrome c detachment and subsequent apoptosis, as well as reducing $\Delta\Psi_m$. The activation of other potassium channels K_{Ca} and K_{ATP} provide an antagonist force, working to close PTP. This figure was created from information in [8, 9].

membrane potential. This decrease as well as the loss of OMM integrity releases cytochrome c from the mitochondria into the cell cytoplasm. This then continues the chain of apoptosis by joining with a set of repeating molecules and forming large enzymes called apoptosomes. From there, these apoptosomes activate the caspase proteins that function to degrade, digest and kill the cell.

The loss of $\Delta\Psi_m$ is considered the "point of no return" in the process of apoptosis, with its total loss being the first irreversible event in many controlled cell deaths [46]. This means $\Delta\Psi_m$ can be measured to establish that the cell is committed to die before this phenotype is displayed in other ways [46]. Changes in $\Delta\Psi_m$ in apoptosis are caused by the actions of ion channels in the IMM, as summarised in Figure 1.4.

Potassium channels are the most common ion channels in mitochondrial membranes and therefore are considered important in the process of apoptosis [9]. One ion channel that is instrumental in intrinsic apoptotic pathways is the mitochondrial Kv1.3 channel. This potassium channel responds to Bax protein signalling from outside the mitochondria, which inhibits the flow of potassium inwardly [45, 8]. This then increases $|\Delta\Psi_m|$, causing an increase in ROS, as described above. These ROS then favour the release of an apoptotic protein from the IMM, cytochrome c. Cytochrome c will relocate to the cytoplasm, eventually activating chemicals responsible for the degradation of cellular content [9]. These ROS also cause the opening of the mitochondrial Permeability Transition Pore (PTP), reducing $|\Delta\Psi_m|$ to below 100 mV, producing further ROS and encouraging further cytochrome c release [41, 32].

Some other mitochondrial potassium channels inhibit PTP opening, thereby acting against the chain of apoptosis. K_{Ca} and K_{ATP} are channels that are activated by calcium and ATP, and are understood to reduce ROS production down to levels remaining under the apoptotic threshold, thereby maintaining $\Delta\Psi_m$ [8, 9].

Channels of calcium and sodium are also know to play a role in apoptosis [45]. The Ca^{2+} uniporter (MCU) is another mitochondrial channel that is sometimes involved with this process. This can act by inducing a permeability transition in the PTP, reducing $\Delta\Psi_m$ and releasing cytochrome c [45, 8].

However, it should be noted that apoptosis does not always proceed via any of these pathways, with $\Delta\Psi_m$ depolarisation sometimes happening later [33], or sometimes not producing cytochrome c despite a reduced membrane potential [47–49], and with the changes later reversed. Many of these processes remain to be further explored.

The situation becomes more complicated in pathological cells, such as cancer. Cancer cells widely exhibit resistances to membrane depolarisation and to apoptosis, in part due to their modified ion channels [43, 45]. These relationships remain complex however, with some cancers showing increased expression of potassium and MCU channels, while others showing reduced expression [45]. Nevertheless, ion channels have been identified and used as a targeting strategy for therapeutics, as apoptotic avoidance via these strategies is known as a hallmark of cancer [43]. Therefore, research to reactivate apoptosis in cancer cells continues to progress [45].

1.1.3 Current Methods of Measuring $\Delta\Psi_m$

$\Delta\Psi_m$ is deeply interconnected with the areas of apoptosis, metabolic rate and reactive oxygen species and these in turn are fundamental in understanding diseases such as cancer. It is therefore clear that $\Delta\Psi_m$ is an crucial parameter of investigation. The most commonly used techniques to measure $\Delta\Psi_m$ are fluorescent dyes, with various advantages and disadvantages associated with them.

Dye Name	Advantages	Disadvantages
JC-1	• Green when it is cytosolic but shifts to red fluorescence when it binds to the mitochondria. This provides an internal normalisation [47, 50].	• This dye does not rapidly efflux when $\Delta\Psi_m$ dissipates and therefore is less useful for graduated measurement. Best used as a binary indicator [47, 49] • Influenced by pH, osmolarity, and oxidative environment of the cells [51] • Toxic [51] • Sensitive to rapid photobleaching • Particularly sensitive to loading concentrations and loading times [52] • Different rates of change for red and green variants [52]
Rhodamine 123	• Rapid cellular uptake and equilibration [53] • Effective over a timescale of minutes [52]	• Forms aggregates that quench [51] • Inhibits mitochondrial respiration [51] • Toxic to most cells. [47]
TMRM/ TMRE	• Of the dyes, least mitochondrial toxicity [51] • Responds closely and reversibly to the Nernst equation [51] • Can be quantitative [51]	• Affected by temperature [49] • Depends on the ratio between the concentration of dye to number of cells [49] • Forms aggregates [51] • Quenches [51] • Illumination provokes ROS [51]

Dye Name	Advantages	Disadvantages
DiOC(6)	• Most suitable for use in flow cytometry studies [52]	• Inhibits mitochondrial respiration [49] • Not specific to mitochondria, also stains the Golgi apparatus, the organelle of intracellular transport [53] • Inhibits respiration [53] • Cell size, PMP affect intensity [53] • Depends on pH [53]

Table 1.1 A comparison of the four most common mitochondrial membrane potential dyes. There are some further disadvantages that are common to all such as dependence of mitochondrial size, mass, time, multidrug resistance pumps, as well as leaking and molecule size.

In addition to the those listed in Table 1.1, there are also other dyes that have been more recently developed, or less frequently used, such as safranin, oxonol, JC-9, CAI and the near infra-red dye, NIMAP [53–57]. Fluorescent dyes generally possess advantages such as ease of use, compatibility with standard confocal fluorescent microscopes, widely developed protocols, ease of basic data analysis, and wide availability [55].

There are also some disadvantages which affect the performance of all of the fluorescent dyes. Firstly, dyes are affected by mitochondrial size and mass [51, 52]. Also, they take time to accumulate and eventually bleach, reducing the time resolution and span that can be measured [55, 51]. They are also known to have different permeability to different cell types [55]. In addition, they are affected by multidrug resistance pumps and so cannot reach an equilibrium that depends only on the potential [51].

There have been multiple efforts to overcome the difficulties associated with fluorescent dyes. Variations in mitochondrial size can been accounted for by using the ratio between forward light scattering and side scattering [46]. Other studies have worked to account for the effects of mitochondria:cell ratio and time lag to produce a quantitative measurement that are verified to patch clamp measurements [58], although the calibration is lengthy and highly complex. Overall, the limitations behind fluorescent dyes such as photobleaching have been understood and only partially overcome.

In addition to fluorescent dyes, other methods have been used to quantify mitochondrial membrane potential. In vivo, a technique has been developed for readout with Positron Emission Tomography (PET) [59]. This technique uses ^{18}F-labelled triphenylphosphonium (TPP, a moiety that targets mitochondria) delivered into three pigs. These molecules are lipophilic cations that more greatly accumulate at stronger membrane potential. This successfully measured the sum of the cellular plasma membrane potential and the mitochondrial membrane potential, but this technique cannot distinguish these parameters, and cannot be used on a single cell level.

Another technique that is used in animals is that of a chemical tracer known as MitoClick [60]. The accumulation of two other molecules in mitochondria produces MitoClick at a rate that depends on $\Delta\Psi_m$. The animals are then subsequently culled, frozen, dissected, and analysed via liquid chromatography - mass spectrometry for uptake. This has the disadvantage of providing only a snapshot of a cell or organism, making it difficult to study biological changes over time. Another disadvantage is the loss of spatial information as tissues are homogenised before analysis to improve signal.

There are also some measurement techniques that rely on the extraction of mitochondria from cells for measurement. The most commonly used is patch clamping, as invented by Neher and Sakmann [61]. After mitochondrial extraction, this usually consists of puncturing the mitochondrial membrane with a glass micropipette to make an electrical connection with the inside of a mitochondrion. The current or voltage of the mitochondrion can then be determined. There are multiple different variants on the patch clamp, and they have revealed most of our current knowledge of ion channels [62, 63]. However, since this technique requires the removal and destruction of mitochondria from cells, it is limited in its ability to studying the connections between $\Delta\Psi_m$ and processes like apoptosis in living cells [58].

Impedance spectroscopy from a Biological Micro-Electronic and Mechanical System (BioMEMS) is another technique used, with electrodes providing voltage along a microfluidic channel that contained mitochondria [32]. The impedance of mitochondria was inferred from the current flow and voltage drop between the electrodes, with increasing impedance corresponding to decreasing $|\Delta\Psi_m|$ [32]. This exhibits the same disadvantages as patch clamping, however, as mitochondria must be removed from cells for study.

Various nanoparticles have been developed for this purpose of measuring membrane potential in cells. Semiconductor Nano-Roads (NRs) have been shown as feasible sensors for membrane voltage by Park et al. [64], although they state the process requires further development to be successful. The authors state there remain challenges associated with membrane insertion and variability that limit the success of this technique. Another nanopar-

ticle approach has been seen with e-PEBBLES, where electric field was measured inside a cell using encapsulated dye [65]. This was able to measure electric field on a timescale of minutes in the cell cytoplasm, and it may be feasible to add targeting compounds to the nanoparticle surface in order to take the nanoparticle to the mitochondria. However, this experiment observed nanoparticle photobleaching and membrane damage [65], so there remains a need for a new sensing nanoparticle in this area.

Overall then, there are serious limitations in the current standard measurement techniques of $\Delta\Psi_m$ and new approaches to this problem should be considered. The hypothesis of this work is that direct electrical and chemical measurement of the mitochondrial membrane will enable a more sensitive assessment of $\Delta\Psi_m$ than is possible with any of the current methodologies that are available as state-of-the-art. Electrical measurement can be made using Nitrogen Vacancy Centres (NVCs) in nanodiamond and chemical sensing can be performed with Raman microscopy.

1.2 Nanodiamonds and Nitrogen Vacancy Centres (NVCs)

Nanodiamond metrology with NVCs has the potential to overcome limitations of current techniques as they have been observed as photostable, non-toxic, precise, specific, local sensors [66, 16].

1.2.1 Nanodiamonds and their synthesis

Nanodiamonds are tiny crystals of carbon of 1–1000 nm. They generally contain an sp^3 carbon core, with sp^2 graphitic carbon covering the surface, along with other functional groups such as carboxyl, hydrogen and hydroxyl groups [67]. They are currently synthesised via three main procedures - Detonation fabrication, Chemical Vapor Deposition, and High-Pressure High-Temperature fabrication. These processes are summarised in Figure 1.5.

Detonation nanodiamond synthesis by detonation was first observed in USSR shock compression tests in the 1960s, and rediscovered in the USA in 1988 [68]. These experiments rely on decomposition of explosive mixtures in a non-oxidising environment, although the exact process is still debated [69].

Fabrication of nanodiamond is also widely achieved via Chemical Vapour Deposition (CVD). CVD is performed by slowly depositing volatile material to build up a solid material layer by layer. Then the substrate is removed by chemical etching and the nanodiamonds are separated by techniques such as conventional planetary milling [70] or Bead-Assisted

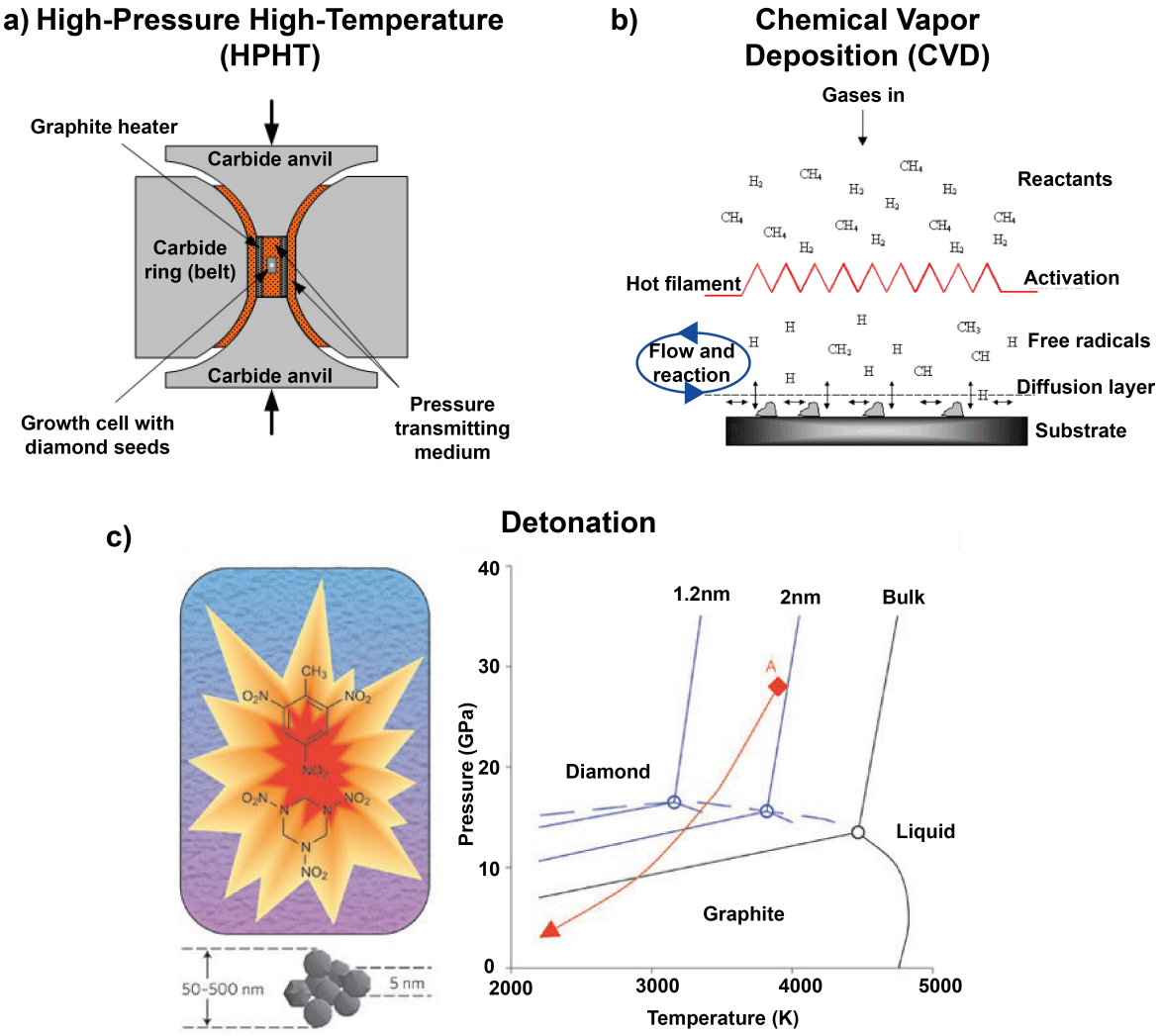

Fig. 1.5 Diamond fabrication methods. a) High Pressure High Temperature synthesis of nanodiamonds involves crushing carbon materials in an anvil. Figure is reproduced from the SubsTech web knowledge source [10]. b) Diamonds can be grown from seeds in Chemical Vapor Deposition and then milled to size. Figure is reproduced from Ashfold et al. [11]. c) This figure describes Detonation Nanodiamond fabrication, where a explosive pressure wave is used to create nanodiamonds. Figure from Mochalin et al. [12].

Sonic Disintegration (BASD) [71]. These nanodiamonds tend to be larger than detonation diamonds, at about 70–80 nm, rather than 4 nm [71, 69].

Creation of nanodiamonds by High-Temperature and High-Pressure (HPHT) synthesis is also commonplace. One example of this type of synthesis begins with graphitic C_3N_4 [72] that is heated to 800–2000 °C and pressurised to 15–25 GPa. This has been observed to contain lower impurities and a more uniform size range [72]. There are also beneficial spin properties of HPHT nanodiamond [73, 74]. There may also be a difference in biocompatibility as detonation and HPHT diamonds are both non-toxic at low concentrations, but there has been evidence for detonation nanodiamond toxicity at high concentrations (1 mg ml^{-1}) [75].

Nanodiamond particles have shown potential in several different industrial areas including lubrication, drug delivery, surgical implants, material strengths, and UV protection [76]. Further applications of nanodiamond particles depend on their ability to make physical measurements via Nitrogen Vacancy Centres (NVCs).

1.2.2 Introduction and physics background to the Nitrogen Vacancy Centre

Diamond lattices have been observed to contain many different defects in structure and atomic substitution that produce a wide variety of colours (Figure 1.6). Diamond has an electronic bandgap in the range 5.47 eV (247 nm), making it transparent in the visible region [77]. These defects can therefore be optically addressed with laser excitation, and measured via their fluorescent emission.

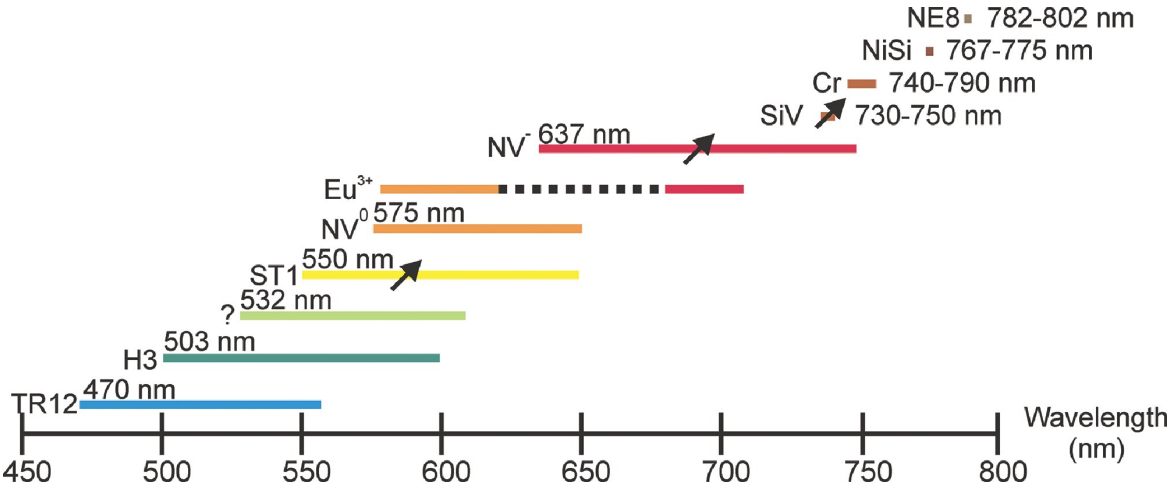

Fig. 1.6 Diamond can host a range of fluorescent colour centres, emitting across the wavelengths shown. [13]. This project will focus on the NV^- centre.

Research into these diamond colour centres has focused on the Nitrogen Vacancy centre (NVC), the Silicon Vacancy (SiVC) centre and the Germanium Vacancy (GeVC) centre. Although the SiVC and GeVC have superior properties in some respects, such as increased quantum efficiency, the NVC is the most widely used due to its convenient 532 nm excitation [78], long coherence times [74, 73], and photostability [79]. NVC synthesis in nanodiamond has also improved in recent years, with implantation and annealing techniques being optimised [79].

Independently of fabrication, NVCs exhibit clearly defined energy levels. These arise from the six unpaired electrons that are localised around the two lattice sites. Since there are normally 4 valence electrons per carbon atom, the NVC has effectively two spin-$\frac{1}{2}$ holes, which combine to form a spin-1 system of energy levels (Figure 1.7).

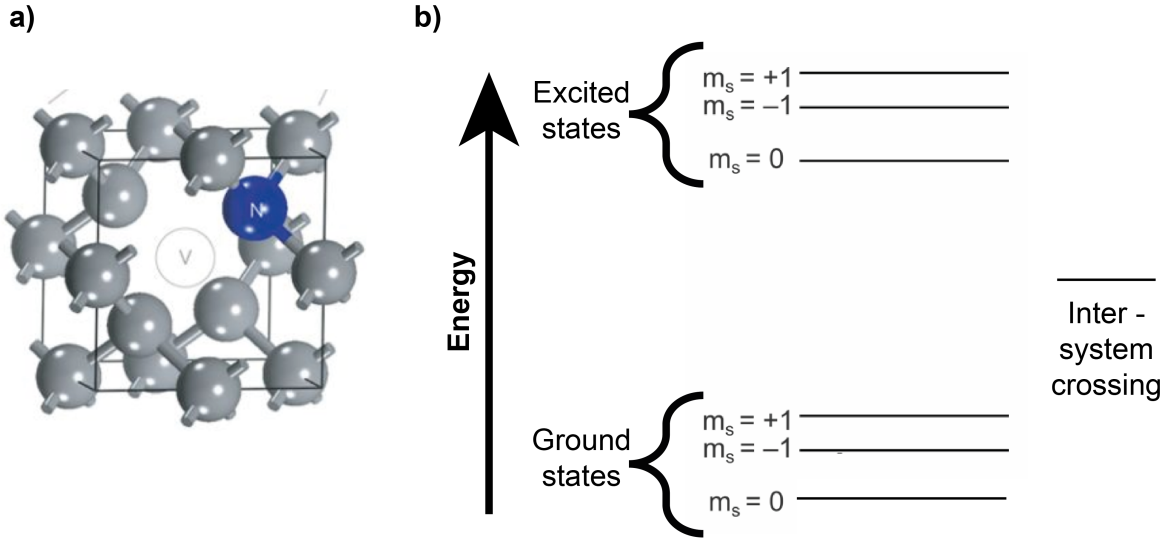

Fig. 1.7 a) A nitrogen-vacancy centre (NVC) exists in a carbon lattice (grey) and consists of a substitutionary nitrogen and vacant lattice site [14]. (b) This produces an energy level system that can be addressed with optics and microwaves. $m_s = \pm 1$ are shown separated, as in the presence of a magnetic field. The frequency gap between $m_s = \pm 1$ and $m_s = 0$ is $\approx$ 2.88 GHz [15].

These energy levels depend on physical quantities such as temperature, magnetic field, electric field and pressure [80–82], and have therefore been developed as sensors for these quantities. The energy level differences can be read out by a technique called Optically Detected Magnetic Resonance (ODMR), as explained in Figure 1.8. The detection of electric field is the most relevant for this project, as the mitochondrial potential will cause an electric field across the membrane.

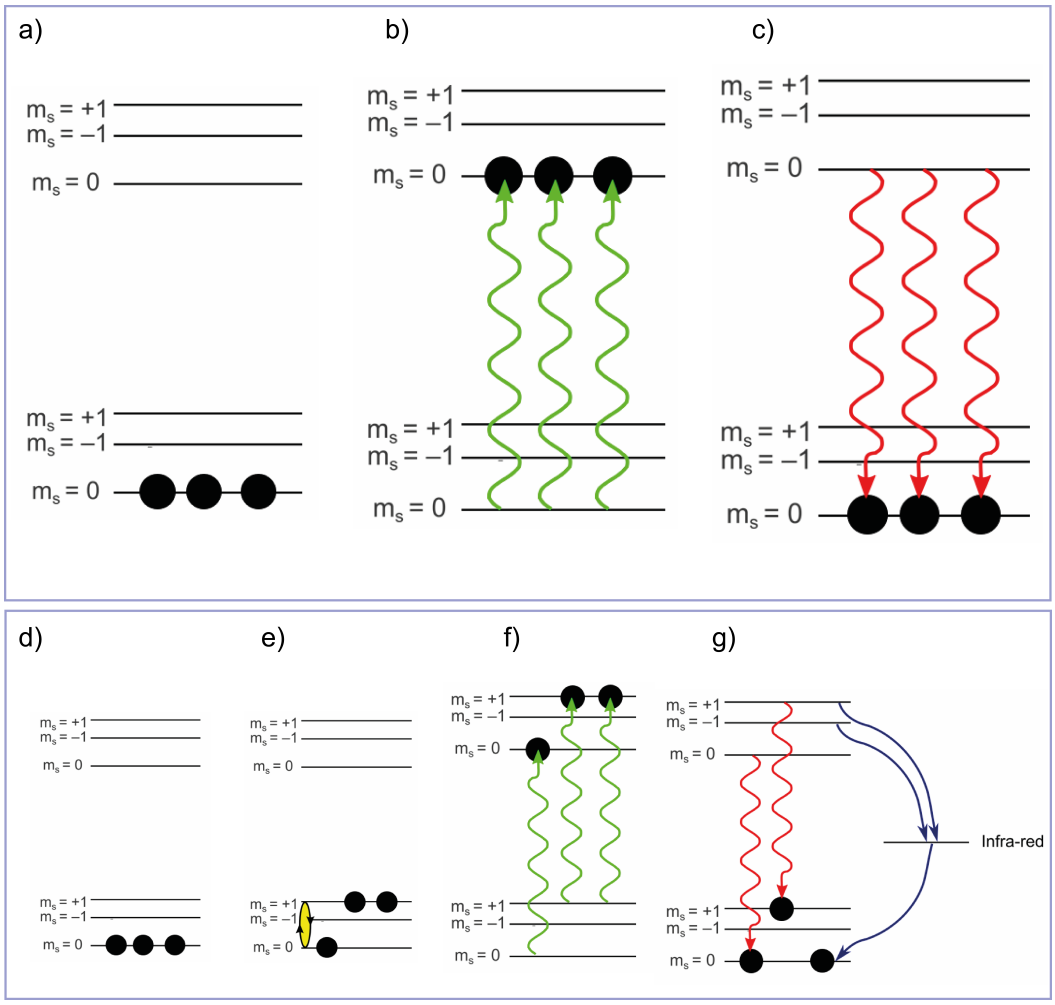

Fig. 1.8 Optically Detected Magnetic Resonance reads out the energy levels of NVCs and is the key method of Nitrogen Vacancy centre metrology. It depends on the shift of energy levels. a-c) A nitrogen vacancy centre has the energy levels shown. Three black dots demonstrate the current state for three different repetitions. Without microwaves, the NVC is promoted to the excited levels, but then returns to its original state. Both of these transitions are spin preserving so an NVC in spin $m_s = 0$ will return to it. d-g) This shows the same with the addition of microwaves. These microwaves can provide transition between the ground state energy levels, if the transition frequency is met (e). This then means that the NVC has the opportunity to be promoted to different excited levels under the green excitation. If it is promoted to $m_s = +1$ or -1, then there is the opportunity for a decay that is not optically radiative. Therefore, if the microwave transition in (e) occurred, then the amount of fluorescence observed is reduced. In this way it is possible to determine the energy levels of the NVC, which sensitively depend on physical properties such as temperature.

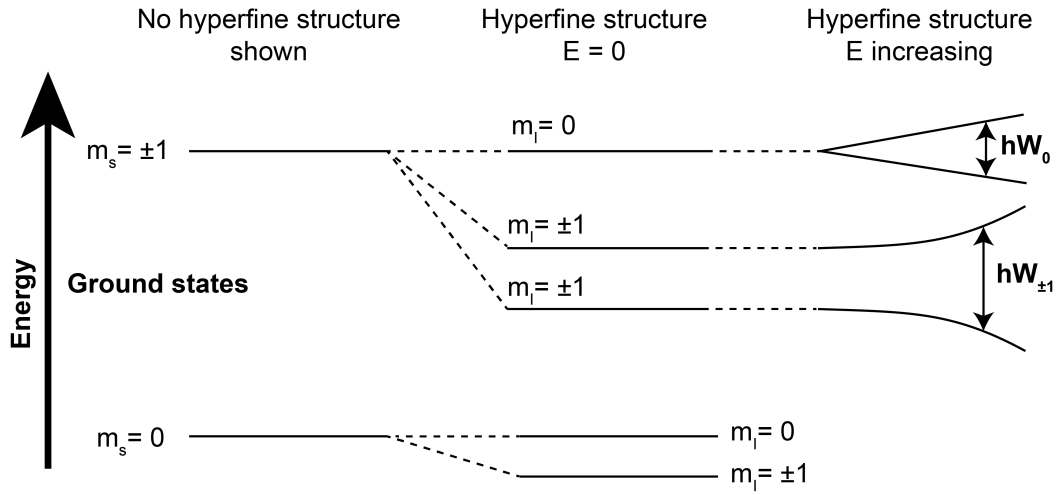

Fig. 1.9 Detailed structure of NVC energy levels. In the absence of magnetic field $m_s = \pm 1$ states are degenerate at the fine structure level. The $m_s = 0$ and $m_s = \pm 1$ states are split by spin interactions with the nitrogen nucleus of the NV centre into hyperfine levels of $m_I = 0$ and $m_I = \pm 1$. These are then shifted in response to transverse electric fields, and these energy levels and their shifts can be measured with ODMR (Figure 1.8). See text for explicit formulae for W_0 and W_1.

The nitrogen vacancy energy levels have been comprehensively studied by analytical, computational and experimental methods [81, 83]. Doherty et al. [83] have shown that the NVC ground state energy levels can be split by interactions with the nitrogen nuclear spin (m_I) into hyperfine structures which depend on electric field. Iwasaki et al. [15] have expanded this E-field dependence of the energy levels explicitly for transverse fields (Figure 1.9) as:

$$W_0 = \frac{2d_{gs}^{\perp}(E_{\perp} + \sigma_{\perp})}{h} \text{ for } m_I = 0$$

$$W_{\pm 1} = \sqrt{\left(\frac{2d_{gs}^{\perp}(E_{\perp} + \sigma_{\perp})}{h}\right)^2 + \left(\frac{2A_{\parallel}}{h}\right)^2} \text{ for } m_I = \pm 1$$

W_0 is the energy splitting on $m_I = 0$ and $W_{\pm 1}$ is the energy splitting on $m_I = \pm 1$. $\perp$ signifies the perpendicular component to the NV axis. $E_{\perp}$ is the electric field, $\sigma_{\perp}$ is the lattice strain field, $d_{gs}^{\perp}$ is the electric dipole moment of the electrons, h is the Planck constant and $A_{\parallel}$ is the hyperfine splitting constant. While both W_0 or $W_{\pm 1}$ can be measured in ODMR, and either could be used for determination of E-field, Iwasaki et al. demonstrated that it is easier to use $W_{\pm 1}$ in the high field regime [15]. They also note that axial E-fields could be measured in principle, but the small electric dipole makes this technically difficult in practice:

$$d_{gs}^{\parallel}/h = 0.35\,\mathrm{Hz}\cdot\mathrm{cm}\cdot\mathrm{V}^{-1} << d_{gs}^{\perp}/h = 17\,\mathrm{Hz}\cdot\mathrm{cm}\cdot\mathrm{V}^{-1}.$$

Due to its underlying physics, the NVC has several beneficial properties for measurements. The first is that NVCs have been shown to be highly precise, measuring a single fundamental charge [82], changes of milli-Kelvin in one second [84], detecting of picolitre volumes with NMR [85] and 3 nT fields [86]. These measurements are also specific, with pulse sequences developed to remove the physical effects that are not under consideration [82, 87]. NVC measurement is also highly local, due to the small size of the host nanodiamonds and the loss of NVC coupling at longer range [88]. This means that biological cells can be studied by internalisation of the small nanodiamonds. Furthermore, the NVC centre has been observed to be exceptionally photostable relative to fluorescent dyes [89].

1.2.3 NVC measurement in biology

Nanodiamonds have been shown to have good biocompatibility, with most studies showing effects on viability to be low or negligible in cells [90–93] and in animals [94–101]. However, further work remains necessary to establish nanodiamonds as innocuous at a deeper level than cell viability. Nevertheless, by considering the properties of NVCs such as sensitivity and the biocompatibility of nanodiamond particles, there has been strong impetus to apply these techniques to biological problems at the single cell level.

The earliest example of this was orientation tracking inside cells [14]. In this work, McGuinness et al. measured the orientation of a single nitrogen vacancy centre using an acquisition time of 89 ms to a precision of 1°, tracking the diamond over >10 hours. This kind of tracking is essential for certain kinds of measurements that depend on knowledge of the orientation [102]. The study also gave possible hints of superoxide radicals produced in apoptosis, but this was not confirmed. Building on this work, the first physical measurements of temperature and magnetic fields were performed in cells. Kucsko et al. [16] added nanodiamonds and gold nanoparticles to embryonic fibroblast cells using silicon nanowires. They were able to heat the gold nanoparticle and measure the local temperature required to kill the cell as 72 ± 6 K (Figure 1.10a). This study was remarkable as the authors were able to achieve a precision of 50 mK at the nanodiamond inside a living cell. However, one limitation of this study was the lack of nanodiamond targeting or intracellular understanding. This experiment therefore functioned as a good demonstration of nanodiamond potential, but did not yield any biological insight.

A similar experiment was later performed by chemical conjugation between gold and diamond nanoparticles [103], and then applied to investigate the stability of membranes via the combined nano-heating and nano-thermometry effects [104]. This work created and observed hyper-local gradients of temperature, potentially impacting on cancer therapy that relies on precise destructive local heating. Temperature mapping was achieved at a wider scale by simultaneous measurement of ODMR across thousands of nanodiamonds in neurons simultaneously [105] and during the development of live bovine embryos [18] (Figure 1.10c). The first of these is notable also for the long time course of imaging, making use of the NVC photostability to collect data over 36 hours. The embryonic study is commendable for using Lanthanide nanoparticles as an independent validation technique for temperature.

Magnetic fields in cells were measured by De Le Sage et al. and Glenn et al. in demonstration experiments. De Le Sage et al. successfully imaged natural magnetosome structures in magnetotactic bacteria [17] (Figure 1.10b), whilst Glenn et al. used magnetic labelling on cells that were then detected using NVCs [106]. The techniques were unique in providing sub-cellular magnetic resolution under ambient conditions, and could be used for study of neurodegenerative disorders, magnetic navigation, or uptake studies. Building on these advances, magnetic sensing was also performed on neurons to measure live action potentials via NVC readout [107]. This study was mostly limited by the lack of single-event action potential detection, and the use of bulk diamond in place of nanodiamond, although the authors suggest this could be possible in the future.

Developments in pulse sequences enabled magnetic sensing to be developed into Nuclear Magnetic Resonance and Magnetic Resonance Imaging techniques, mostly in bulk diamond [108]. This culminated in the first measurement of a single protein under ambient conditions [109] in 2015, with species such as hydrogen and fluorine distinguished later [110]. From then, imaging has also been achieved [111], as well as the chemical shifts on small molecules [85].

1.2.4 Other biological uses of nanodiamonds

Nanodiamonds have shown promise in a variety of other biological applications, outside of the use of NV measurement. For example, the unlimited photostability of NVCs has been used for long-term targeting and tracking of stem and cancer cells via fluorescence [112, 113, 88], as well as observing liver tumours as an MRI contrast agent [114]. Internal cellular organelles have also been located via nanodiamond functionalisation, including

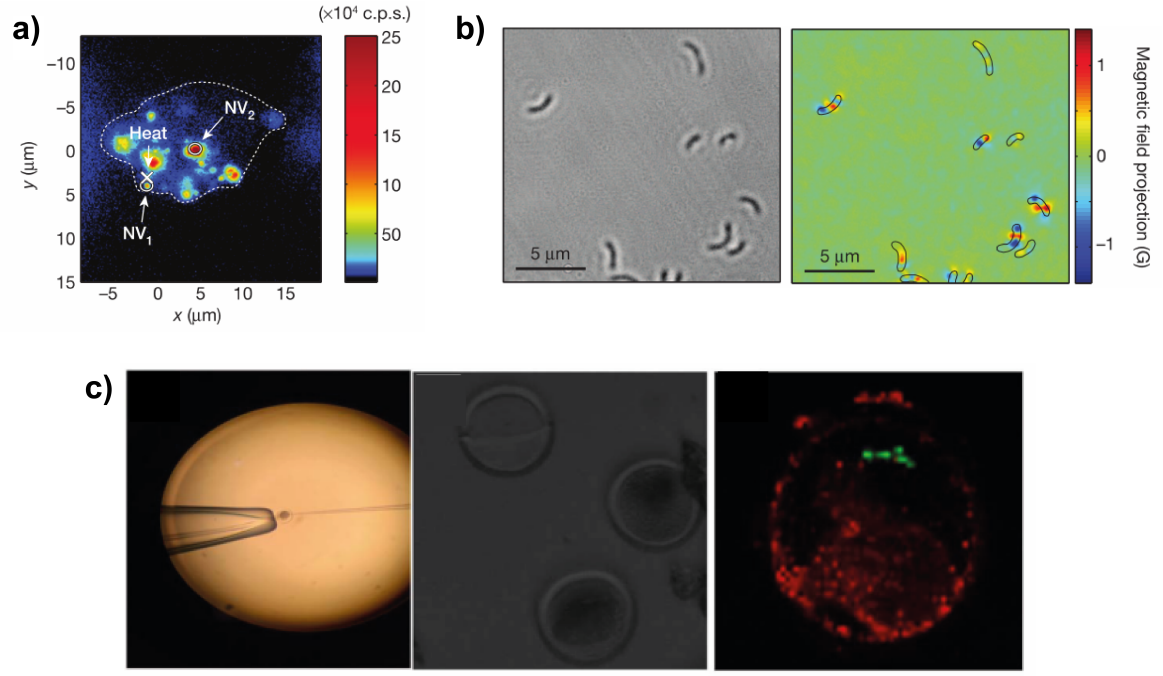

Fig. 1.10 Nitrogen-vacancy centres (NVCs) have been used for biological measurements. a) An early example of this was in measuring the temperature change required to kill a human embryonic fibroblast cell (WS1). This was achieved by ODMR on two nanodiamond NVCs inside the cell with heating from a gold nanoparticle up to 72 ± 6 K [16]. b) Detection of magnetic structures inside magnetotactic bacteria was performed for this first time in ambient conditions using NVC ODMR in bulk diamond [17]. c) Thermometry was also achieved in bovine embryos with NVC ODMR, and verified by Lanthanide nanoparticles [18].

cell surface antigens [115], protein assemblies [116, 117] and the molecules involved in transmembrane signalling [118].

Another way that nanodiamonds have been widely used is as drug delivery systems. It has been commonly observed that attaching nanodiamonds to chemotherapeutic drugs can overcome the multi-drug resistance of cancer cells by reducing efflux [119–121], and therefore enhances efficacy [122]. Drug delivery via nanodiamond has also been optimised by enclosing the particles in microfilm devices to control the rate of drug release [123]. Based on the potency of nanodiamond delivery, other materials have been delivered to cells in this way, including genes [124] and plasmids [125].

1.2.5 Prospects of the application of NVCs to measure $\Delta\Psi_m$

Measurement of mitochondrial membrane potential is critical task in exploring important cellular processes such as apoptosis. The current standard methods exhibit issues such as photobleaching, toxicity, as well as a lack of quantitative precision, local specificity and single cell resolution. Nanodiamond metrology with NVCs therefore can therefore provide transformative new capabilities as they are photostable, non-toxic, precise, specific, local sensors [66, 16]. Overall then, the measurement of $\Delta\Psi_m$ via its electric field may be one area that NVCs can provide a transformative new tool to uncover new understanding in biomedical research.

To achieve this, it is necessary to investigate the biocompatibility of nanodiamonds at a deeper level than viability, and also to collect complementary cellular information to gain broader insight into the processes that nanodiamond can measure. For this second aim, Raman microscopy is a promising candidate.

1.3 Raman spectroscopy

1.3.1 Introduction and physical background to Raman spectroscopy

Raman spectroscopy uses inelastic scattering of light to measure the abundance of chemical bonds in a sample. Molecules have vibrational energy levels that depend on their symmetry and electronic bonds. When a photon encounters a molecule, the most common interaction is elastic scattering. The photon leaves the interaction with the same energy as it possessed beforehand ($\hbar\omega_0$), but it may change direction. However, in about 1 in 10^6-10^8 interactions [126], the photon will inelastically scatter by providing energy for the molecule to change between its vibration energy states, and so leave the molecule carrying a different energy

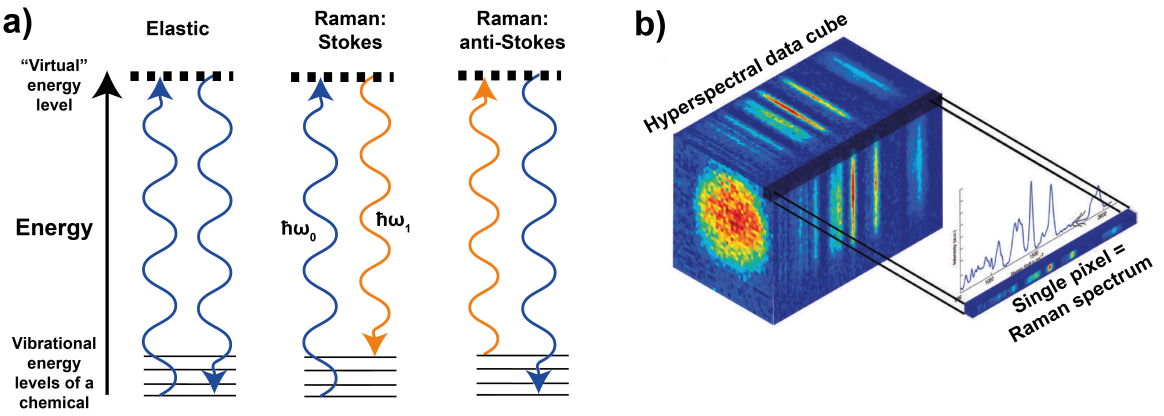

Fig. 1.11 a) An energy diagram of a spontaneous Raman scattering event. The photon after the collision carries information about the possible energy levels of the molecule. b) A Raman hyperspectral datacube. This is collected by taking a spectrum at every point in a two dimension plane. This figure was created by Schie et al. [19]

($\hbar\omega_1$). It is possible to spectrally filter out elastically scattered photons and detect only inelastically scattered photons. By measuring the shift in energy ($\hbar(\omega_0 - \omega_1)$) from the known input light, it is possible to infer that the scattering molecular bond has an opposite energy difference, thereby revealing chemical information about a sample. If the molecule gains energy overall in this process, then this is classified as Stokes Raman scattering, and if it loses energy, this is known as anti-Stokes Raman scattering (see Figure 1.11a and Smith et al. [126]).

There are two main theoretical frameworks that are used to describe Raman scattering events. The first is classical optics as outlined in detail in Shipp et al. [127]. This starts with the model of a polarisable molecule in an oscillating electric field. By assuming a small displacements of the charges, it is possible to derive that the electric dipole moment is:

$$\mu = \alpha_0 E_0 sin(\omega_{rad} t) + \frac{E_0}{2} \frac{\partial \alpha}{\partial x}\bigg|_{x=0} x_0 (cos[(\omega_{rad} - \omega_{vib})t + \phi] - cos[(\omega_{rad} + \omega_{vib})t + \phi])$$

where α_0 is the magnitude of the polarisation, E_0 is the amplitude of the applied electric field, x is the displacement of the charges in the molecule, ω_{rad} is the frequency of the applied electric field, ω_{vib} is the vibrational frequency of the molecule, t is time, and ϕ is the phase of the vibration. From this formalism, it is possible to see that there is an oscillation at $\omega_{rad} - \omega_{vib}$ that corresponds to the Raman scattered photon. Furthermore, the radiation

intensity from a dipole is given by:

$$I = \frac{\omega^4 \mu_0^2 sin^2(\theta)}{32\pi^2 \varepsilon_0 c^3}$$

where μ_0 is the magnitude of the induced dipole, and θ is the angle of observation with respect to the dipole axis. This equation shows that Raman signal is increased with the fourth power of the frequency (ω^4). Furthermore, since μ_0 scales linearly with E_0, the Raman scattering intensity (I) increases linearly with the input light intensity ($\propto E_0^2$) [127].

The second theoretical framework is the application of Fermi's Golden Rule, also described in Shipp et al. [127]. This is a quantum mechanical description of Raman scattering, starting from the equation:

$$R_{|i\rangle \to |f\rangle} \approx |\langle f|\mu_{if}|i\rangle|^2 |E_0|^2 \delta(\varepsilon_f)$$

where $R_{|i\rangle \to |f\rangle}$ is the transition rate from the initial state $|i\rangle$ to the final state $|f\rangle$, μ_{if} is the perturbation of the Hamiltonian that couples $|i\rangle$ to $|f\rangle$, E_0 is the electric field strength of the incident light, and $\delta(\varepsilon_f)$ is the density of states at the final energy. By inserting the dipole transition for Raman scattering, the rate simplifies to:

$$R_{|i\rangle \to |f\rangle} \approx \sum_e \left| \frac{\langle f|\mu_{ef}|e\rangle \langle e|\mu_{ie}|i\rangle}{\omega_{rad} - \omega_{ei} + i\Gamma_e} \right|^2 |E_0|^2 \delta(\varepsilon_f)$$

where $|e\rangle$ is an arbitrary excited electronic state, Γ_e is the linewidth of that state. This equation again exhibits the quadratic dependence of E_0^2, as well as describing the transition as two steps - from $|i\rangle$ to $|e\rangle$, then from $|e\rangle$ to $|f\rangle$, where $|e\rangle$ acts as a virtual energy state, as seen in Figure 1.11a.

Raman microscopy (or 'micro-spectroscopy') refers to collecting a Raman spectrum at each point across two spatial dimensions in order to build an image (Figure 1.11b). Development of these techniques has lead to live cell Raman microscopy that provides insight into things such as organelles, cell types and apoptosis.

1.3.2 Applications of Raman in cell imaging

Raman microscopy has been developed in live cell imaging so that the major components of the cell can be identified, such as DNA, RNA, amides, proteins such as phenylalanine, and

lipids such as fatty acids [19]. These correspond to peaks and groups of peaks, and can be assigned based on previous research and cellular distribution ([19, 128], Figure 1.12a,c)

Organelle and sub-cellular classification

Localisation of cellular organelles has been a key research theme of Raman microscopy over time. This leverages the key advantage of Raman spectroscopy that it is label-free, and can therefore provide classification of areas of the cell into the component organelles and molecule types without the introduction of a fluorescent dye or other label that may perturb the system under study. Uzunbajakava et al. were the first to show that fixed blood lymphocytes and eye lens epithelial cells have completely different internal protein distributions [129]. This was shortly followed by work from the same group, identifying RNA using fixed Raman microscopy for the first time [130]. More complete fixed cellular maps were produced by Krafft et al., who identified the nucleus, cytoplasm, endoplasmic reticulum, vesicles and peripheral membrane [131]. Details on this process of identification from the chemical signatures are outlined in Section 3.3.3. Building on the previous work in fixed cells, this was repeated in live cells, with mitochondrial distribution also measured [132], followed by protein beta sheets and lipids [133], carbohydrates [134], and synapse-forming actin [135]. Having developed the subcellular classifications and chemical sensing, research has focused on understanding their properties and differences, with the metabolism and composition of lipid bodies being commonly used to distinguish and understand cancer [136, 137, 21] (Figure 1.12b), as well as similar achievements with proteins and DNA [138]. Another common biomolecule class of investigation are the apoptotic proteins, including cytochromes [62, 133, 139–141].

Classification of cell type and status

One area that live cell Raman microscopy has been consistently and successfully developed is in classification of cells, including into different cell types, lines, cycle states, and observing cellular differentiation.

Raman microscopy for cell type classification has also been used multiple times in cancer research. For example, Raman microscopy was able to differentiate live human metastatic melanoma cells from skin fibroblast cells, showing promise as a clinical tool [138]. Raman microscopy was also used to evaluate the degree of difference between different cells types, with Swain et al. finding that A549 cells were a less representative model of cancerous lung tissue than TT1 cells [142]. In another study, Raman microscopy was able to demonstrate

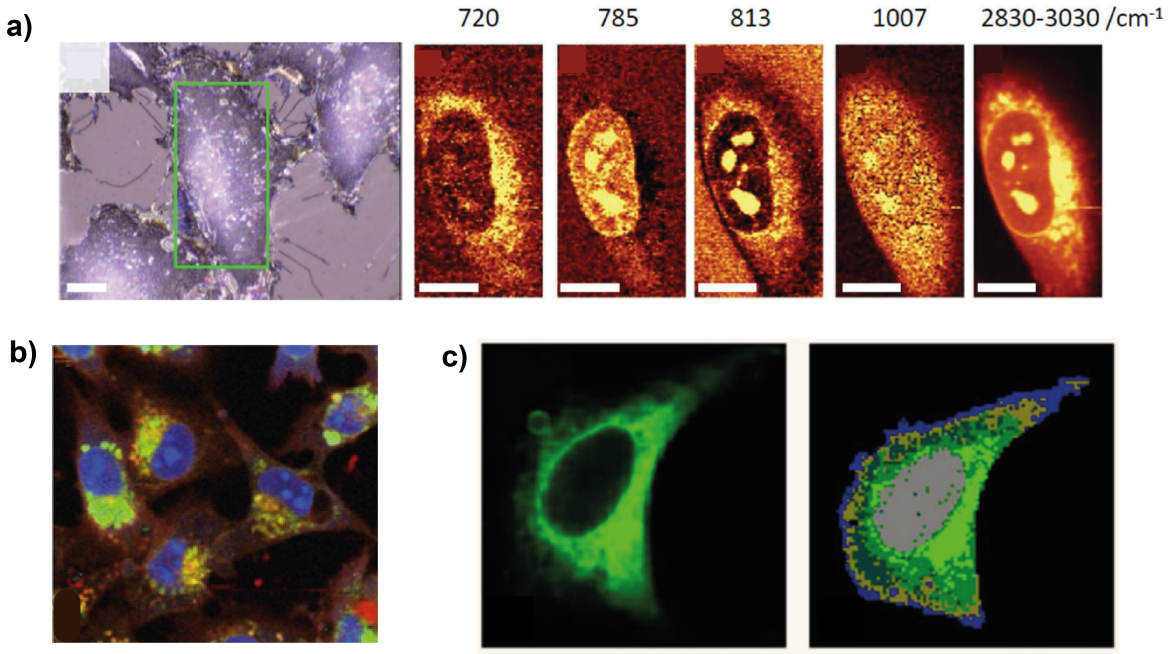

Fig. 1.12 Raman microscopy can be used for live cell mapping. a) The simplest spatial maps are obtained by peak integration of the Raman spectrum. These were obtained by integration of characteristic bands for phospholipids (720 cm^{-1}), DNA & RNA (785 cm^{-1}), RNA (813 cm^{-1}), proteins (1007 cm^{-1}) and all biomolecules in the range of 2830–3030 cm^{-1} [20]. b) Raman microscopy can reveal intracellular components such as actin (red), nucleus (blue) and golgi apparatus (green). This study developed a mutual information approach to compare to fluorescent dyes [21]. c) Mitochondria have also been imaged with Raman microscopy and co-registered to MitoTracker Green [22].

altered lipid metabolism in cancer cells as compared to non-malignant cells, relying on organelle classification to examine lipid droplets as described above [137].

Another important way that Raman microscopy has been shown to distinguish cells is in their progress through the process of normal division and growth, known as the cell cycle. The first phase after division, G1 phase, was first differentiated via nucleic acid concentrations by Notingher et al. [143] and the other cell cycle phase (G0/G1/G2/M phases) cells were later discriminated at 97% in other work [144, 145] with correlation to confluency [146].

Observing cellular differentiation is a key example of the capabilites of Raman microscopy. Differentiating stem cells (cells that are becoming specialised) were measured by Notingher et al [143]. In this work, it was observed that there were significant differences in nucleic acids after differentiation, with the RNA peak ($813\,\mathrm{cm}^{-1}$) decreasing by 25%. A longer time course study was later done on cardiac cell differentiation from stem cells, observing this process online with Raman spectral changes at 482 and $577\,\mathrm{cm}^{-1}$ [147]. Further to this, stem cells were observed to have distinguishing features even before differentiation [148] and that differentiation was linked to tumour progression in fixed cancer cells [149].

The motivation for doing experiments like these in live cells was independently justified in work that found that detrimental artefacts were produced by fixing the cells in paraformaldehyde so that cellular classification was less effective [150]. Some of these Raman microscopy studies also utilise the advantage of online detection of changes, where the cells are characterised whilst they are still alive so that further experiments, like waiting for the next stage of the cell cycle or further differentiation, are possible. These time course studies have the advantage that each cell can act as its own control, meaning small chemical changes can be detected and understood in relation to the changes in the cell. This is a clear advantage of the label-free and non-destructive nature of Raman microscopy, where alternative techniques such as mass spectrometry and fluorescent dyes interfere with the system under interrogation.

A general weakness of the Raman studies listed above is the difficulty involved with transferring them to different instruments and different research groups. It has been observed that even supposedly identical protocols and instruments on different sites present variations in the data that must be considered and overcome [151]. Furthermore, most studies have not published their data analysis techniques, perhaps due to restrictions on the commercial software used. A final weakness that is broadly true is that there is a lack of explicit consideration and justification for the live cell protocol used in the experiments.

Apoptosis

Apoptosis is the process of controlled cell death and has been repeatedly been investigated by Raman microscopy. Uzunbajakava et al. observed dense nuclear fragmentation during apoptosis in fixed cells, with DNA observed in much higher concentrations than in control cells [130]. DNA breakdown was observed in other work, where apoptosis was linked to DNA base degradation observed in bands around 782, 788, and 1095 cm^{-1} [152], considered to the DNA phosphdiester backbone and nuclei acids disintegrating [153]. Other classes of molecules were observed to change through the apoptotic process, including a decrease in proteins (1005, 1342 cm^{-1}), phosphodiester bonds (788 cm^{-1}) and an increase in the concentration of lipids (1303, 1660 cm^{-1}) [154, 155]. Subsequently to this, different processes of cell death started to be distinguished. For example, the cellular changes instigated by ricin and sulphur mustard were distinctly classified, as was the pathway of death between apoptosis and necrosis [156]. The role of lipid membranes in this classification has recently been acknowledged [157]. Autophagic apoptosis is another processes of cell death that was characterised by Raman microscopy [158]. Raman microscopic investigation of apoptosis has benefited from organelle and chemical classification by focusing on mitochondria and the associated group of molecules called cytochromes, which are involved in oxidative phosphorylation controlled by the mitochondria. Mitochondrial metabolic rate decrease in death (at 1602 cm^{-1}) was first observed in yeast cells by Naito et al. [159]. This was later repeated in human cells, where it was observed that active mitochondria contained this signal, and that it was related to relative ion concentrations [160]. Cytochrome c is known to be dramatically changed in apoptosis [161, 162, 133], so it was useful for this to be strongly detected in Raman spectroscopy [133] via Resonant Raman scattering at 532 nm. The release of cytochrome c during apoptosis (Section 1.1.2) was confirmed via co-registered fluorescence and Raman microscopy [163] and in co-registration to mitochondria [164].

Oxidative stress

Oxidative stress is a cellular state that can be indirectly measured by Raman microscopy in single live cells, including as part of the process of apoptosis. It is a state of high concentration of reactive oxygen species (ROS), and these have effects on cellular components such as DNA, lipids and proteins.

In one of the most comprehensive studies of ROS effects via Raman spectroscopy, Yadav et al. [165] studied cell damage under the application of a cancer chemotherapeutic, doxorubicin. They observed that that DNA that was co-localised with mitochondria increased

seven-fold under ROS-induced damage. One proposed mechanism for this is that the ROS damage the functionality of the existing mitochondrial DNA so that more must be synthesised to compensate. DNA damage was also observed by live cell Raman microscopy under the application of intense laser light that revealed the breakdown of chromosomes, in one of the earliest cell studies [166]. Induction of oxidative damage by Fenton's reaction was also observable by this technique, where Fenton's reaction consists of the production of reactive oxygen species by (1) $Fe^{2+} + H_2O_2 \rightarrow Fe^{3+} + OH\cdot + OH^-$ and then (2) $Fe^{3+} + H_2O_2 \rightarrow Fe^{2+} + OOH\cdot + H^+$ [167]. Under this reaction, the peak ratio 1050/1095 cm^{-1} correlated well with later state-of-the-art flow cytometry [167]. ROS generated from the Fenton reaction was also observed to breakdown the phosphodiester backbone of nucleic acids, and Raman microscopy is therefore shown to be an excellent non-invasive tool for the detection of oxidative stress. Lipids are another class of chemicals that have been shown to change in conditions of oxidative stress. Various live cell Raman microscopic studies have showed decreased lipid content in the presence of by processes such as lipid peroxidation [168, 167], disruption of mitochondrial lipids [165], and the creation of lipid radicals [139].

The main focus of live cell Raman microscopy in proteins and ROS has been towards cytochromes, which are heme containing proteins associated with mitochondria. From their Raman spectrum it is possible to gain information about their redox state, that is influenced by the surrounding level of oxidative stress as seen in extracellular experiments [169]. This redox state is often measured in Raman spectroscopy by measuring cytochromes, where a higher peak intensity at 750 cm^{-1} corresponds to more oxidised cytochrome molecules. These cytochrome molecules are taken as an indicator of the redox state of the cell. Oxidised and reduced forms of cytochromes b and c were only all detected in living cells via Raman microscopy approximately five years ago [170]. This has been seen in live cells with oxidative stress from hydrogen peroxide associated with a decrease in reduced cytochrome c in the cell centre. This is in accordance with the idea that cytochrome c is released from mitochondria in periods of stress and apoptosis [139, 171]. Furthermore, the Raman spectroscopic observation of an increased quantity of reduced cytochrome c from sodium dithionite is claimed to lead to increased ROS during its subsequent reoxygenation [172, 173].

Overall, effects of ROS have been seen with Raman microscopy in live cells, though the data are complex, and more work remains to be done on these topics. This includes developments to Raman protocol, as some experiments have seen photobleaching of cytochromes [174], as well as considering data analysis protocols such as Biomolecular Component Analysis from Yadav et al. [165].

Metabolic state

As with oxidative stress, metabolic rate is a key biological concept linked with apoptosis and mitochondrial membrane potential. It has also been measured by live cell Raman microscopy in various indirect ways. Firstly, mitochondrial respiration is a highly efficient metabolic process occurring in healthy cells. When apoptosis triggers are present (such as drug-inducing apoptosis), increased mitochondrial activity is associated with increased protein levels in the mitochondria. These increased protein levels can be detected with Raman microscopy as correlated with oxidative phosphorylation levels as measured later with a spectrophotometer [165] . Secondly, when a cell such as a cardiomyocyte is energetically compromised (ie low ATP levels), cytochrome b and c levels drop and the mitochondial membrane is depolarised [139]. The decreased presence of reduced cytochrome c associated with ATP depletion can be observed by Raman microscopy [172]. Finally, the termination of metabolic activity can be detected in living cells where hydrogen has been replaced by deuterium (incubation in heavy water) by measuring the spontaneous Raman peaks [175].

1.3.3 Prospects of live cell Raman microscopy to complement NVC measurements

Live cell Raman microscopy has been demonstrated as a useful tool in the analysis of single cells, particularly in the areas of organelle classification, and apoptosis, including study of cytochrome c. Due to improved detection sensitivity and data analysis, it is likely this progress will continue in the future. Here, we propose combining the abilities of live cell Raman microscopy with NVC sensing. This will allow for detection of cells and organelles, as well as complementary metrology of biological processes. It is also useful that Raman microscopy is able to detect diamond signal [176].

1.4 Project motivation and outline

Mitochondrial membrane potential in cells remains a critical biological parameter that is related to many important processes such as apoptosis, metabolic rate and oxidative stress. However, investigation of the role of $\Delta\Psi_m$ in these biological processes remains limited due to the current state-of-the-art methods for measurement, particularly fluorescent dyes, which are often toxic and photobleaching.

Nitrogen Vacancy Centres (NVCs) in nanodiamond and Raman microscopy are techniques that have recently been developed in the measurement of cells and respectively give

rise to electrical and chemical sensing measurements. The aim of this work is to develop electrical and chemical sensing methods that enable detection of changes in $\Delta\Psi_m$ in single cells, particularly for the application to detection of apoptosis in cancer cells. We propose to use the sensitivity of NVCs to electric field to directly measure the mitochondrial membrane potential, and simultaneously measure chemical changes via Raman microscopy.

One thing that has restricted the application of NVCs in this way is the lack of specialised microscopes that include biological compatibility, sensitive photodetectors, and microwave delivery. In addition, the width of fluorescence spectrum of the NVC reduces the ability to co-register with fluorescent dyes such as those that are used for organelle staining. This leads to difficulties in making and verifying intracellular measurements. Furthermore, the biological impacts of nanodiamonds have not been fully explored, with most investigation limited to cell viability testing. Raman microscopy also faces challenges, including a need for greater understanding in the experimental and analytical protocols that are used for intracellular segmentation.

To achieve the goal of complementary NVC and Raman measurement in cells, several parallel lines of development have been necessary. In this thesis, Chapter 2 outlines the construction of a dedicated microscope to measure both NVC fluorescence and Raman spectroscopic signal simultaneously, demonstrating the design considerations and effectiveness of the instrument. This instrument overcomes the current challenges by combining photobleaching-free, long time-course, single cell microscopy that avoids the need for fluorescent dyes by observing cells, organelles and nanodiamonds via Raman signal under a common 532 nm excitation. Chapter 3 outlines the development of protocols and analytical techniques for live cell Raman microscopy and the optimisation of them for this work, providing insight into the field with a thorough investigation of parameters. Chapter 4 investigates the impact of nanodiamonds as nanoparticles for biological sensing, including surface modifications like oxidation. This impact is evaluated on cells at a deeper level than viability, in ways such as uptake and oxidative stress.

Finally, Chapter 5 discusses the impact and limitations of this project, drawing conclusions and proposing next steps in the development of NVCs and Raman microscopy to measure mitochondrial membrane potential.

Chapter 2

Characterisation of a combined Nitrogen Vacancy fluorescence and Raman microscope

Figure 2.4 diagram was created by Dr Jonghee Yoon. Some LabView instrumentation programming was completed by Jeffrey Holzgrafe, Dr Helena Knowles and Alexander Grigoroiu. Jeffrey Holzgrafe also added temperature control to the microscope. All other work in this chapter was completed by Ben Woodhams.

2.1 Introduction and Motivation

To measure mitochondrial membrane potential ($\Delta\Psi_m$) by simultaneous Nitrogen Vacancy Centre (NVC) sensing and Raman microscopy, it is necessary to construct a dedicated microscope that is capable of acquiring these sets of data, unlike conventional microscopes. A dedicated microscope also allows custom design choices including: evaluations of wavelength; maximising sensitivity of Raman spectroscopy; optimising spatial scanning; the orientation of the sample and optics; and the type of spectrometer. Each of these design aspects has been considered to achieve the maximum performance of the dedicated microscope.

This chapter begins by describing some of the instrumentation development and multimodal combinations already achieved for both Raman microscopy and NVC sensing, in order to consider how this thesis might develop them further. The next section then outlines more specific design considerations for the custom microscope and describes the reasoning

for the decisions in light of the existing literature. After this, the instrument is characterised and evaluated on whether the predicted advantages are successfully realised, and whether it achieves the parameters necessary for measurement of $\Delta\Psi_m$.

2.1.1 Innovations and combinations in Raman microscopy

Raman spectroscopy instrumentation has been developed in various ways in the recent past, including: the first adaptions for live cellular measurements [177]; line scanning systems [164], to collect more data simultaneously; spatially offset systems [178, 164], to acquire data at depth in scattering media; wide-field systems [179, 180], to enable increases in acquisition speed; miniaturisation advances, for the portability of measurement systems [181]; and LED instruments [182–184], to avoid the need for laser illumination of samples. Another recent development is a type of Raman spectrometer that has High-Throughput Virtual Slit (HTVS™, Tornado Spectral Systems, Canada) technology, that was developed to provide higher light throughput for biological applications [185].

Combinations of multi-modal systems including Raman scattering detection have also been built, with Atomic Force Microscopy (AFM) [186] and Laser Ablation spectroscopy [187]. Other methodologies combined with Raman spectroscopy include: patch clamp [188], for electrophysiological measurement; Optical Coherence Tomography (OCT) [189], for microstructural imaging; AFM, for measurements that need to relate chemical and shape changes of nanoparticles [186]; and light sheet Raman for acquisition of data in thick specimens [190].

2.1.2 Innovations and combinations in NVC sensing

Microscopes to measure nitrogen-vacancy centres have also been developed over time. This includes the development of systems that: use ultra-high power microwaves [191]; do not rely on microwaves [192]; achieve super-resolution [193–197]; exhibit fast 3D tracking [198]; have a large field of view (4 mm) [106, 199]; and use solid immersion lenses to improve counts [200]. There have also been improvements in readout schemes and protocols [201].

NVCs have also been used in combination with other techniques, including microscopes with AFM [202–207], including incorporating commercial instruments ([201]) and later co-registration with Tunnelling Electron Microscopy (TEM) [208, 209].

2.1.3 Summary

From these examples, it is possible to see that both Raman and NVC microscopes have been improved upon and advantageously combined with other imaging techniques. However, there remains an opportunity for the power and precision of NVC sensing to be combined with complementary sensing of molecular bonds via Raman spectroscopy. This electrical and chemical sensing approach will enable the measurement of mitochondrial membrane potential in cells, unlocking new understanding of biological processes like apoptosis. To achieve this, the NVC sensing must be able to sense an electric field of $\sim$10 000 V/mm over (a voltage of 100 mV over a distance of 10 nm [42, 210]) over a period of minutes [60]. From experience outlined in Chapter 3, Raman spectroscopy needs to be able to sensitively and rapidly locate peaks over a few seconds.

Given this biological aim, and the techniques proposed to achieve it, there remain many design choices that need to be made for the optimum components and parameters.

2.2 Design considerations for the custom optical microscope

2.2.1 Wavelength considerations

There are multiple different considerations in choosing an excitation wavelength for this instrument. Nitrogen Vacancy Centre excitation is optimised when the NV^- excitation spectrum is at a maximum, and when population switching to NV^0 is minimised. By experimentally investigating these factors, Aslam et al. found that 480–610 nm was an advantageous range for excitation, with 510–540 nm as the optimal wavelengths [78]. In NVC excitation, 532 nm is the standard wavelength used [81], although some experiments use 561 nm [211, 212] and 575 nm [213].

For Raman spectroscopy, wavelength is a parameter that must be optimised by compromise between signal strength and background fluorescence. Raman signal varies by approximately the inverse fourth power of wavelength [214] suggesting that shorter wavelengths would be advantageous for Raman studies. However, a major challenge in this regard is cellular autofluorescence, i.e. fluorescence arising from molecules intrinsic to cells that are excited by optical illumination. For HeLa cells, it has been observed that 488 nm and 514.5 nm produce 167$\times$ and 12$\times$ higher autofluorescent background than 532 nm, whereas the Raman signal varies only within a factor of two, implying that 532 nm is advantageous for this application [133]. Furthermore, Hamada et al. find that 633 nm reduces the Raman

signal by a greater amount than desirable, and conclude that 532 nm is the best wavelength to image cells [133].

In addition to this balance between signal and autofluorescence, it is important to consider the signal enhancement received via Resonant Raman scattering. If the excitation wavelength coincides with an energy transition of the molecule, then Raman scattering becomes greatly more probable, and therefore the signal is much clearer. For 532 nm, apoptotic proteins called cyctochromes become resonant, leading to their observation at 753 cm^{-1}, 1127 cm^{-1}, 1314 cm^{-1} and 1583 cm^{-1} [133]. This is useful as these chemicals are intricately linked with cellular processes that affect membrane potential, and therefore choosing this wavelength will allow us to investigate biological problems by both NVCs and Raman spectroscopy simultaneously.

Selection of 532 nm as the excitation laser means that the NVC zero phonon line is at 3098 cm^{-1} (637 nm). This means that we cannot spectrally differentiate the Raman Carbon-Hydrogen (CH) vibration peak from the NVC fluorescence. Therefore, we chose to use a dichroic beamsplitter at 605 nm (2270 cm^{-1}) to direct all of the Raman signal at lower wavenumbers to the spectrometer, and all of the longer wavelengths to an Avalanche Photodiode for NVC fluorescence detection.

Although this means that some Raman signal is not measured, and that it becomes noise on the fluorescence channel, this compromise does allow full capture of the NVC signal. There are more details on this in the spectral throughput results below.

2.2.2 Selection of laser type

After choosing the wavelength, it is then necessary to consider the other required properties of the excitation laser. One of the more restrictive requirements is narrow linewidth. Lasers naturally produce light over a small range of wavelengths, and broader linewidth is known to reduce Raman data quality [164]. In order to understand the effect of this parameter, a cell spectrum was closely fitted and then convolved with gaussian peaks of varying linewidths using the Matlab *conv2* function (Figure 2.1). It was found that 30 GHz and 3 GHz noticeably reduced the height (and therefore contrast) of the Raman signal peaks. Therefore a linewidth of 0.3 GHz and below is an appropriate requirement for the laser source.

Diode-pumped solid state (DPSS) lasers have gained in popularity for Raman spectroscopy, as they can generally fulfil this condition [215]. Since NVC emission is comparatively insensitive to linewidth, excitation can be performed by a cheaper conventional diode

laser [216]. Nevertheless, DPSS lasers also exhibit low noise, and have therefore been chosen for sensitive NVC experiments [105, 106, 217].

Multiple 532 nm DPSS lasers were investigated for purchase, including the: Cobolt Samba 532, with linewidth <1 MHz; Lasos GLK DPSS, with linewidth <1 MHz; and Laser Quantum Torus with linewidth ∼1 MHz. Correspondence with these companies was conducted to compare other physical parameters such as noise, power stability, wavelength stability, mean time to failure, as well as general parameters such as cost and delivery time. The companies specified that some of this information was to be kept private. Under consideration of all these parameters, the Cobolt Samba 532 was found to be most suitable.

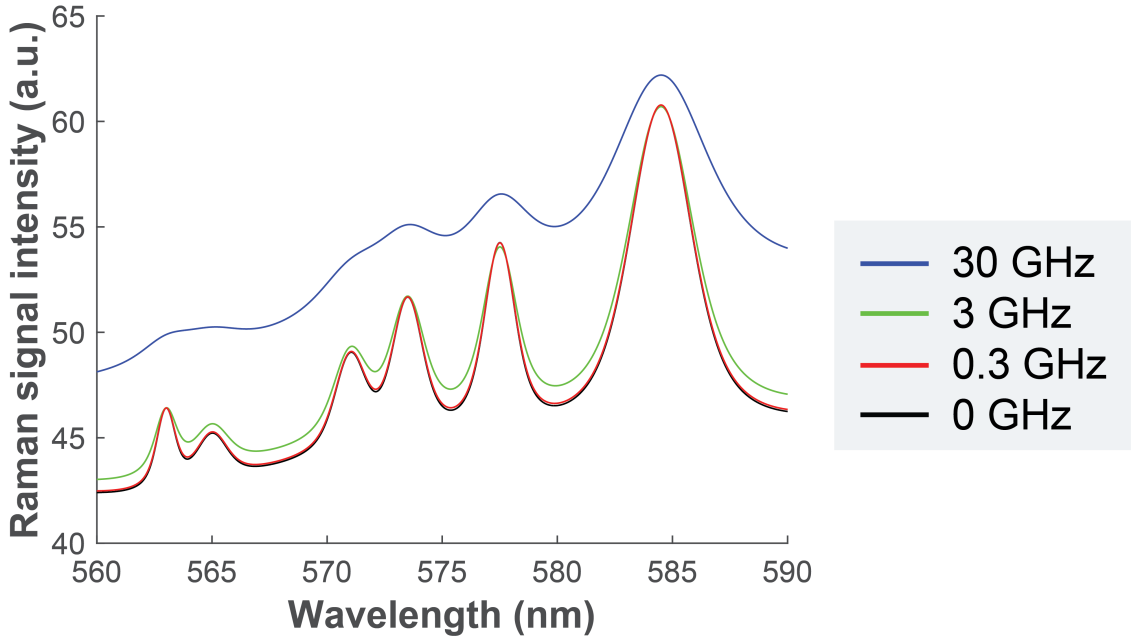

Fig. 2.1 Simulation of the effect of different laser excitation linewidths on the collected Raman spectrum. The peaks are a close representation of a cell spectrum in terms of intensity and wavelength (excluding noise). These wavelengths correspond to a wavenumber range of 940–1850 cm^{-1}.

2.2.3 Sample and optics orientation: Upright or inverted

Biological microscopes can be divided into two categories depending on orientation of the optics relative to the sample. It is possible to interrogate cells on a substrate covered in liquid either from above in upright configuration, or through the substrate in inverted configuration. Upright configuration reduces the ability of the substrate or air gap to interfere with the measurements. However it does require the objective to be suitable for water immersion

and possess a longer working distance due to fluctuations in the position of the cell surface. There may also be disadvantageous refractive index changes in different media, and from medium to cells.

In contrast, an inverted configuration has the advantages of: keeping the optics separate from any environmental conditions such as temperature or water; reducing the amount of vertical movement of the objective when loading a sample; and the potential for using a numerical aperture via an oil immersion objective lens. Furthermore, it is possible to use coverglass corrected objectives to counteract the problem of seeing through a sample, although this does place limitations on the lateral range of motion by the fact that thin substrates cannot be made arbitrarily large. Additional requirements on substrates are imposed by Raman spectroscopy, which is outlined in Section 3.2.1. This substrate is held between metal pieces that screw together with silicon gel creating a water-tight seal. This was designed in Autodesk Inventor™ and fabricated by the Cambridge University Department of Physics workshop. Temperature control was then added by Jeffrey Holzegrafe by addition of a flexible resistive foil heater (HT10K, Thorlabs).

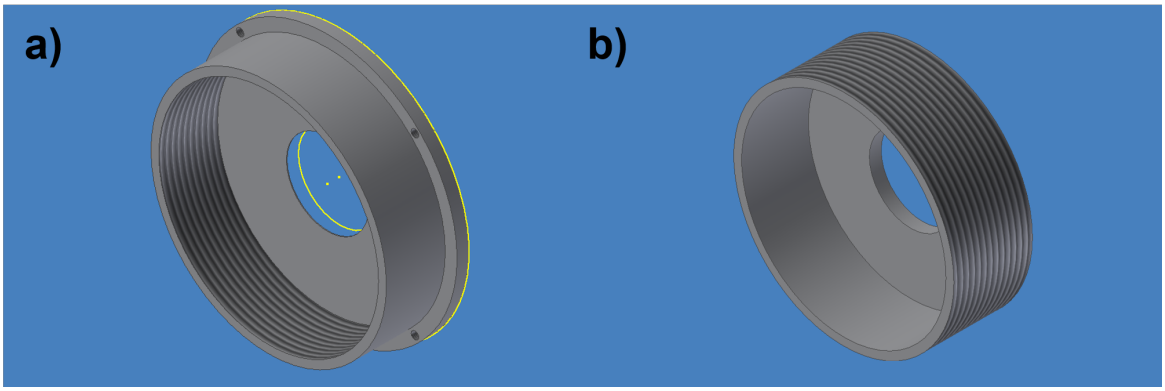

Fig. 2.2 A Computer Aided Design image of the water-tight substrate holder. a) The base piece that is held in place on the nanopositioner stage. b) The top piece that screws into the base, clamping the substrate between them.

2.2.4 Dimensions of spatial scanning

The physical dimensions (0D, 1D, 2D) of the excitation and signal collection are of important consideration as they affect issues such as imaging speed, field of view, resolution, and signal. Raman spectroscopy has been achieved by illumination via: zero-dimensional confocal point illumination and detection [218], one-dimensional line scan excitation with point spectra

gathered along that line [164]; and two-dimensional illumination of an area the size of a cell to collect one average spectrum [219]. Each of these formats has particular strengths.

Confocal point measurement can be used to generate high-resolution Raman maps of cells, and is therefore useful in identifying cellular components and making measurements of a specific axial slice [21, 220]. This has been expanded in work by Kong et al. to make scans of multiple points which are then independently and simultaneously measured [221]. One dimensional line scanning has been shown to be faster to achieve the same signal intensity compared to confocal point scanning [222, 164]. For a two dimensional excitation, cell-size laser beam illumination has been useful in applications that require very high throughput, such as cellular classification for disease on thousands of cells [219].

In the proposed bespoke microscope, laser excitation is from a common source and the Raman and NVC collection channels are partly shared. Therefore it is also important to consider NVC excitation and collection when deciding on the physical dimensions of measurement. There are two predominant dimensional formats of NVC measurement: Two dimensional wide-laser beam excitation with a wide-field camera detection; and confocal point illumination coupled to a single point photon detector.

Single point confocal microscopes are the standard instrument of NVC sensing as these allow removal of much of the background signal at the collection pinhole [198, 74, 86, 223, 78, 209]. However, some applications require two dimensional excitation and collection. One example of a recent wide-field camera application is to map neuronal temperature, where a wide laser beam ($\sim$10 mm) was used to excite thousands of NVCs, which were then collected as a wide field image in an sCMOS camera [105]. There is technical complexity and cost for this type of measurement, with both phase lock-in detection and specialised cameras required [224].

Overall, confocal point scanning is the most suitable option for Raman and NVC measurements. This is because it encompasses the advantages of axial depth scanning, organelle resolution and low technical complexity. For this, the sample will be scanned with a translation stage (an nPBio200 Piezo Nanopositioner Stage on a Zaber ASR100B120B-E03T3), rather than a mirror galvonometer. This has the dual advantages of increasing the area that may be scanned to larger than the objective field of view, and avoiding spherical aberration of the illumination spot as it reaches the edge of the field of view. The nanopositioning translation stage has a settling time of under 20 ms, which is fast enough for scanning and tracking required.

2.2.5 Detectors: spectrometer and NVC photon detection

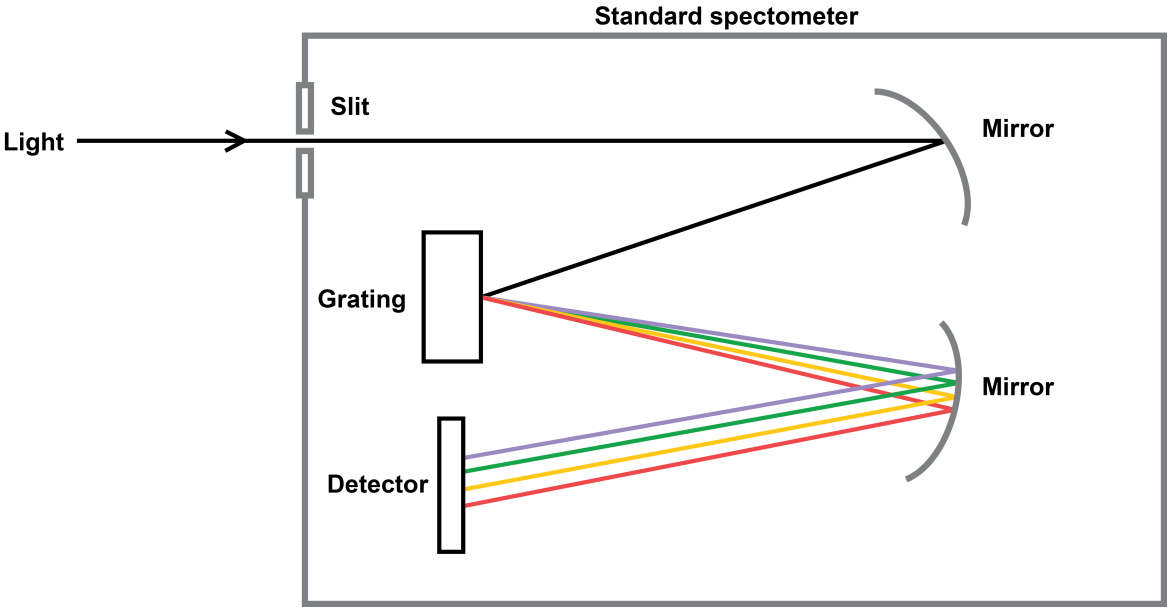

Fig. 2.3 A diagram of a conventional spectrometer. Conventional spectrometers remove 80–90 % of the light at entry due to the slit [23].

Standard spectrometers remove 80–90 % of the light at entry due to the slit [23]. The slit is used to select a narrow portion of the input light that is then dispersed by the grating. A narrower slit leads to a greater dispersion at the grating, leading to improved spectral discrimination [225].

Since Raman spectroscopy and many applications depend on both high spectral resolution and high signal throughput, there have been several attempts to improve this. These include improvements such as increasing the quantum efficiency of spectrometer cameras [226], adding a curvature to the slit [227], using a Hadamard entrance pattern [228–231], observing the zeroth order diffraction [231] and using refocusing optics to avoid the need for a slit [185]. To maximise the sensitivity for detection of the weak Raman scattering signal in the microscope, a specialised spectrometer using refocusing optics (Hyperflux™ U1 as manufactured by Tornado Spectral Systems, in Canada) was selected for use in this instrument.

This spectrometer provides far higher throughput than conventional Raman spectrometers, with the drawback that the wavelength range is fixed at manufacture. This is suitable here as the wavelength range for Raman spectroscopy is known and fixed for all experiments.

For single point detection of NVC fluorescence, Avalanche Photodiodes (APDs) are commonly used [232–241], although photomultiplier tubes (PMTs) have occasionally been

used [242–244]. This is probably because APDs exhibit higher quantum efficiency than PMTs in the longer wavelength range of the visible spectrum [245, 246], and therefore are selected for this custom instrument.

2.2.6 Other decisions

Several other options were considered in the construction of the bespoke microscope. In Section 1.2.2, it was described how continuous wave laser light and microwaves were able to perform measurement by the Optically Detected Magnetic Resonance (ODMR) measurement scheme. Recently though, new measurement schemes have been developed that rely only on optical control, without microwaves [247, 192]. This has the advantage that cells are not be exposed to microwaves that could potentially cause an adverse heating effect. However, all optical techniques require precise timing control and instrumentation to create pulses, adding complexity that is not necessarily required for the desired measurements. Therefore, it was decided that this could be added to the instrument at a later stage, if it were found to be necessary.

Another hardware consideration for NVC measurement is the addition of magnetic fields. External magnetic fields are sometimes applied to NVC experiments to aid in spatial orientation tracking [14]. This was also considered non-essential for the objective of measuring mitochondrial membrane potential, but could be added to the setup later if required.

2.2.7 Design conclusions

The options for building a custom NVC and Raman microscope have been carefully considered with reference to the literature. The resulting design is included in Figure 2.4. This includes key advantages such as simultaneous measurement of both NVC fluorescence and Raman spectroscopy including: low background fluorescence from cells at 532 nm; resonance Raman for apoptotic proteins; a resolution suitable for intracellular organelles; a high-throughput spectrometer for sensitive measurements; and the convenience of sample switching on an inverted setup.

The microscope was built and characterised to determine whether the design and equipment choices were successful in achieving the aim of measuring mitochondrial membrane potential. The performance characterisation consisted on quantifying spectral transmission, NVC and Raman signal, spatial resolution, and the overall measurement capability.

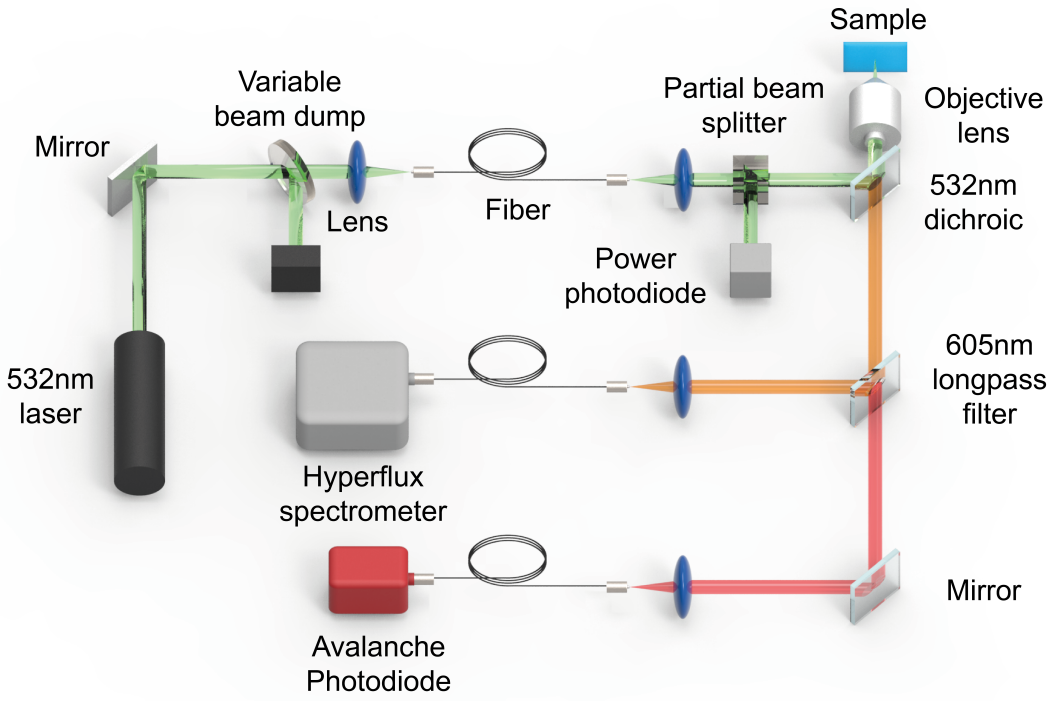

Fig. 2.4 The optical setup combines simultaneous fluorescence detection and Raman spectroscopy. The fluorescence channel is suitable for detecting Nitrogen Vacancy Centres (NVC) in diamond using an Avalanche Photodiode (>605 nm) with simultaneous Raman spectroscopy achieved using a Tornado Hyperflux™ U1 spectrometer. Both processes are dependent on excitation by one 532 nm laser, and both are collected confocally.

2.3 Materials and Methods for Microscope Characterisation

2.3.1 Nanodiamonds and nanodiamond test sample

The nanodiamonds used in the experiments were sourced from NaBond, with a nominal size of 45 nm, and received in powder form. These nanodiamonds were specifically selected for these characterisation measurements to have higher nitrogen vacancy implantation than those available from other suppliers. A nanodiamond test sample was prepared on quartz. The quartz coverslip (CFQ-2520, UQG optics, UK) was sonicated (Sonorex Digital 10P, Bandelin, Germany) for 30 min in acetone and then isopropanol to clean any dirt from the surface. The nanodiamonds were sonicated in ethanol at 0.4 mg ml^{-1} for 90 min to reduce aggregation. The nanodiamonds were then deposited on the quartz using a nebuliser (NE-U22-E, Omron,

Japan) and blown dry using compressed air to prevent contaminants from the solution being deposited on the substrate. This produced approximately 250 fluorescent points in an area of 50 µm × 50 µm, some of which are single NV centres, and some of which are multiple NV centres that are closely packed together.

2.3.2 Spectral transmission

Spectral transmission was modelled by downloading the factory specifications of all optical components and multiplying their fractional transmission profiles. A typical Raman spectrum of cell data and NVC spectrum from the literature [241] were also plotted on the same graph for reference.

Spectral transmission was measured using a white light source (Thorlabs, USA) put through a monochromator (CM110, Spectral Products, USA) with an average spectral full-width half-maximum of 5 nm. The light was then was passed through a fibre, and the output from the fibre was collimated by a triplet lens (TRH127, Thorlabs, USA) in place of the normal objective lens to maximise signal intensity. The throughput for the Raman and NVC fluorescence beam paths was measured using their incorporated respective detectors, the Tornado Hyperflux spectrometer and the Avalanche Photodiode. For the Raman measurement, calibration of the input light was performed using a calibrated reference spectrometer (Avantes AvaSpec ULS2048, The Netherlands) to normalise the results by dividing by the input intensity. This was not performed for the NVC signal as the Avantes spectrometer was far less sensitive at the longer wavelengths needed.

Errors were calculated by standard error in the mean across the Raman spectra, and poisson noise from the NVC Avalanche Photodiode detector.

The spectral variation in the detection of NVC fluorescence measured was used to determine the spectral contribution to signal loss. The NVC spectrum [241] was multiplied by the measured spectral transmission to produce an effective transmitted spectrum that can be collected in the NVC channel. The original NVC spectrum and the effective transmission spectrum were integrated to estimate the signal reduction as a result of spectral variation.

2.3.3 Optical signal intensities

At low power, NVC generally emit photons in a linear relationship to excitation power. However, under strong illumination, their rate of output photons is limited by the decay time required to return the centre to the ground state. This means that increasing laser power

produces less than a proportional linear increase in emission count rate, and the NVC count rate saturates.

For NV fluorescence measurement, the test sample was scanned to find single nitrogen-vacancy centres and the saturation curves were measured by varying the laser power and recording the counts. This gives a measure that is independent of laser power, and can therefore be compared to other reference NVC systems. A background was collected away from the NV centres and subtracted from this measurement. The Raman signal was evaluated by comparing the custom microscope with a Renishaw Confocal Raman microscope. The sample was chosen to be the gold standard method of interrogating a piece of silicon, with the laser power as 240 µW for 500 ms. The bespoke system was used with a 50× objective lens with a numerical aperture (NA) of 0.8, and the Renishaw system was used with a 50× objective lens with NA = 0.75.

Data were processed by subtracting the mean of a signal-free part of each spectrum (2500–3000 cm^{-1}) and then integrating the Voigt fit of the 1st order Silicon peak at 520.5 cm^{-1}.

2.3.4 Spatial resolution

Spatial resolution is a key characteristic to determine the capabilities of an optical system. The predicted confocal resolution is given by [248]:

$$\text{Confocal lateral resolution} = \frac{0.37\bar{\lambda}}{NA}$$

where

$$\bar{\lambda} = \sqrt{2}\frac{\lambda_{ex}\lambda_{em}}{\sqrt{\lambda_{ex}^2 + \lambda_{em}^2}}$$

For NVC fluorescence, with excitation wavelength as λ_{ex} = 532 nm and using the zero phonon line at 637 nm as the emission wavelength λ_{em}, and NA = 0.8, the resolution is predicted as 267 nm. For Raman signal, using diamond peak at 1332 cm^{-1} (573 nm), in the middle of the range predicts the resolution as 255 nm.

Nitrogen Vacancy Centre fluorescence spatial resolution was measured using the nanodiamond test sample. For lateral (XY) resolution, the sample was scanned to create multiple images of 10 µm × 10 µm, with square pixels of size 50 nm. Each point above 1 kcounts · s^{-1} was then selected as an NVC and the point spread function was then estimated by the Laplacian of Gaussian solution in Python *scikit-image.blob_log()* function. For the smallest of these, the spot was precisely fitted by a two dimensional gaussian function using the python function *scipy.optimize.leastsq*. The average width of these was taken as the resolution and

the error was estimated by dividing the standard deviation by the square root of 2 (for two samples - one in the x direction, and the other in the y direction).

For Raman micro-spectroscopic resolution, the same sample was scanned to create an image of 50 µm × 50 µm with square pixels of size 250 nm. The larger pixel size was used to reduce image acquisition time.

After the smallest detectable spots were chosen to measure the lateral resolution, these spots were moved in the perpendicular direction for axial (Z) resolution in steps of 1 µm to determine NVC resolution. 10 measurements were collected at each point and averaged. The standard error in the mean of these measurements is presented on the graph. The data points above 20% of the maximum intensity were fitted linearly, and this line was used to calculate the half-width half-maximum. The half-width half-maximum was taken as an estimate of the resolution, with the error estimated from the error in the fit. Raman axial resolution was not able to be measured due to a stage breakage. The nanodiamonds on this sample are essentially point sources relative to the size of the confocal optical resolution of the microscope, so they are a good measure of resolution.

2.3.5 Sensing capability of the instrument

The ability of the system to use nitrogen vacancy centres for metrology was evaluated by Optically Detected Magnetic Resonance (ODMR). ODMR involves scanning a microwave frequency to observe a characteristic drop in NVC fluorescence that reveals the presence of an NVC and provides data that can be fitted to determine physical quantities.

Optically detected magnetic resonance spectra were measured by continuous wave laser and microwave excitation. This was useful in determining the sensing capability of the instrument. A Stanford Research Systems SG384 signal generator was used to generate microwaves, which were then amplified by a Windfreak ZHL-42W+ microwave amplifier into an antenna of bent copper wire. Microwave frequencies were scanned between 2.81–2.91 GHz in 0.5 MHz increments at 7 dBm of microwave power with an integration time of 100 ms on each point. This was done in a random order to reduce any unwanted correlations with time.

ODMR contrast is the ability to see a dip in fluorescence at a specific microwave frequency. This is essential for NVC measurement and to confirm that a fluorescent point is an NVC, and so it is necessary to establish how quickly this can be seen. ODMR contrast was determined by integrating between the baseline fluorescence level and the dips below.

In addition to contrast, ODMR stability is an important parameter. NVCs are used to measure physical parameters by their effects on an ODMR spectrum. If ODMR spectrum dips move even when the physical conditions of the environment are not apparently changing, then their ability to be a reliable measurement tool is reduced. ODMR stability was measured by repeatedly measuring the ODMR spectrum and using the python *scipy.optimize.curve_fit* routine to fit two gaussian dips. The square roots of the diagonal values of the covariance matrix were used as errors. Pearson's correlation coeffecient (python *np.corrcoef*) was then used to determine correlation.

The ability of the system to resolve molecular bond vibrations in Raman spectra is largely determined by the ability to locate a peak on a spectrum. This was measured by fitting the main silicon peak ($520.7\,\mathrm{cm}^{-1}$) by a Voigt profile and taking the errors in the fit. Both the NV fluorescence sensitivity and Raman spectral sensitivity were plotted over time, and compared to appropriate thresholds for measurement.

2.4 Results of Microscope Characterisation

2.4.1 Spectral transmission

Light throughput in the system as a function of wavelength was first modelled (Figure 2.5a) and then measured into the two detectors in the system (Figure 2.5b). Normalised to direct input into a spectrometer, the Raman collection path collected a maximum light fluence at 593 ± 5 nm, with >40% of this signal intensity being collected in the wavelength range from 543–603 nm (wavenumber range 381–$2213\,\mathrm{cm}^{-1}$). The NV fluorescence collection path collects maximum light intensity at 773 ± 5 nm, and >40% of this maximum signal between 663–843 nm.

The measured light throughput as a function of wavelength is broadly comparable to the predicted spectrum, with a few minor differences. Firstly, the Raman collection path signal is non-uniform across the expected range. This is most likely due to interference effects, possibly at the detector where the spectra were sometimes observed to be double peaked. Another possibility is that the input triplet lens (TRH127, Thorlabs) or doublet lens that is just prior to spectrometer (AC254-045-A-ML, Thorlabs) are not perfectly achromatic. Another discrepancy is the slow increase on the slope on the NV collection path, which could also be a chromatic lens focus issue, or may correspond to the dichroic beamsplitter failing to meet specifications. Furthermore, we observe the NV collection path to have reduced detection

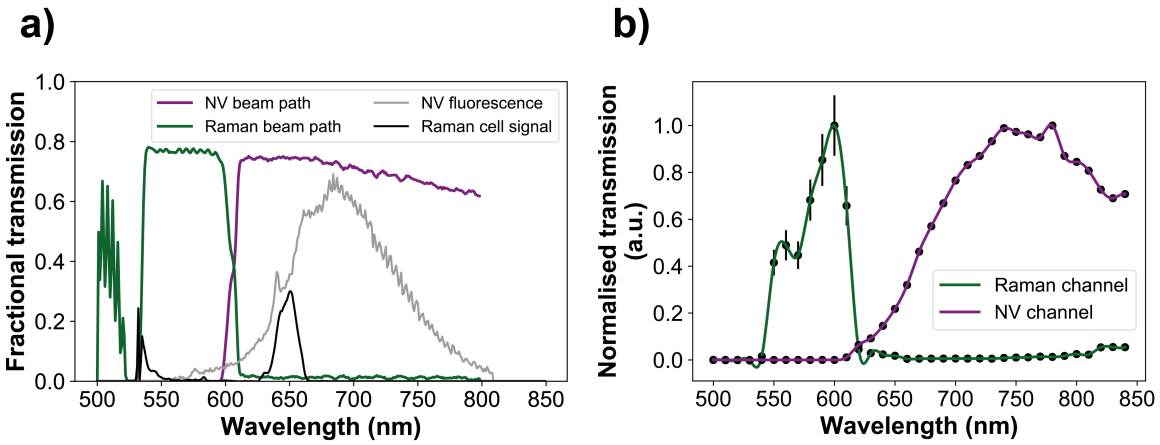

Fig. 2.5 Spectral transmission into the two detection channels - Nitrogen Vacancy (NV) centre fluorescence and Raman spectroscopy. a) A simulation created by combining spectral profiles of components. This is displayed as the fraction of light that would be transmitted at each wavelength. Spectral data was downloaded from the relevant manufacturers' websites. NVC and Raman cell data are shown for reference. b) The spectral transmission profile of light throughput as detected experimentally in the NV fluorescence Avalanche Photodiode and Tornado spectrometer that are the usual detectors in the setup. This was measured by sequentially changing a monochromator to input different wavelengths into the custom microscope. Both the Raman measurement and NVC measurement are normalised so that their maxima are equal to 1. Errors in the NV channel are too small to appear on the graph. The experimental profile (b) broadly matches the simulated profile (a), with some differences.

above 800 nm, which may be a result of reduced APD sensitivity above this wavelength that was not accounted for in the modelling.

The effect of these spectral profiles is to reduce the amount of light that was collected for NVC fluorescence and Raman cell measurements. For NVCs, the lower spectral throughput around 650 nm in the NVC channel (Figure 2.5b) causes a 38 % reduction in the amount of fluorescence that can be received by the detector. For Raman measurement, Figure 2.5a shows that cells typically have a strong peak around 650 nm ($\sim$3500 cm^{-1}). This is comprised of the water signal and signal from the bond between carbon to hydrogen (the CH peak). The CH peak is clearly outside of the range of detection for Raman detection in both the simulated and experimental results, negatively impacting the ability of the instrument to detect cells, and changes in cells. This is not the case with commercial Raman instruments such as a WITec confocal 300 alpha+ Raman microscope, as it is a loss unique to this combination instrument. On the other hand, the simulated and experimental Raman detection captures the 'fingerprint region' of the cells well, as this is below 588 nm (1800 cm^{-1} [127]).

2.4.2 Optical signal intensity

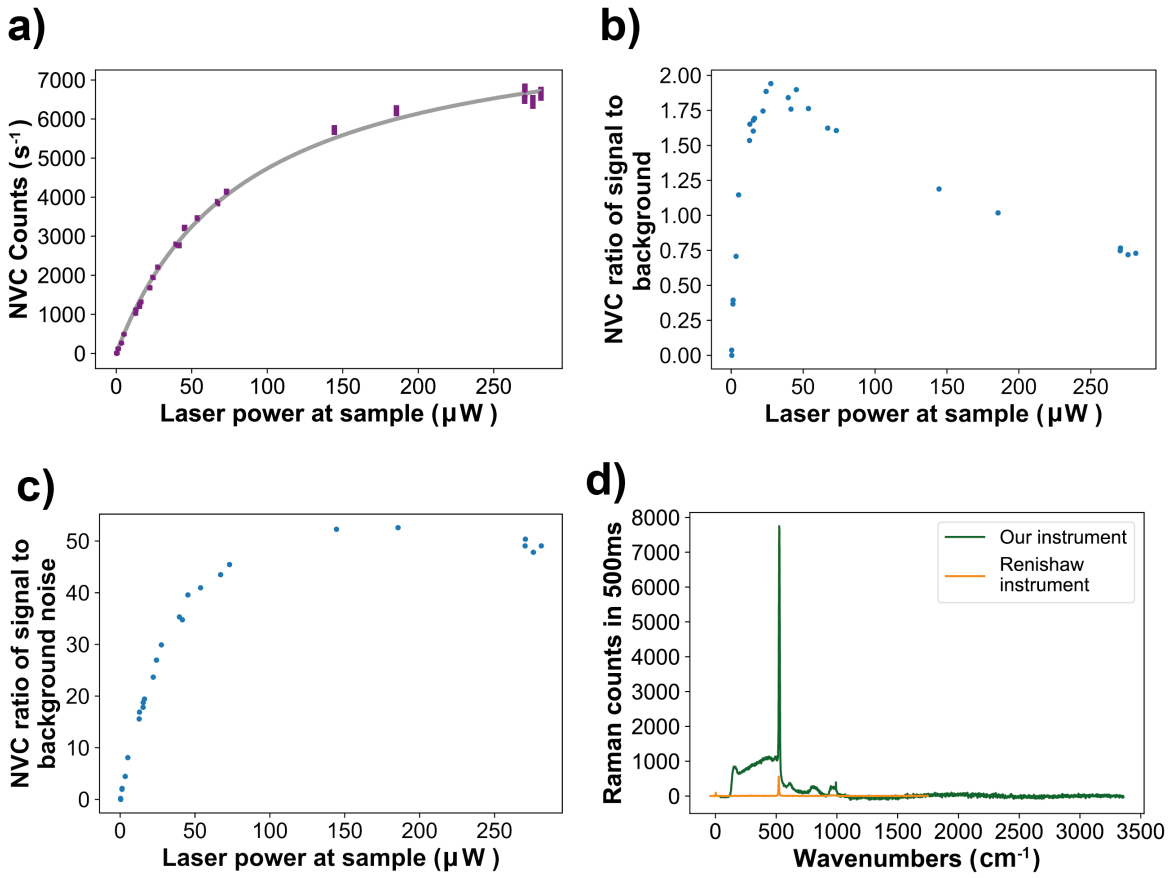

Fig. 2.6 a) NV centre saturation curve with half saturation NV counts at 4360 ± 70 counts $\cdot\, s^{-1}$. Vertical sizes are an estimate of errors from poisson shot noise. b) The NVC signal-to-background ratio as a function of laser power. The background comes predominantly from the slide of NVC, either by reflection or unwanted fluorescence. c) The signal-to-background-noise as a function of laser power. This is often a more relevant parameter to optimise in situations where the background can be subtracted a constant. d) Raman signal is dramatically increased on our system, relative to a commercial system, with our system achieving $18\times$ the signal-to-noise ratio due to the inclusion of the high throughput virtual slit.

Fluorescent signal was measured on standard samples of NV nanodiamonds to be 4360 ± 70 counts $\cdot\, s^{-1}$ at the saturation half-power of $85 \pm 3\,\mu W$ (Figure 2.6a). This is above measurements of detector dark counts at 40 ± 6 counts $\cdot\, s^{-1}$, and the 'white noise' of the laser focused on an empty area of the sample at 2930 ± 50 counts $\cdot\, s^{-1}$. This results in a signal to background ratio of 1.49 ± 0.03. This can be slightly improved by reducing the power to around $30\,\mu W$, as shown in Figure 2.6b. However, the background is fairly constant over

the sample, making the noise from the slide background and detector noise a more relevant parameter. The ratio of the signal to this noise is given in Figure 2.6, with a maximum shown around 150 µW.

These two different powers would be used in different situations. If a measurement of a single point is required to determine the presence of an NVC at a given location, (i.e. background is unknown) then 30 µW should be used. If a large scan is being performed for NVCs, then the background can be subtracted as a constant, and the faintest NVCs can be discriminated most easily at 150 µW. However, it is important to note that these powers are dependent on the specific format of NVCs on a quartz slide, and would be different for the noise levels inside a cell.

Raman signal was quantified on a standard Si sample by integration of the 1st order peak as 55 000 counts $\cdot s^{-1}$ at 137 µW (Figure 2.6d). This in greatly in excess of the noise on the detector at an equal bandwidth wavenumber range yielding a signal-to-noise ratio of 150 ± 30 in this experiment. This is $15\times$ the signal and $18\times$ the signal-to-noise ratio of the Renishaw inVia Raman Microscope.

2.4.3 Spatial resolution and field of view

A lower bound for lateral spatial resolution (i.e. the spatially smallest) was measured for both Raman and NV optical detection on a sample of deposited nanodiamonds. The smallest lateral spot size observed for NV fluorescence was 290 ± 30 nm (Arrow 1 in Figure 2.7a) and 290 ± 40 nm for a Raman spot (Figure 2.7b). The NVC resolution is close to, and consistent with, the predicted value of 267 nm, and the Raman resolution was slightly larger than the predicted value of 255 nm, although within error range.

In the axial direction, the spot size is 3.3 ± 0.3 µm for NV fluorescence (Figure 2.7c). Precision scanning with accuracy to 5 nm is achieved with a nanopositioner stage over a 200 µm × 200 µm × 200 µm field of view. These image scans are stable to within 0.5 µm over the course of several hours, making it easy to return to previously scanned diamonds. If needed, coarser scanning is possible with step size 0.16 µm over a field of view that is limited by sample holder design to 1 cm^2.

A demonstration co-registered scan was performed to produce Figures 2.7(b) and (d). Figures 2.7(b) and (d) both showed the same nanodiamond (or nanodiamond aggregate), as labelled '3'. The NVC scan also revealed another NVC centre that was not obvious from the Raman image. This made it clear that the nanodiamond fluorescence is a superior way of detecting nanodiamonds than Raman spectroscopy on the microscope.

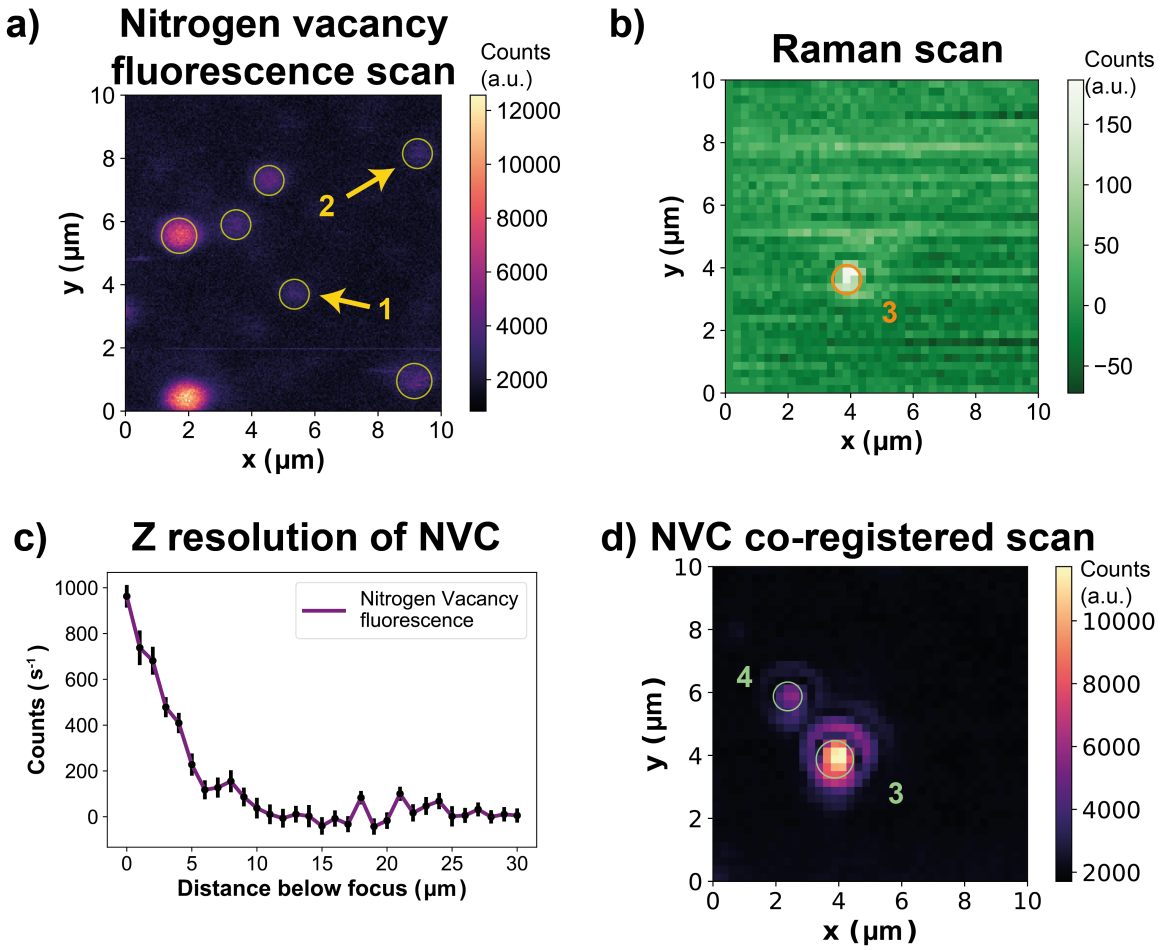

Fig. 2.7 a) Spatial scan of NVCs to determine lateral resolution in the fluorescence channel. The smallest spot size observed was 290 ± 30 nm (arrow 1), with arrow 2 measured at 300 ± 10 nm. b) Spatial scan of deposited nanodiamonds to determine the resolution of the Raman channel. The smallest spot size observed was 290 ± 40 nm, but this is signal-to-noise limited. c) Axial resolution was measured as 3.3 ± 0.3 µm for the NV fluorescence channel. Raman z resolution was not able to be measured due to an equipment malfunction. d) An NVC scan that was taken simultaneously with the Raman scan in (b), labelled '3'. It shows the same nanodiamond/NVC as (b), and reveals another that was not clear from the Raman image, labelled '4'.

2.4.4 Sensing capability of instrument

NVC sensing requires a fluorescence spectrum to be collected with respect to microwave frequency via the ODMR technique, examples of which are shown in Figures 2.8a and 2.8b after different numbers of scans. The contrast-to-noise ratio of the ODMR spectrum was measured at 31 ± 9 after 20 s of integration (Figure 2.8c), which is the time for a single scan. This agrees with the observation of ODMR dips in Figure 2.8a that are then confirmed after more averaging in Figure 2.8b. The observation of these dips after one scan is strongly beneficial for this study, as it allows rapid identification of NVCs that can be used for measurement.

ODMR stability measurements are displayed in Figure 2.9. These show that there are no significant trends in the data over a time period of 45 minutes. This should enable good sensitivity to external parameters.

An ODMR spectrum is shown in Figure 2.10a. Data were repeatedly collected from this NVC and averaged to ascertain the precision of the ODMR measurements over time. This is displayed for electric field in Figure 2.10b. It was found that a precision of 0.2% of the mitochondrial membrane potential ($\Delta\Psi_m$) within 3 minutes is suitable for the purpose of this project.

Raman sensing requires excellent spectral resolution so that different molecular vibrations can be resolved. We measured this parameter on the 1st order silicon peak (shown in Figure 2.10c) finding the Full-Width Half-Maximum (FWHM) to be $4.2 \pm 0.2\,\mathrm{cm}^{-1}$, which is comparable to the Renishaw system ($3.08 \pm 0.04\,\mathrm{cm}^{-1}$). By fitting it repeatedly over time, the Raman peak was quickly resolved to $0.05\,\mathrm{cm}^{-1}$ in 1 s (Figure 2.10d). Since $0.05\,\mathrm{cm}^{-1}$ is a typical value quoted for Raman spectral changes, this sensitivity is appropriate for measurement of cells.

2.5 Discussion

In this chapter, the design, construction and characterisation of a combined instrument for NVC fluorescence and Raman spectroscopy sensing was achieved. This is the first reported instrument to enable such combined measurement.

2.5.1 Spectral transmission

The first area of characterisation was optical throughput as a function of wavelength, and there are some compromises on the system because of this. For cell applications, this means

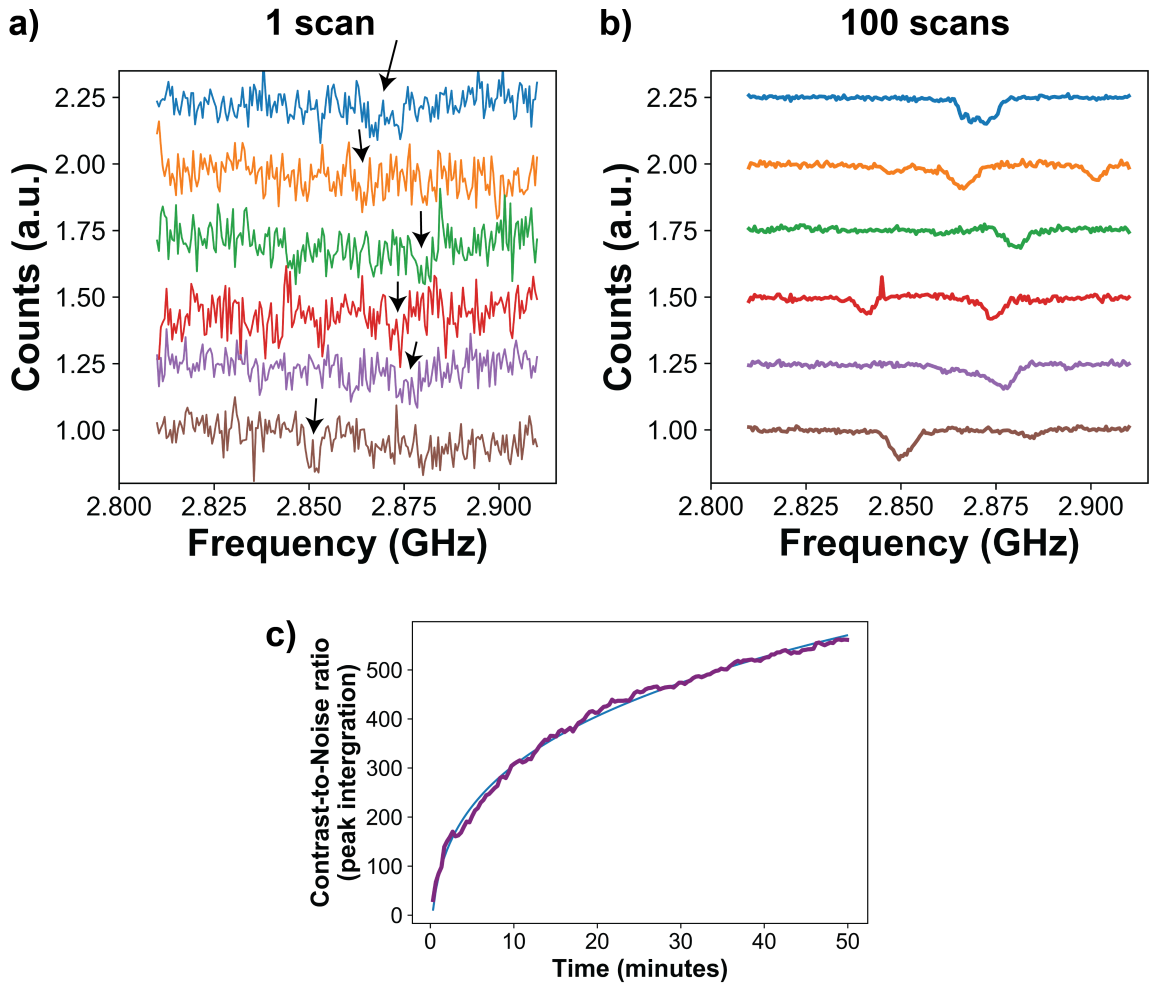

Fig. 2.8 a) Examples of ODMR spectra after 1 scan across the microwave wavelength range (2.81–2.91 GHz). Each colour corresponds to a different NVC. This shows that the ODMR dips (labelled) are observable even after only 100 ms of integration at each microwave frequency. b) The same NVCs, plotted with the same colour scheme, after 100 scans (∼30 minutes) clearly show ODMR dips below the noise. These are located in the same position as was observed in (a). Contrast of dip depth compared to the baseline NVC fluorescence is around 10% of counts. c) Contrast to noise ratio of an ODMR spectrum over time, as measured by peak integration. This was fitted with a power law, and increases with time to the power of 0.27, slower than pure noise averaging (power of 0.5). It is clear that the contrast is detectable at a few minutes or less.

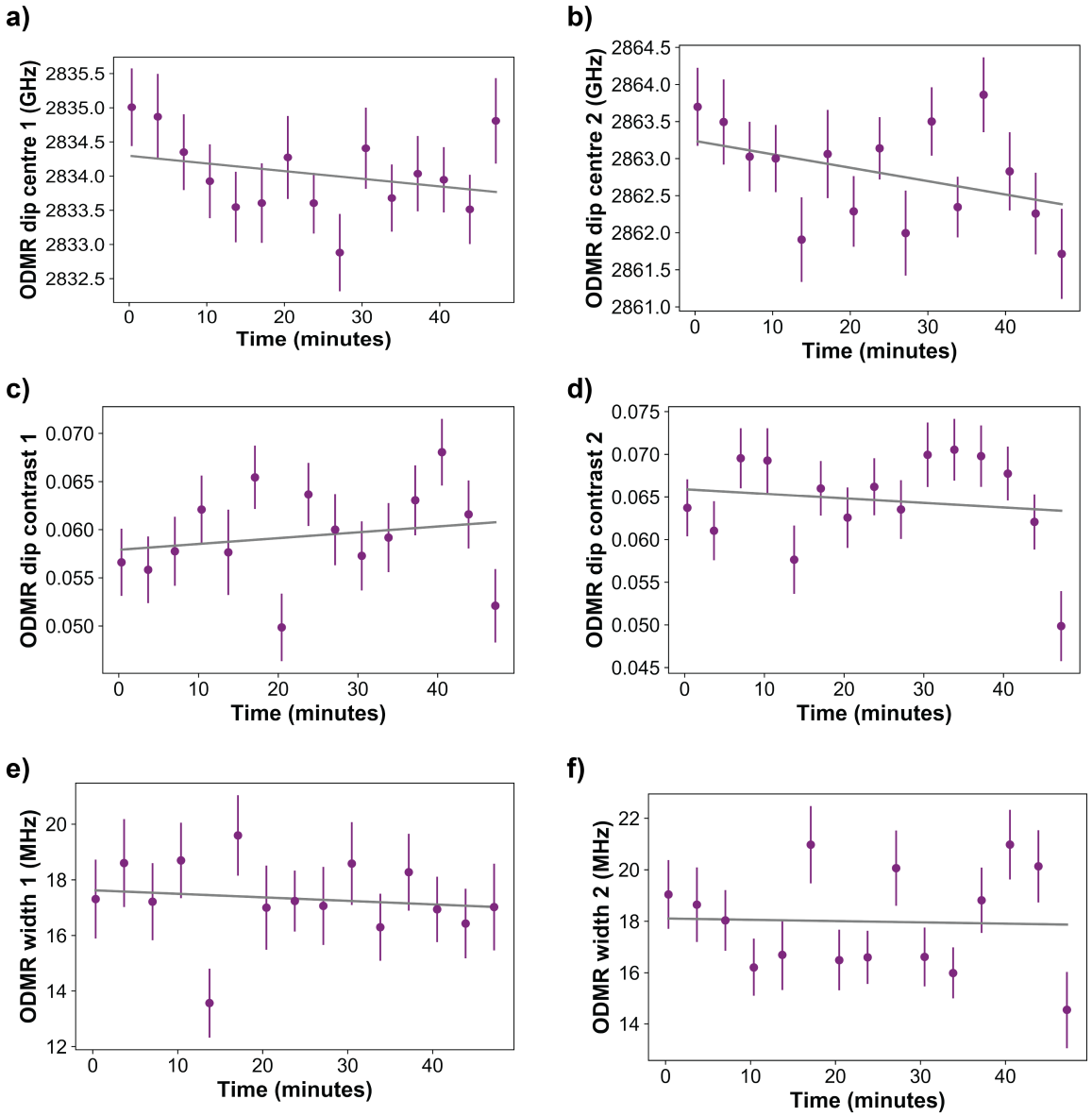

Fig. 2.9 ODMR stability on ODMR fit parameters for a gaussian double dip. ODMR spectra were individually fitted over time. a,b) Fit measurements of the centre of the ODMR are the most important parameter for making measurements of electric field. The linear trendlines indicate a decreasing position of the dips, but these exhibited low Pearson Correlation Coeffecient values of -0.28 and -0.40, meaning that there is probably not a linear trend over this timescale. c-d) Dip contrast is maintained throughout the measurement, indicating stability, with small correlation coeffecients of 0.19 and -0.14 respectively. e-f) ODMR width is also observed to be a stable quantity, with no linear trend over time (correlation coeffiecients = -0.14 and -0.04 respectively).

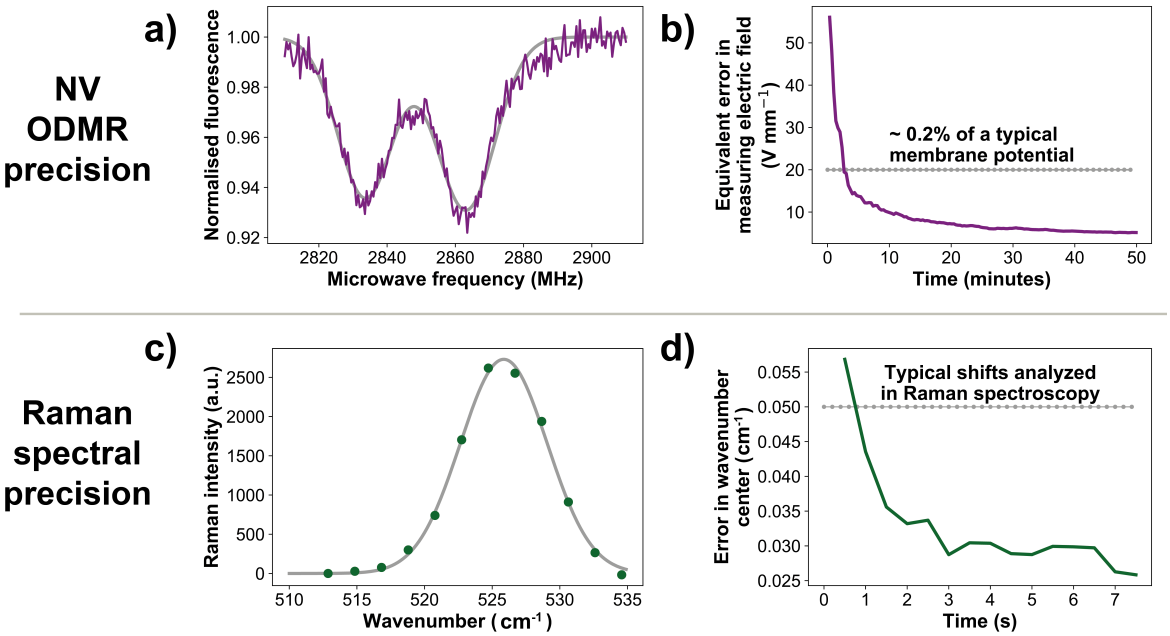

Fig. 2.10 a) An Optically Detected Magnetic Resonance (ODMR) spectrum on an NVC. The fluorescence reduces under the application of microwaves at certain frequencies. The positions of these troughs enable physical metrology. b) The ability of the instrument to make an electric field measurement using a NVC. The ODMR spectrum (a) is fitted with less error over time, enabling a precision equivalent to 0.2% of the mitochondrial membrane potential ($\Delta\Psi_m$) within 3 minutes. c) Raman scattering signal from the silicon first order peak with a fit to determine the central position. d) The precision of our setup to localise the Raman peak shown in (c) over time. 1 s of integration is sufficient to localise to 0.05 cm^{-1}.

the instrument collects the desirable and important 'fingerprint-region' of the cells in 500–1800 cm^{-1}, but removes the strongest lipid and protein peaks (2848 cm^{-1} and 2930 cm^{-1}, respectively) [249]. These detected wavenumbers also allow the co-registration of diamond in the Raman channel by integration at 1332 cm^{-1} [250].

It was chosen to excite the Raman signal and NVC fluorescence using one 532 nm laser. This is a good compromise for Raman spectroscopy, as the autofluorescence of cells is 150× lower than at 488 nm [133], but the signal is only $\sim$ 1.5× lower. This wavelength results in resonant Raman signal on several peaks from cells, which would, for example allow for clear classification between normal and cancerous breast tissue [251] in a future application. This wavelength is also optimal for NVC excitation, as it has been shown to reduce charge switching to increase fluorescence [78]. The next longer wavelength that is common for Raman spectroscopy, 633 nm [252], would not be appropriate for NVC excitation. Overall, the instrument achieves suitable wavelengths in emission and detection for cellular measurement, Raman signal and NVC sensing.

2.5.2 Optical signal intensity

With respect to the total signal detected, this instrument compares well with others, outperforming comparison with the commercial Renishaw system by 18× the signal-to-noise ratio. This is likely due to the nature of the Hyperflux™ High Throughput Virtual Slit in the system. If a further sensitivity increase were desired, the spectrometer CCD camera could be replaced by an sCMOS or EMCCD sensor. The disadvantage of the virtual slit spectrometer is that it fixes the system to one excitation wavelength and spectral range from the design stage, whereas other spectrometers can work with different excitation lasers and collection ranges by rotation of the internal gratings. In the desired application, however, this is not problematic. Since the Renishaw Raman microscope is used to measure cells, surpassing this level means that the custom microscope is suitable for this task. The Hyperflux spectrometer has been used to measure the Raman signal of cells in other work by Strola et al. [185].

The NVC fluorescence count rate at saturation half-power is of the same order of magnitude as another instrument in the group. As yet, however, it is unclear whether this is sufficient at the level of single NVCs to locate them inside cells, though there has been some promising preliminary work in this area (Figure 5.2). If needed, it may be possible to improve signal throughput by modelling the system in ray tracing software such as Zemax™ , considering different lenses and filters and the potential for further optical alignment [253]. This would involve close comparison with other systems have measured NVCs in cells [16].

2.5.3 Spatial resolution and scan area

Evaluating the lateral spatial resolution, we found that we achieved 290 ± 30 nm and 290 ± 40 nm laterally for NVC and Raman measurements respectively. The true Raman resolution may be better than this measurement, as it is not possible to discount that there are smaller nanodiamonds that would appear as a smaller spot, but that are below the signal detection limit. However, both NVC and Raman channels are close to the expected lateral resolution at 267 nm and 255 nm. These values are sufficient for the purposes of this project, since mitochondria are generally 1 µm are therefore the Raman resolution is at an appropriate level to measure them. The achievement of a resolution close to the confocal limit for NVC is suitable as this rejects background signal from nearby fluorescent objects.

For axial resolution it was not possible to obtain Raman data due to the long-term failure of a part of the equipment. For NVCs, the axial resolution was measured at 3.3 ± 0.3 µm. This is approximately the thickness of cells [254], so is an appropriate resolution for determining whether an NVC is endocytosed, rather than floating in solution above. After this, truly simultaneous detection of Raman signal and NVC fluorescence was demonstrated.

Lateral and axial resolution were maximised by coupling the light into and out of optical fibres. This acts as a confocal microscope to reduce the spot size by eliminating light entering from wide angles and from out of plane. This reduces noise by restricting the collection angle and plane of the instrument. The drawback is that the effective confocal aperture size is not flexible, unlike common confocal fluorescence microscopes which can be adjusted depending on the application. NVC spatial resolution may also be improved by super-resolution techniques [196, 209, 195], taking the localisation down to 10s of nanometres, inside cells that are approximately 10 µm. However, this would greatly increase the complexity of the system.

To build images, we have chosen to use stage-translation point scanning. Raman imaging is also achieved by line scanning [164] and wide field techniques [224]. Point scanning is advantageous in the area of depth scanning, resolving organelles and simplicity, as has previously been noted [222, 21, 220]. By translating the stage, we avoid some optical aberrations that arise from a scanning mirror off-axis measurement, although we physically disturb the sample a little in this process. It is unclear whether this minor movement will adversely affect biological samples or measurements, although this does appear to have no effect on other systems such as the WITec Confocal alpha 300+ Raman microscope.

Stage scanning also provides us with a an effective field of view of 200 µm (side length) for extremely precise measurements (to $\sim$5 nm in practice with the nPBio stage), and1 cm for scanning that is accurate to 160 nm (from the Zaber specifications). This dual scanning

approach combines precision at the cellular levels, where cells are typically ∼10s of microns across, with the ability to scan across a large number of cells. The absolute scanning extent is larger than other systems at 1 mm [199], and 4 mm [106]. Precise local scanning across of the whole of a cell is essential for the desired measurements, as it enables tracking of a nanodiamond during an experiment. Wider scanning is also useful as multiple different cells can be investigated, and the centre of the sample can be reached easily to avoid edge effects.

2.5.4 Sensing capability of the instrument

The final class of characterisation measurements were also sufficient for the aim of this project. NVC completed the sensitivity equivalent of a membrane potential measurement to a precision of 0.2% within 3 minutes. This is suitable, as fluorescent dyes that measure $\Delta\Psi_m$ typically measure changes over this timescale [60]. It may be that there are interesting and significant changes in a cell mitochondrial membrane at shorter timescales than this.

This NVC measurement was achieved with ODMR. One issue with this is that ODMR fitting also depends on the locations of the ODMR dips. For bulk diamond, this can be well predicted, but for nanodiamonds, these have lattice strain, and so the ODMR dips vary in location from nanodiamond to nanodiamond [73]. The consequence of this is that some nanodiamonds may be better at measurement of electric field than others, given their well separated dips. Further, strain manifests as an electric field on the NVC, potentially adversely affecting the measurements.

A further consideration is that although ODMR spectra were stable over 45 minutes, there may be stability issues in longer term sensing that could impact measurement. This would reduce a key advantage of nanodiamonds over fluorescent dyes, photostability, and so needs to be further investigated. It should be noted again that this sensitivity may be worse inside a cell with background fluorescence, so this remains a topic for further investigation. Finally, ODMR peak width and sensitivity may depend on microwave power, and this has not been interrogated in the experiments here. It is worth noting that upgrading the system to pulsed measurements may overcome these challenges, if required. However, as far as the evidence in this chapter suggests, the custom microscope has the sensitivity required.

The Raman spectral measurement also collected data rapidly, with a $0.05\,\mathrm{cm}^{-1}$ localisation of a Raman peak after 1 s. This is suitable for the measurements as 1 second is a typical integration time for cellular experiments [255], and $0.05\,\mathrm{cm}^{-1}$ is the type of chemical shift that is desired to be resolved [256].

2.5.5 Adaption to live cells

There are some considerations on adapting the microscope to live cells. Primarily, live cells need to be maintained at 37 °C. This has been achieved by the work of Jeffrey Holzgrafe who added a resistive heater to the sample chamber. This needs to be further tested to find whether it conforms to the standard of temperature control that is common in the field: ± 0.1°C [257]. Another cellular requirement for live cell imaging is carbon dioxide. While this could be supplied by a sealed container and a gas cylinder, it is intended to be achieved via the easier addition of HEPES (hydroxyethyl piperazineethanesulfonic acid) to buffer the solution correctly. Maintaining humidity and liquidity is also an issue for live cells. The simplest means to achieve this is to frequently check the water level of the cell culture container and refill this if needed.

2.6 Conclusion

To achieve simultaneous measurement of NVC and Raman microscopy, it was necessary to design and construct a bespoke instrument. The design of this microscope was optimised towards the measurement of $\Delta\Psi_m$, and the characterisation of it in this chapter has provided evidence that it should be able to realise that potential.

Overall, the instrument was found to be suitable for its design purposes by realising the proposed advantages. Possible future developments are suggested in Chapter 5 Section 5.2.1. To use the microscope effectively in studies of $\Delta\Psi_m$ in live cells, next it is necessary to develop protocols and analysis methods for both Raman and NVC microscopy on living cells. These are described in Chapters 3 and 4.

Chapter 3

Raman spectroscopy protocol development - experimental and data analysis

Raman experimental protocol methods were developed by Ben Woodhams (BW) in collaboration with Dr Jakub Surmacki (JS) and published as Surmacki et al. [2], with BW as second author. Data analysis methods were developed and programmed by BW using open source libraries, and all data analysis was performed by BW except Figures 3.15h, 3.15i and 3.16h. Experiments to measure substrate and medium were performed by JS (Figures 3.5 and 3.6). BW collected the data of organelle change over time on an A549 cell (Figure 3.17). The other A549 and MRC5 cell data in this chapter were collected by JS. All other work was completed by BW.

3.1 Introduction

Biological changes within cells are spatially and temporally correlated to chemical changes detectable via Raman microscopy. This project aims to develop Raman microscopy as a supportive and complementary technique for direct nanodiamond sensing of mitochondrial membrane potential ($\Delta\Psi_m$) without the addition of toxic and photobleaching fluorescent dyes. Raman microscopy provides unique capabilities in pursuing this goal, such as locating cells without staining, subcellular organelle spatial mapping, and observing processes such as apoptosis that are closely linked to $\Delta\Psi_m$. Accurately locating cells is essential for these measurements as it is necessary to choose locations to scan for intracellular nanodiamonds,

and stop the measurement if these nanodiamonds are exocytosed [258]. The subcellular organelle mapping is useful to track the position of the nanodiamonds with respect to mitochondria, as the particles could become trapped in endosomes or attracted to other organelles. The third application of Raman spectroscopy is to detect general biological changes in the cell that that might be linked to change in $\Delta\Psi_m$. This is plausible as biological activity such as apoptosis, metabolic rate and oxidative stress have been shown to relate to both $\Delta\Psi_m$ and chemical changes detected by Raman spectroscopy (Sections 1.1.2 and 1.3.2).

Using Raman microscopy for organelle mapping and chemical changes in live cells requires the precise control of experimental conditions such as laser power, integration time, objective lens, spatial scanning protocol, buffer solution, sample format, and substrate. In addition to experimental conditions, data analysis methods also require optimisation of parameters such as the software used, and spectral pre-processing techniques. The use of hyperspectral methods, including Principal Component Analysis (PCA) and k-means clustering were tested.

3.1.1 Raman experimental protocol review

Live cell spontaneous Raman imaging was first performed approximately two decades ago [177]. Since then, the desire for label-free live cell imaging has led to improvements in experimental procedures. These protocols often involve compromises between increasing signal, reducing collection time, and reducing the laser-induced damage to live cells.

Several studies described the impact of variations in protocol on the measurements. One example of this is the comparison between fixed cells and live cells for imaging. Chan et al. showed that fixation changed the intensity of specific Raman markers that are commonly assigned to DNA, RNA, protein, and lipid vibrations [150], and as such have an adverse impact on Raman measurement. The difference between two dimensional (2D) and three dimensional (3D) cell growth has also been considered. Standard imaging protocols use cells that are attached to a flat substrate and spread out in two dimensions [164, 137]. As for the substrate material, quartz and calcium fluoride (CaF_2) are commonly used for Raman imaging to reduce the collection of background signal [259]. However, recent work on tumour microenvironments has motivated development of 3D cell structures in order to replicate the *in vivo* environment [260]. This has been performed in Raman microscopy to investigate spatial variation across cells [168].

The choice of cell imaging medium has also been varied. Some live cell Raman experiments use solutions of Phosphate Buffered Saline (PBS) [261], Tyrode's solution [133],

medium without serum [262], medium with serum [163], with other solutions such as Hank's Balanced Salt Solution (HBSS) and Live Cell Imaging Solution (LCIS) also used generally for live cell experiments [263, 264]. A problem with Raman imaging of cells is that at high power and short wavelengths, the laser can damage the cells' DNA [265]. Raman signals also risk being very low [266].

Overall, there are a variety of techniques used to collect Raman data from cells. The experimental parameters therefore need to be optimised according to the scientific aim and to avoid cell damage.

3.1.2 Raman data pre-processing review

Advanced data processing is essential for subcellular organelle mapping and chemical investigations using Raman microscopy. In Raman microscopy, spectral information is collected at different spatial locations, forming a hyperspectral data set (Figure 3.1). Gaining insight into cellular processes or clustering requires specialised data analysis techniques such as Principal Component Analysis (PCA) and k-means clustering (see Section 3.1.3). Furthermore, since the measured Raman signal is low, it is necessary to perform pre-processing steps to improve accuracy and repeatability. Pre-processing steps mainly involve artefact removal and noise reduction via cosmic ray removal, background removal and smoothing algorithms.

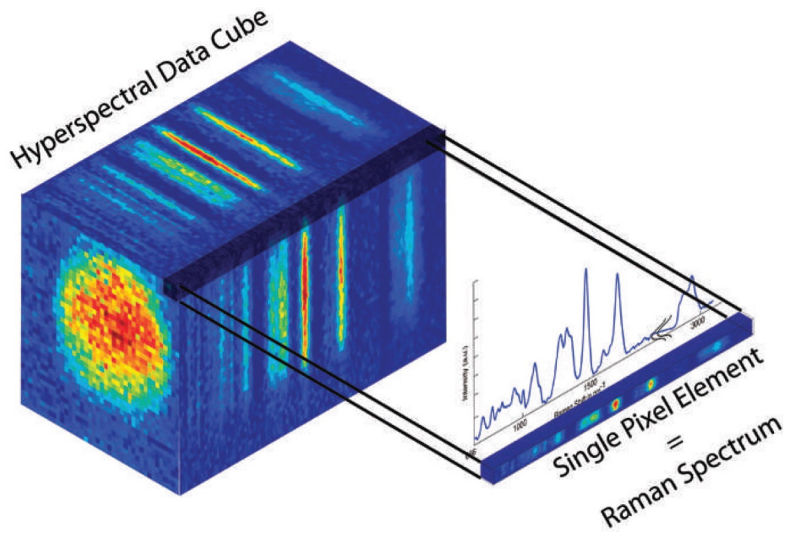

Fig. 3.1 A hyperspectral data cube. Raman microscopy is performed by collection of one spectrum at every point in a two dimensional area, creating a data set that is spatial $\times$ spatial $\times$ spectrum, known as a hyperspectral data cube. This figure is taken from Schie et al. [19].

Cosmic ray removal

Cosmic rays consist of ionising particles that can interact with CCD (Charge Coupled Device) detectors [267], causing spikes in spectra. Since many Raman instruments include CCD detectors, removing these spikes is a common first step in pre-processing [20, 135, 137, 164, 268, 255, 269, 270]. This can be achieved via manual inspection [269], nearest neighbour methods [271, 272], median filters [273], wavelet or Fourier analysis [267], and derivative approaches [274].

Background removal

The acquired Raman spectra typically have an underlying background spectrum that is not generated by Raman scattering. This, typically broad or flat background spectra, is usually a combination of background fluorescence, camera offset and camera noise. Various hardware and experimental protocols have been developed to remove these effects. These include using a longer wavelength [272], quenching the fluorescence [275], or time gating to collect only the 'instantaneous' Raman signal, while excluding fluorescence [276, 272]. There is also a background removal technique that is achieved by quickly switching between two lasers that are closely spaced in wavelength [277], as further described in future work, section 5.2.2.

Mathematical techniques to pre-process the data also exist. One of the most extensively used is polynomial subtraction [272], which involves fitting all, or part of, the spectrum with a polynomial function which is subsequently subtracted from the original spectrum. This is effective with low order polynomials (usually up to 5) as these describe and remove the low frequency background spectrum whilst leaving the Raman signal peaks. Another common technique is to subtract all spectra from the average of all spectra, or a background area such as the media surrounding the cell [147, 148, 157, 158, 270, 278]. Other techniques include: first or second derivative filters [272]; Principal Component Analysis (PCA) techniques [279], as will be explained in Section 3.1.3; as well as wavelet and Fourier filters [272].

Smoothing

Random photon and electron detector noise are also present on Raman spectra. Several smoothing techniques can be used to remove random photon and electron detector noise from the Raman spectra. The simplest is a moving average window [270, 149], though this can produce unwanted oscillations [280]. The most common method for spectral smoothing was developed in 1964 by Savitzky and Golay [281]. This works by fitting a low degree polynomial to successive groups of points along a spectrum, thereby removing local noise

spikes by convolution. This is widely used in Raman spectroscopy [137, 138, 260]. The other major technique for smoothing is to use Principal Component Analysis (PCA) via Singular Value Decomposition [130, 163] (see Section 3.1.3). Other smoothing algorithms include an information-based maximum-entropy approach [146] and the one-parameter Whittaker smoother [282].

Spectral cropping (shortening)

Peaks from extracellular sources can be reduced by careful choice of substrate and medium. Nevertheless, it is necessary to crop each spectrum to remove the spectral features from the substrate (such as quartz around 500 cm^{-1}) and medium (including water around 3500 cm^{-1}) [128] while preserving the CH bond region (2806–3024 cm^{-1}) and the 'fingerprint region' (approximately 600–1800 cm^{-1}) as much as possible. This method has been implemented several times in the literature, but has yet to be studied in depth. [185, 151].

Normalisation

Random laser power and detector sensitivity variations over time can be corrected for by normalisation. Three common methods of normalisation are 'Area under curve', 'Manhattan' and 'Euclidean'. 'Area under curve' involves dividing each spectrum by the integrated area under itself and has been used for Raman spectroscopy by Moritz et al. [261]. This can be problematic though, as the background subtraction protocol can often make parts of the spectra have negative values, thereby increasing the values of the final spectra undesirably. 'Manhattan' normalisation overcomes this issue by calculating the sums of the distances from the axis and using that to divide the original spectrum and has been used in Raman spectroscopy by Majzner et al. [283]. 'Euclidean' normalisation also attempts to overcome the 'area under curve' negativity issue by using the sum of the square distances to the axis and has been used in Raman spectroscopy by Olmos et al. [284].

Other pre-processing techniques

In addition to background removal and smoothing, additional pre-processing steps are occasionally required. These include: wavenumber calibration to standard samples; spectral throughput correction to correct for the different transmission efficiency of different wavelengths; interpolation to linear spacing and others [285]. After pre-processing, a variety of hyperspectral data analysis techniques can be applied such as PCA and clustering algorithms.

3.1.3 Raman data analysis methods review

It is often desired to extract underlying chemical components, classify spatial regions and describe changes in hyperspectral Raman data. Achieving such objectives requires specialist analytical techniques. These include, but are not limited to, Vertex Component Analysis [286], Hierarchical Component Analysis [259], Spectral Angle Mapping [287], Independent Component Analysis dimensionality reduction [288], Partial Least Squares Discriminant Analysis [289], and curve devolution by Levenberg-Marquardt to create individual peaks [290]. A detailed review of the different spectral analysis techniques has been written by Hedegaard et al. [291]. Here we discuss (and use) two of the most common methods: PCA and k-means clustering.

Principal Component Analysis (PCA)

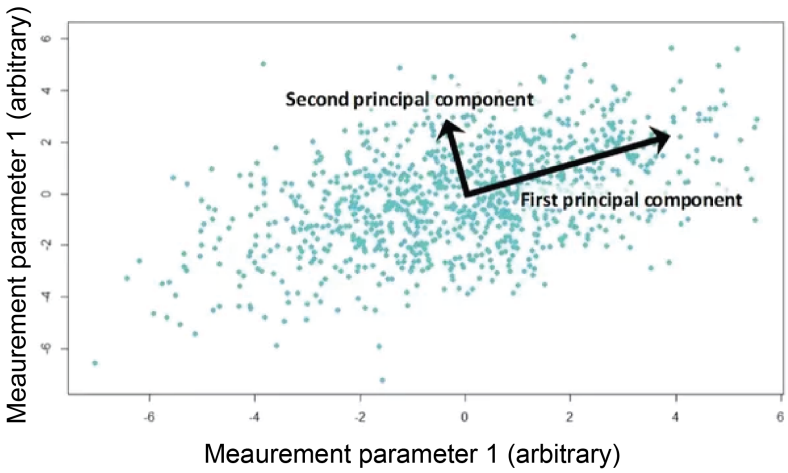

Fig. 3.2 Principal Component Analysis (PCA) is a hyperspectral analysis technique. It is implemented by constructing a orthogonal basis for the data where the new axes are along the directions of greatest variation that is not already mapped to an axis. This can be used in noise reduction, clustering and to provide insight into the underlying components. This figure is adapted from Nazrul et al. [24].

Principal Component Analysis (PCA) is the generation of new orthogonal basis axes that are useful for representing the data, reducing noise, and accelerating calculations. The data points exist in a multidimensional space which is spanned by axes that represent different wavenumber frequencies. The distance of the point along each direction given by the intensity at that wavenumber (Figure 3.2). PCA constructs each new axes along directions that show

the greatest variation in the data, with the condition that it is orthogonal to all assigned axis directions.

This can be useful as a visual representation to observe clumping of the data, by plotting points against the first few principal components, and by plotting the spatial distribution of each component. It works for noise reduction as principal components above a certain threshold contain only noise, and can therefore be removed. This also helps to increase the speed of calculations. In practice, PCA of Raman images has been used on cells to separate cells that are prepared in different ways [292], understand the biochemical effects of a drug [278], compare cell types [293], identify intracellular regions [138, 260, 19], examine cell state [148, 294, 147], and develop a prognostic marker for breast cancer [137].

K-means clustering

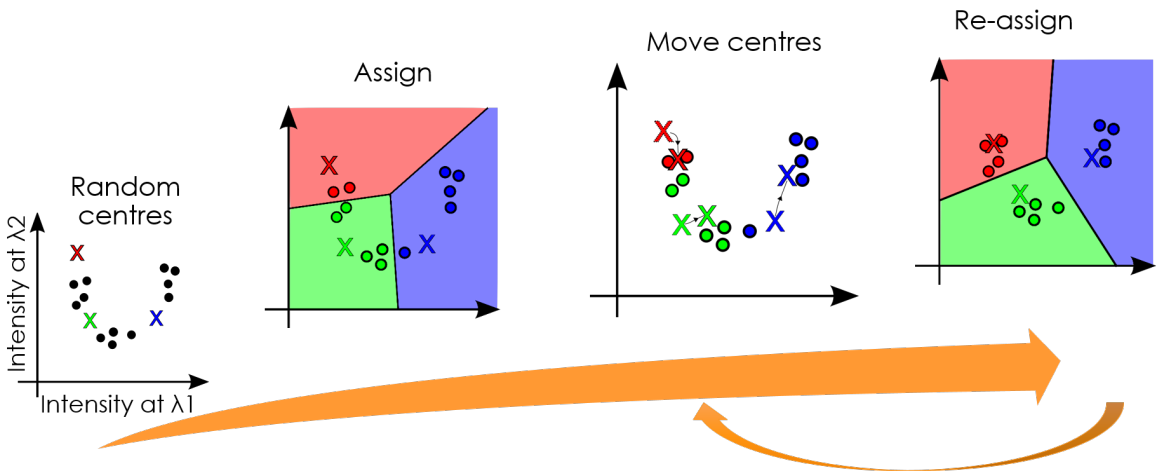

Fig. 3.3 K-means clustering is a technique to group similar spectra. It starts by arbitrarily defining as many cluster centres as requested by the experimentalist. All spectra are then assigned to their nearest cluster centre. The centres are then moved to the average position of the group. The process repeats between assigning spectra to cluster centres, and moving the position of those centres depending on the group, until the solution becomes stable.

K-means clustering is a hyperspectral analysis technique that groups similar spectra into clusters (Figure 3.3). The process starts by arbitrarily defining cluster centres. Following this, all spectra are assigned to a cluster that has the nearest cluster centre. Then, the centres of the clusters are moved to the average of all the points in that cluster. The process is then repeated by iteration, reassigning data points to their nearest cluster and then moving the centres of the clusters. Each spectrum has membership of only one cluster. The clusters can be shown as areas of similar composition on a real space image with their average spectra extracted [295].

In the context of cell Raman imaging, k-means clustering has been widely used for organelle identification [296, 20, 259, 131, 136, 260], to measure protein accumulation [296], and to measure the effect of drugs [20].

K-means clustering and PCA are powerful analytical methods that can help interrogate Raman data. Both are useful in the Raman live cell analysis to outline cell boundaries, find intracellular organelles and observe spectral changes over time.

3.2 Methods

3.2.1 Live cell protocol methods

WITec commercial Raman instrument

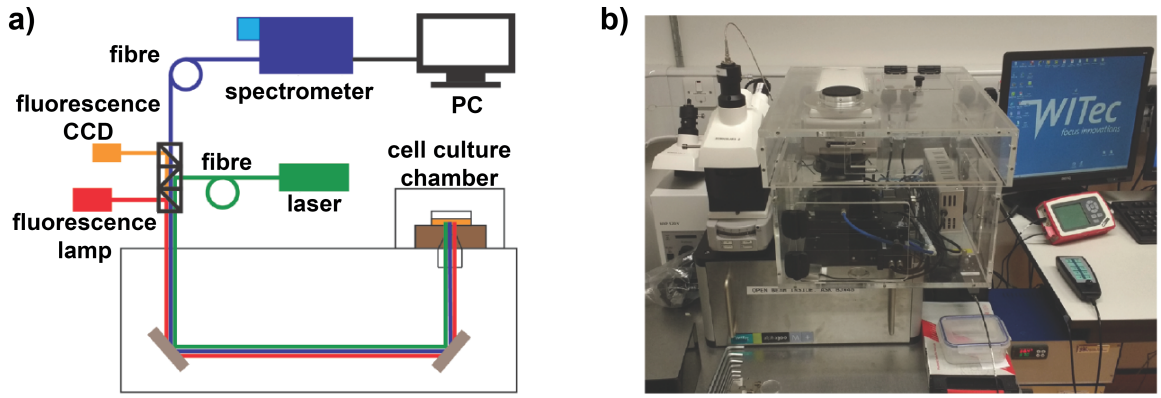

Fig. 3.4 a) A diagram of the WITec confocal Raman microscope in inverted configuration. Raman scanning on live cells was performed using a 488 nm laser. b) A photo of the system with the transparent live cell enclosure for temperature, humidity and CO_2 control. Figure is reproduced from Surmacki et al. [2].

A WITec confocal Raman microscope (WITec Alpha 300M+, WITec GmbH, Germany) was used to develop experimental and analytical protocols for Raman spectroscopy. A live cell enclosure for temperature, humidity and CO_2 was added by Digital Pixel Microscopy Systems (Brighton, UK). The system is equipped with a 488 nm laser that is directed through an inverted 60× water-immersion objective lens (Nikon CFI Plan Apo IR 60×WI, MRD07650, NA = 1.25). This objective lens was chosen as it had the highest numerical aperture on the microscope, thereby increasing spatial resolution and contrast. It has a Princeton Instruments Acton SpectraPro SP-2300 spectrometer that has a grating of 300 lines/mm and is blazed at 500 nm. The system was calibrated by WITec and by peak alignment to a silicon sample to the first order 520.7 cm^{-1}.

The instrument works with WITec Control Center 4.0 and Raman hyperspectral data were collected by point scanning across a two dimensional area of live cells at a step size of 0.5 µm and an integration time of 0.5 s. Data can then be analysed within the collection software WITec Control Center 4.0, or by using the same tools externally in WITec Project Plus 4.0. These include data analysis techniques such as cosmic ray removal, background subtraction, smoothing, shortening, normalisation, principal component analysis, k-means clustering and others. This software is unable to analyse data collected on devices from other commercial manufacturers.

In this project the WITec Raman microscope was used as a standard system to develop experimental and analytical protocols for later use in a combined custom-made nanodiamond and Raman system.

Choices for cell experimental methods

As described in the literature review (Section 3.1.1), various choices must be made to optimise data collection from cells. Firstly, we chose to work with live rather than fixed cells to avoid the artefacts generated by most fixatives. Secondly, while three dimensional culture methods enable the study of tissue microenvironments, this is not a current application of this project, and therefore the technically simpler option of two dimensional culture was chosen. A third parameter is laser power. For cell detection and organelle classification, cells were illuminated at 4 mW in the beam path at 488 nm (Sections 3.3.2 and 3.3.3). For observing change over time, this power was increased to 10 mW in order to provoke a change in the cells (Section 3.3.4), as discussed in section 3.4. The optimal substrate and medium were experimentally determined.

Optimising substrate

To choose the most suitable substrate for our Raman microscopy experiments, four different materials were evaluated. A549 were plated onto the following substrates: microscope cover glass (Marienfeld Cover glasses thickness No.1.0 circular, diameter 25mm, 0111650); quartz cover slips (UQG Optics, CFQ-2520); calcium fluoride slides (UV and IR grade, Crystran Limited); and a plastic cell culture dish traditionally used in live cell fluorescence microscopy (Greiner Bio-one, 627160). It was observed that quartz and UV-CaF_2 had the lowest signals in the range typically used for cellular measurements 800–3100 cm^{-1} (Figure 3.5). Since quartz is known to be the better substrate for cell growth [259], this substrate was chosen for all subsequent experiments.

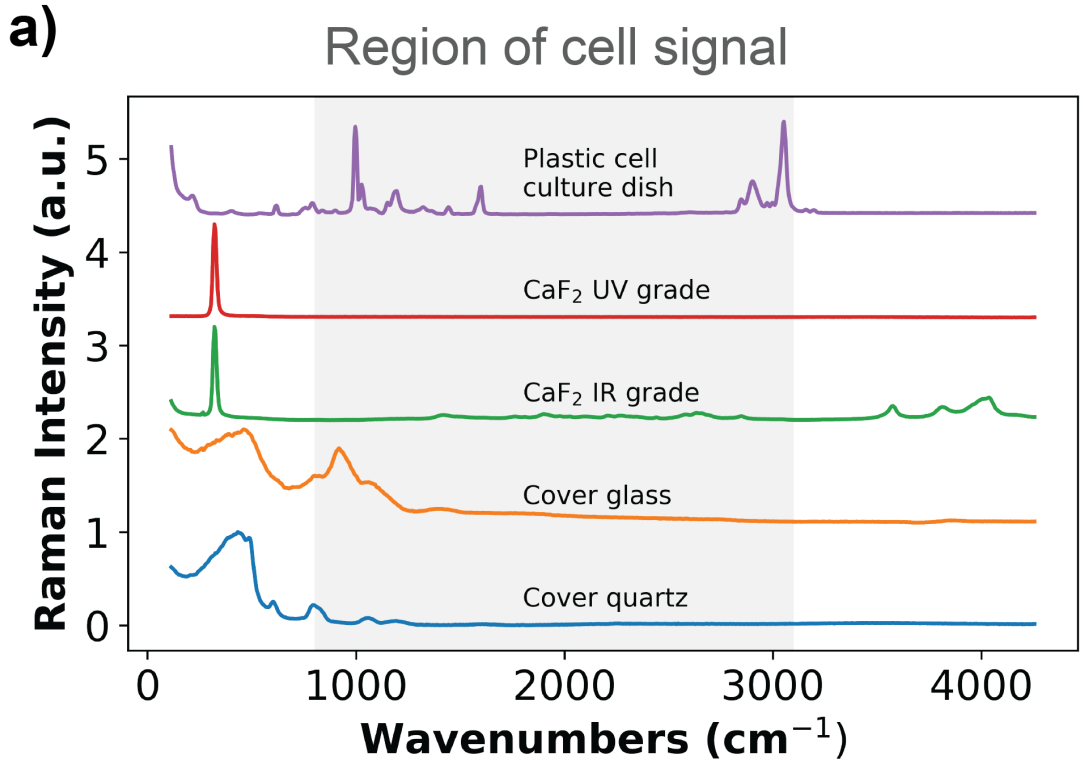

Fig. 3.5 a) Raman spectra of different substrates. Cell culture plastic, 'IR-grade' calcium fluoride (CaF_2) and cover glass substrates contain more Raman signal than quartz and UV-CaF_2, making UV-CaF_2 and quartz most suitable for collecting Raman measurements. Data is published in Surmacki et al. [2].

Optimising medium

To decide on the most suitable medium for the Raman imaging, solutions of different media were measured on the WITec instrument at 488 nm. The solutions tested were: standard cell culture DMEM/F-12 medium without phenol red (tested both with and without serum); and salt solutions: Hanks' Balanced Salt Solution (HBSS) with 5.5 mM glucose (Gibco, Life Technologies, 14025-050), Live Cell Imaging Solution with 17.5 mM glucose (LCIS, ThermoFisher, A14291DJ), and Phosphate Buffered Saline (PBS, Life Technologies, 10010-056) with 17.5 mM glucose (Sigma, G8270). The results are shown in Figures 3.6a and 3.6b. Cell proliferation was also monitored for PBS with glucose, LCIS, HBSS, medium with serum and medium without serum (Figure 3.6c). Cell growth rate, a marker of cell health, was recorded with an automated phase contrast microscope (Incucyte, Essen Biosciences).

It was found that medium with serum was superior for cell growth, and HBSS had the highest growth rate among the solutions with lowest Raman peaks. To maintain cells in a healthy state during time course experiments (over 2 hours), complete medium supplemented with serum is preferred while shorter experiments (less than 1 hour) can be performed using HBSS. Since this project involves long time course experiments, medium with serum will be systematically used.

Protocol for cell experiments

Two cell lines were used to develop experimental and analytical protocols for cell work: human lung carcinoma A549 (ATCC) immortalised cells and human fetal lung MRC5 pd19 (ECACC). MRC5 cells were incubated and imaged in Minimum Essential Medium (MEM, 51200-046, Gibco, Life Technologies, UK) supplemented with 10% fetal bovine serum (Gibco, Life Technologies, 16000-044) and 2 mM L-glutamine (Life Technologies, 25030-024). A549 cells were incubated and imaged in DMEM/F-12 with L-glutamine (Gibco, Life Technologies, 11039-021) supplemented with 10% fetal bovine serum (Gibco, Life Technologies, 16000-044). To reduce fluorescence, phenol red free media was used. These cell lines were selected based on experimental availability. Furthermore, since one line is cancerous and the other is not, it is possible to see whether these different types of cell need different analytical protocols.

Cells were incubated and imaged at 37 °C in humidified atmosphere containing 5% CO_2. Cells for Raman microscopic analysis were seeded 12 hours prior to analysis in a 6-well plate with a 25 mm circular quartz coverslip (UQG Optics, CFQ-2520) at a density of 2×10^5 A549 cells or 1×10^5 MRC5 cells per 3 ml well and incubated with phenol red free medium with

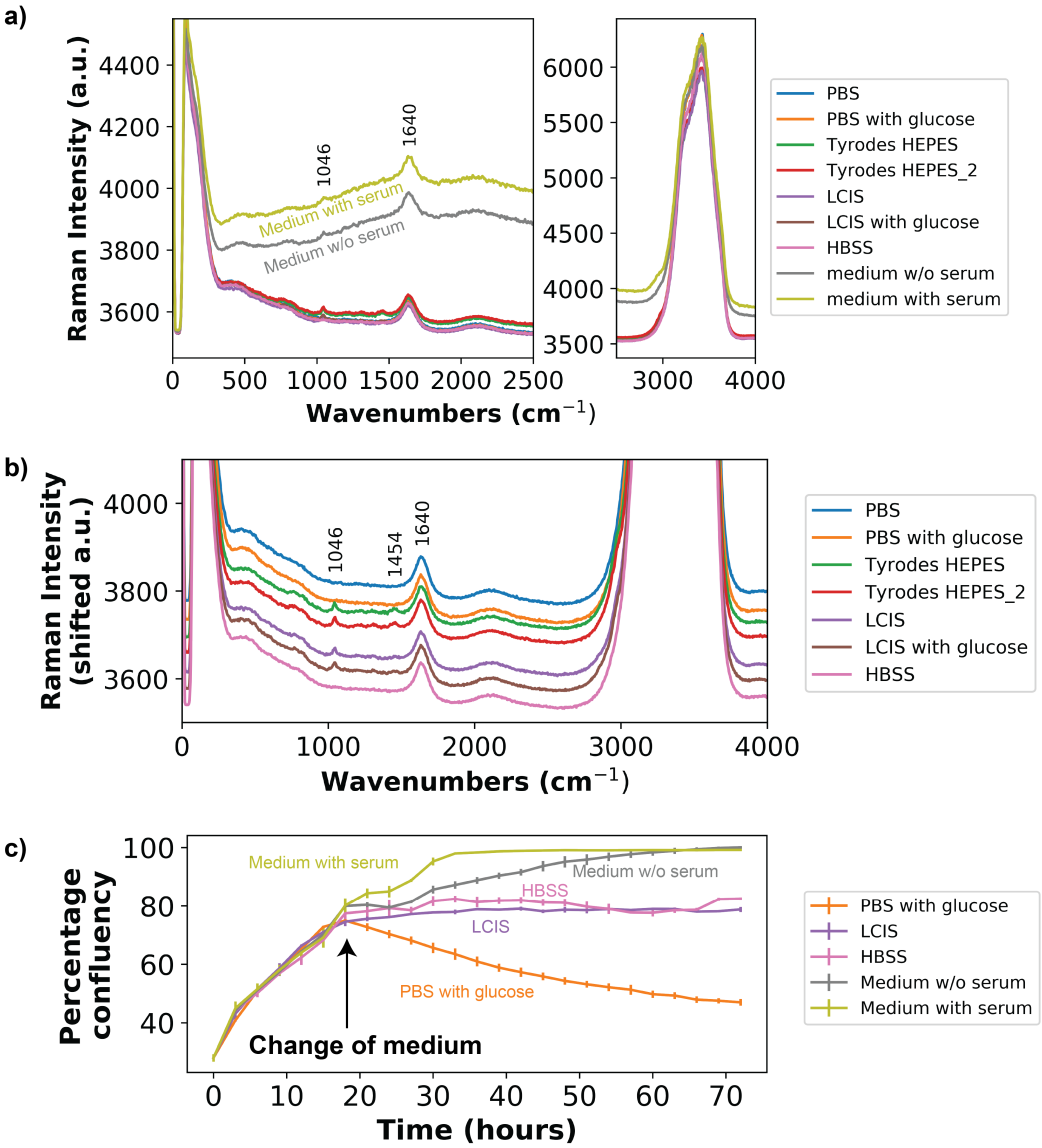

Fig. 3.6 a) Raman spectra of different types of media that could be used in live cell Raman imaging at 488 nm excitation. Full cell medium (DMEM/F-12) with and without serum showed the largest fluorescence of any of the media, as seen by their broad increased background level. b) A zoomed version of (a), with each spectra vertically shifted by a constant amount. Tyrode HEPES solution showed a small amount of fluorescence, slightly increasing their baseline. Tyrode HEPES, LCIS, LCIS with glucose showed Raman peaks at 1454 cm^{-1} and 1046 cm^{-1}, in addition to the water peak at 1640 cm^{-1} that is common to all of them. Data from Surmacki et al. [2]. c) A cell growth experiment in different media. The fastest cell growth was observed in complete medium with serum. In absence of serum, cells grown in media also reached the maximal confluency, but at a later stage. Cells grown in HBSS and LCIS did not proliferate and their numbers remained constant. Maintaining cells in PBS with glucose resulted in their death.

serum (vendor as above). Immediately prior to Raman microscopy measurement, coverslips were mounted into the Attofluor cell chamber (Invitrogen, cat. no. A-7816). Cells were washed with PBS to remove any unattached cells and fresh complete medium was added.

3.2.2 Hyperspectral data analysis methods

Since Raman microscopy collects a complex hyperspectral data cube, it is essential to develop appropriate techniques in order to create intracellular clusters or consider whether chemical changes are significant. These hyperspectral techniques also rely on effective pre-processing, where both are performed in python.

Software - Python, Jupyter and Hyperspy

The hyperspectral analysis was performed in Python in Jupyter notebook, with Hyperspy v1.3 [25]. Jupyter, is an integrated development environment that runs Python in a web-browser, and can blend rich text, code, in-line figures, and external windows (Figure 3.7a). Hyperspy is an existing library built on top of this, with analytical and navigational tools that are specialised for hyperspectral data (Figure 3.7b).

This combination has the advantages of being open-source, extensible, fast, available without cost, and easily reproducible. One of the particular advantages of Hyperspy in Jupyter is the combination of command line interface and graphical user interface. This allows easy navigation and processing of the data that combines the reproducibility of code with the accessibility of an interface (Figure 3.7c).

Principal Component Analysis

Principal Component Analysis (PCA) was used in this project firstly to discover the artefacts that are present in the raw Raman data, in order to motivate specific data processing techniques (shown in Section 3.3.1).

PCA was then used on processed data (after cosmic ray reduction, background removal, etc.) in cellular edge detection where the component that best represented the cell was chosen by the presence of a Raman peak in the spectrum at 2840–3000 cm^{-1} [137] and a spatial extent greater than two microns. Triangle thresholding [297] was observed to capture the full extent of the cell, unlike some other thresholding techniques, such as Otsu thresholding [298].

Subcellular clusters were identified with PCA using a combination of spatial distribution and spectral features as has been attempted elsewhere [299]. For clarity, one principal

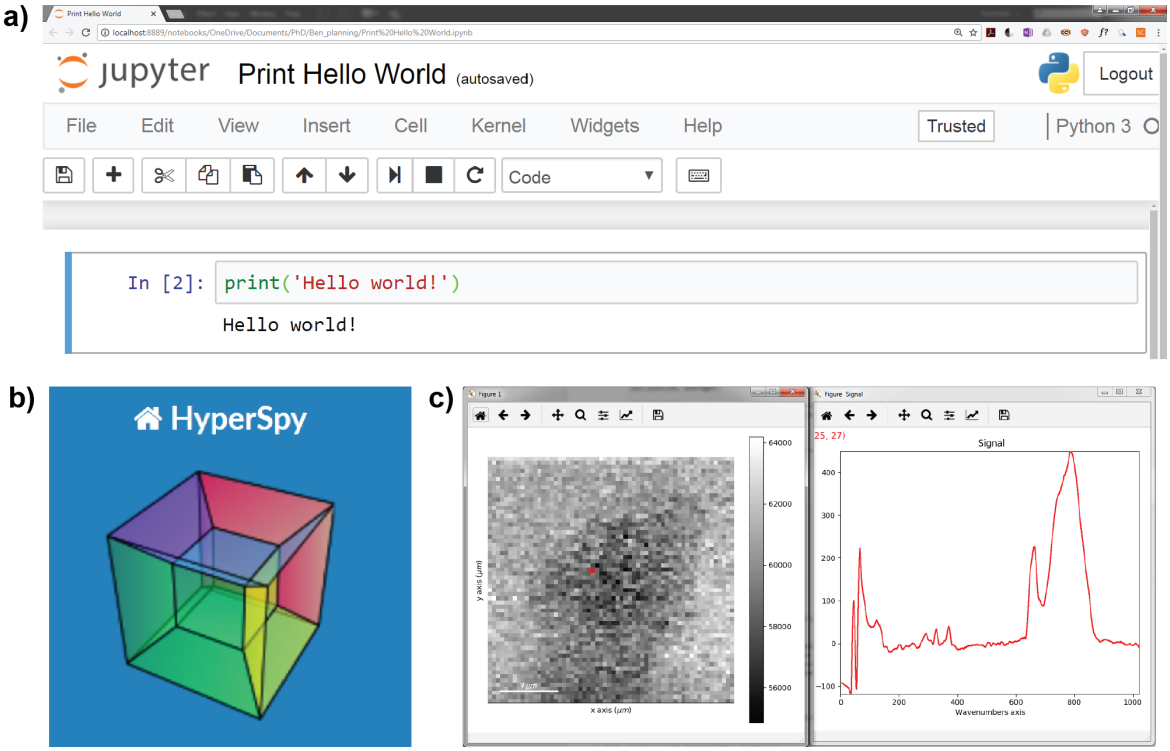

Fig. 3.7 Software used for Raman hyperspectral data analysis - python, Jupyter and Hyperspy. a) The Python programming language is open source and easily used in a browser-based Jupyter notebook. b) Hyperspy is a Python library built for hyperspectral data analysis [25]. c) Hyperspy allows graphical navigation of the data by conveniently separating navigation and signal dimensions.

component of A549 cells (PC2) was multiplied by negative 1 in the spectral factors and 2D image loadings.

PCA was implemented within Hyperspy, under the *hyperspy.learn.mva.MVA* decomposition model [25]. Images are max-min scaled.

Pre-processing

After identification of the need by PCA, the data were pre-processed via cosmic ray removal, background subtraction, smoothing, spectral cropping and normalisation. The first step was to remove cosmic rays by a combination of a derivative approach and manual inspection. Firstly, a derivative histogram was plotted using the Hyperspy *spikes_removal_tool()*, where it was clear that cosmic rays were distinct from the genuine spectral peaks by the rate of change by wavenumber of 400 counts. Therefore, it was possible to set the following parameters: Add Noise = no, Interpolator = Spline, Default spike width = 5, spline order = 1, and remove the peaks, confirming each via manual inspection. It was not necessary to employ further techniques such as nearest neighbour, median or Fourier filters [271–273, 267] as the signal to noise ratio in our data was sufficient to clearly show the peaks above the noise floor.

Background removal was achieved via a polynomial fit function of order 5. The spectrum was fitted excluding the quartz substrate (below $820\,\mathrm{cm}^{-1}$) and the C-H and O-H peaks between 2667–$3829\,\mathrm{cm}^{-1}$. This technique was chosen as it is simple, fast and commonly used [127, 272, 300]. Figure 3.10 shows that it removed the high baseline spectrum whilst preserving the Raman peaks.

Smoothing of individual spectra was achieved with a Savitzky - Golay filter set with a window length of 11 points and a polynomial order of 2. These parameters were chosen according to the literature [137, 260, 293], and confirmed by visual comparison of the spectrum beforehand and afterwards to reveal the Raman peaks above the noise.

Shortening of spectra was done by removing the lowest and highest wavenumbers from all spectra. Wavenumbers $<818\,\mathrm{cm}^{-1}$ were cropped away to remove the quartz peaks from the underlying substrate, and $>3073\,\mathrm{cm}^{-1}$ were cropped away to remove the water that surrounds and is contained within the cells.

Spectra were then normalised by ‘Manhattan’ normalisation. This normalisation is the most suitable for this work, as it corrects for linear whole-spectrum variations in laser power and detector sensitivity in a way that is not as detrimentally affected by negative values as ‘Manhattan’ normalisation. The spectra were normalised to a ‘Manhattan’ area of 1, meaning that the intensity of the peaks corresponds to a value much smaller than 1.

Peak integration

Here, integration of different peaks was used for revealing the cells and some internal organelles. Integration was achieved by linear background subtraction from a straight line fitted to five points on either side of the integration range. One, three and five points on each side were investigated, and three showed marked improvement in contrast (due to averaging over the noise), and five points was observed to be of similar quality to three. The integration range was chosen based on the literature [2, 301, 249, 128, 19, 22].

For cell detection, triangle thresholding [297] was observed to be most effective to observe the cell, as judged by spectral change at the C-H peak (2840–3000 cm^{-1}) and manual observation of the images. However the segmentation image of A549 cells by peak integration at 1160–1504 cm^{-1} resulted in a better capture of variations in the image when mean thresholding was applied. Consequently, mean thresholding was used in this specific case while triangle thresholding was applied in all remaining images. For observing organelles, the spectral ranges were chosen by a combination of knowledge from the literature, and by systematically plotting sets of wavelength intervals to find spatial correlations within the cell on an image.

K-means clustering

K-means clustering was used for cell and subcellular organelle observation. For cell segmentation, clusters of two and three were used as an attempt to include the thin cell periphery. K-means clustering was performed using python library Scikit Learn (*sklearn.cluster.KMeans* [302]) with its default parameters and initialisations.

The results of cell segmentation then were used in the process of organelle segmentation. K-means clustering was then used to evaluate the impact of data processing (Cosmic Ray Reduction, etc). The main part of the cell was clustered into four groups, and then these groups were identified as organelles via spatial and spectral information with reference to the literature. These were also compared with a published independent analysis [2], as well as co-registered fluorescence imaging of the nucleus (NucBlue).

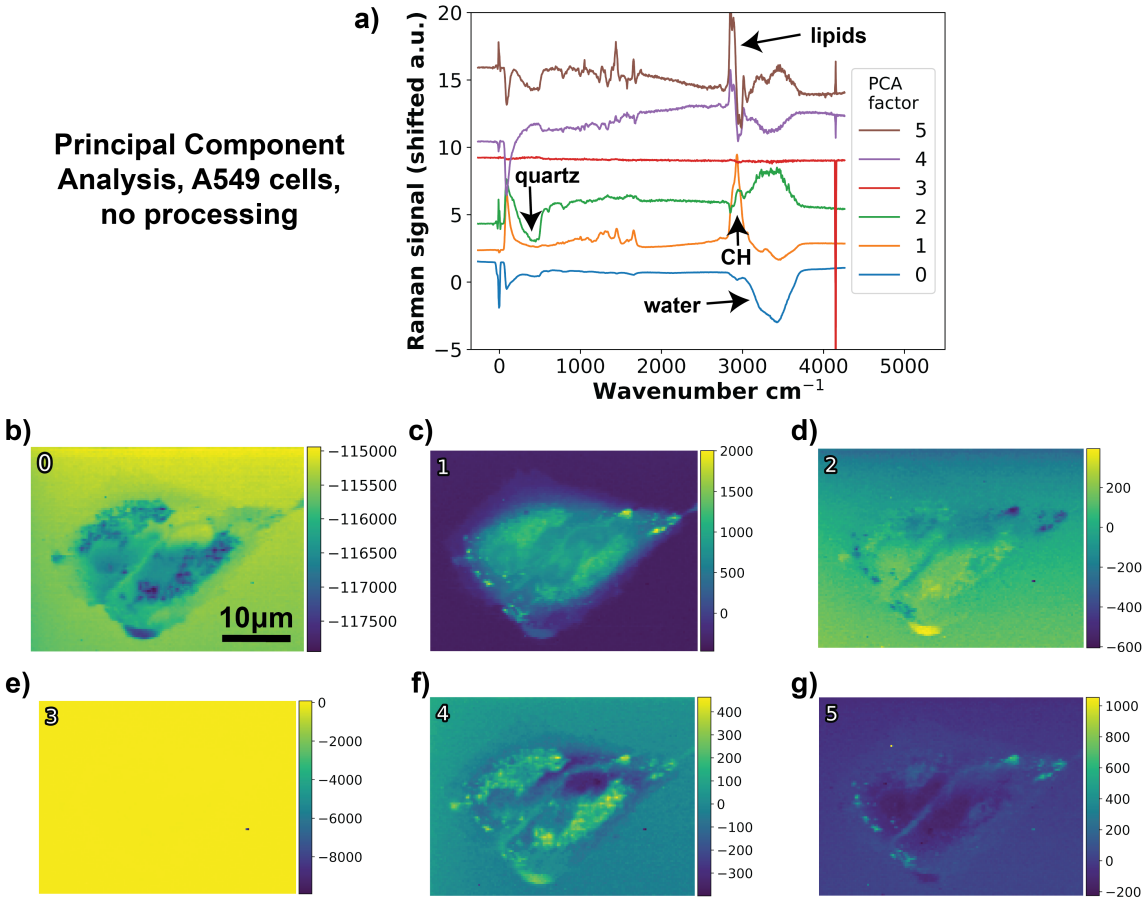

Fig. 3.8 Principal Component Analysis on an area scan of an A549 cell. Completed without any prior data processing to demonstrate which types of processing are required. a) Principal Component (PC) spectra 0-5 show the directions of most spectral variation. b) PC0. An intracellular component that is mixed with top to bottom heterogeneity of the image. c) PC1. This is the clearest outline of the cell and depends on the CH peak at 2807–3025 cm^{-1}. d) PC2. Another image that displays top to bottom heterogeneity, with a cellular component mixed in. The corresponding spectrum in (a) shows anti-correlation between water (3000–3700 cm^{-1}) and quartz (250–550 cm^{-1}), indicating that lower in the image, the imaging collection plane moves higher relative to the sample plane (i.e. in the axial (z) direction, up out of the page). e) PC3. The variation corresponding to a cosmic ray on the detector. In (a), this is shown as a very narrow and intense spike. f) PC4. An intracellular component of the cell. g) PC5. Lipid droplets inside a cell, as identified by the positive spike in 2815–2915 cm^{-1}, the lower half of the CH peak.

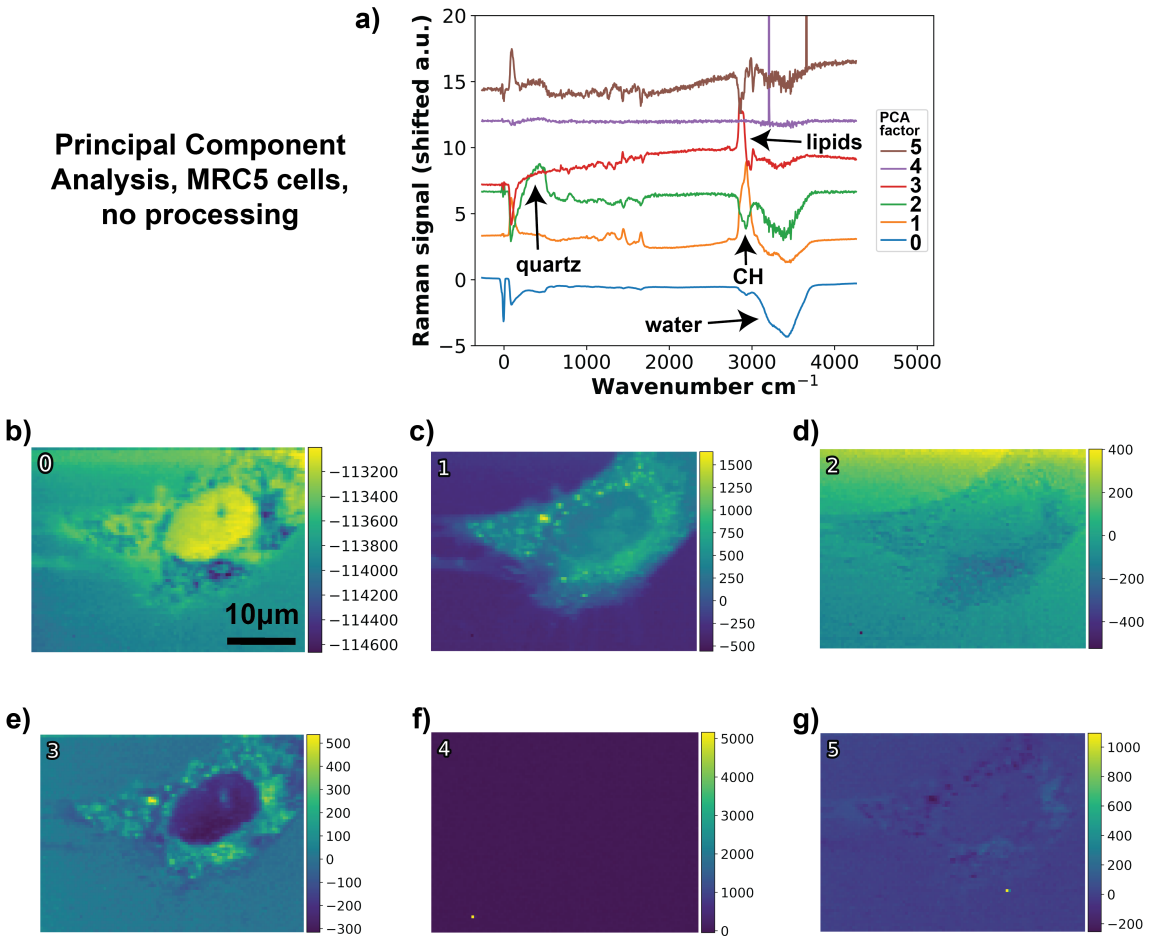

Fig. 3.9 Principal Component Analysis on an area scan of an MRC5 cell. Completed without any prior data processing to demonstrate which types of processing are required. a) Principal Component (PC) spectra 0-5 b) Spatial map of PC0 - has artefactual heterogeneity between the top and bottom of the spatial field. Appears to have a strong nuclear component of the cell. c) PC1 - makes a good cell outline, from the cell CH bond 2807–3025 cm^{-1}, including some component from lipid droplets. d) PC2. The clearest component of top (near $y = 0$) and bottom (near $y = 30$) heterogeneity. The associated spectrum (2) shows that there is a anti-correlation between water (3000–3700 cm^{-1}) and quartz (250–550 cm^{-1}), implying that the sample is angled relative to the imaging plane. e) PC3. A component with information about intracellular organelle distribution. f) PC4. A cosmic ray given a one pixel spike event that is independent of the sample. This can be seen in (a), in the associated spectrum. g) PC5. Another cosmic ray, mixed with intracellular signal.

3.3 Results

3.3.1 Identifying data processing needs

Principal Component Analysis

Principal component analysis (PCA) was applied to the cells (Figures 3.8 and 3.9) to find the spectral variation across the sample. The results of the PCA were used to inform and direct further analysis. Firstly, both figures show variation due to cosmic rays (Figures 3.8e, 3.9f and 3.9g). These images show a few pixels of intense and narrow spikes and are independent of the sample, with most of the image appearing uniformly flat. This is a result of charged particles interacting with the detector, producing a strong signal, the variation of which covers over useful cellular variation. These spikes over just a few pixels should therefore should be removed from the data by spectral pre-processing.

A second artefact is the presence of a broad, non-zero sloping baseline, observed Figures 3.8a, spectrum 2 and Figures 3.9a, spectrum 3. These broad increases are a result of fluorescent signal from the cells. This acts to obscure the Raman signal, and therefore motivates some background subtraction.

A third artefact of the data is observed most clearly in Figures 3.8d and 3.9d with their associated spectra. In these cases, variation is caused by a change in height of the imaging plane relative to the sample substrate top surface, which manifests in top and bottom heterogeneity. The associated spectra (2) show an anti-correlation between water (3000–3700 cm^{-1}) and quartz (250–550 cm^{-1}), implying that the samples are angled relative to the imaging plane. Since these peaks are mostly separate from the cellular data, it is possible to pre-process the data by spectrally cropping them out. Normalisation may also help reduce this effect.

A fourth type of artefact stems from signal strength variations in time, with slight variations in the collected signal intensity during the measurement. In the images this manifests in the a small increase (or decrease) of intensity in adjacent pixels that are scanned immediately after each other (along a horizontal line), that is not shown for pixels that are adjacent in space, but scanned some time apart (the vertical in-plane direction). An example of this is along the top line of Figure 3.9b (and also in Figure 2.7b). To reduce these variations, normalisation is an appropriate pre-processing step to examine the biological data without the misleading changes of the measurement technique.

By observing these artefacts of unprocessed data with PCA images (Figures 3.8 and 3.9), it is clear that spectral pre-processing would be advantageous for revealing biological

information by reducing irrelevant signals. These pre-processing steps include cosmic ray removal, background subtraction, spectral cropping (shortening), and normalisation. To aid human interpretation, spectral smoothing was also implemented. These techniques are described in detail in Section 3.2.2 and Figure 3.10.

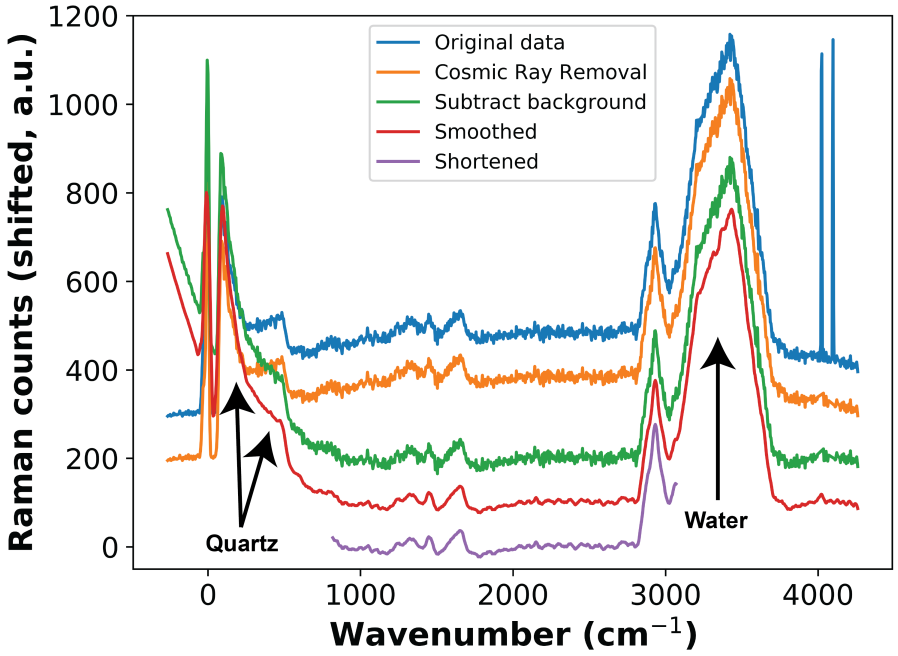

Fig. 3.10 Sequential steps for Raman pre-processing to remove artefacts from the data shown on an example single spectrum from A549 cells. The data is originally collected (blue) on a CCD camera, and therefore is affected by artefactual cosmic rays. There are removed with an in-built function of Hyperspy based on derivatives and inspection (blue to orange). A fluorescent background from the cells is also collected and removed via polynomial subtraction (orange to green). Data are then smoothed with a Savitzky-Golay smoothing algorithm to reduce noise (green to red). The spectra are then cropped between 818–3072 cm^{-1} to remove the quartz and water peaks (red to purple). After this, spectra are then normalised by a scale factor to absolute area under curve (ie negative values are taken as positive and then integrated), known as 'Manhattan' normalisation (normalised spectrum not shown here).

Additionally from these PCA images, it is possible to observe that the signal that is characteristic of the main cell body decreases towards the edges. This is likely as a result of the fact they are thinner there, and the signal is becoming more similar to the spectrum of the medium (Figures 3.8c and 3.9c). This means clustering strategy should try to account for these edges in order to correctly segment the cells from the background. The PCA images

also show the location of the nucleus and lipid droplets, implying that these data are sufficient for at least some sub-cellular clustering.

3.3.2 Cell detection

Raman spectroscopy is principally used to locate the cells. Cell detection was performed with different analysis methods including peak integration, PCA and k-means clustering (Figures 3.11 and 3.12). Peak integration between 1160–1504 cm^{-1} reveals some of the cell before any data processing. This is advantageous as it makes it possible to find cells to scan, that are otherwise unstained and difficult to find. Furthermore, this can be applied quickly without complicated processing, making it suitable for fast cell identification during the experiment. Peak integration of the same range after processing does not improve the cell detection, a phenomenon that perhaps results from the loss of intracellular fluorescence. However, in the A549 image (Figure 3.11b), there appears to be a central line dividing the total cell area in two equivalent halves, suggesting there may be two cells in the field of view. Peak integration of the CH peak at 2806–3024 cm^{-1} (panels c and d of Figure 3.11) leads to better segmentation of the cell, with the thinner area around the cell being included. The improvement at this wavenumber range is likely a result of the higher signal intensity in this peak.

Principal Component Analysis was also applied as an attempt to outline the cell. Principal Component 1 provides a good map of the location of the cell, whilst also excluding the background. This is true before and after processing. The similarity to the integration of the CH peak implies that most of the information content for PC1 is in the CH peak. PCA also falsely captures a number of small background points. The segmentation could therefore be improved by using a size threshold for segmentation.

Thirdly, k-means cluster analysis was used to observe the cell. For two clusters, the main cell body was segmented, but without most of the cell periphery. Processing the data provided an improvement in this respect, correctly expanding the clustered cell area. For k-means analysis with three clusters, the analysis before data processing revealed top-to-bottom image heterogeneity, and also failed to include the cell periphery. After data processing however, the cell periphery and main body are well segmented in both the A549 and MRC5 cells. This is a demonstration of the advantage of using the full spectra range in clustering. This segmentation is further justified by the spectra of these clusters, where the cell periphery clearly exhibits the Raman peaks of cells, such as the 2930 cm^{-1} CH peak.

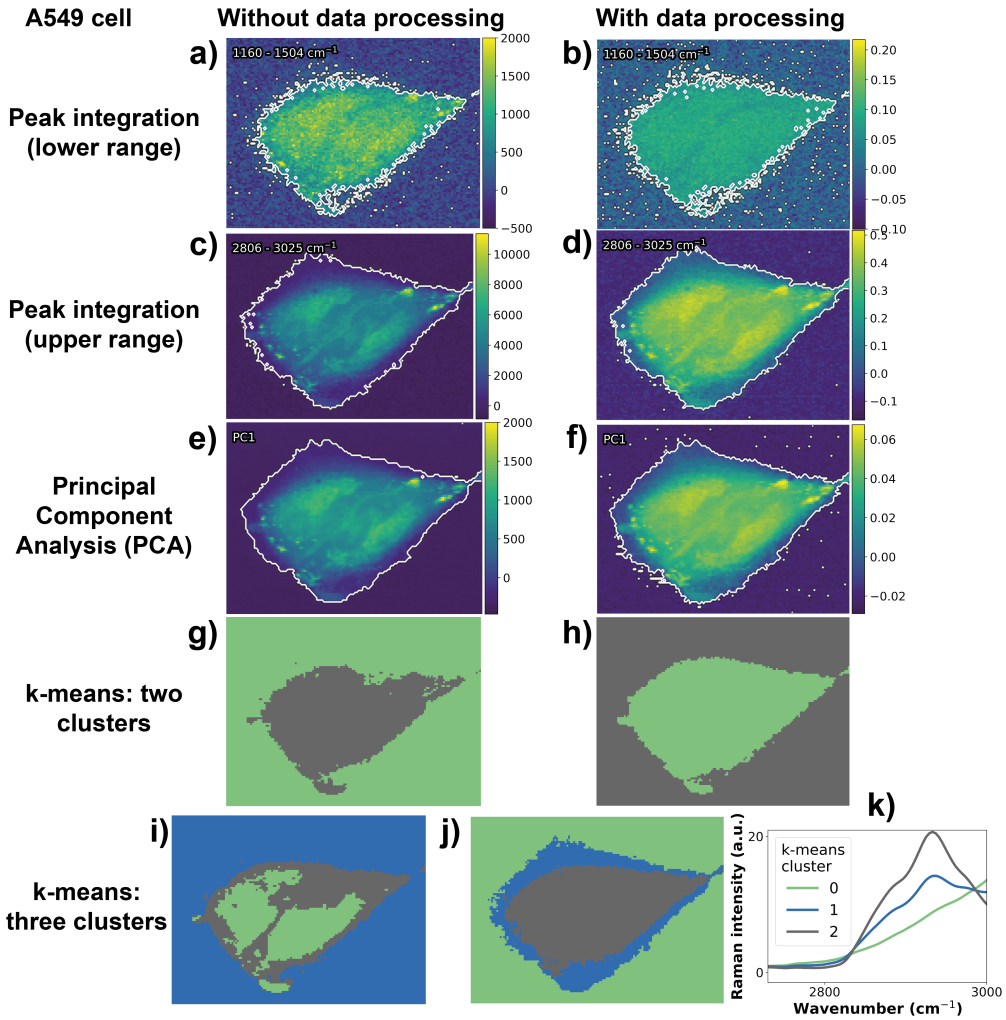

Fig. 3.11 Cell detection with Raman data using different analysis methods. a) Peak integration between 1160–1504 cm^{-1} reveals some of the cell before any pre-processing. b) Peak integration between 1160–1504 cm^{-1} reveals some of the cell after all pre-processing (cosmic ray removal to normalisation). c) Peak integration between 2806–3025 cm^{-1} leads to a better segmentation of the cell, with the thinner area at the edge also being included and the surrounding background successfully removed. d) Peak integration between 2806–3025 cm^{-1} after processing gives a similarly good cell identification as (c). e) Principal Component 1 (PC1) before processing provides near-perfect segmentation that includes the cell periphery. f) PC1 after processing. g) K-means cluster analysis with two clusters fails to capture cell periphery and has top to bottom heterogeneity. h) K-means cluster analysis with two clusters after data processing correctly finds the cell, though excludes the periphery. i) K-means cluster analysis with three clusters places another cluster inside the main body of the cell. j) K-means clustering of three clusters after processing is the most successful at usefully discriminating the whole cell, including its centre and weak periphery. k) A Raman spectrum of the clusters in (j) indicate that the cell periphery contains cellular peaks in the CH region of 2807–3025 cm^{-1}.

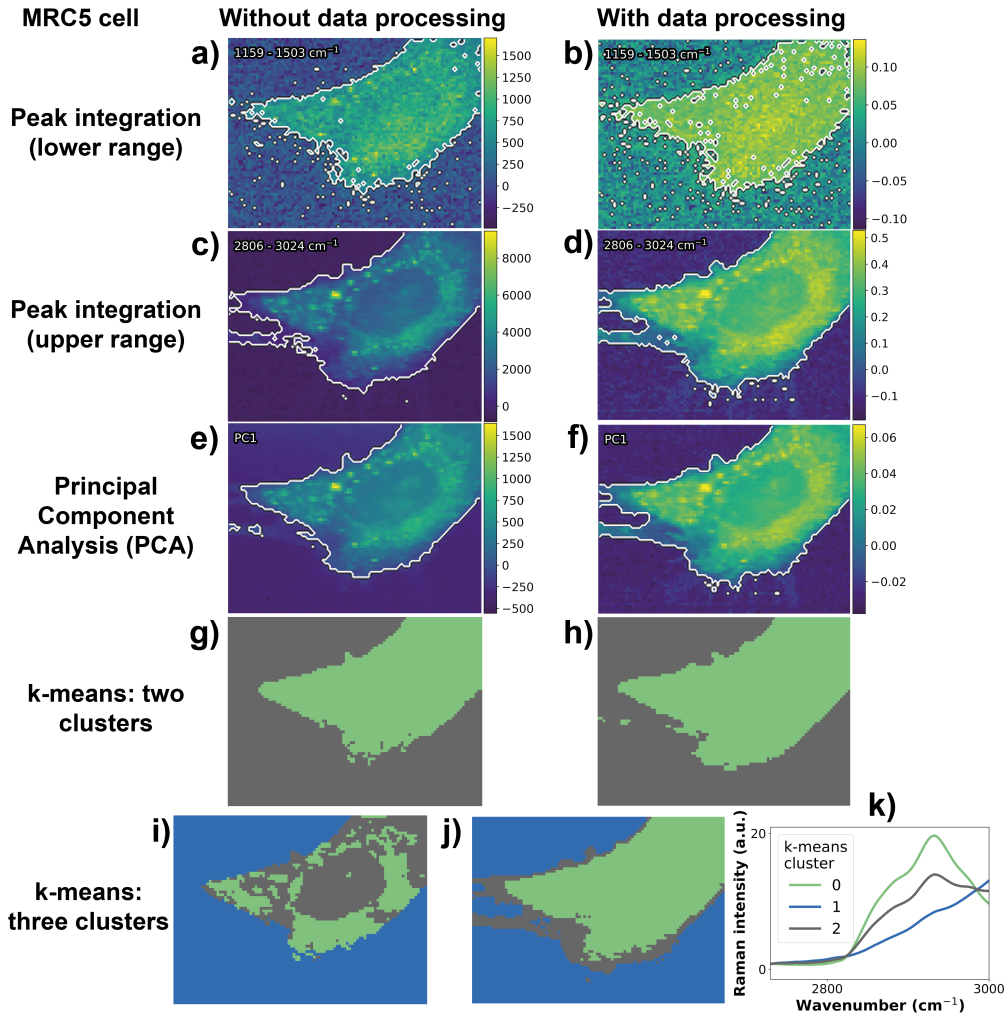

Fig. 3.12 Different techniques to detect an MRC5 cell. a) Peak integration in the region 1159–1503 cm^{-1} without any prior processing. This is successful for the main cell body, but fails to segment the cell periphery, and also includes some background points. b) Peak integration in the region 1159–1503 cm^{-1} without any prior processing. This segmentation is similar, with no cell periphery, and some background points included. c) Peak integration in the region 2806–3024 cm^{-1} without any prior processing. The cell periphery is partially included. d) Peak integration in the region 2806–3024 cm^{-1} after processing. The cell is well segmented, with only a few external points wrongly included. e) PC1 before processing segments only the cell body, and the image is again similar to (c). f) PC1 after processing. g) K-means clustering on unprocessed data for two clusters finds the main body of the cell. h) K-means clustering on processed data into two clusters captures part of the cell periphery in addition to the main cell body. i) K-means clustering on unprocessed data into three clusters. This shows the main cell body, as well as some information on intracellular components. j) K-means clustering on processed data reveals cell periphery and cell body clearly. k) The spectra of the clusters in (j). The cell periphery cluster (dark grey), contains peaks similar to the cell body in the CH peak region 2807–3025 cm^{-1}.

3.3.3 Intracellular clustering

Peak integration and PCA intracellular clustering

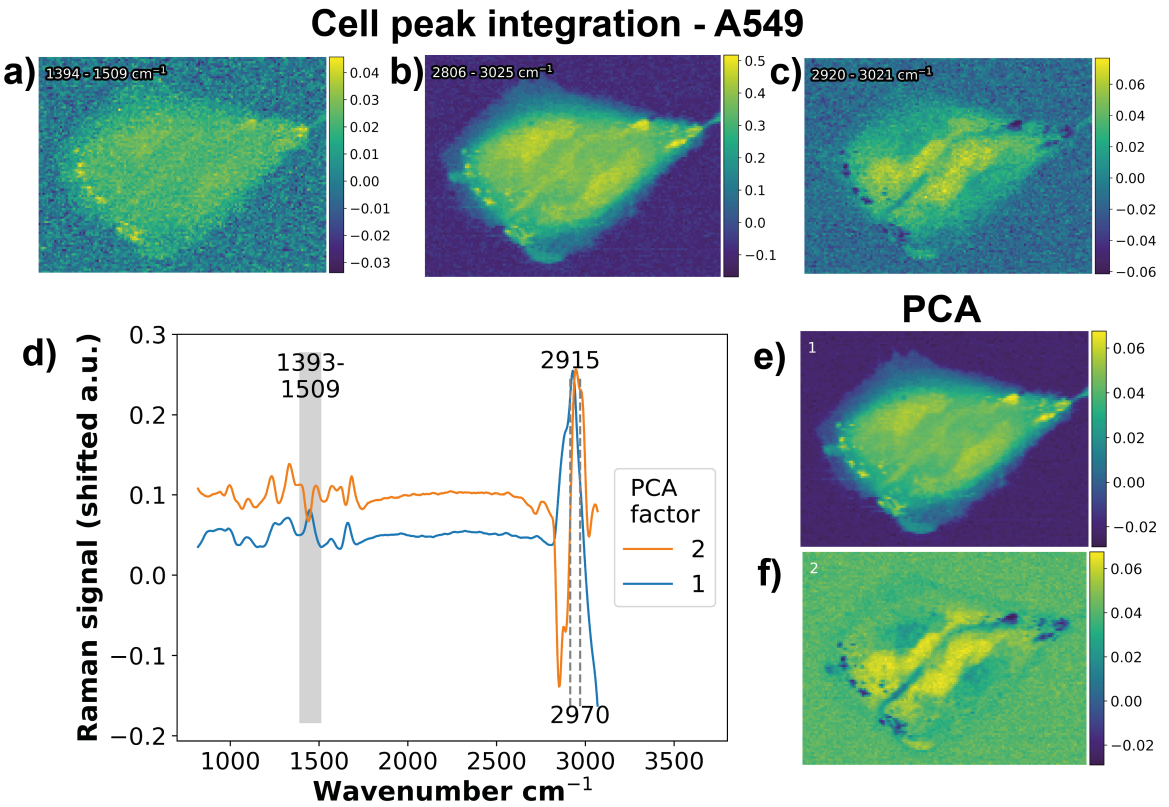

Fig. 3.13 Peak integration and Principal Component Analysis of Raman signal to observe intracellular components in an A549 cell. a) Peak integration in the range 1393–1508 cm^{-1}. b) Peak integration of the CH peak 2806–3024 cm^{-1}. c) Peak integration in the region 2920–3021 cm^{-1} shows a separate intracellular component in the centre of the cell(s). This corresponds to the upper half of the CH peak. d) Principal Component spectra of the data, with integration regions marked. e) PC1 shows similar spatial distribution to the CH peak (b), with lipid droplets highlighted. f) PC2 shows a similar region to (c) peak integration, with the upper half of the CH peak being a major component.

As well as detection of the cell itself, it is possible to analyse Raman microscopic data to reveal intracellular components. This can be partially done with peak integration and PCA after pre-processing as demonstrated in Figures 3.13 and 3.14. In the 'fingerprint region' (800–1800 cm^{-1}), the peak from 1394–1509 cm^{-1}, derives strongly from lipids at 1448 cm^{-1} [22], and so can be integrated (Figure 3.13a and 3.14a). These lipids are also observed in the higher wavenumber region by integration across the whole CH peak (2806–3025 cm^{-1}), which also appears to pick up other cytoplasmic components more strongly

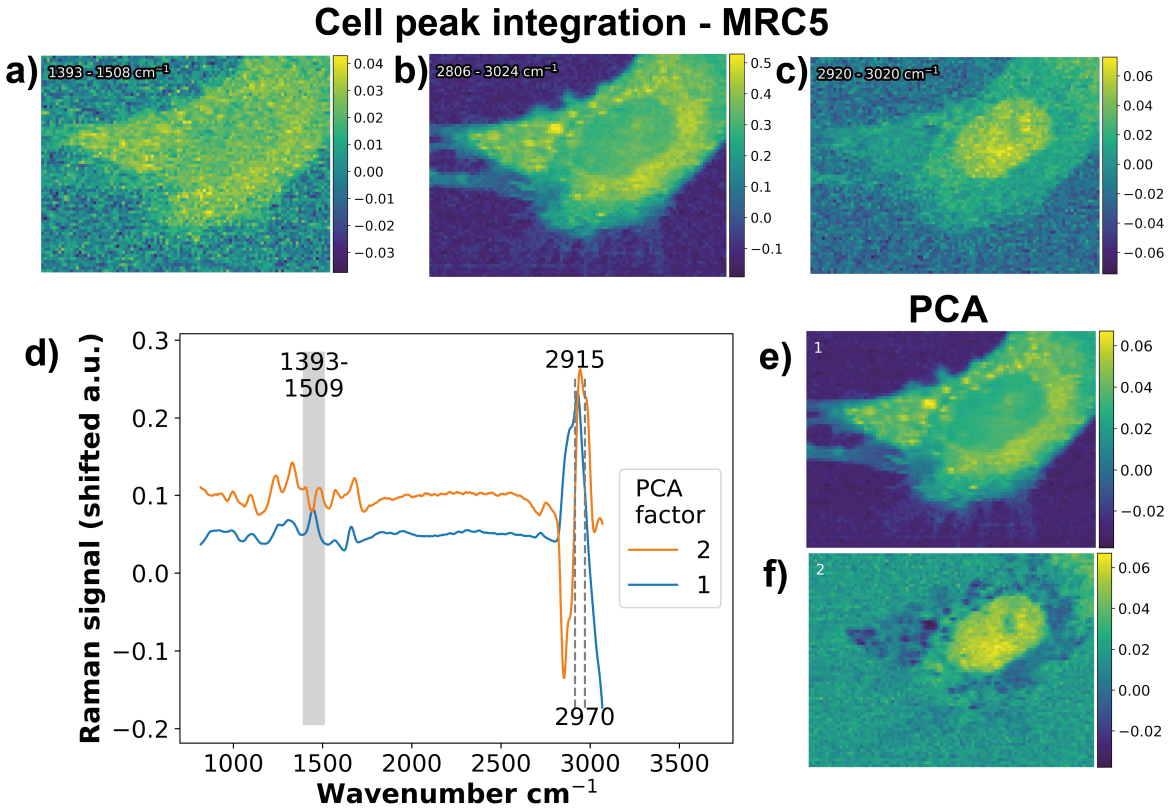

Fig. 3.14 Peak integration and Principal Component Analysis of Raman signal to observe intracellular components in an MRC5 cell. a) Peak integration in the range 1393–1508 cm^{-1} reveals intracellular components in the cytoplasm. b) Peak integration of the CH peak, in 2806–3024 cm^{-1} leads to segmentation of cytoplasmic components, such as lipid droplets. c) Peak integration of the upper half of the CH peak 2920–3020 cm^{-1} reveals the nucleus of the cell. d) Principal component spectra 1 and 2, with the regions of integration marked. e) PC1 is again similar to 2806–3024 cm^{-1} f) PC2 marks a nuclear component, marking a similar region to (c).

(Figure 3.13b and 3.14b). Another intracellular component can be observed by integrating in the range 2920–3021 cm^{-1}, which has previously been associated with nucleic acids [19] (Figure 3.13c and 3.14c).

Principal component analysis reveal similar structures as simple peak integration, with Principal Component 1 (PC1) being dominated by the lipid droplets and structures, as seen in the (d) and (e) panels. This component had a strong positive variation in the lower half (at and below 2915 cm^{-1}) of the CH peak, as has been associated with lipids [22]. PC2 incorporates the nuclear components (such as high wavenumber CH), whilst also removing the lipid peaks. This produces images (Figure 3.13f and 3.14f) where the lipid droplets are outlined as negative features.

K-means intracellular clustering

K-means clustering is another technique that is suitable for intracellular clustering to observe sub-cellular organelles. This can be applied through the stages of data processing to demonstrate the effectiveness of these techniques, as shown in Figures 3.15 and 3.16. For this technique, the cell was first clustered into three as in Figures 3.11 and 3.12 (i and j), and then the main cell body was further clustered.

The first pre-processing step applied to the data was cosmic ray reduction. In Figures 3.15 and 3.16 (a) to (b), cosmic ray removal appears to induce colour modifications. However, each image uses a different, independent, arbitrary colour-coding scale and colour changes between images are not consequential.

The next data processing step involves removal of background fluorescence by polynomial subtraction, as seen in Figures 3.15 and 3.16 in panels (b) to (c). This actually makes the spatial correlation of the intracellular clusters worse, particularly in the A549 cells. This could be because information in the fluorescence helps to cluster the cells. However, these signals are insufficiently specific so it is correct to remove the fluorescence to leave only the Raman data.

Smoothing under the Savitzsky - Golay algorithm was then applied, and did not affect the clusters. This was expected as k-means clustering is an algorithm that depends of averages, and should therefore not be strongly affected by random noise. This is still an useful part of data processing, nonetheless, as it makes the peaks clearer when observing the spectrum, thereby aiding interpretation. After smoothing, high and low wavenumbers were removed from the spectrum, leaving the range 818–3072 cm^{-1}. This was to remove the water (3500 cm^{-1}) and quartz peaks (500 cm^{-1}), as an attempt to remove some of the heterogeneity from top to bottom, which was partially observed in the k-means clusters.

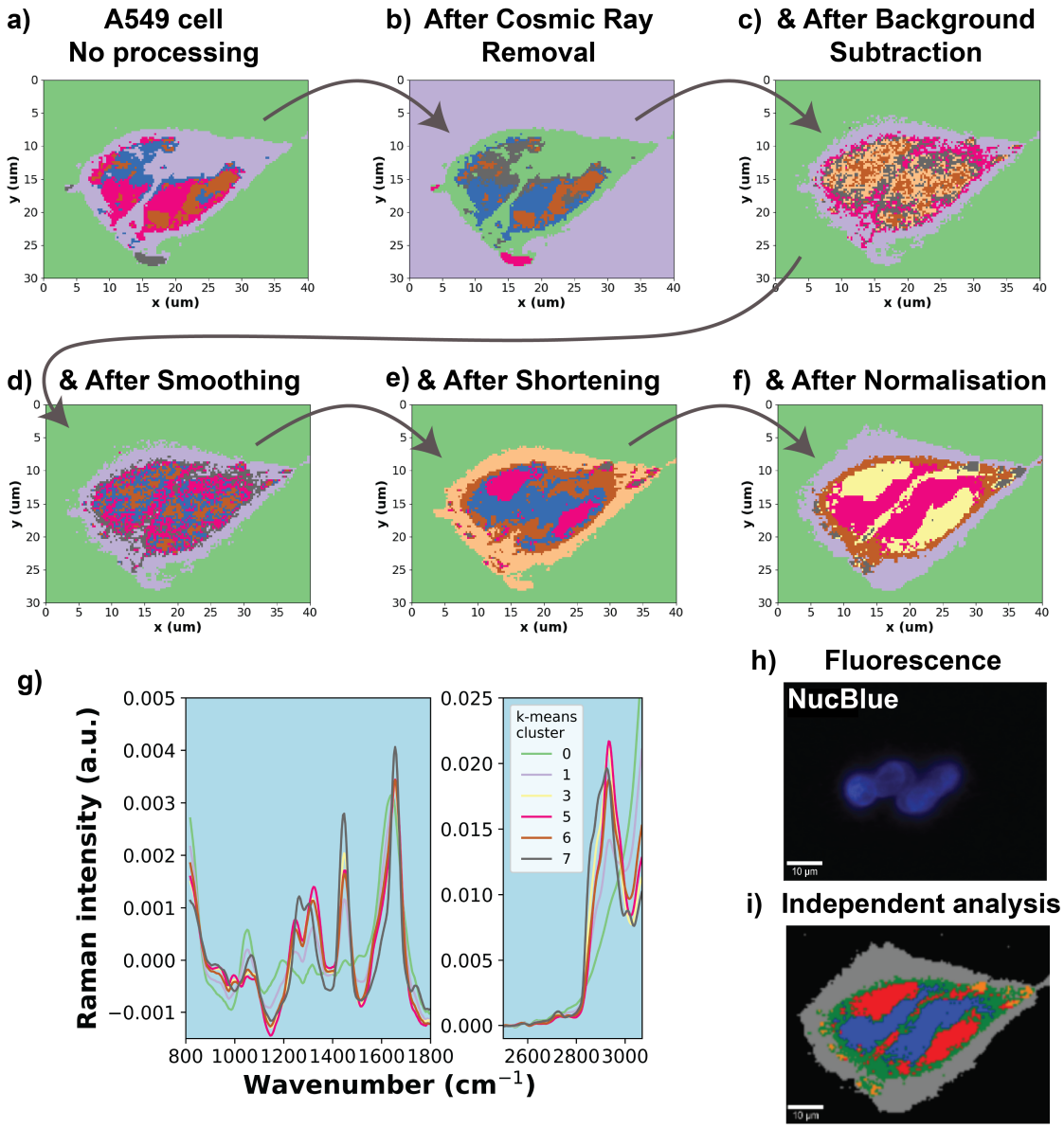

Fig. 3.15 K-means clustering on an A549 cell to display organelles. a) Some top to bottom heterogeneity ($y = 0$ to $y = 30$) can be seen in the clusters. b) Cosmic Ray Removal seems to make little difference to the sub-clusters. c) Background subtraction removes most of spatial correlation in the clusters. d) Smoothing does not alter the clustering from background subtraction very strongly. e) Shortening the spectra restores the appearance of intracellular spatial clusters. f) Normalisation creates clusters that are similar to (h) and (i). g) The Raman spectra of the clusters shown in (f). Clusters have been assigned as described in the main text. A549 Cluster 0 (AC0): background medium; AC1: cell periphery; AC3: cytoplasmic component; AC5: nucleus; AC6: cytoplasmic component; AC7: lipid droplets. (h) Fluorescent staining using NucBlue (Blue) shows the nuclear region. h) Independent analysis from Dr Jakub Surmacki using WITec Project Plus for data analysis, as published in Surmacki et al. using the same pre-processing techniques [2].

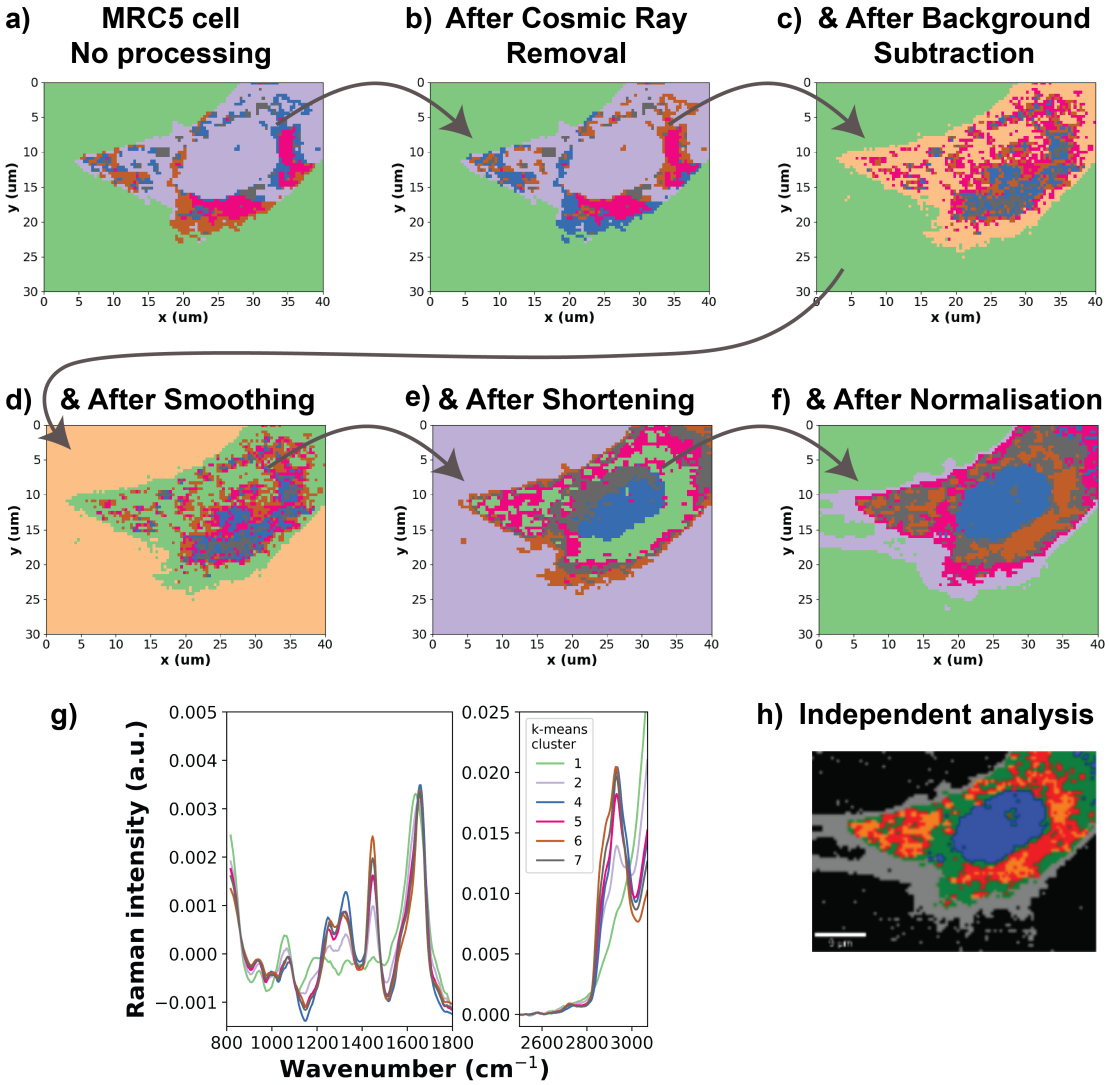

Fig. 3.16 K-means clustering on an MRC5 cell to display organelles. a) Some clusters are more pronounced at the bottom of the cell ($y = 20$) indicating artefactual heterogeneity. b) Cosmic ray removal again makes no noticeable difference to the sub-clusters. c) Background subtraction seems to decrease spatial correlation in the clusters. d) Smoothing again does not alter the clustering from background subtraction very strongly. e) Shortening the spectra causes more spatial clustering of the k-means clusters, though still with y-direction heterogeneity. f) Normalisation creates clusters that are similar to (h). g) K-means cluster spectra from (f). Clusters were assigned by peak information as described in the main text. h) Independent analysis of the data from Dr Jakub Surmacki using WITec Project Plus for data analysis as published in Surmacki et al. [2].

Finally, normalisation was used to further remove heterogeneity, including that which comes from general variations in signal intensity, such as varying laser power.

After normalisation, k-means clustering allows identification of some of the clusters. Firstly, the cell medium is observed surrounding the cell in A549 Cluster number 0 (AC0, green) and MRC5 Cluster number 1 (MC1, green). This is similar on both, with peaks as expected from full medium with serum in the 'fingerprint region' 800–1800 cm^{-1} (Figure 3.6a). MC0 has a very small CH peak at 2930 cm^{-1}, indicating there may be a small amount of cell periphery in this component.

The cell periphery is identified as before (Figures 3.11 and 3.12), and shown here as AC1 (purple) and MC2 (purple). This contains a weaker CH peak 2930 cm^{-1} [22] due to the physical thinness of the cell periphery. By displaying the processing steps and k-means clustering together it is clear that normalisation is essential to find this.

An intracellular organelle that is clearly found in each cell is the nucleus - AC5 (pink) and MC4 (blue). These clusters show a strong peak at 1326 cm^{-1}, which is known as a DNA peak [22]. The A549 scan actually appears to contain two separate nuclei, indicating that an original cell may have divided into two, and the nuclear shape elongation may indicate another division is imminent. In any case, these reproduce the nuclear identification as seen from peak integration and PCA (Figures 3.13 and 3.14).

Another component that can be identified is related to the lipids of the cells. AC7 (grey) and MC6 (brown) both exhibit a peak at 2880 cm^{-1}, known to be associated with lipids [22]. The spatial distribution of AC7 means that it can be described as lipid droplets, where MC6 has a wider spatial extent. MC5 (pink), MC7 (grey), AC3 (yellow), AC6 (brown) are other cytoplasmic components, likely containing endoplasmic reticulum and mitochondria, given their nuclear proximity.

As well as the peak data, partial confirmation for these clusters comes from fluorescence (Figure 3.15h) and spatial similarity to a separate analysis. The nuclear cluster in A549 cells is matched closely to the co-registered fluorescence of the NucBlue stain, as expected. Furthermore, analysis on the same data by Dr Jakub Surmacki in the commercial software, WITec Project Plus, produced similar clusters, with differences in the MRC5 perinuclear region (Figure 3.16h [2]).

3.3.4 Chemical changes over time

Using the k-means clustering and data processing techniques developed above, it is possible to observe changes inside the cell. In this case, an A549 cell was scanned 15× at 9.8 mW

over a period of 3 hours (Figure 3.17). Over time, the cell shows two major changes. With each scan, the cell periphery (green in the first image) reduces in size, including showing some circular structures (Figure 3.17k), that may correspond to blebs. Secondly, the cell experiences nuclear fragmentation in scans (Figure 3.17 n to p). Both of these are typical of apoptotic cell death [44]. This cell death is related to the measurement process, as cells that were not measured remained well extended in their periphery. This is an indication that 10 mW is too high for this pattern of repeated scans.

3.4 Discussion

Hardware

In this chapter a commercial instrument was used in order to develop data analysis protocols for Raman microscopy. The commercial instrument was used while the custom setup described in the previous chapter was under construction, and it differs from the bespoke instrument in various ways. Firstly, this Raman system operates at 488 nm, unlike the custom 532 nm microscope. While most of the Raman peaks will be common to both wavelengths, some differences in fluorescence intensity and peaks are likely. Samples will probably have lower fluorescence intensity at the longer wavelength [164]. In addition, the custom system's wavenumber range is restricted and does not include the helpful information content of the CH peak for clustering as these wavelengths overlap with the diamond nitrogen vacancy fluorescent centre. On the other hand, in addition to successfully exciting NV nanodiamonds, working with an excitation at 532 nm may prove very useful for mitochondria imaging as cytochrome c is resonantly excited at this wavelength, producing measurable Raman peaks that both help locate mitochondria, and measure apoptosis [133]. A further difference is that cells will likely experience different biological impacts at 532 nm as compared 488 nm. While lower energy (longer wavelength) light is likely to be less harmful, it is not possible to optimise the parameters such as laser power, integration time and scan number on the commercial system, as these would not be applicable on the custom system.

Live cell imaging

The live cell Raman imaging protocol was developed with lung cancer cells (A549) and fetal lung fibroblast cells (MRC5). The similarity of the protocol and analysis for these cells is an indication that these techniques are not narrowly dependent on cell type. Nevertheless, if significantly different cells such as stem cells or neurons were to be used in future, both

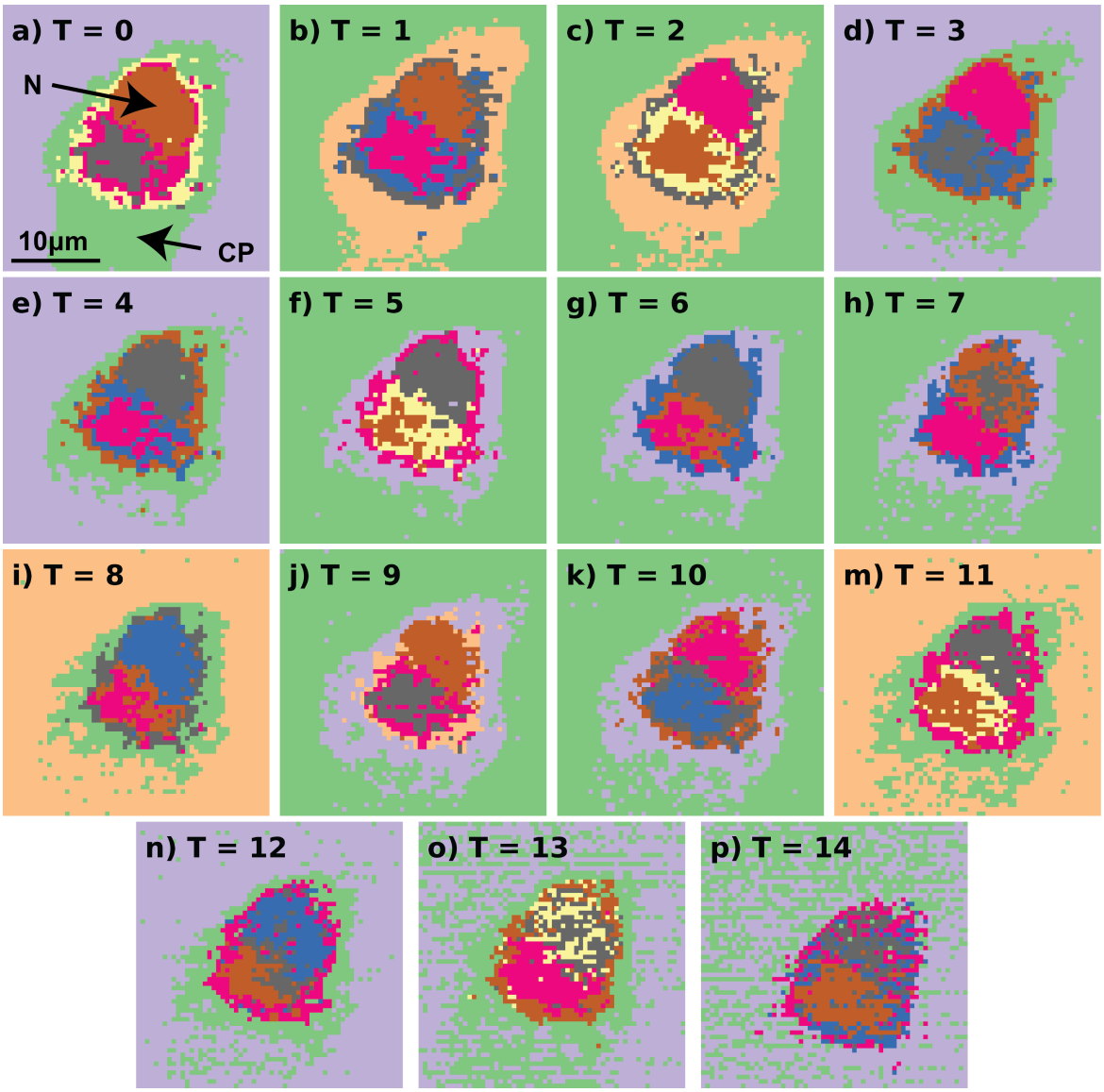

Fig. 3.17 An A549 cell were scanned 15 times at a beam path laser power of 9.8 mW over a period of 3 hours. K-means clustering was applied to each Raman scan independently, in the same way as described in Figure 3.15. Colours represent arbitrary labels for the clusters. Image (a) labels the nuclear region (N, in brown) and the Cell Periphery (CP, in green). Scans (a)-(p) show the recession of the cell periphery as the cell is damaged, and scans (n)-(p) show the disintegration of the nuclear cluster.

practical and analytical protocols will have to be optimised. In addition, the optimisation of scanning parameters (e.g. collecting a few points per cell only) remains to be explored. A further protocol choice that has not been investigated is the choice of objective lens. The highest numerical aperture lens was used to increase signal from low concentrations of chemicals. However, there may be circumstances where it is advantageous to increase the size of the spot with a lower magnification objective, in order to get a more representative signal.

Software

The software used in the data analysis of this chapter consists in Python libraries, particularly Hyperspy. Other programming languages may be used to achieve similar results. However, Python combines the properties of speed, open source, high level easy programming and extensive libraries in a way that is not common to many other languages such as Matlab. The commercial instrument includes WITec Project 4.0 analysis software. The use of Hyperspy presents several advantages over the WITec Project. Firstly, all analysis in this chapter can be easily checked and reproduced by display in Jupyter notebooks, improving the reproducibility and integrity of the science done. Secondly, WITec Project does not always comprehensively describe the methods behind its use, with the exact algorithms being protected under commercial secrecy. Thirdly, data stored under Python analysis appears to be approximately half the size of the equivalent WITec file. Fourthly, Hyperspy provides a clear conceptual framework of navigation spaces and signal spaces which are particularly user-friendly. Finally, the free open source nature of Python means that this analysis can be applied on custom built systems while the WITec Project relies on licenses covering specific hardware and software and it is not possible to import data into the software from a non-WITec machine.

However, there are also some disadvantages of using the Python-based approach. For some users, the greatest issue is that the WITec Project approach is fundamentally based around a Graphical User Interface (GUI), rather than a coding interface. This is partially offset by the close implementation of GUI elements in Hyperspy, but there still remains a barrier to entry for some. Secondly, the WITec software also has more advanced features built in, though Hyperspy can easily interface with other libraries to provide additional support (such as SKLearn for k-mean clustering). Thirdly, the WITec software allows quick analysis whilst data is being collected. However this is not required for the project discussed here. Finally, it is worth noting both WITec Project and Hyperspy systems are optimised for hyperspectral data, and run at a convenient speed on all analysis.

Principal Component Analysis

In this chapter, PCA was used to find artefacts in the data, as well as displaying the cell and some organelles. It could be further developed to remove noise from the data by removing the noisiest components, though noise removal was adequately provided by the Savitzky-Golay technique. The Savitzky-Golay technique has the advantage that it can also be used on a single spectrum, therefore making the pre-processing analysis pipeline more flexible [272]. For analysis in this work, PCA components were selected visually on their spatial distribution, but this could be improved in future by using 'scree plots' to only choose components that have a certain amount of information.

Pre-processing

The data preparation techniques in this chapter were performed on the data with reference to common processes in the literature [303]. Nevertheless, there were still some challenges with implementing these. One example is that the Raman peaks in the fingerprint region (800–1800 cm^{-1}) are too close to each other for the background to be observed and effectively fitted. Unfortunately this means that polynomial background subtraction can reduce the signal to below zero, as seen in Figure 3.15. There may also be a limitation associated with the smoothing applied after this. The Savitzky-Golay algorithm depends on an window length given by the user. This was chosen to remove noise while preserving the signal peak amplitudes. However this parameter and others are somewhat arbitrary, and it is unclear whether minor modifications could have significant clustering implications. Another possible limitation with data pre-processing is the spectral cropping procedure (shortening). This was chosen to remove peaks associated with water and quartz, leaving the fingerprint region and the CH peak. However, some cellular information is likely to exist in these regions, possibly reducing clustering efficacy. On balance though, it is more useful to remove the associated artefacts (see Figure 3.15 d to e). The final step of data processing used was normalisation. 'Manhattan' normalisation was used for direct comparison with WITec Project, but 'area under curve' or 'Euclidean' (square root of sum of square differences) could also be explored. An overall uncertainty with the pre-processing scheme is the order in which the techniques are applied. While some are independent effects, it is also possible that the clustering could be altered by the order in which these are applied.

K-means clustering

After processing the data, k-means clustering was applied to find cells, find intracellular organelles, and track changes through time. For simplicity, k-means clustering was used to assign each point to a single cluster. For further development, fuzzy c-means clustering could be used to account for the fact that a single point may contain multiple organelle components. This technique works by assigning probabilities that each point belongs to each cluster, rather than a complete assignment of each point to only one cluster. A problem with k-means clustering is that it relies on a number of clusters that is chosen by the user, independently of the variation within the sample. Following that, many of these clusters appear very similar (unlike in PCA), making it difficult to interpret some of the clusters (e.g. in Figure 3.15g).

For cellular segmentation, k-means clustering with pre-processing and three components was observed to be the most effective at outlining the cell without the inclusion of background. Peak integration is a simpler approach however, and so is more useful during an experiment to find cells for scanning. There is a potential issue with this in that peak integration requires a threshold to be set, which requires a whole cell scan to be accurate. However in approximate terms, this corresponds to the existence of a peak above the noise floor, and so a cell can be identified from a single point with sufficient confidence. For the whole cell scanning of Figures 3.11 and 3.12 the cell detection could be improved by setting spatial size thresholds to remove the small background spots.

For organelle segmentation, cluster identification was performed as in other studies [22]. Although some cytoplasmic components were not unambiguously identified, it is reasonable to hope that mitochondria and cytochrome c signal will be identified using the same technique at 532 nm [133, 141, 164].

Cellular change over time was observed via organelle clustering. It would also be possible to view cellular changes spectrally, as outlined in chapter 1. This would be advantageous as it would not be necessary to continue to do whole cell scans during measurement. During the scanning experiment, apoptosis of the cell was observed. The cause of apoptosis in the cell is unclear, but may be related to repeated laser scanning. It will be necessary to carefully check power levels at 532 nm to ensure that there is no similar cell damage. These changes were important to observe as they provide complementary and related information to the proposed nanodiamond measurement. Mitochondrial membrane potential ($\Delta\Psi_m$) has been shown to be linked to biological processes such as apoptosis, with $|\Delta\Psi_m|$ first increasing as potassium channels are blocked [45, 8] and then decreasing as the mitochondrial Permeability Transition Pore is opened [41, 32]. These links have been described in more detail in Section

1.1.2. Furthermore, (section 1.3.2), this rich data could be analysed in order to investigate other processes such as metabolic rate and reactive oxygen species.

3.5 Conclusion

Overall, imaging protocols and data analysis protocols have been developed to measure cells with Raman microscopy. This technique removes the need for adding fluorescent dyes that could interfere with nanodiamond measurement spectrally and biologically. Artefacts in the data were identified and removed, and techniques were developed to make use of the full spectral information, such as PCA and k-means clustering.

These successfully detected a cell, both in a helpful way for an ongoing experiment, and in a different way for exact segmentation later. This supports the direct measurement of mitochondrial membrane potential using nanodiamonds by restricting the area of search to find only intracellular nanodiamonds.

Cell segmentation also enabled organelle detection and partial identification, which was supported by fluorescence data and independent analysis. This can support the process of nanodiamond membrane potential measurement by specifying the location of the nanodiamond within the cell. In the future, the nanodiamonds will be targeted to mitochondria, although Raman detection of this specific organelle was not possible at the wavelength used here. However, this should be possible at 532 nm, the illumination wavelength of the custom system.

These cellular organelles were then observed to change through the process of apoptosis. By monitoring the process of apoptosis with Raman spectroscopy simultaneously with nanodiamond measurement of $\Delta\Psi_m$, it will be possible to have a broader understanding of the cell changes, that helps to bring insight into mechanisms of cell death.

Importantly, the data acquired on the commercial system were analysed in Python, a free, open source language, enabling the translation of these techniques onto a new custom Raman microscope tailored for Nitrogen-Vacancy Centre measurements for the investigation of mitochondrial membrane potential in cells.

Having developed Raman protocols in this chapter, and previously developed a custom instrument (Chapter 2), it is necessary to develop biological understanding and protocols with nanodiamonds to complement this. This is the subject of Chapter 4.

Chapter 4

Biological effects of nanodiamond oxidation

Dr Laura Ansel-Bollepalli (LB) performed the proliferation measurements as shown in Figure 4.13 and prepared the samples shown in Figure 4.5. Dr Jakub Surmacki (JS) performed the oxidative stress experiment in Figure 4.17. The images for these experiments were analysed by Ben Woodhams (BW). All other work was completed by BW. Most of this work is published as Woodhams et al. [1].

4.1 Introduction

4.1.1 Oxidation: motivation and literature review

Nanodiamonds have been proposed as a reliable and capable replacement for fluorescent dyes in biomedical applications, that would overcome some of the limitations associated with dyes. Owing to their superior spin properties over detonation nanodiamonds, High-Pressure High-Temperature (HPHT) nanodiamonds are commonly exploited for measurements using the nitrogen vacancy centre (NVC) [74, 73].

After HPHT and detonation nanodiamond fabrication, the nanodiamond surface is typically a layer of sp^2 graphitic carbon [304–306]. For metrology in cells, this graphitic layer is often removed by oxidation, which has been to shown to: reduce charge switching between the NV^- and NV^0 charge states [241]; improve brightness [307]; and facilitate surface functionalisation to target nanodiamonds to particular intracellular sites [67, 308]. Identifying and understanding any cellular perturbations caused by the biological application of nanodiamonds with different surface chemistries is vital. This chapter focuses on optimising

the process of oxidation, characterising the physiochemical differences that result and the biological consequences of these. Overall this project aims to measure $\Delta\Psi_m$ with nanodiamonds as a key parameter that is linked with processes such as apoptosis and oxidative stress. Therefore it is particularly important any impact of oxidised nanodiamonds on these processes.

The ability to perform intracellular measurements using nanodiamonds relies on a robust knowledge of the processes that govern their internalisation and retention. Both graphitic and oxidised nanodiamonds have been observed to be internalised [309, 310], with oxidised nanodiamonds explicitly shown to be actively internalised by clathrin-mediated endocytosis [234]. Oxidised nanodiamonds also appear to enhance the uptake of various pharmaceuticals compounds thus increasing their efficacy [119]. The rate at which graphitic and oxidised nanodiamonds are expelled from cells has been reported to be slow, with only about 15 % oxidised nanodiamonds expelled after six days in HeLa cells [309, 258].

Next, consideration must be made of their potential to cause apoptosis. Both graphitic and oxidised nanodiamonds have been demonstrated to have little or no short-term cytotoxicity in human cells in complete culture media at sizes above 30 nm [311] and in the size range 2–20 nm [90–92, 312–314] which correspond to detonation nanodiamonds. However, in one study on detonation nanodiamonds, there have been cytotoxic effects observed in bacteria with both surface types [315]. Many studies have focused on short-term viability; for the longer term experiments enabled by the chemical- and photo-stability of nanodiamonds, a greater impact may be observed on proliferation over time, where slow cell division and death processes can be examined. Application of 2–10 nm graphitic unmodified detonation nanodiamonds in serum-free media over 24, 48 and 72 h has been shown to reduce cell number [121], although a similar study at 24 h for 2–10 nm graphitic and oxidised nanodiamonds did not observe a significant effect [91]. Furthermore, in full medium over 48 h, 100 nm oxidised diamonds have been shown to have little influence on cell number [316].

In addition to changes in cellular proliferation, nanoparticles may cause transient stress responses [317, 318], which have yet to be fully explored for nanodiamonds. For example, oxidative stress, an imbalance of free radical species and antioxidants, is an important parameter that is linked to many cell processes such as apoptosis, DNA degradation, as well as cardiovascular and neurodegenerative diseases, and cancer [319, 320], as outlined in Section 1.1.2. If nanodiamonds are to be exploited as a potential replacement for fluorescent dyes, they should not only be benign in terms of their impact on proliferation, but they should also avoid induction of cellular stress responses. There have been a limited number of studies of nanodiamond induced oxidative stress responses; while 3–10 nm unmodified detonation

nanodiamonds showed a small antioxidant effect [321], 5 nm oxidised detonation diamonds were found to generate low levels of reactive oxygen species in one cell line [92]. Detonation nanodiamonds often contain more chemical impurities than HPHT nanodiamonds, likely changing their biological impact [125]. Acid-oxidised 15 nm diamonds were observed to have no effect on unstressed neural cells and actually protected stressed cells from oxidative damage [322].

In this chapter, the biological impacts of both graphitic and oxidised HPHT nanodiamonds are investigated by analysing cellular uptake as well as proliferative and stress responses in two breast cancer cell lines. The focus is on HPHT nanodiamond rather than detonation diamond due to the aforementioned advantageous sensing capability. The first direct comparison of graphitic and oxidised HPHT nanodiamonds using realistic concentrations for single cell measurements ($\leq 1\,\mu g\,ml^{-1}$), rather than the higher concentrations typically used for drug delivery is presented.

4.2 Methods

4.2.1 Chemical characterisation

Nanodiamonds (Non-detonation, NaBond Technologies Co., China) were manufactured by a High-Pressure High-Temperature (HPHT) bulk diamond process then milled to a nominal 45 nm, with less than 50ppm nitrogen impurities and containing fluorescent nitrogen-vacancy centres. Oxidation to remove the graphite by burning was performed in a Vecstar VTF1SP tube furnace in air, calibrated with a K-type thermometer to $445 \pm 5\,^{\circ}C$. The error is given by the uncertainty in spatial positioning of the sample within the tube. Nanodiamonds were drop-cast onto a quartz coverslip (CFQ-2520, UQG Optics, UK) or contained in a crucible (SS22, Almath, UK) with water. Following a literature review of previously applied conditions for oxidation in air (Table 4.1), the sample was heated in air at 450 °C for 5 hours (Figure 4.1). Initially, thermogravimetric analysis was performed to optimise the experimental conditions, then the success of the removal of the graphitic layer was evaluated.

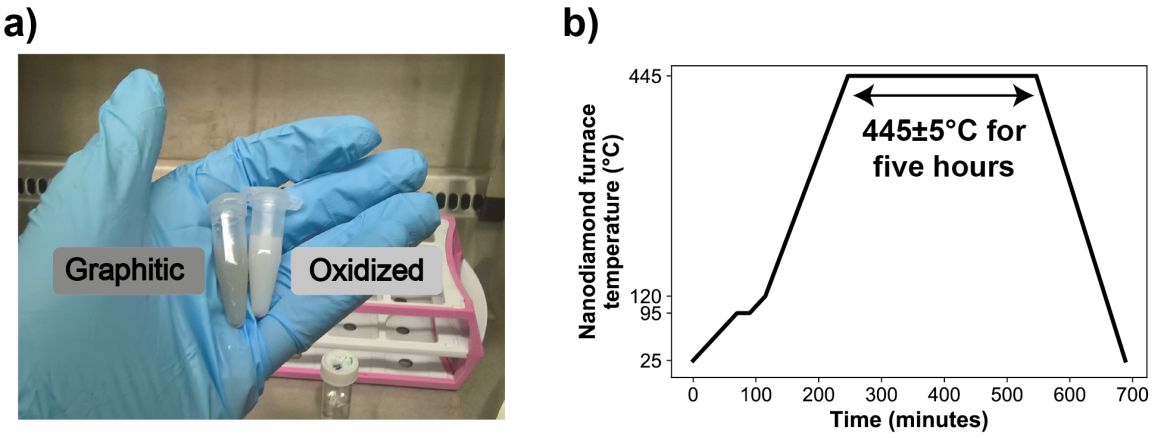

Fig. 4.1 Nanodiamond oxidation by heating in air. a) A photograph of graphitic and oxidised nanodiamonds at 1 mg ml^{-1} in water shows a colour change after oxidation. b) Temperature profile for the procedure of nanodiamond oxidation. This was performed in air.

Conditions	Comments	Reference
425 °C	Above 450 °C all forms of carbon are etched. Most likely surface functional group afterwards is COOH. This work is a review paper of oxidation conditions.	Krueger and Lang (2012) [67]
400 °C for 1 hour (h)	5 nm nanodiamonds still contain a graphitic Raman peak as high as diamond after oxidation, so this is not completely effective.	Smith et al. (2010) [304]
450 °C for 6 h		Zhao et al. (2014) [323]
500 °C, 550 °C, 600 °C for 5h	Some mass loss was observed.	Sotoma et al. (2015) [324]
510 °C for 4.5 h	These authors found 4.5 h to be better than 1 h or 2 h.	Havlik et al. (2013) [307]
Different temperatures between 25–1000 °C for 2 h	G band does not completely burn away	Cebik et al. (2013) [325]

Conditions	**Comments**	**Reference**
600 °C for 6 h in O_2	70% mass loss was observed.	Aramesh et al. (2015) [326]
425 °C for 4 h	This was a careful and slow process, described as 'layer-by-layer'.	Etzold et al. (2014) [327]
425 °C for 5 h	This protocol is widely used and cited.	Osswald et al. (2006) [328]
450 °C for 1 h then piranha acid cleaning at 100 °C for 3 h		Mohan et al. (2010) [329]

Table 4.1 A review of oxidation techniques in the literature implies that most groups use approximately 400–500 °C. Most work above 450 °C incurs significant mass loss and most work uses 4–6 h. Therefore, this implies that it is reasonable to investigate heating conditions of 425 °C and 450 °C for 5 h.

Thermogravimetric Analysis (TGA) was used to investigate the weight loss as a function of temperature to identify the temperature at which graphite was burnt away whilst preserving the diamond. TGA was performed with 14 mg of nanodiamond powder (TGA 4000, PerkinElmer, USA). To evaluate optimal conditions for oxidation, the heating temperature was increased at 3 °C min^{-1} or 1 °C min^{-1} up to 900 °C in air and the weight was measured every second. A plateau was observed at 650 °C. The temperature was held at 120 °C for 30 minutes to remove water. Heating at 3 °C per minute decreased the nanodiamond mass remaining from 75% to 25% between 546 ± 1 °C and 592 ± 1 °C. Upon slower heating at 1 °C per minute, the nanodiamonds were reduced from 75% to 25% mass between 534 ± 1 °C to 545 ± 1 °C (Figure 4.2a). The largest mass loss rate is found at a consistent temperature, 537 ± 1 °C (3 °C min^{-1}) and 535 ± 1 °C (1 °C min^{-1}), as an exothermic reaction occurs to sustain a burning phase. These results place an upper bound on the temperature required to conserve most of the sample mass in a heating plateau profile at 535 ± 1 °C. Considering the derivative of this curve (Figure 4.2b), 425–450 °C appears to be sufficiently far below the onset of burning to perform the oxidation.

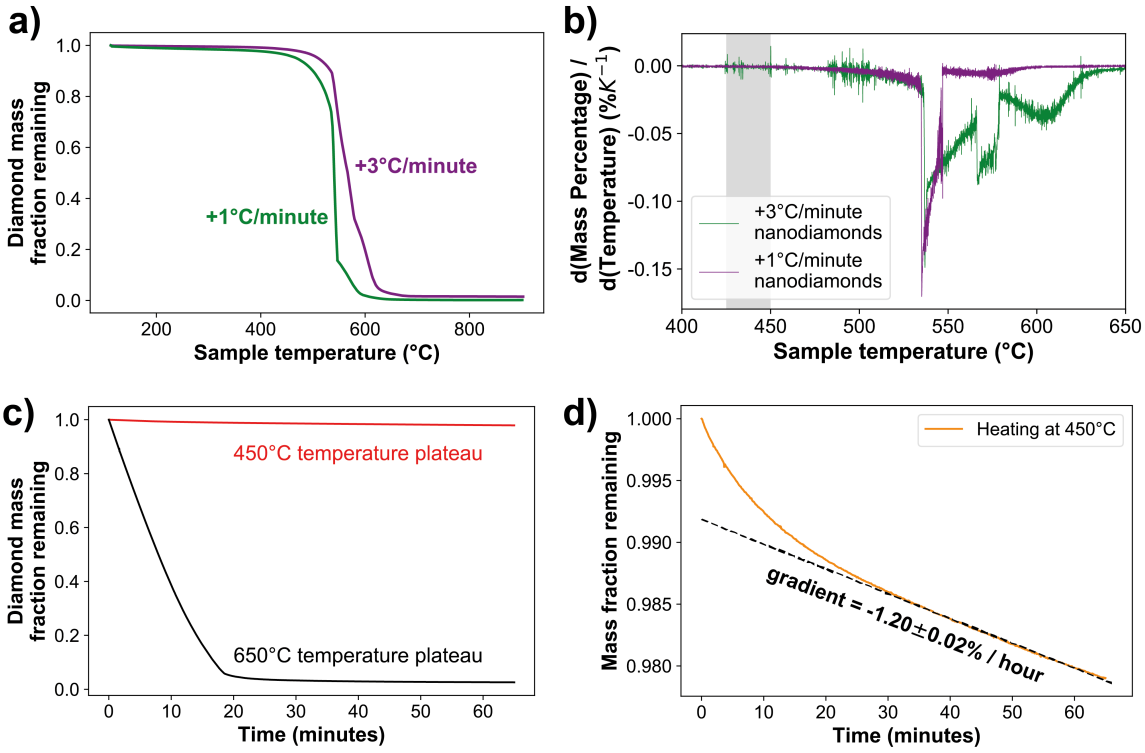

Fig. 4.2 Thermogravimetric analysis to establish appropriate conditions for oxidation. Heating nanodiamonds in air on a weight balance indicates that 450 °C is an appropriate temperature to oxidise the surfaces of nanodiamonds. a) The mass of a nanodiamond sample as the furnace temperature is increased causing the diamonds to burn. b) The mass change plot is the derivative of (a) and shows that the onset of major mass loss occurs at 535 ± 1 °C and 537 ± 1 °C for the two samples. c) Temperature plateaus at 450 °C and 650 °C show that 450 °C only causes slow mass loss. d) A zoomed version of (c) on the 450 °C temperature plateau where it is observed to cause mass loss at -1.20±0.02%/hour.

In order to understand the effect of 450 °C heating on nanodiamonds, the temperature was increased to 450 °C in 5 min, and then held at that level while the mass change was monitored at 1 s intervals (Figure 4.2). The instrument temperature was calibrated by alumel, perkalloy and iron magnetic phase transitions at the temperatures 154.2 °C, 596 °C and 780 °C to be accurate to ±1 °C across this range. The error in the mass fraction decrease is given by combining the errors in the linear fit with the nominal error in mass accuracy of 0.02%.

To assess the impact of the oxidation process on the nanodiamond chemistry, optical spectroscopy was performed. In Raman spectroscopy it is possible to observe the amount of graphite relative to diamond carbon, so this was the primary technique used to optimise the oxidation procedure [250]. Fourier Transform Infra-Red (FTIR) spectroscopy was also used, as it is able to determine the type of oxygen groups present on the surface.

Raman micro-spectroscopy was performed with a WITec Alpha 300 R Confocal Raman microscope (WITec GmbH, Germany). Samples were prepared by drop-casting diamonds onto a calcium fluoride substrate (CAFP25-1U, UQG Optics, UK) and Raman spectra were recorded using 4 mW 488 nm excitation (CMX1-04813, Newport Corporation, USA) and a 20× NA=0.4 objective (421350-9970-000, Nikon, Japan). The power of the laser was chosen so that there was no damage of the sample after 10 scans, which was observed when operating at 10 mW. Data were collected across a 400 μm × 400 μm area in 1 μm steps with 0.5 s integration time per point and the wavenumber positions were calibrated by measuring a silicon standard. This comprehensive scan was necessary to average over the variation observed from taking single spectra.

Raman spectra were analysed using k-means clustering (WITec Project 4, WITec GmbH, Germany) to extract the diamond signal. Fluorescence background was removed by fitting and subtraction of a 5th order polynomial between 800–1300 cm^{-1} and 1710–2500 cm^{-1}. Data were normalised to the integral of the pure diamond peak between 1280–1390 cm^{-1}. The relative amount of amorphous carbon on the sample was calculated by integration between 1490–1660 cm^{-1} and this wavenumber range was used for p-value significance, error calculation and percentage reduction. The area was calculated by using trapezium rule, and its error was estimated by the standard deviation of the data around a cubic fit. P-value significance was investigated by a two-tailed Mann-Whitney U test as the data did not pass a normality test.

Fourier-Transform Infrared (FTIR) spectroscopy was conducted in air with a Nicolet iS10 transmission instrument (ThermoFisher Scientific, USA) with the sample of nanodiamonds on NaCl windows (Z527130, Sigma-Aldrich, USA). 64 scans per sample were taken with 2 cm^{-1} resolution. For each measurement, a background of air and an empty slide was used.

FTIR spectra were processed by subtracting a cubic polynomial background in the ranges 700–3100 cm^{-1} and 3800–4000 cm^{-1}, and smoothed using a Savitzky-Golay filter (width 201, order 2). Figure 4.3 illustrates the optimisation of spectral resolution and choice of background for collection of reliable FTIR spectra.

4.2.2 Size characterisation

Atomic Force Microscopy was used to measure individual particle size, to ascertain whether the smallest particles were burnt away, and this was complemented by Dynamic Light Scattering (DLS) and optical scattering microscopy to measure aggregate particle size in solution. DLS and optical scattering measurements are important as they are a better measure of the size of particles that the cells will be exposed to. This is important to know as cells may use different uptake mechanisms depending on particle size.

Firstly, two intersecting scratches were made with a diamond cutter onto a quartz substrate (CFQ-1250, UQG optics, UK) for localisation. The substrate was cleaned in acetone then isopropanol in a Sonorex Digital 10P Ultrasonic bath at 63 °C (Bandelin GmbH, Germany) without a probe for 30 minutes each. The nanodiamonds were suspended in ethanol at 1.6 $mg\,ml^{-1}$ and sonicated for 90 minutes at 320 W of ultrasonic power before deposition on the quartz by a respiratory nebuliser (U22, Omron Healthcare Co., Kyoto, Japan). A 15 µm×15 µm, 4096×4096 scan was taken at 0.2 Hz per line with Nanoworld Arrow-FM-20 Force Modulation tips using non-contact air topographical imaging. AFM was chosen over Scanning Electron Microscopy (SEM) as it better resolves surface features that are hidden by the sputter coating normally used in SEM preparation.

AFM data were processed in Gwyddion (GNU General Public License at *www.gwyddion.net*). At least 861 nanodiamonds were assessed. The data were linearly subtracted during collection to correct for tilt. Each image was rotated by 2.2° for mutual alignment and an identical background area on each was set to zero. The images were cropped to show the same diamonds. Data were collected by applying a threshold mask that selected all observed diamonds (3 nm for each), then all diamonds in the shadow of the large particles were removed and the maximum height of the remaining particles was exported. The error in the mean was calculated by dividing the standard deviation by the root of the population size and the distributions were compared by the Mann-Whitney U test.

Dynamic Light Scattering (DLS) data were collected with a Malvern Zetasizer Nano ZSP instrument to interrogate the particles in solution. Samples were vortexed for 2 minutes at 2025 Hz on a VWR Mixer (444-0203, VWR International Ltd., USA), followed by sonication

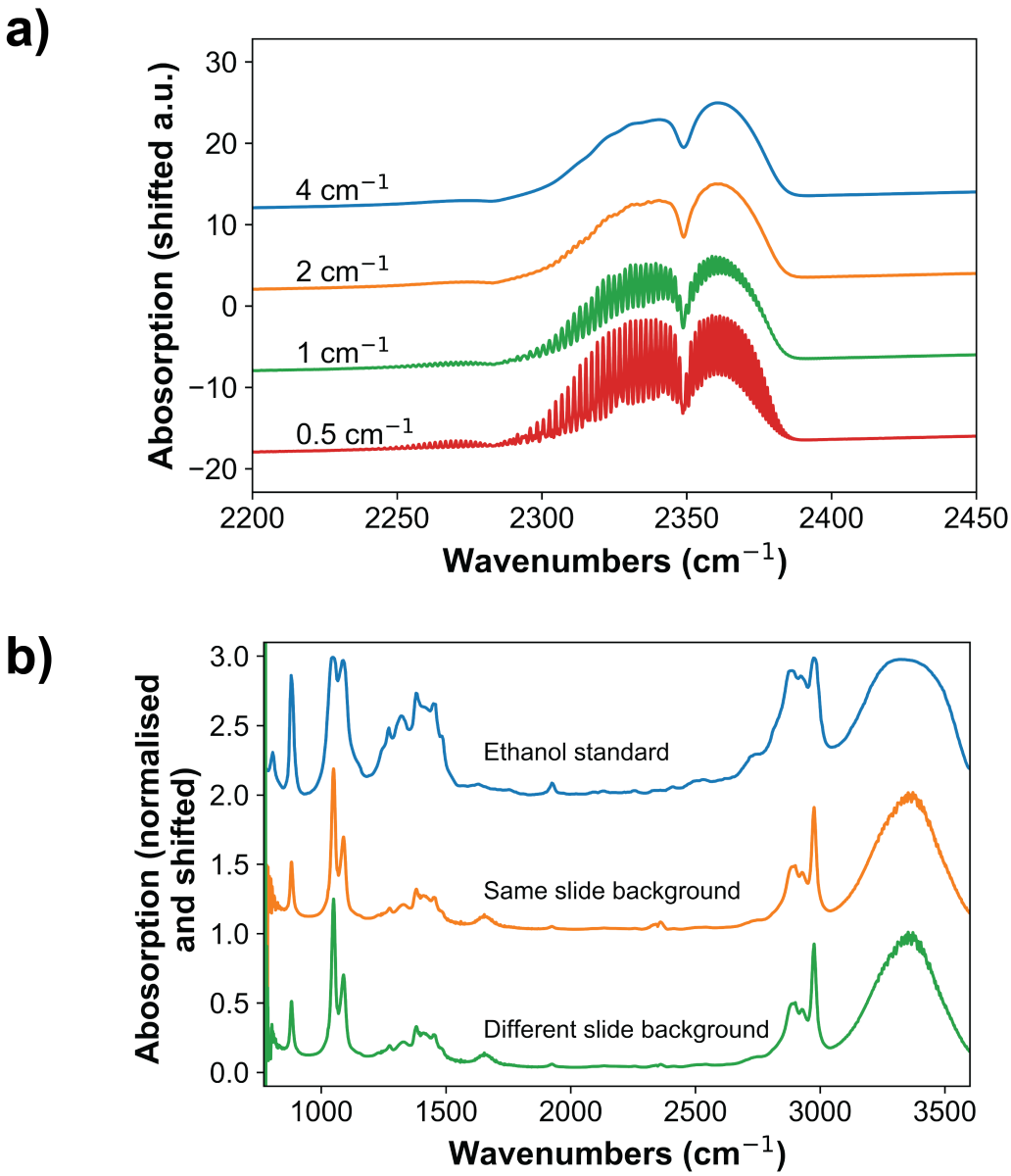

Fig. 4.3 FTIR scan parameter optimisation. a) Scanning air at different spectral resolutions 0.5–4 cm^{-1}, zoomed in on the carbon dioxide peak. Choosing a spectral resolution more precise than 2 cm^{-1} causes oscillations that are artefacts that obscure the signal. These are likely a result of inference of a part of the instrument [26]. b) The ethanol standard spectrum (blue) was downloaded from Collection© 2009 copyright by the U.S. Secretary of Commerce. The orange spectrum is the FTIR spectrum of ethanol on a NaCl slide, with the same slide used as a background. The green spectrum the FTIR spectrum of ethanol on a NaCl slide, with a different NaCl slide used as a background. The FTIR results are higher resolution than the standard sample, but otherwise similar. Using the same slide or a different slide as background seems to be make no difference to the result.

in an Ultrawave U300H (Ultrawave Ltd., UK), a repetition of vortexing, then filtration through a 0.45 µm Polyethersulfone syringe filter (514-0075, VWR International Ltd., USA). The sample was placed within a plastic cuvette for the experiment (67.754 Polystyrene, Sarstedt AG & Co., Germany) with 637 nm excitation and collection via 173° backscattering. Data were only used when meeting the automated quality criteria from the Malvern Zetasizer software 'Expert advice: data meet quality criteria'.

For optical scattering microscopy was performed on an Olympus Confocal Fluorescence Microscope FV1200, nanodiamonds were added to DMEM/F-12 medium without cells at a concentration of 1 µg/ml. This was chosen as a independent measurement of aggregates in solution alongside DLS. The aggregates were observed with confocal optical scattering imaging by collecting an image z-stack near the base of the well by scanning at 633 nm using a 60× oil objective. The scan size is 30 µm of 30 z-direction slices of 210 µm×210 µm images of 2048×2048. This makes the lateral pixel size 103 nm and the axial pixel size as 1 µm. Scattering interference artefacts from the bottom of the well were averaged over by z-projection and then using a rolling ball correction [330] of 50 pixels in size. Aggregates were then thresholded and analysed for oxidised and graphitic diamonds.

4.2.3 Biological characterisation

MDA-MB-231 and MCF-7 adherent breast cancer cells were grown in phenol-free Dulbecco's Modified Eagle Medium (DMEM, 11880-028, ThermoFisher Scientific, USA) with 10% heat inactivated Fetal Calf Serum (FCS, 1050064, ThermoFisher Scientific, USA) and 1 mM pyruvate (11360070, ThermoFisher Scientific, USA). The cells were sub cultured at 80% confluence in ratios 1:20 for MDA-MB-231s and 1:10 for MCF-7s. MDA-MB-231 and MCF-7 origins were verified by short tandem repeat genotyping (performed via the Cancer Research UK Cambridge Institute, UK). These two cell lines were chosen for investigation based on their properties: MCF-7 is a slow-growing, oestrogen dependent cell line, whereas MDA-MB-231 is a fast growing, oestrogen independent cell line. They have also been used in multiple different uptake studies for nanoparticles [331–336], and show different levels of expression for uptake proteins [337].

The number of nanodiamonds per cell was calculated using the following parameters. C: Concentration = (0.01, 0.1 and 1 $\mu g\,ml^{-1}$); V: Volume of medium in a well = 0.3 ml; L: Mean characteristic dimension of the individual nanodiamonds [338] = 23 nm; ρ: Density of

diamond = 3.5×10^3 kgm^{-3}; and N: Number of cells per well = 3×10^5.

$$\text{Number of diamonds per cell (200, 2000, 20\,000)} = \frac{CV}{\rho L^3 N}$$

Uptake experiment

Cells were seeded into six optical-quality eight-well plates (IB-80826, ThermoFisher Scientific, USA) at 5×10^4 cells per well, and incubated overnight to allow for attachment. Graphitic and oxidised nanodiamonds at 1 μg ml^{-1} in 300 μl phenol-free medium with serum were added to three wells each per plate, and fresh medium without nanodiamonds was added to two wells per plate as controls. The plates were left for 1, 2, 4, 8, 24 and 48 hours. At the completion of the uptake time, the wells were washed 3× in medium. They were then fixed in a solution containing 4% paraformaldehyde (HT5011, Sigma-Aldrich, USA) for 15 minutes, followed by three washes in Hank's Balanced Salt Solution (HBSS, 14025092, ThermoFisher Scientific, USA). Cell nuclei and membranes were stained by addition of 3 ml HBSS containing 2 drops of NucBlue Live Ready Probes Reagent (R37605, Invitrogen, USA) and 5 μg ml^{-1} Wheat Germ Agglutinin - AlexaFluor 488 membrane dye (W11261, Invitrogen, USA) simultaneously for 10 minutes. The wells were then washed in phosphate buffered saline (PBS) (2×) and suspended in PBS (Figure 4.4).

This protocol was developed through various stages of optimisation. In the first format, coverslips were placed in petri dishes. However this was unsuitable as nanodiamonds moved underneath the coverslip, altering the concentration that the cells were exposed to. Secondly, petri dishes with glass bases were used (81218-200, Ibidi), but the glass dust on these interfered with the nanodiamond signal, even after washing. Another issue was the detachment of cells due to the large number of washing steps. Moving the fixation step prior to the washes ensured good cell adherence to the substrate and resolved the issue.

The fixed cell samples were scanned with an Olympus Confocal Fluorescence Microscope FV1200, using a 60× oil objective, a pixel size of 132 nm, a scan speed of 4 μm s^{-1} and a confocal size of 71 μm with a resolution of better than 215 nm. Bright field illumination was used to locate cells, so that at least 175 nuclei were captured per condition. The z position was set by moving upwards until the substrate was not observed. The samples were sequentially raster scanned with 405 nm, 488 nm and 633 nm lasers to the collect the nuclear, membrane and nanodiamond signal respectively. Nanodiamond aggregates were detected by elastic light scattering around 633 nm using a collection filter 575–675 nm. Light scattering was found to be the an easiest method of nanodiamond observation than fluorescence by varying the excitation and collection wavelengths (see Figure 4.5).

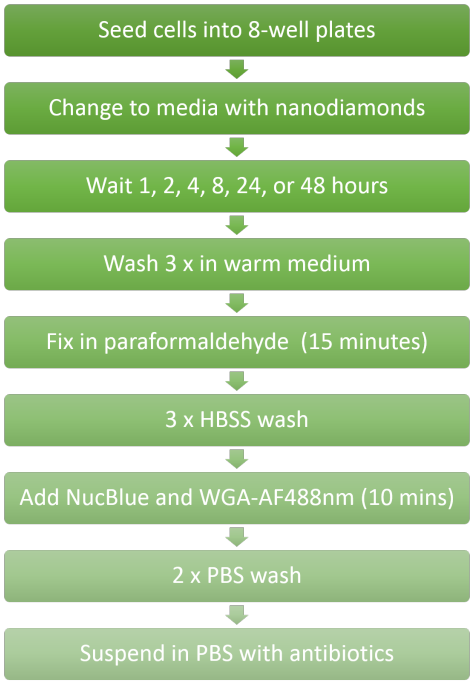

Fig. 4.4 Protocol for nanodiamond uptake experiment into cells.

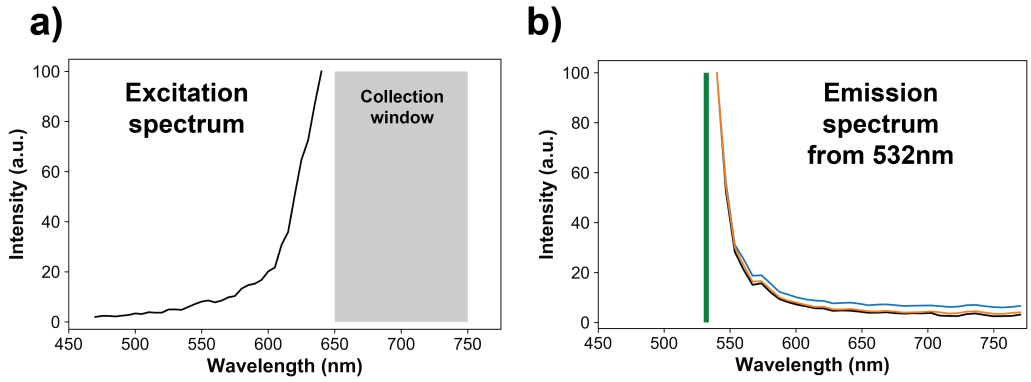

Fig. 4.5 a) Excitation and emission spectrum for nanodiamond particles. For the excitation spectrum, signal was collected between 650–750 nm (grey shaded region) and the excitation was varied (grey line). The excitation spectrum asymptotes to a maximum as it approaches the detection region. b) For the emission spectrum, the nanodiamonds were excited at 532 nm (green vertical line) and the collection was repeated three times at 10 nm bandwidth from 550–750 nm (blue, orange and black lines). and the emission spectrum does likewise as it approaches the excitation. The best explanation for these data is that it is elastic scattering from the particles that produces the signal, rather than any fluorescence from the nitrogen-vacancy centres. This is likely Rayleigh scattering.

Microscopy images were processed using custom software written in Fiji/ImageJ [27] from the intensity image (as collected) in Figure 4.6a to the segmented Figure 4.6b. For the uptake experiment, image filenames were initially blinded and artefacts were removed, including the scattering signals from fragmenting nuclei. After this, nuclear areas were measured and counted using the 'Thresholding' and 'Particle Analyzer' (>50 µm) functions. The membrane stain was used to define the edges of cells, and filled to designate areas enclosed by membrane. These areas were then removed if found not contain a nucleus (Binary Feature Extractor [28]). The nanodiamond scattering channel was thresholded by considering nine representative images, including empty controls, and setting the value as closely as possible for both cell lines. All diamonds that were not totally contained within cells were removed (Binary Feature Extractor, 100% overlap [28]) and the remaining particles were analysed. This is described in detail in Figure 4.7. Two factor ANOVA via Regression was applied to account for unbalanced control with post-hoc t-tests under Dunn-Šidák were used.

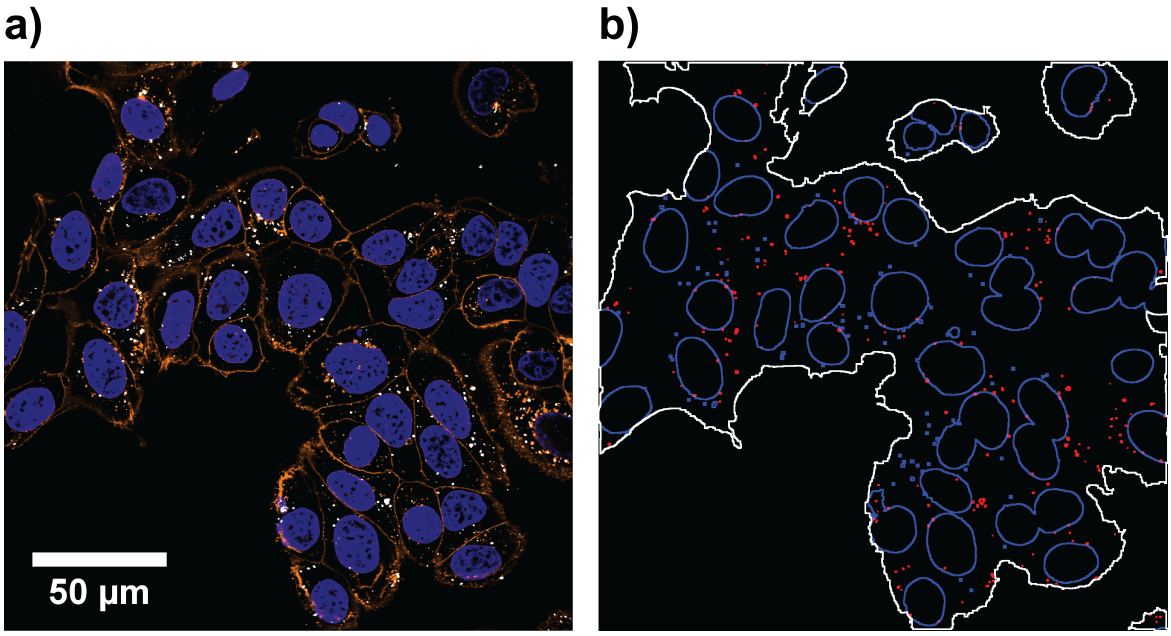

Fig. 4.6 a) Image of nanodiamond uptake experiment in MCF7 cells. Blue is nucleus (NucBlue staining), orange labels the cell membrane (Wheat Germ Agglutinin - AlexaFluor488nm) and white labels the nanodiamonds (as seen by light scattering). b) A segmented version of (a), for quantification. Blue is nucleus, white is membrane and red is nanodiamond. Details are provided in Figure 4.7.

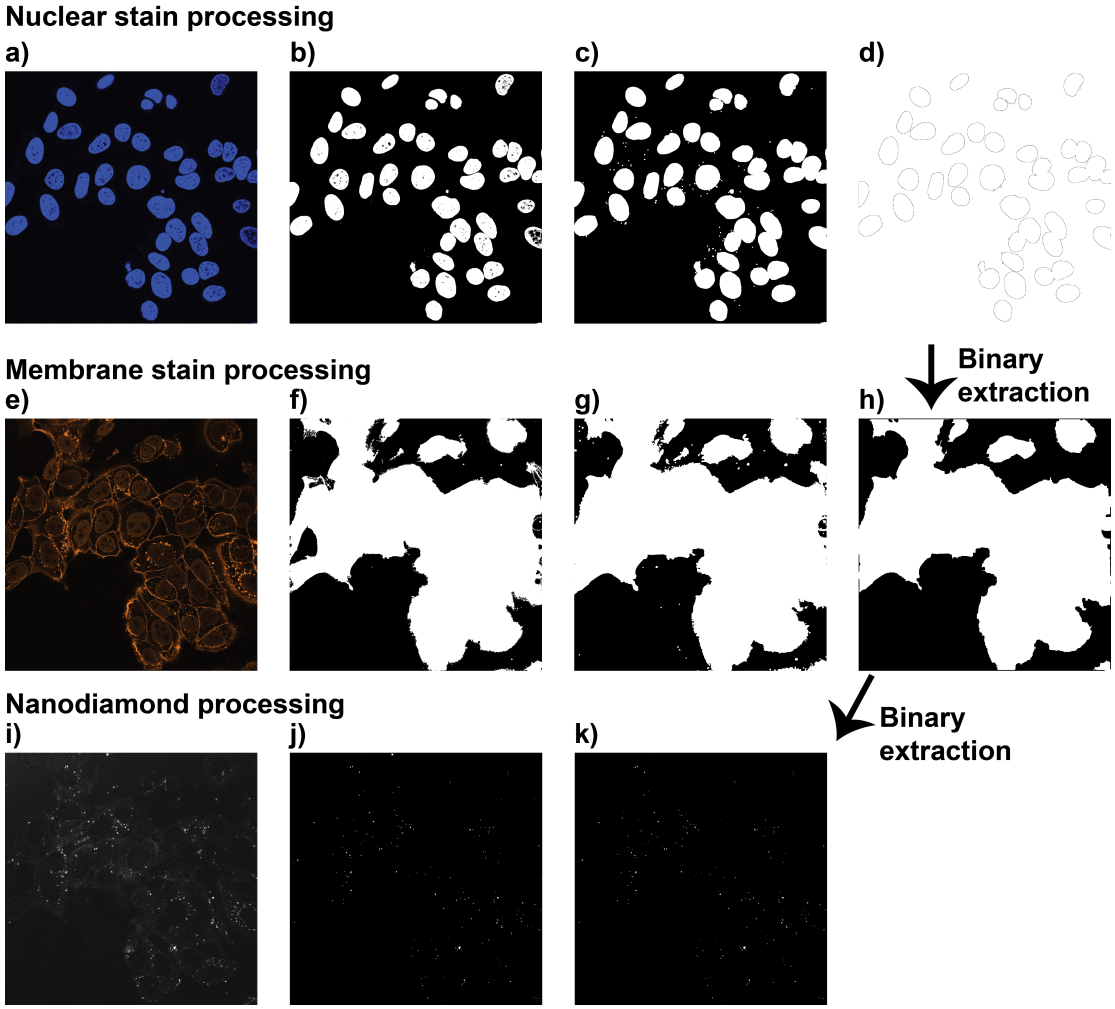

Fig. 4.7 Image processing for nanodiamond uptake quantification in Fiji/ImageJ [27]. a-d) Nuclei segmentation. a) The image channel of the NucBlue stain. ImageJ Automatic Threshold was set on these intensities to produce (b). The mask of (b) is then filled for holes, dilated three times and the filled for holes again to produce (c). Particles smaller than 50 pixels (7 µm) are then removed to form image (d). e-h) Cell membrane segmentation. e) The WGA-AF488nm channel (contrast corrected). A threshold was set by inspection on MCF7 and MDA images as 13/255. The holes were then filled to produce (f). The image was then dilated three times to complete the cell outlines and then all holes were filled to produce (g). (g) was then eroded five times and Binary Feature Extraction [28] was used in combination with (d) to remove areas of membrane that did not contain a nucleus. The erosion was necessary as the previous dilations had expanded the cells beyond their true boundaries. i-k) Diamond selection in order to count only nanodiamonds that are inside cells. i) Light scattering signal from the sample. Thresholding of this image was chosen by considering MCF7 and MDA images and set to 155/256 to produce (j). Then Binary Feature Extraction is used select only diamonds in the area outlined in (h), which corresponds to the boundaries of cells.

Proliferation

Cellular proliferation measurements were conducted with an Incucyte Zoom System (Essen Bioscience, USA). Four replicates of 0, 0.01, 0.1 and 1 $\mu g\,ml^{-1}$ nanodiamonds were added to MCF-7 or MDA-MB-231 cells in phenol-free DMEM media supplemented with Glutamax (35050-038, ThermoFisher Scientific, USA) and 10 % FCS. A positive control for proliferation change was induced using 1 mM H_2O_2 (386790-100, VWR, UK). Images were analysed with the Incucyte Zoom software version 2016, and a size threshold of 350 μm^2 was used so that nanodiamonds were not counted as cells. This was verified by observation of images with and without cells, and with and without nanodiamonds. Proliferation tests were analysed with standard ANOVA.

Oxidative Stress

Cells were seeded into eight-well plates at a density of 5×10^4 cells per well. Cells were incubated overnight and then washed in DMEM/F-12 medium (21041-025, ThermoFisher Scientific, USA) with serum. Graphitic and oxidised diamonds were each added into two wells at 1 $\mu g ml^{-1}$ in 300 µl media with serum and incubated for four hours. As a positive control to induce oxidative stress, 200 µM *tert*-Butyl hydroperoxide (TBHP) was added to two wells one hour before imaging. Just prior to imaging, media was removed from all wells and was replaced by media containing two drops of NucBlue dye according to the recommended protocol and 0.5 µM CellRox™ Orange Reagent (C10443, Invitrogen, USA) for 30 minutes. Cells were then washed in fresh media and imaged live at 37 °C and 5% CO_2 using an excitation laser at 405 nm with collection within 425–475 nm, and an excitation laser at 559 nm with detection within 570–670 nm. A scan speed of 10 ms/pixel at a confocal aperture of 105 µm were used to capture images (512×512 pixels).

Images were processed with Fiji/ImageJ [27] to remove background and quantify the average fluorescence intensity above a certain a background threshold. Datasets violated the assumptions of a standard ANOVA under the homogeneity of variances condition, so Kruskal-Wallis ANOVA was instead. It was desired to compare each sample with the control, so Dunnett's post-hoc test was used.

4.3 Results

4.3.1 Surface characterisation

Oxidised nanodiamonds were prepared by heating in air using conditions measured via thermogravimetric analysis to achieve low mass loss of approximately 2% over one hour, converging to a linear rate of -1.20 ± 0.02 % per hour (Figure 4.2). Verification of the oxidation process was made using optical spectroscopy. Raman spectroscopy (Figure 4.8) showed that the peak associated with graphitic carbon (1575 cm^{-1}) was reduced in relative area under curve compared to that of diamond (1332 cm^{-1}) from 51.8 ± 0.5 to 12.2 ± 1.1 (arbitrary units, $p = 2.2 \times 10^{-12}$). Fourier Transform Infrared Spectroscopy also provided further evidence of oxidation, through increased carboxyl C=O (1786 cm^{-1}) and C-O-C peaks (1089 cm^{-1}) relative to C=C between 1430 cm^{-1} and 1490 cm^{-1} (Figure 4.9). Also, as expected, the spectrum exhibited a shift in the C=O groups from aldehyde (1721 cm^{-1}) to carboxyl (1784 cm^{-1}) as the groups were converted into the most oxidised form through the heating process [328, 339–342, 305, 315].

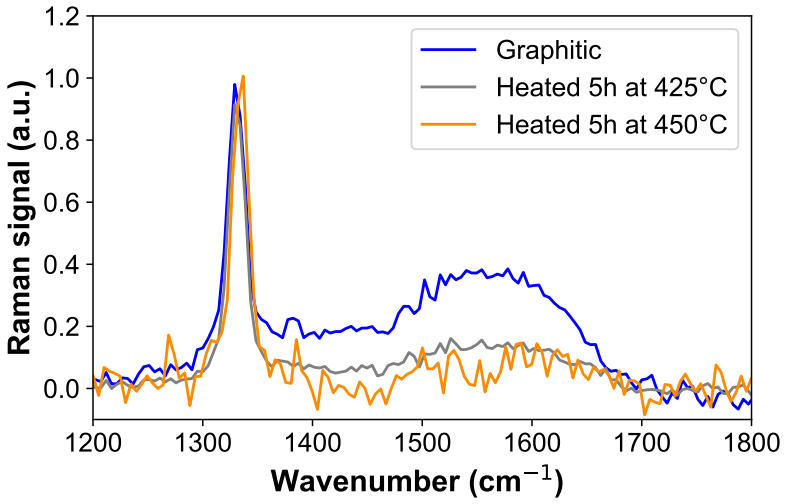

Fig. 4.8 Graphite is effectively removed by heating at 445 ± 5 °C for 5 hours. Raman spectra show that the graphitic signal (1575 cm^{-1}) is reduced relative to the diamond signal (1332 cm^{-1}) after heating. At 425 ± 5 °C, the area under the curve is reduced by 59±2% indicating the sample has been oxidised ($p = 2.2 \times 10^{-12}$). At 445 ± 5 °C, the area under the curve is reduced by 76±9% indicating the sample has been oxidised compared to the original graphitic nanodiamonds ($p = 2.2 \times 10^{-12}$). The nanodiamonds at 445 ± 5 °C have significantly reduced graphitic signal compared to 425 ± 5 °C, showing a 42±9% relative decrease ($p = 2 \times 10^{-7}$). $N_{\text{Data Points}} = 16000$. The additional noise on the 445 ± 5 °C data is a result of unintentionally leaving a reflective beamsplitter in the optical path.

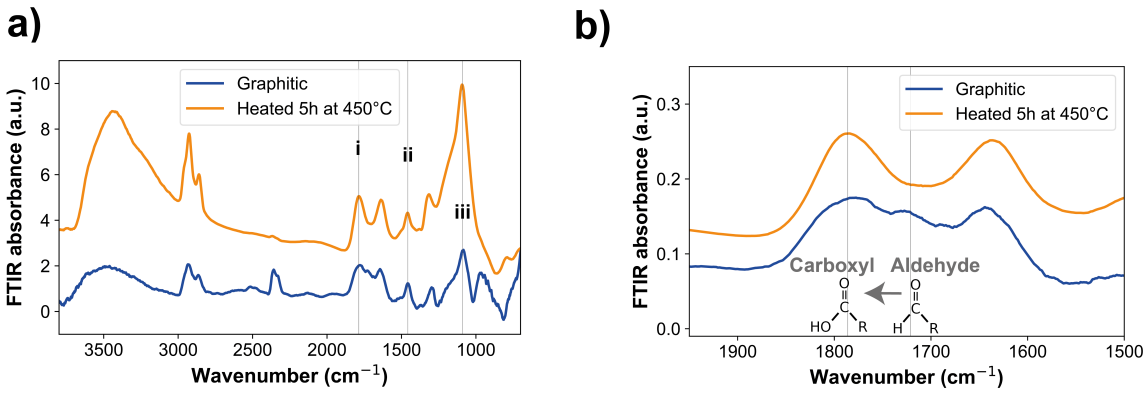

Fig. 4.9 Nanodiamond characterisation by FTIR spectroscopy. a) Fourier Transform Infrared Spectroscopy (FTIR) of nanodiamonds, normalised to the C=C bond peak (ii) between 1430 cm^{-1} and 1490 cm^{-1}. The peaks for carboxyl C=O (i) at 1786 cm^{-1} and C-O-C (iii) 1089 cm^{-1} show a relative increase after oxidation. N_{Sample} = 1. Note that the peak at 2350 cm^{-1} is only CO_2 from the air, not from the sample. b) A zoomed FTIR spectrum, normalised between between 1550 cm^{-1} and 1900 cm^{-1}. This shows that C=O groups are converted into the most oxidised form through the heating process (1721 cm^{-1} aldehyde to 1784 cm^{-1} carboxyl).

4.3.2 Nanodiamond Size and Aggregation

Atomic Force Microscopy (AFM) was used to assess whether there is any change in nanodiamond size due to removal of the graphite layer during oxidation (Figure 4.10a). The mean size of the individual particles before oxidation was 8.1 ± 0.2 nm, and after oxidation it was 7.5 ± 0.2 , a reduction of 0.6 ± 0.2 nm. From TGA we expect to see a $\sim$6% mass decrease after five hours, which would correspond to a $\sim$0.2 nm radius decrease on a spherical 7.6 nm nanodiamond, which is consistent with these AFM findings.

Nanodiamonds were suspended in water to measure their aggregation size (Figure 4.10b). It was observed that the size of nanodiamond aggregates was significantly reduced from 195 ± 3 nm to 168 ± 2 nm by the oxidative heating process for 66 µg/ml. Oxidised diamonds were observed to be more stable in solution, with noticeable deposition of graphitic diamonds after seconds, whilst oxidised diamonds remained in suspension for minutes. Reducing the concentration was measured to correspond to a further size decrease, with 1 µg/ml of nanodiamonds forming aggregates of 147 ± 3 nm. There was also a reduction in average size observed with optical scattering microscopy (Figures 4.10c, d).

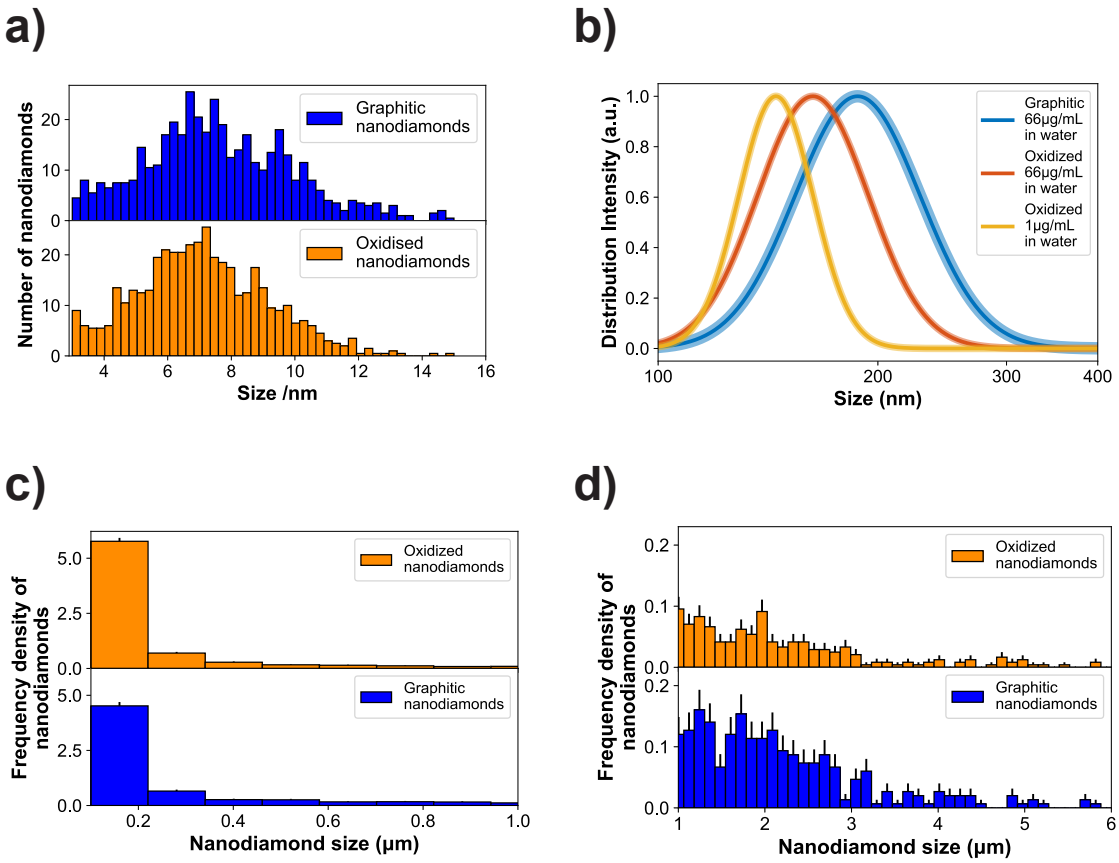

Fig. 4.10 Comparison of nanodiamond size, before and after oxidation. a) Atomic Force Microscopy data from individual nanodiamonds measured in air of 861 nanodiamonds. The mean size before oxidation was 8.1 ± 0.2 nm, and after oxidation it was 7.5 ± 0.2 b) Dynamic Light Scattering measured in water shows the nanodiamonds aggregate, but the overall size of the aggregates decreases after oxidation and at lower concentration. c) Nanodiamonds were added to DMEM/F-12 medium without cells at a concentration of 1 µg ml^{-1} and the aggregates were observed directly with confocal optical scattering microscopy and plotted between 0.01–1 µm. There was a small reduction in the average size of aggregates after oxidation. The percentages of aggregates below 250 nm were 56% and 72% for graphitic and oxidised nanodiamonds, respectively. 0.01–1 µm d) The same as c, but expanded to visualise the range from 1–6 µm

4.3.3 Intracellular uptake of nanodiamonds

Cellular experiments were performed using two different breast cancer cell lines - MDA-MB-21 and MCF-7 cells. Cells were exposed to nanodiamonds for up to 48 h and microscopy images (Figures 4.11 and 4.12) show a clear increase in the accumulation of nanodiamonds over time, many of which were present as aggregates of similar sizes.

Our data show that MDA-MB-231 cells showed a significantly higher uptake of oxidised rather than graphitic nanodiamonds (Figure 4.13a), with both a greater number of particles ($p = 4 \times 10^{-8}$), as well as a greater observed area of nanodiamond signal ($p = 8 \times 10^{-9}$). MDA-MB-231 cell uptake reached a peak after four hours of exposure of $4.7 \pm 0.9\,\mu m^2$ per cell and $14 \pm 2\,\mu m^2$ per cell average for graphitic and oxidised diamonds respectively. The subsequent decline in signal is likely due to cell division over the following hours. By contrast, MCF-7 cells showed a similar uptake of graphitic and oxidised nanodiamonds until 24 h, at which point the uptake of graphitic nanodiamonds appeared to reach saturation (Figure 4.13b). MCF-7 cells also showed a level of uptake that was an order of magnitude higher than that seen in MDA-MB-231 cells. Nonetheless, oxidised diamond uptake was also significantly higher than graphitic diamond uptake in MCF-7 cells ($p = 3 \times 10^{-5}$), making this a consistent finding across both cell types.

A detailed summary of the size distribution of oxidised and graphitic nanodiamond aggregates in both cell types can be found in Figure 4.14 and 4.15. Interestingly, when examining the distributions of particle sizes in cells, the number of particles below $0.02\,\mu m^2$ apparently decreases in MDA-MB-231s over time, whereas the number of particles above $1\,\mu m^2$ increases up to four hours, and then decreases between 8-24 hours. In contrast, MCF-7 cells continuously uptake particles throughout the 48 hour experiment.

4.3.4 Nanodiamond impact on proliferation and cellular stress

Next, experiments were performed to assess whether the uptake of graphitic and oxidised nanodiamonds had any impact on the proliferation of MDA-MB-231 and MCF-7 breast cancer cell lines. This would reveal any apoptotic effects from the nanodiamonds that would be detrimental to this project's aims. Nanodiamond concentrations of 0, 0.01, 0.1 and $1\,\mu g\,ml^{-1}$ were added to cell grown in 24-well plates, corresponding to approximately 200, 2000 and 20 000 nanodiamonds per cell. Hydrogen peroxide was used as a positive control of cell death and phosphate buffered saline as a negative control. Automated phase contrast microscopy (Incucyte, Essen Biosciences) was used to count cells and determine confluency within the wells. Considering the growth phase between 48 and 108 hours, cell confluency

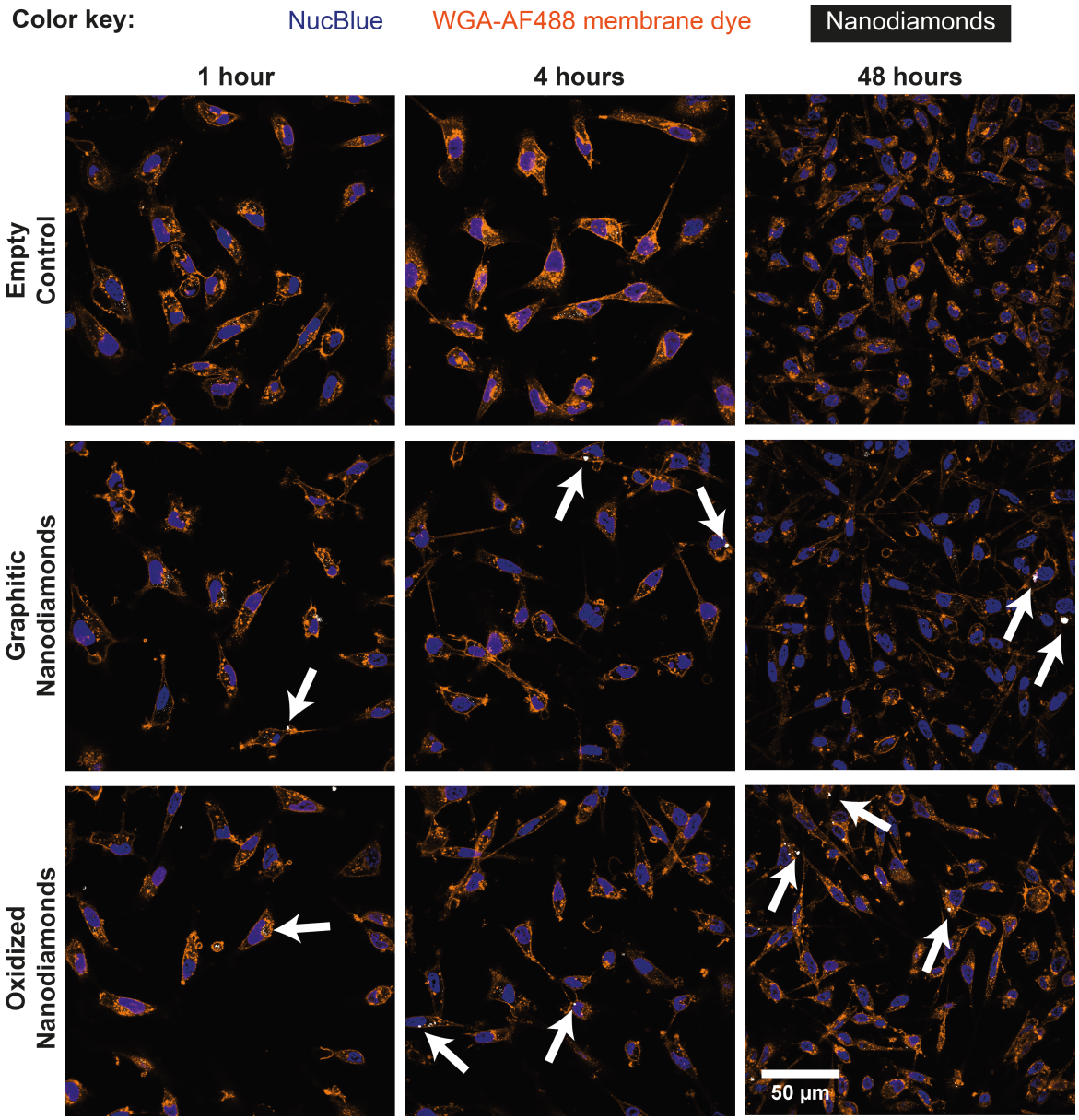

Fig. 4.11 Nanodiamond uptake observed in MDA-MB-231 cells. Cells were incubated with 1 µg/ml graphitic or oxidised nanodiamonds for 1, 2, 4, 8, 24 and 48 hours before fixation. Cells were then co-stained with NucBlue nuclear stain and membrane stain Wheat Germ Agglutinin-Alexa Fluor 488. Nanodiamond scattering signal was detected at 633 nm. An increase in the number of nanodiamonds within cells may be observed over time up to 48 h (white arrows denote dense cellular uptake).

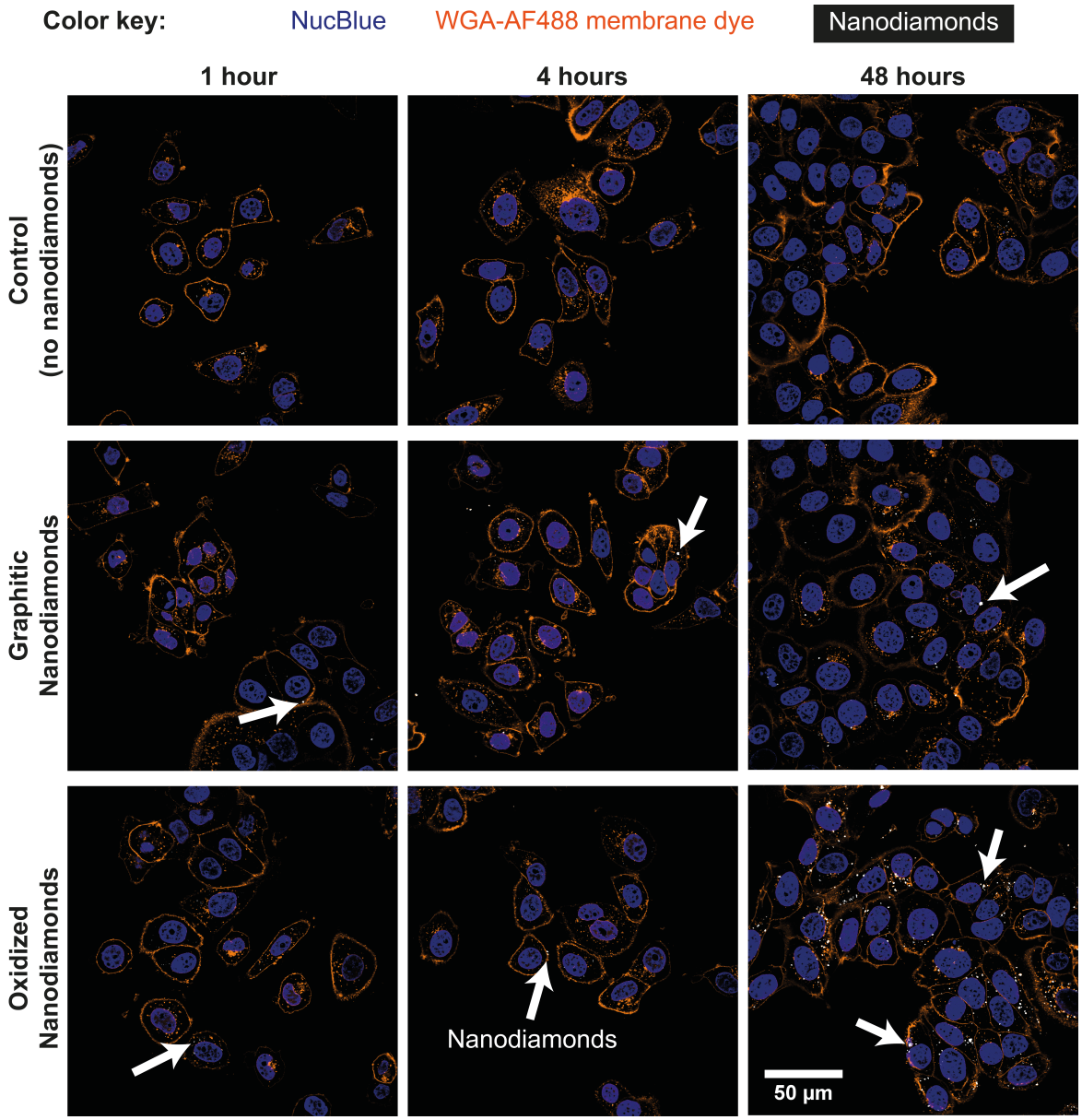

Fig. 4.12 Nanodiamond uptake observed in MCF-7 cells. Cells were incubated with 1 µg/ml graphitic or oxidised nanodiamonds for 1, 2, 4, 8, 24 and 48 hours before fixation. Cells were then co-stained with NucBlue nuclear stain and membrane stain Wheat Germ Agglutinin-Alexa Fluor 488. Nanodiamond scattering signal was detected at 633 nm. An increase in the number of nanodiamonds within cells may be observed over time up to 48 h (white arrows denote dense cellular uptake).

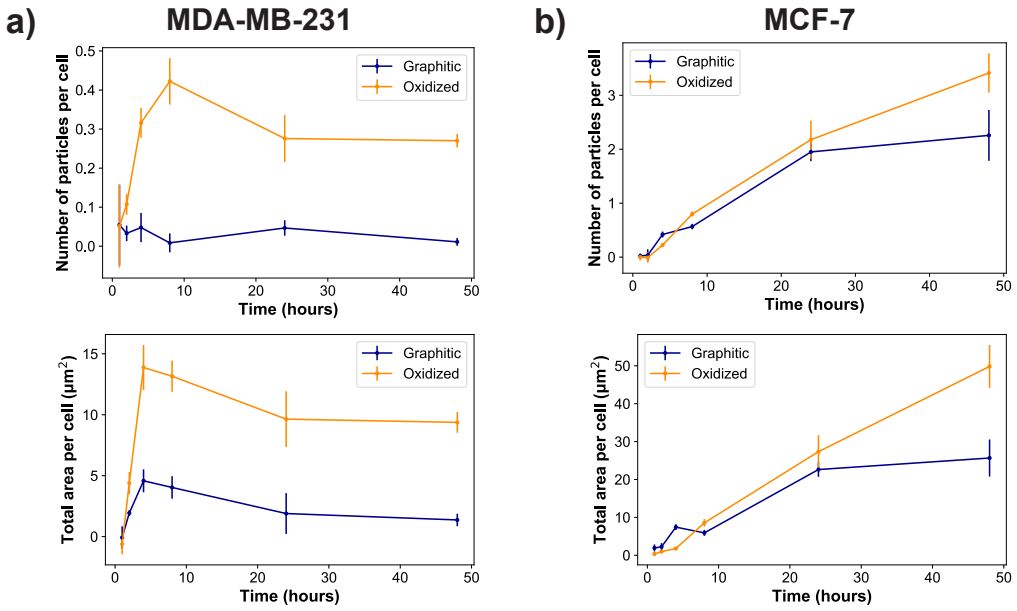

Fig. 4.13 Nanodiamonds were internalised into cells over time in two different breast cancer cell lines: (a) MDA-MB-231 and (b) MCF-7 cells. 'Total area per cell' refers to the total nanodiamond intracellular area in the images divided by the number of nuclei observed in that image. oxidised diamonds were taken up in a greater amount than graphitic diamonds ($p = 4 \times 10^{-8}$ for MDA-MB-231s and $p = 3 \times 10^{-5}$ for MCF-7s). $N_{\text{Biological replicates}} = 2$ (control) and 3 (nanodiamond sample). $N_{\text{Nuclei}} = 500 \pm 200$ per condition for MDA-MB-231 and 430 ± 170 per condition for MCF-7.

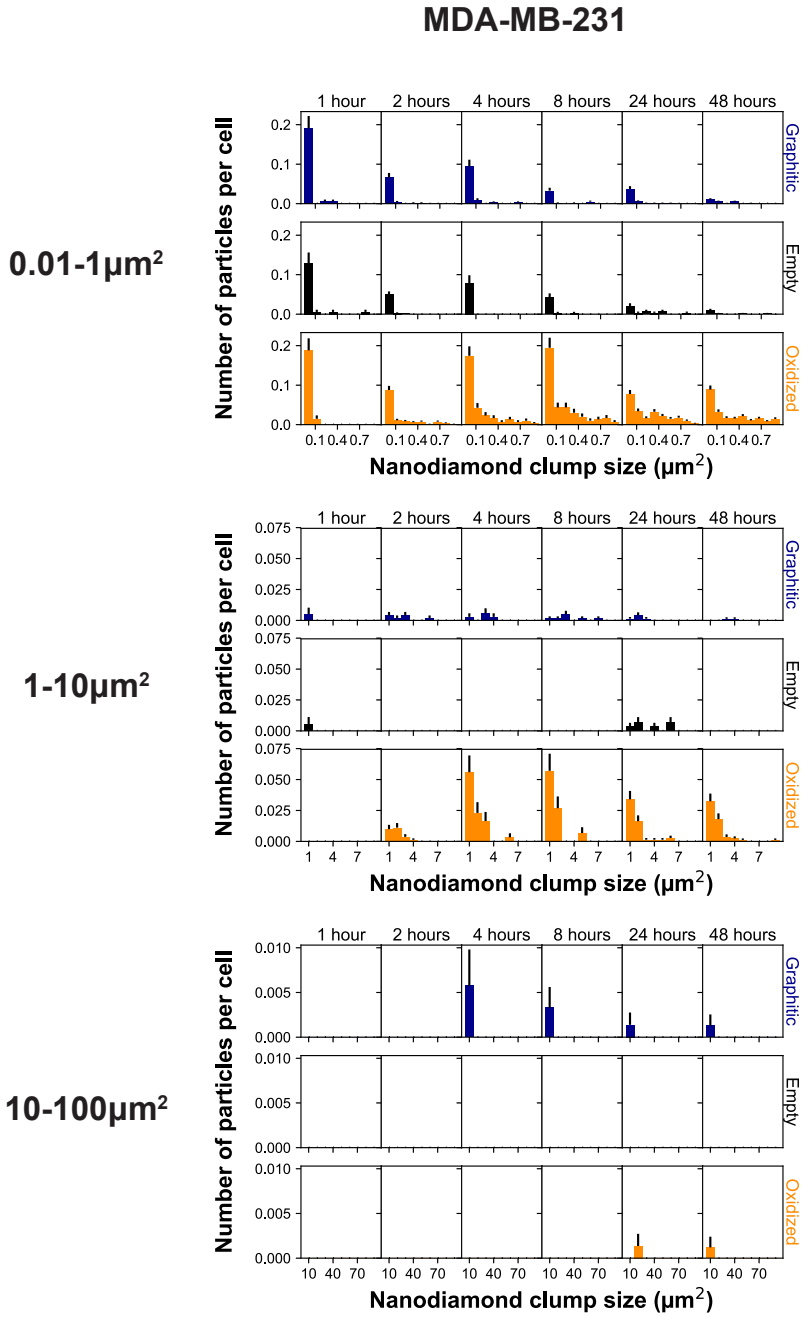

Fig. 4.14 Size distribution histograms from the uptake experiment for the MDA-MB-231 cell line. The background for 24 h was observed to be anomalous, as it contained a contamination of scattering particles. It was therefore removed from the analysis.

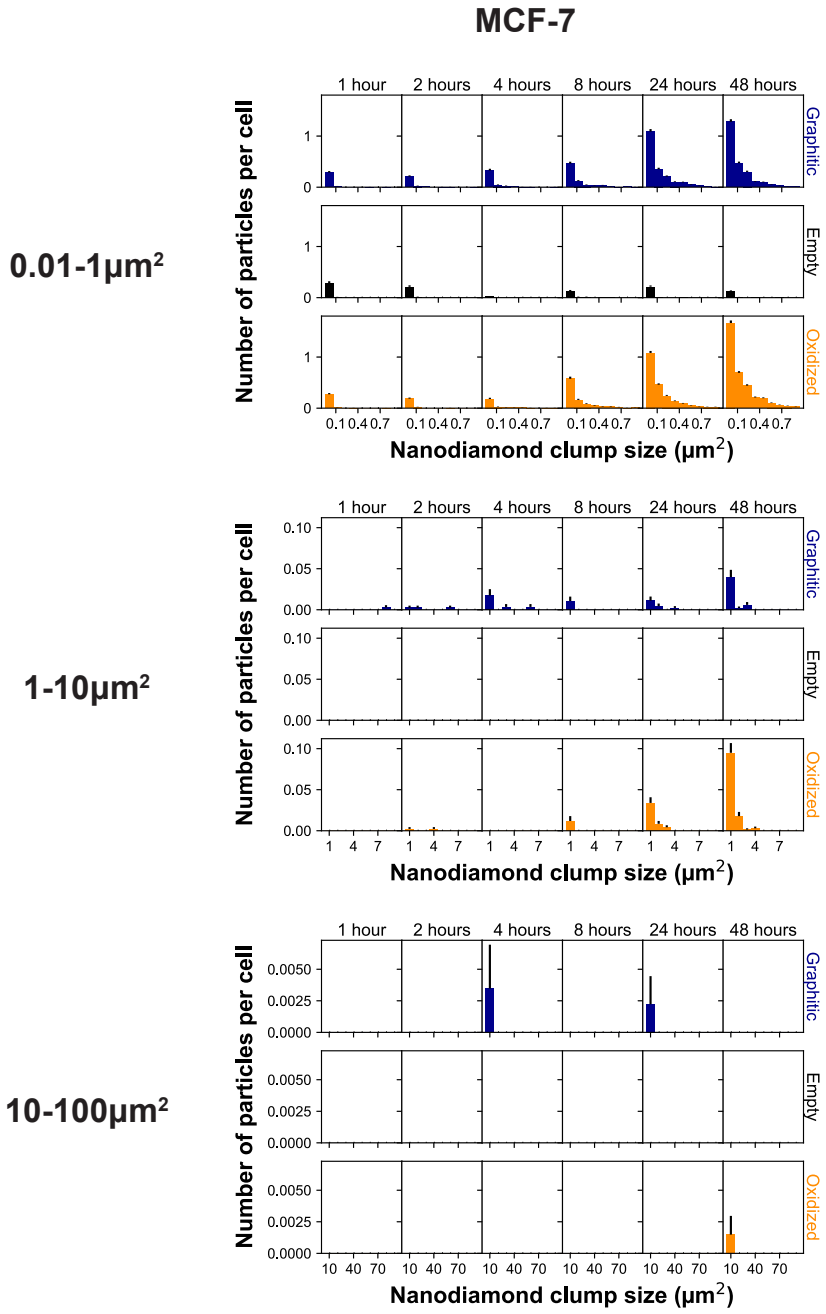

Fig. 4.15 Size distribution histograms from the uptake experiment for the MCF-7 cell line.

was slightly reduced at 1 $\mu g\,ml^{-1}$ for graphitic nanodiamonds in the MDA-MB-231 cells (-5±2%, p = 0.0014), but no change was observed with oxidised diamonds (+1±4% p = 0.89). MCF-7 cells appeared to be unaffected by the addition of nanodiamonds of either type (graphitic: +2±2%, p = 0.37; oxidised: -1±3%, p = 0.73).

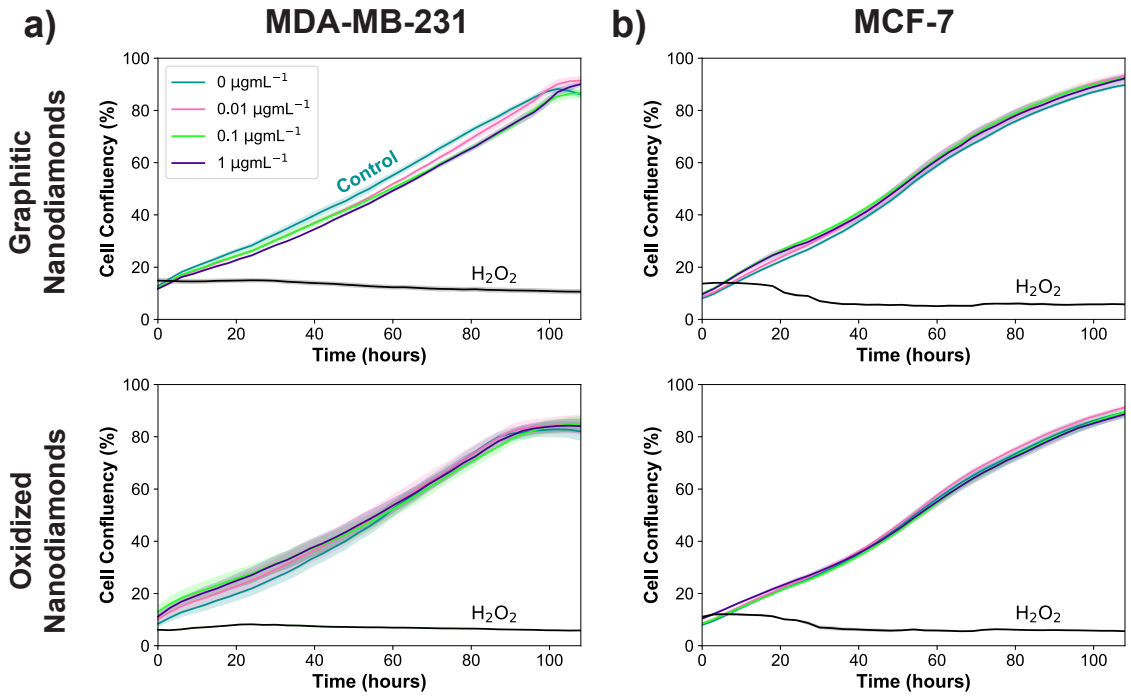

Fig. 4.16 Nanodiamonds have negligible anti-proliferative effect. Graphitic diamonds cause a small decrease in confluency at 1 $\mu g\,ml^{-1}$ in MDA-MB-231 cells (top left, -5±2%, p = 0.0014), but no other experiments showed any significant decrease at these concentrations. $N_{replicates} = 4$.

Finally, the cellular oxidative stress responses were examined to evaluate whether any transient effects not resulting in slowed growth exist (Figure 4.17). These effects are important as they could limit the possibility of using nanodiamonds to measure cellular processes that are connected to mitochondrial membrane potential, such as oxidative stress (Section 1.1.2).

MDA-MB-231 cells showed significant increase in oxidative stress under application of the positive control TBHP and for incubation with graphitic nanodiamonds (ANOVA p = 6×10^{-5}). In post-hoc comparison, the critical threshold of the d-statistic was 2.3, which was surpassed by the TBHP (d-stat = 8.7) and the graphitic diamonds (d-stat = 4.6). Oxidised nanodiamonds did not show any effect on ROS production, with levels remaining comparable to the control condition (d-stat = 1.8). This pattern of response was repeated in MCF-7 cells, where TBHP and graphitic diamonds were found to induce stress at a level above the control

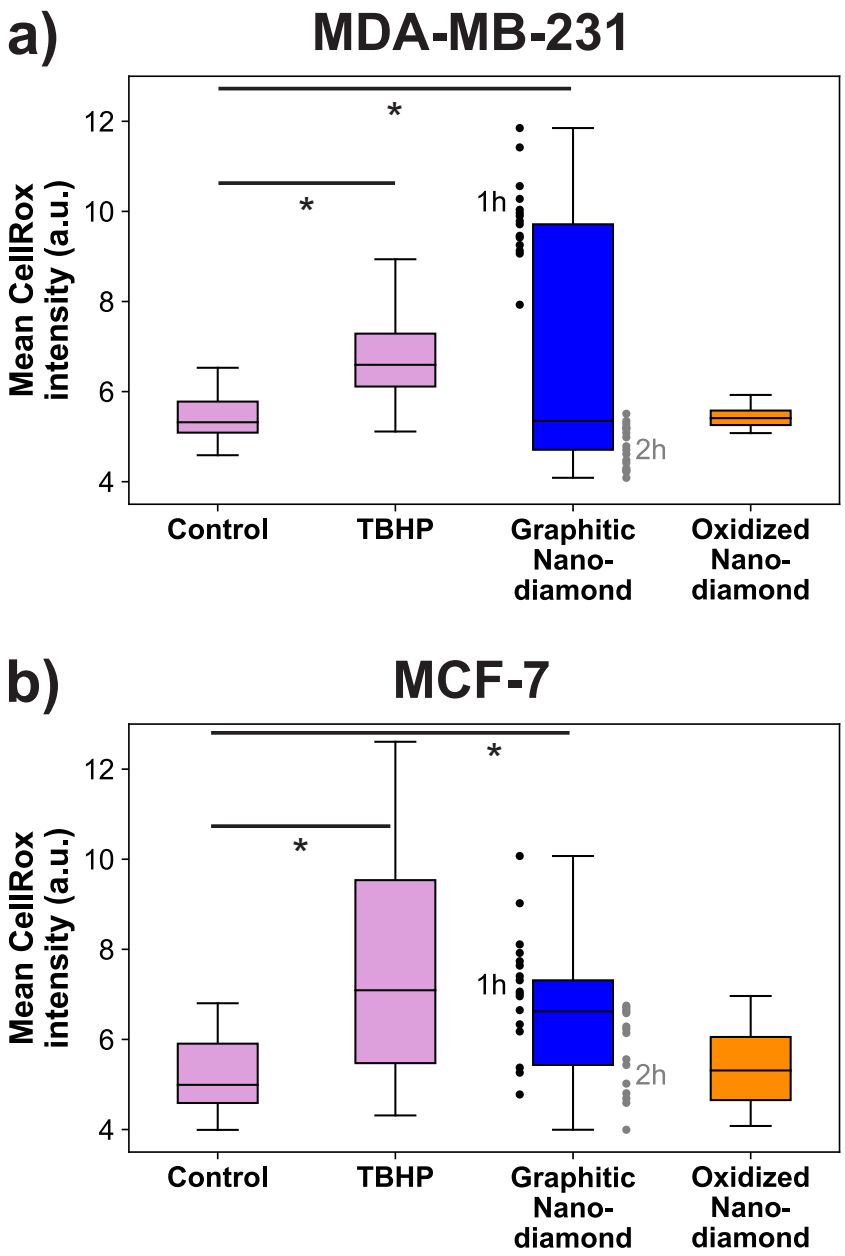

Fig. 4.17 Graphitic nanodiamonds produced increased levels of cellular oxidative stress for (a) MDA-MB-231 cells. Graphitic diamonds had a significant d-statistic (= 4.6 > d-critical = 2.3) and TBHP performed successfully as the positive control (significant d-statistic = 8.7 > d-critical = 2.3) (b) As (a) for MCF-7 cells. (significant d-statistic = 5.7 > d-critical = 2.3). TBHP, the positive control performed as expected 3.6 > d-critical = 2.3. oxidised diamonds did not increase the cellular stress in either cell line. Oxidative stress was generally higher at 1h time point for graphitic diamonds. Outliers greater than 1.5× the interquartile range were not plotted. D-statistics were used in place of p values, as the sample did not reflect a normal distribution, and so the analysis was done on ranked data. N_{images} = 24, 31, 33, 15, 25, 24, 33, 31 (column order), N_{cells} = 451, 478, 671, 368, 530, 433, 897, 773.

(d-stat = 3.6, d-stat = 5.7 respectively) and oxidised diamonds did not show a significant change (d-stat = 1.7).

Oxidative stress measurements were made at both 1h and 2h time points; by separating these it was apparent that MDA-MB-231 cells were most stressed in the initial 1h but had largely returned to normal stress levels after 2h. MCF-7 cells had a more similar response at both time points. The higher stress levels from graphitic nanodiamonds are of particular note given the lower uptake of these nanodiamonds into cells.

4.4 Discussion

Nanodiamonds containing NVCs have been explored as a chemical- and photo-stable replacement for fluorescent dyes in cells for applications such as organelle tracking and temperature sensing. In this chapter, the biological impacts of both graphitic and oxidised HPHT nanodiamonds were examined in relation to cellular uptake as well as potential impacts on proliferation and importantly, cellular stress responses. HPHT nanodiamonds where used because of their superior spin properties that have led to wide use for biological sensing applications [17, 237, 241, 343, 344], both in graphitic [14] and oxidised forms [343]. Oxidised forms of nanodiamond have often been used in biological experiments due to their improved fuctionalisation capability, but direct comparison of biocompatibility via oxidative stress in graphic and oxidised HPHT nanodiamonds from the same batch has yet to be reported.

Oxidised HPHT nanodiamonds were shown for the first time to have improved biocompatibility compared to graphitic HPHT nanodiamonds. In breast cancer cell lines, graphitic nanodiamonds induced higher levels of oxidative stress despite lower uptake compared to oxidised nanodiamonds. An order of magnitude greater nanodiamond uptake in MCF-7 cells over time was observed, particularly at the later time points, when compared against MDA-MB-231 cells. This is consistent with the increased expression of clathrin protein in MCF-7 cells [337], as nanodiamonds have previously been observed to be mostly internalised by clathrin-mediated endocytosis [234]. Oxidised nanodiamond was observed to be taken up at a higher rate than graphitic nanodiamonds in both cell lines, but with a more dramatic difference in the MDA-MB-231 cells.

Oxidised nanodiamonds formed smaller aggregates in cell culture media, which may go some way to explain these differences. In particular, at least 72% of oxidised nanodiamond aggregates were below 250 nm in diameter, while at least 56% of graphitic nanodiamond aggregates were below this size. If further size reduction were needed in future applications, it would be possible to use techniques such as bead-assisted sonic disintegration or salt-assisted

dry attrition milling for temporary physical separation of the particles [345], or the addition of chemicals to the nanodiamond surface such as serum proteins [346, 347], surfactants [348], lysine [349] or various polymers [350–354] for chemical separation.

Uptake dynamics have been shown to be shape dependent in nanodiamonds, with rounder particles remaining in cells for longer [309], so it may be that oxidised nanodiamonds form aggregates of different roundness; this could be verified using TEM. Furthermore, nanoparticle surface charge can be an important factor in intracellular uptake, although contradictory findings have been reported in the literature with regard to how nanoparticle interactions with the cell surface relates to surface charges [355, 356]. Oxidised nanodiamonds have been reported to exhibit more electronegative zeta potentials [357, 347, 100, 358], so the difference in surface charge between the two nanodiamond types studied here may contribute to the differences in uptake.

In proliferative studies, a small but significant decrease in proliferation was observed under the highest concentration of HPHT graphitic diamonds in MDA-MB-231 cells. No significant difference was observed at any of the tested concentrations of oxidised nanodiamonds, enabling them to be good sensors of apoptosis. This low cytotoxicity profile is consistent with other published work, which generally shows low or non-existent nanodiamond cytotoxicity [99, 359, 92, 90, 360, 91, 361, 362], over similar time courses [314, 93, 363, 364]. The work in this chapter on HPHT diamond aligns with studies on detonation diamond despite the compositional differences [125], with graphitic nanodiamonds suppressing cell proliferation and oxidised nanodiamonds having the lowest cytotoxic effect [313, 305]. Although no anti-proliferative effect of oxidised nanodiamonds was observed, the cells were exposed to a concentration range suitable for experiments interrogating local organelle tracking or temperature sensing, rather than those used for drug delivery, which would be substantially higher. At higher concentrations such as 1 $\mu g\,ml^{-1}$ effects including apoptosis have been observed even with oxidised nanodiamonds [75].

Evaluating oxidative stress under nanodiamonds, it was observed that graphitic HPHT diamonds cause a high degree of stress in cells, exceeding that of the positive control. This agrees with previous studies where unmodified nanodiamonds were observed to produce oxidative stress [365, 366], though neither the amount of graphite nor the fabrication procedure were defined in these studies. The observation of oxidative stress under graphitic nanodiamonds is also reported for other forms of sp2 carbon [367–369], especially pure carbon black particles, which are observed to cause the production of reactive oxygen species [370–372]. Horie et al. also examined three varieties of nanodiamonds with different zeta potentials [93]. Those with positive zeta potentials caused oxidative stress, while the negative

ones did not, which may be consistent with our findings. Of particular interest in the results in this chapter is the fact that we did not observe any oxidative stress when cells were exposed to oxidised diamonds, consistent with previous reports at both the cellular [322] and organism levels [329]. This is advantageous when considering nanodiamonds as a measurement tool for processes related to oxidative stress.

The results of this chapter therefore suggest that the impact of the surface chemistry of nanodiamonds can be significant for biological applications. It would therefore be prudent for nanodiamonds to be oxidised prior to application in cells, regardless of whether they are being subjected to functionalisation. According to these findings, oxidation can increase cellular uptake and minimise any potential oxidative stress response. These benefits exist in addition to the well known benefits of reduced charge switching between the NV^- and NV^0 charge states[241], improved brightness [307] and facilitating surface functionalisation for targeting [67, 308].

Despite the promising findings of this direct comparison of the biological impacts of graphitic and oxidised nanodiamonds in two different cell types, there remain some limitations to this study. Firstly, biocompatibility is expected to be determined by surface chemistry and shape [373], so it is reasonable to expect that differences in the fabrication methods such as HPHT or detonation processes could cause variations in the cellular response. A direct comparison of nanodiamonds of a similar size and shape produced by the two different processes would be of interest in future work. Secondly, the oxidised nanodiamonds were prepared by heating in air alone. While this is a commonly used procedure [67], it is also often replaced or combined with cleaning by acids, UV-Ozone, or oxygen plasma, which may exaggerate the differences in surface chemistry, potentially leading to different results in uptake, proliferation and oxidative stress. Thirdly, the optical scattering measurement used in the uptake experiments above has been shown to be insensitive below a diameter of 37 nm for nanodiamonds [374], so some signals associated with any free nanodiamonds undergoing passive uptake may have been missed, as suggested elsewhere [234]. However, given the size distributions of the nanodiamonds in solution, this is expected to be a relatively minor contribution to the overall signal.

4.5 Conclusion

Nanodiamonds were successfully oxidised by heating in air at 450 °C for 5 hours. This enables surface functionalisation, a crucial step in the path to the use of a nanodiamond sensor for membrane potential in cells. In addition to this and the expected improvement

in optical properties, the results in this chapter suggest further motivation for the process of oxidation. Oxidised nanodiamonds have been observed to increase in uptake into the cells, relative to graphitic nanodiamonds whilst also producing less oxidative stress. These novel findings are crucial for the use of nanodiamonds as a revolutionary biomedical tool as it is vitally important for any sensor used to perform measurements in a biological system to avoid perturbation of the system that it is measuring.

This chapter has described insights into and improvements of the biological impact of nanodiamond, and has shown how to avoid causing oxidative stress and apoptosis from nanodiamonds. Using this it is therefore possible to combine the custom microscope in Chapter 2, the Raman protocols and analysis of Chapter 3 and this work to make simultaneous NVC and Raman measurements in cells. In Chapter 5, the conclusions of the project are brought together, and some next steps for this research are proposed.

Chapter 5

Summary

5.1 Conclusions

Mitochondrial membrane potential ($\Delta\Psi_m$) in cells is a critical biological parameter that is related to diseases such as cancer through biological processes including metabolism, oxidative stress and apoptosis. Studying $\Delta\Psi_m$ in normal and diseased states is limited by the current state-of-the-art methods for measurement, particularly fluorescent dyes, which are often toxic and prone to photobleaching.

The aim of this work was to develop electrical and chemical sensing methods to enable sensitive detection of changes in $\Delta\Psi_m$ in single cells. Fluorescent Nitrogen Vacancy Centres (NVCs) in nanodiamond were identified as potential sensors of electric field that could be applied in living cells to directly measure $\Delta\Psi_m$. Furthermore, Raman spectroscopy was identified as a label-free chemical sensing technique that could reveal cells, reveal intracellular organelles and track changes associated with apoptosis. This enables and contextualises the measurement from the NVCs, since $\Delta\Psi_m$ is closely linked to processes such as apoptosis.

To achieve the aim of detecting changes in $\Delta\Psi_m$ using these two methods, complementary NVC and Raman measurements in live cells were needed. In chapter 2, a specialised microscope was designed, built and validated to enable measurement of both NVC fluorescence and Raman spectroscopic signals simultaneously. The custom microscope developed was shown to fulfil the design requirements, including sensitivity. For NVCs measurement, a sensitivity equivalent to measurement of 0.2% of $\Delta\Psi_m$ within three minutes was achieved, and for Raman measurement, the sensitivity was such that a Raman peak was localised to $0.05\,\mathrm{cm}^{-1}$ after 1 s.

Next, in chapter 3, protocols and analysis techniques were developed for live cell Raman microscopy using a commercial reference instrument. Raman microscopy was developed to be able to detect cells, detect intracellular organelles, and detect apoptotic changes over time.

An investigation of the impact of nanodiamonds as nanoparticles for biological sensing within live breast cancer cells, including surface modification by oxidation, was then conducted in chapter 4. Diamond nanoparticles were observed to behave differently in oxidised and graphitic forms. This work showed for the first time that oxidation of nanodiamonds improved uptake and reduced cellular stress. The reduced oxidative stress is vital so that nanodiamonds do not affect the system they are measuring.

By developing both NVC and Raman techniques in these ways, this project is primed to leverage the complementary advantages of long time course measurement, common laser excitation, the observation of nanodiamonds via Raman signal, with live single cell interrogation.

The thesis concludes with an outlook on the future development needed to utilise NVCs and Raman spectroscopy in the measurement of cellular $\Delta\Psi_m$. Achieving this will provide new biological understanding of $\Delta\Psi_m$ in normal and diseased states, allowing changes in $\Delta\Psi_m$ in response to biological processes such as apoptosis in single cancer cells to be investigated.

5.2 Future Work

5.2.1 Instrument upgrades

Continuing from the work outlined in chapter 2, it would be possible to further improve the custom microscope. Adding pulsed measurements would enable a gain in sensitivity. This would involve adding a SpinCore timing card and an Acousto-Optic Modulator to create laser pulses. Iwasaki et al. [15] use continuous wave measurements in order to detect fields with a sensitivity of the order of $100\,\mathrm{kV\,cm^{-1}}$. However, using pulsed measurement techniques, Dolde et al. were able to achieve detection of field as small as $0.01\,\mathrm{kV\,cm^{-1}}$ [375]. Some of this difference may attributed to differences in experimental setup, but nevertheless it is clear that pulsed measurements can offer order of magnitude improvements in sensitivity.

Another hardware upgrade to the custom microscope could be an implementation of Shifted Excitation Raman Difference Spectroscopy (SERDS) [376, 377]. This technique relies on two lasers that are close in wavelength ($<$1 nm) that are quickly switched as spectra are recorded. This method assumes that the fluorescence excitation profile is sufficiently

broad so that a small shift in excitation wavelength will not change the emission. In contrast, a small shift in excitation will cause a similar small shift in the wavelength of Raman signals, allowing them to be separated from the fluorescent background. This would be useful in the context of biological cells, where background fluorescence is strong. This process also allows the extraction of a pure signal of the fluorescence. This would also open new possibilities, such as the potential detection of NV^0 fluorescence and the use of complementary fluorescence dyes.

5.2.2 Raman analysis development

Continuing from the work in chapter 3, Raman spectral data analysis could be improved by implementing Biomolecular Component Analysis, as used by Yadav et al. [165]. This involves the collection of Raman spectra from basic classes of biological molecules such as proteins, DNA, RNA, lipids and enabled the observation of apoptotic changes. This technique was found to be more appropriate for sub-cellular clustering than Principal Component Analysis [378], and similar techniques have been developed elsewhere [379]. There may also be other hyperspectral data analysis methods to be explored such as fuzzy c-means clustering [380], and artificial neural networks [127, 252]. Combining these types of analysis with a switch to excitation at 532 nm, where cytochrome c is resonant should provide new insights in locating and understanding mitochondria [133].

5.2.3 Surface functionalisation

Continuing the work from chapter 4, there remain many more opportunities for understanding biological impacts and performing surface functionalisation of nanodiamonds. Although oxidised nanodiamonds were found to not induce oxidative stress in cells, it is possible that other harmful responses do occur. It would be possible to test more generally for inflammation with a TaqMan™Array for Human Inflammation (4414074, Applied Biosystems, ThermoFisher Scientific) or using polymer chain reactions for DNA damage [381]. Some DNA damage from nanodiamonds has been seen in an experiment by Dworak et al. [365].

Building on the oxidation work, it is possible to functionalise the diamonds in order to target mitochondria in the cell. In collaboration with Dr Ljiljana Fruk's group in the Department of Chemical Engineering and Biotechnology (University of Cambridge), a process of surface modification has been proposed. This consists of the addition of dopamine, tetrazole, malemide and triphenylphosphonium (TPP) as shown in Figure 5.1a and 5.1b.

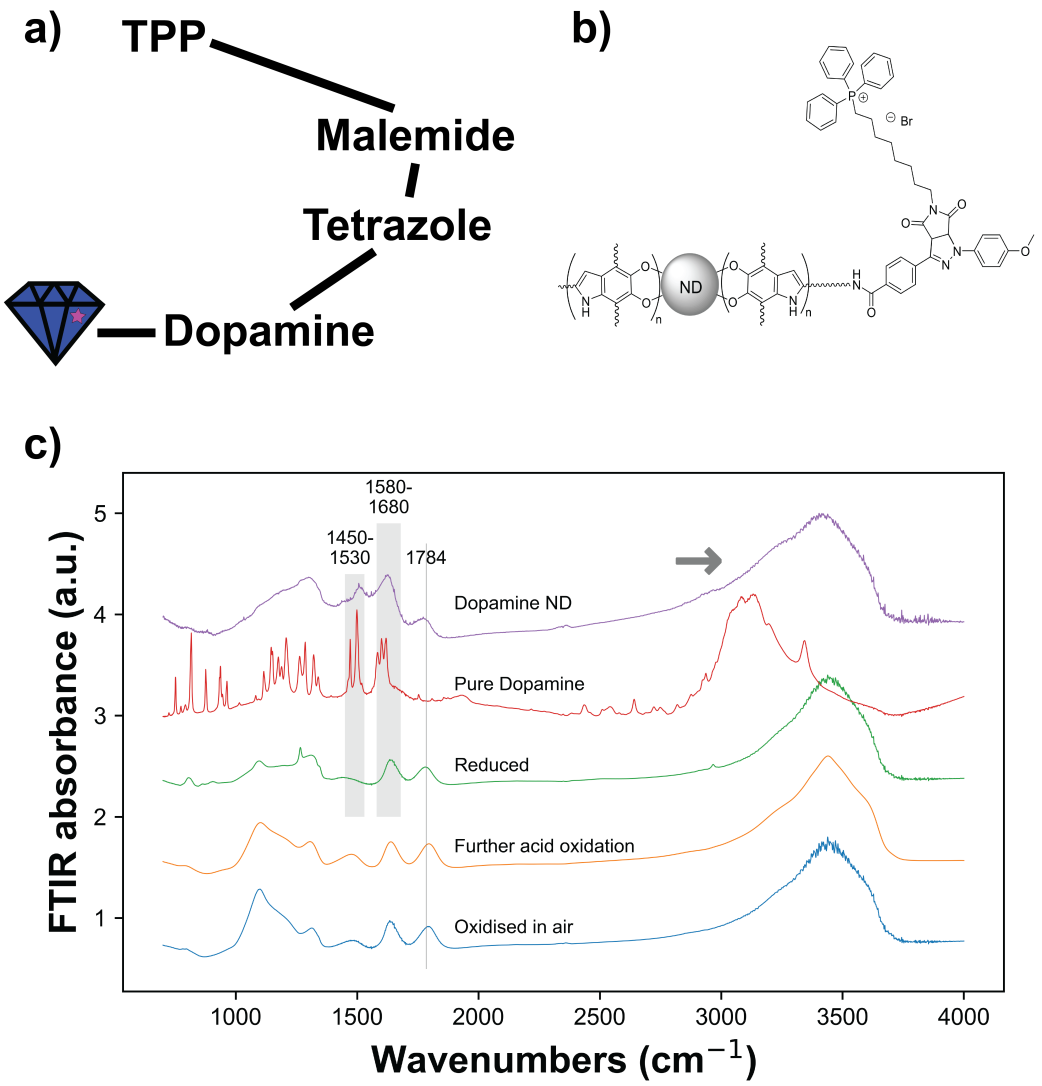

Fig. 5.1 a) Nanodiamond functionalisation scheme to target mitochondria. TPP is triphenylphosphonium. This is devised and worked on by collaborators Dr Antonia Kerbs, Alexandra Fux and Dr Ljiljana Fruk. b) Chemical structure of (a). c) Some promising steps on nanodiamond functionalisation have recently been observed. Modifications of the nanodiamonds are displayed in this FTIR graph. Firstly, the oxidation procedure outlined in chapter 4 was used to remove graphite and produce oxidised nanodiamonds. The nanodiamonds were then further oxidised with strong acids and then reduced. This reduction can be seen in the intensity reduction and shift to 1784 cm^{-1} of the C=O peak. The nanodiamonds were then coated with dopamine, as verified by the appearance of a peak in the range 1450–1530 cm^{-1}, and the relative strengthening of the peak at 1580–1680 cm^{-1}. These are both clear in the pure dopamine spectrum. Furthermore, there appears to be a shoulder around 3000 cm^{-1} (labelled by an arrow), that is also evidence for successful dopamine attachment to nanodiamond.

Dopamine is used as a versatile foundation for other chemical attachment [382, 383], and has been previously attached to nanodiamonds [384]. The tetrazole and malemide are then proposed as fluorescent linkers that provide easier tracking on commercial microscopes than the relatively dark NV^- centre. TPP is a lipophilic cation that is commonly used to attach molecules to mitochondria [385, 386].

To achieve this, the nanodiamonds that have been oxidised in air were further oxidised with strong acids H_2SO_4, HNO_3 and HCl for six days [387]. This is intended to remove the final graphitic fragments and produce a good covering of -COOH surface groups. These nanodiamonds were reduced with a borane tetrahydrofuran complex ($BH_3 \cdot THF$). Then, dopamine is polymerised onto nanodiamonds in a 200 mM Tris bufferin a 10:1 ratio. Figure 5.1 shows promising evidence that these first steps are successful.

If this method is not successful, then other mitochondrial targeting methods are available, such as small cell-penetrating peptides [388] or antibodies [308]. After this, it would be desirable to repeat the biocompatibility experiments in chapter 4 on any newly functionalised nanodiamonds.

5.2.4 Temperature in cells

After completing the surface functionalisation of nanodiamonds to target mitochondria, it will then be possible to investigate a specific biological question as a demonstration of capability. Over the past two years, there has been ongoing discussion in the scientific community about the temperature of mitochondria that has centred around the publication of work measuring it controversially at 50 °C [389, 390]. Nanodiamonds are capable of measuring temperature to a precision of 0.2 K [81, 216], and so could provide convincing evidence to resolve this problem.

The custom microscope described in chapter 2 has detected NV fluorescence inside cancer cells. Figure 5.2 shows preliminary work that has achieved the detection of nanodiamond aggregates inside cancer cells. In order to measure temperature using NV fluorescence it is necessary to detect single NV centres, as has been done in other work [16]. Therefore, prior to any temperature measurement experiment it may be necessary to optimise the concentration of nanodiamonds and optimise the detection technique to find and track them, such as in McGuinness et al. [14]. This would include a study of a suitable microwave power for the cells.

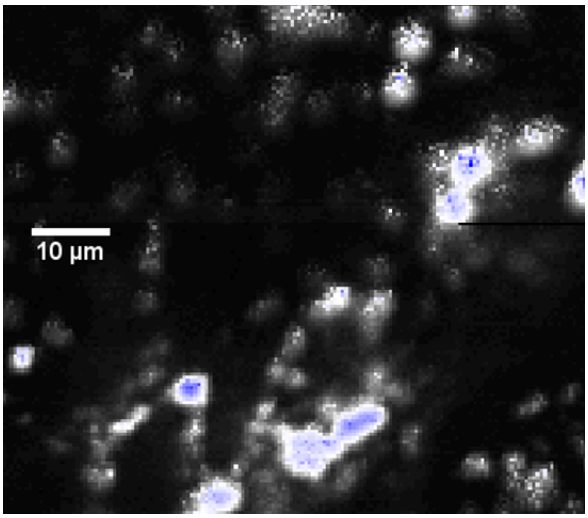

Fig. 5.2 Aggregates of nanodiamonds at 100 µg/ml containing nitrogen vacancy centres detected inside fixed A549 lung cancer cells. The maximum count rate is approximately 8000 s^{-1} at 32 µW of laser power. The concentration of diamonds needs to be reduced towards detection of single nitrogen vacancy centres.

5.2.5 Measuring $\Delta\Psi_m$ through a cell death

Using a similar cell protocol as developed to measure mitochondrial temperature, it will then be possible to measure mitochondrial membrane potential. This should be demonstrated by comparison to a well-characterised membrane potential decreasing agent such as valinomycin [32]. Nanodiamonds would be used to repeatedly probe the electric field as it decreased to zero. This would then be correlated with changes detected through Raman spectroscopy as already described, such as the release of cytochrome c from mitochondria, and nuclear fragmentation.

Following from this, it would possible to use a standard chemotherapeutic agent such as etoposide to induce apoptosis, and to track this process through NV centres and Raman microscopy [255]. It is expected that the magnitude of the mitochondrial membrane potential would first increase in magnitude and then decrease [45, 8, 41, 32]. It should be possible to provide new insights into the mechanism of these chemotherapeutic agents, and perhaps to better understand how they should be used. It would be particularly interesting to investigate cancer cells that have modified ion channel expression that is thought to enable the avoidance of apoptosis, a trait classified as a key hallmark of cancer [45, 43].

5.2.6 Cancer stem cells

With nanodiamonds and Raman microscopy providing new insights into mitochondrial membrane potential through the process of apoptosis, it is then attractive to investigate broader biological problems. One example is to focus on cancer stem cells. There are cells that are hypothesised to exist as undifferentiated cells that are responsible for the occurrence, development and recurrence of malignant tumours [391]. These cells are noted to have characteristics that are detectable with the techniques of this project, including higher $\Delta\Psi_m$ and lower mitochondrial DNA content [391, 34]. Since these cells express unique and interesting pathological reactive oxygen species, metabolic states and apoptotic processes, they could be an important focus of study as future work [391, 34]. Furthermore, understanding these processes better has been suggested as a promising avenue for new cancer therapy [34].

Bibliography

[1] Benjamin J. Woodhams, Laura Ansel-Bollepalli, Jakub M. Surmacki, Helena S. Knowles, Laura Maggini, Michael De Volder, Mete Atatüre, and Sarah E. Bohndiek. Graphitic and oxidised high pressure high temperature (HPHT) nanodiamonds induce differential biological responses in breast cancer cell lines. *Nanoscale*, pages 26–32, 2018. doi: 10.1039/c8nr02177e. URL www.dx.doi.org/10.1039/c8nr02177e.

[2] Jakub M. Surmacki, Benjamin J. Woodhams, Alexandria Haslehurst, Bruce A. J. Ponder, and Sarah E. Bohndiek. Raman micro-spectroscopy for accurate identification of primary human bronchial epithelial cells. *Scientific Reports*, 8(1):12604, 2018. ISSN 2045-2322. doi: 10.1038/s41598-018-30407-8. URL http://www.nature.com/articles/s41598-018-30407-8.

[3] David W Ball, John W Hill, and Rhonda J Scott. *Introduction to Chemistry: General, Organic, and Biological*. Creative Commons Publication, 2011. ISBN 9812561420. doi: 10.1038/087179b0. URL http://openedgroup.org/books/Chemistry.pdf.

[4] C. A. Mannella, D. R. Pfeiffer, P. C. Bradshaw, I. I. Moraru, B. Slepchenko, L. M. Loew, C. E. Hsie, K. Buttle, and M. Marko. Topology of the mitochondrial inner membrane: Dynamics and bioenergetic implications. *IUBMB Life*, 52(3-5):93–100, 2002. ISSN 15216543. doi: 10.1080/15216540152845885.

[5] T. El Bacha, M. Luz, and A. Da Poian. Dynamic Adaptation of Nutrient Utilization in Humans. *Nature Education*, 3(9):8, 2010. URL http://www.nature.com/scitable/topicpage/dynamic-adaptation-of-nutrient-utilization-in-humans-14232807.

[6] Michael P. Murphy. How mitochondria produce reactive oxygen species. *Biochemical Journal*, 417(1):1–13, 2009. ISSN 0264-6021. doi: 10.1042/BJ20081386. URL http://biochemj.org/lookup/doi/10.1042/BJ20081386.

[7] Vitor M C Madeira. *Overview of mitochondrial bioenergetics*, volume 810. Springer Protocols, 2012. ISBN 9781617793813. doi: 10.1007/978-1-61779-382-0{_}1.

[8] B. O'Rourke. Mitochondrial Ion Channels: Gatekeepers of Life and Death. *Physiology*, 20(5):303–315, 2005. ISSN 1548-9213. doi: 10.1152/physiol.00020.2005. URL http://physiologyonline.physiology.org/cgi/doi/10.1152/physiol.00020.2005.

[9] Vanessa Checchetto, Michele Azzolini, Roberta Peruzzo, Paola Capitanio, and Luigi Leanza. Mitochondrial potassium channels in cell death. *Biochemical and Biophysical Research Communications*, 500(1):51–58, 2018. ISSN 10902104. doi: 10.1016/j.bbrc.2017.06.095. URL https://doi.org/10.1016/j.bbrc.2017.06.095.

[10] SubsTech. Substances and Technologies: Synthetic diamonds. URL http://www.substech.com/dokuwiki/doku.php?id=synthetic_diamonds.

[11] M. N. R. Ashfold, P. W. May, C. A. Rego, and N. M. Everitt. Thin film diamond by chemical vapour deposition methods. *Chemical Society Reviews*, 23(1):21, 1 1994. ISSN 0306-0012. doi: 10.1039/cs9942300021. URL http://xlink.rsc.org/?DOI=cs9942300021.

[12] Vadym N. Mochalin, Olga Shenderova, Dean Ho, and Yury Gogotsi. The properties and applications of nanodiamonds. *Nature nanotechnology*, 7(1):11–23, 1 2011. ISSN 1748-3387. doi: 10.1038/nnano.2011.209. URL http://dx.doi.org/10.1038/nnano.2011.209http://www.ncbi.nlm.nih.gov/pubmed/22179567http://www.scopus.com/inward/record.url?eid=2-s2.0-84855292426&partnerID=tZOtx3y1http://www.nature.com/nnano/journal/v7/n1/full/nnano.2011.209.html.

[13] Igor Aharonovich and Elke Neu. Diamond nanophotonics. *Advanced Optical Materials*, 2(10):911–928, 2014. ISSN 21951071. doi: 10.1002/adom.201400189. URL https://onlinelibrary.wiley.com/doi/abs/10.1002/adom.201400189.

[14] L. P. McGuinness, Y. Yan, A. Stacey, D. A. Simpson, L. T. Hall, D. Maclaurin, S. Prawer, P. Mulvaney, J. Wrachtrup, F. Caruso, R. E. Scholten, and L. C. L. Hollenberg. Quantum measurement and orientation tracking of fluorescent nanodiamonds inside living cells. *Nature nanotechnology*, 6(6):358–363, 6 2011. ISSN 1748-3395. doi: 10.1038/nnano.2011.64. URL http://www.ncbi.nlm.nih.gov/pubmed/21552253http://www.nature.com/doifinder/10.1038/nnano.2011.64http://www.ncbi.nlm.nih.gov/pubmed/21552253%5Cnhttp://www.nature.com/nnano/journal/v6/n6/pdf/nnano.2011.64.pdf.

[15] Takayuki Iwasaki, Wataru Naruki, Kosuke Tahara, Toshiharu Makino, Hiromitsu Kato, Masahiko Ogura, Daisuke Takeuchi, Satoshi Yamasaki, and Mutsuko Hatano. Direct Nanoscale Sensing of the Internal Electric Field in Operating Semiconductor Devices Using Single Electron Spins. *ACS Nano*, 11(2):1238–1245, 2017. ISSN 1936086X. doi: 10.1021/acsnano.6b04460.

[16] Georg Kucsko, P. C. Maurer, N. Y. Yao, M. Kubo, H. J. Noh, P. K. Lo, H. Park, and M. D. Lukin. Nanometre-scale thermometry in a living cell. *Nature*, 500(7460):54–8, 8 2013. doi: 10.1038/nature12373. URL http://dx.doi.org/10.1038/nature12373.

[17] D Le Sage, K Arai, D R Glenn, S J DeVience, L M Pham, L Rahn-Lee, M D Lukin, A Yacoby, A Komeili, and R L Walsworth. Optical magnetic imaging of living cells. *Nature*, 496(7446):486–9, 4 2013. ISSN 1476-4687. doi: 10.1038/nature12072. URL http://www.pubmedcentral.nih.gov/articlerender.fcgi?artid=3641584&tool=pmcentrez&rendertype=abstracthttps://www.nature.com/articles/nature12072.

[18] Masfer Alkahtani, Linkun Jiang, Robert Brick, Philip Hemmer, and Marlan Scully. Nanometer-scale luminescent thermometry in bovine embryos. *Optics Letters*, 42(23):4812, 2017. ISSN 0146-9592. doi: 10.1364/OL.42.004812. URL https://www.osapublishing.org/abstract.cfm?URI=ol-42-23-4812.

[19] Iwan W Schie and Thomas Huser. Methods and applications of Raman microspectroscopy to single-cell analysis. *Applied spectroscopy*, 67(8):813–28, 8 2013. doi: 10.1366/12-06971. URL http://www.ncbi.nlm.nih.gov/pubmed/23876720.

[20] Krzysztof Czamara, Filip Petko, Malgorzata Baranska, and Agnieszka Kaczor. Raman microscopy at the subcellular level: a study on early apoptosis in endothelial cells induced by Fas ligand and cycloheximide. *The Analyst*, 141:1390–1397, 2016. ISSN 0003-2654. doi: 10.1039/C5AN02202A. URL http://xlink.rsc.org/?DOI=C5AN02202A.

[21] Katharina Klein, Alexander M. Gigler, Thomas Aschenbrenner, Roberto Monetti, Wolfram Bunk, Ferdinand Jamitzky, Gregor Morfill, Robert W. Stark, and Jürgen Schlegel. Label-free live-cell imaging with confocal Raman microscopy. *Biophysical Journal*, 102(January):360–368, 2012. ISSN 00063495. doi: 10.1016/j.bpj.2011.12.027.

[22] Birthe Kann, Herman L. Offerhaus, Maike Windbergs, and Cees Otto. Raman microscopy for cellular investigations - From single cell imaging to drug carrier uptake visualization. *Advanced Drug Delivery Reviews*, 89:71–90, 2015. ISSN 18728294. doi: 10.1016/j.addr.2015.02.006. URL http://dx.doi.org/10.1016/j.addr.2015.02.006.

[23] Jeffrey T. Meade, Bradford B. Behr, Yusuf Bismilla, Andrew T. Cenko, and Arsen R. Hajian. In-depth performance analysis of the HyperFlux spectrometer. *Proceedings of SPIE*, 8572:85720V, 2013. ISSN 16057422. doi: 10.1117/12.2005285. URL http://proceedings.spiedigitallibrary.org/proceeding.aspx?doi=10.1117/12.2005285.

[24] Syed Sadat Nazrul. The DOs and DON'Ts of Principal Component Analysis, 2018. URL https://medium.com/@sadatnazrul/the-dos-and-donts-of-principal-component-analysis-7c2e9dc8cc48.

[25] Francisco de la Peña, Tomas Ostasevicius, Vidar Tonaas Fauske, Pierre Burdet, Eric Prestat, Petras Jokubauskas, Magnus Nord, Mike Sarahan, Katherine E. MacArthur, Duncan N. Johnstone, Joshua Taillon, Jan Caron, Vadim Migunov, Tom Furnival, Alberto Eljarrat, Stefano Mazzucco, Thomas Aarholt, Michael Walls, Tom Slater, Florian Winkler, Ben Martineau, Gaël Donval, Robert McLeod, Eric R. Hoglund, Ivo Alxneit, Ida Hjorth, Trond Henninen, Luiz Fernando Zagonel, Andreas Garmannslund, and 5ht2. hyperspy/hyperspy: HyperSpy 1.3.1, 4 2018. URL https://zenodo.org/record/1221347#.WzNOqtVKiUk.

[26] John M. Chalmers. Mid-Infrared Spectroscopy: Anomalies, Artifacts and Common Errors. In John M. Chalmers, editor, *Handbook of Vibrational Spectroscopy*, pages 2327–2347. John Wiley & Sons, Ltd, Chichester, UK, 8 2006. doi: 10.1002/0470027320.s3101. URL http://doi.wiley.com/10.1002/0470027320.s3101http://turroserver.chem.columbia.edu/group/instrument/MidIRCommonErrors.pdf.

[27] Johannes Schindelin, Ignacio Arganda-Carreras, Erwin Frise, Verena Kaynig, Mark Longair, Tobias Pietzsch, Stephan Preibisch, Curtis Rueden, Stephan Saalfeld, Benjamin Schmid, Jean-Yves Tinevez, Daniel James White, Volker Hartenstein, Kevin Eliceiri, Pavel Tomancak, and Albert Cardona. Fiji: an open-source platform for biological-image analysis. *Nature Methods*, 9(7):676–682, 7 2012. ISSN 1548-7091.

URL http://dx.doi.org/10.1038/nmeth.2019http://www.nature.com/nmeth/journal/v9/n7/abs/nmeth.2019.html#supplementary-information.

[28] J. Brocher. The BioVoxxel Image Processing and Analysis Toolbox. In *EuBIAS-Conference*, Madison, Wisconsin, 2015. URL http://www.biovoxxel.de/development/.

[29] Patrick D. Bhola and Anthony Letai. Mitochondria-Judges and Executioners of Cell Death Sentences. *Molecular Cell*, 61(5):695–704, 2016. ISSN 10974164. doi: 10.1016/j.molcel.2016.02.019. URL http://dx.doi.org/10.1016/j.molcel.2016.02.019.

[30] Sabzali Javadov and Andrey V Kuznetsov. Mitochondria: the cell powerhouse and nexus of stress. *Frontiers in physiology*, 4:207, 1 2013. ISSN 1664-042X. doi: 10.3389/fphys.2013.00207. URL http://journal.frontiersin.org/article/10.3389/fphys.2013.00207/abstract.

[31] Damon Poburko, Jaime Santo-Domingo, and Nicolas Demaurex. Dynamic regulation of the mitochondrial proton gradient during cytosolic calcium elevations. *Journal of Biological Chemistry*, 286(13):11672–11684, 2011. ISSN 00219258. doi: 10.1074/jbc.M110.159962.

[32] Divya Padmaraj, Rohit Pande, John H Miller, Jarek Wosik, and Wanda Zagozdzon-Wosik. Mitochondrial membrane studies using impedance spectroscopy with parallel pH monitoring. *PloS one*, 9(7):e101793, 1 2014. ISSN 1932-6203. doi: 10.1371/journal.pone.0101793. URL http://www.pubmedcentral.nih.gov/articlerender.fcgi?artid=4091947&tool=pmcentrez&rendertype=abstract.

[33] J. D. Ly, D. R. Grubb, and A. Lawen. The mitochondrial membrane potential ($\delta\psi$m) in apoptosis; an update. *Apoptosis*, 8(2):115–128, 2003. ISSN 13608185. doi: 10.1023/A:1022945107762.

[34] Bei-bei Zhang, Dao-gang Wang, Fen-fen Guo, and Chao Xuan. Mitochondrial membrane potential and reactive oxygen species in cancer stem cells. *Familial Cancer*, 14(1):19–23, 2015. ISSN 1389-9600. doi: 10.1007/s10689-014-9757-9. URL http://link.springer.com/10.1007/s10689-014-9757-9.

[35] J Pokorný, A Jandová, M Nedbalová, F Jelínek, M Cifra, O Kučera, D Havelka, J Vrba, A Coček, and J Kobilková. Mitochondrial metabolism - neglected link of cancer transformation and treatment. *Prague medical report*, 113 (2):81–94, 2012. ISSN 1214-6994. URL http://www.mendeley.com/catalog/mitochondrial-metabolism-neglected-link-cancer-transformation-treatment/http://apps.webofknowledge.com/full_record.do?product=UA&search_mode=CombineSearches&qid=21&SID=Z2ZMEgoorokknwIHRtK&page=1&doc=2.

[36] Simon Wisnovsky, Eric K. Lei, Sae Rin Jean, and Shana O. Kelley. Mitochondrial Chemical Biology: New Probes Elucidate the Secrets of the Powerhouse of the Cell. *Cell Chemical Biology*, 23(8):917–927, 2016. ISSN 24519448. doi: 10.1016/j.chembiol.2016.06.012. URL http://dx.doi.org/10.1016/j.chembiol.2016.06.012.

[37] Jaroslaw Dzbek and Bernard Korzeniewski. Control over the contribution of the mitochondrial membrane potential (DeltaPsi) and proton gradient (DeltapH) to the protonmotive force (Deltap). In silico studies. *The Journal of biological chemistry*,

283(48):33232–9, 11 2008. ISSN 0021-9258. doi: 10.1074/jbc.M802404200. URL http://www.jbc.org/content/283/48/33232.full.

[38] Bernhard Kadenbach, Rabia Ramzan, and Sebastian Vogt. Degenerative diseases, oxidative stress and cytochrome c oxidase function. *Trends in Molecular Medicine*, 15(4):139–147, 2009. ISSN 14714914. doi: 10.1016/j.molmed.2009.02.004.

[39] Eduardo N. Maldonado and John J. Lemasters. ATP/ADP ratio, the missed connection between mitochondria and the Warburg effect. *Mitochondrion*, 19(Part A):78–84, 2014. ISSN 18728278. doi: 10.1016/j.mito.2014.09.002. URL http://dx.doi.org/10.1016/j.mito.2014.09.002.

[40] Matthew G Vander Heiden, Lewis C Cantley, Craig B Thompson, Proliferating Mammalian, Cells Exhibit, and Anabolic Metabolism. Understanding the Warburg Effect : Cell Proliferation. *Science*, 324(May):1029, 2009. ISSN 00368075. doi: 10.1126/science.1160809.

[41] D. B. Zorov, M. Juhaszova, and S. J. Sollott. Mitochondrial Reactive Oxygen Species (ROS) and ROS-Induced ROS Release. *Physiological Reviews*, 94(3):909–950, 2014. ISSN 0031-9333. doi: 10.1152/physrev.00026.2013. URL http://physrev.physiology.org/cgi/doi/10.1152/physrev.00026.2013.

[42] L.D. Zorova, V.A. Popkov, E.J. Plotnikov, D.N. Silachev, I.B. Pevzner, S.S. Jankauskas, S.D. Zorov, V.A. Babenko, and D.B. Zorov. Functional Significance of the Mitochondrial Membrane Potential. *Biochemistry (Moscow) Supplement Series A: Membrane and Cell Biology*, 12(1):20–26, 2018. ISSN 19907494. doi: 10.1134/S1990747818010129.

[43] Douglas Hanahan and Robert a Weinberg. Hallmarks of cancer: the next generation. *Cell*, 144(5):646–74, 3 2011. ISSN 1097-4172. doi: 10.1016/j.cell.2011.02.013. URL http://www.ncbi.nlm.nih.gov/pubmed/21376230.

[44] Rebecca C. Taylor, Sean P. Cullen, and Seamus J. Martin. Apoptosis: Controlled demolition at the cellular level. *Nature Reviews Molecular Cell Biology*, 9(3):231–241, 2008. ISSN 14710072. doi: 10.1038/nrm2312.

[45] Artem Kondratskyi, Kateryna Kondratska, Roman Skryma, and Natalia Prevarskaya. Ion channels in the regulation of apoptosis. *Biochimica et Biophysica Acta - Biomembranes*, 1848(10):2532–2546, 2015. ISSN 18792642. doi: 10.1016/j.bbamem.2014.10.030. URL http://dx.doi.org/10.1016/j.bbamem.2014.10.030.

[46] Lorenzo Galluzzi, Naoufal Zamzami, Thibault De La Motte Rouge, Christophe Lemaire, Catherine Brenner, and Guido Kroemer. Methods for the assessment of mitochondrial membrane permeabilization in apoptosis. *Apoptosis*, 12:803–813, 2007. ISSN 13608185. doi: 10.1007/s10495-007-0720-1.

[47] Lisa Bouchier-Hayes, Cristina Muñoz-Pinedo, Samuel Connell, and Douglas R. Green. Measuring apoptosis at the single cell level. *Methods*, 44:222–228, 2008. ISSN 10462023. doi: 10.1016/j.ymeth.2007.11.007.

[48] Yan Mi, Caixin Sun, Chenguo Yao, Chengxiang Li, Dengbin Mo, Liling Tang, and Huan Liu. Effects of steep pulsed electric fields (SPEF) on mitochondrial transmembrane potential of human liver cancer cell. *2007 Annual International Conference of the IEEE Engineering in Medicine and Biology Society, Vols 1-16*, pages 5815–5818, 2007. ISSN 1094-687X. URL http://apps.webofknowledge.com/full_record.do?product=WOS&search_mode=GeneralSearch&qid=26&SID=T2IWCx2Vc82S4PID3Bo&page=2&doc=52.

[49] Melinda E. Christensen, Elisa S. Jansen, Washington Sanchez, and Nigel J. Waterhouse. Flow cytometry based assays for the measurement of apoptosis-associated mitochondrial membrane depolarisation and cytochrome c release. *Methods*, 61 (2):138–145, 2013. ISSN 10462023. doi: 10.1016/j.ymeth.2013.03.020. URL http://dx.doi.org/10.1016/j.ymeth.2013.03.020.

[50] Andrea Cossarizza, Miranda Baccarani-Contri, Galina Kalashnikova, and Claudio Franceschi. A new method for the cytofluorometric analysis of mitochondrial membrane potential using the J-aggregate forming lipophilic cation 5,5',6,6'-tetrachloro-1,1',3,3'-tetraethylbenzim idazolcarbocyanine iodide (JC-1). *Biochemical and Biophysical Research Communications*, 197(1):40–45, 1993. ISSN 10902104. doi: 10.1006/bbrc.1993.2438.

[51] Elena N. Dedkova and Lothar a. Blatter. Measuring mitochondrial function in intact cardiac myocytes. *Journal of Molecular and Cellular Cardiology*, 52(1):48–61, 2012. ISSN 00222828. doi: 10.1016/j.yjmcc.2011.08.030. URL http://dx.doi.org/10.1016/j.yjmcc.2011.08.030.

[52] Seth W Perry, John P Norman, Justin Barbieri, Edward B Brown, Harris A Gelbard, A Harris, and Harris A Gelbard. Mitochondrial membrane potential probes and the proton gradient: a practical usage guide. *BioTechniques*, 50(2):98–115, 2 2011. ISSN 1940-9818. doi: 10.2144/000113610. URL http://www.pubmedcentral.nih.gov/articlerender.fcgi?artid=3115691&tool=pmcentrez&rendertype=abstract.

[53] Cécile Cottet-Rousselle, Xavier Ronot, Xavier Leverve, and Jean-François Mayol. Cytometric assessment of mitochondria using fluorescent probes. *Cytometry. Part A : the journal of the International Society for Analytical Cytology*, 79(6):405–25, 6 2011. ISSN 1552-4930. doi: 10.1002/cyto.a.21061. URL http://onlinelibrary.wiley.com/doi/10.1002/cyto.a.21061/full.

[54] Gerhard Krumschnabel, Andrea Eigentler, Mario Fasching, and Erich Gnaiger. *Use of safranin for the assessment of mitochondrial membrane potential by high-resolution respirometry and fluorometry*, volume 542. Elsevier Inc., 1 edition, 2014. ISBN 9780124166189. doi: 10.1016/B978-0-12-416618-9.00009-1. URL http://dx.doi.org/10.1016/B978-0-12-416618-9.00009-1.

[55] Dany S Adams and Michael Levin. General principles for measuring resting membrane potential and ion concentration using fluorescent bioelectricity reporters. *Cold Spring Harbor protocols*, Volume2012(4):385–97, 4 2012. ISSN 1559-6095.

[56] Fang Miao, Weijia Zhang, Yuming Sun, Ruoyao Zhang, Yong Liu, Fuqiang Guo, Guofen Song, Minggang Tian, and Xiaoqiang Yu. Novel fluorescent probes for

highly selective two-photon imaging of mitochondria in living cells. *Biosensors and Bioelectronics*, 55:423–429, 2014. ISSN 09565663. doi: 10.1016/j.bios.2013.12.044. URL http://dx.doi.org/10.1016/j.bios.2013.12.044.

[57] Wei Ren, Ao Ji, Omran Karmach, David G. Carter, Manuela M. Martins-Green, and Hui-wang Wang Ai. A membrane-activatable near-infrared fluorescent probe with ultra-photostability for mitochondrial membrane potentials. *The Analyst*, 141 (12):3679–3685, 2016. ISSN 13645528. doi: 10.1039/c5an01860a. URL http://xlink.rsc.org/?DOI=C5AN01860A.

[58] Akos a Gerencser, Christos Chinopoulos, Matthew J Birket, Martin Jastroch, Cathy Vitelli, David G Nicholls, and Martin D Brand. Quantitative measurement of mitochondrial membrane potential in cultured cells: calcium-induced de- and hyperpolarization of neuronal mitochondria. *The Journal of physiology*, 590:2845–71, 2012. ISSN 1469-7793. doi: 10.1113/jphysiol.2012.228387. URL http://www.pubmedcentral.nih.gov/articlerender.fcgi?artid=3448152&tool=pmcentrez&rendertype=abstract.

[59] Nathaniel M. Alpert, Nicolas Guehl, Leon Ptaszek, Matthieu Pelletier-Galarneau, Jeremy Ruskin, Moussa C. Mansour, Dustin Wooten, Chao Ma, Kazue Takahashi, Yun Zhou, Timothy M. Shoup, Marc D. Normandin, and Georges El Fakhri. Quantitative in vivo mapping of myocardial mitochondrial membrane potential. *PLoS ONE*, 13(1): 1–16, 2018. ISSN 19326203. doi: 10.1371/journal.pone.0190968.

[60] Angela Logan, Victoria R. Pell, Karl J. Shaffer, Cameron Evans, Nathan J. Stanley, Ellen L. Robb, Tracy A. Prime, Edward T. Chouchani, Helena M. Cochemé, Ian M. Fearnley, Sara Vidoni, Andrew M. James, Carolyn M. Porteous, Linda Partridge, Thomas Krieg, Robin A.J. Smith, and Michael P. Murphy. Assessing the mitochondrial membrane potential in cells and in vivo using targeted click chemistry and mass spectrometry. *Cell Metabolism*, 23(2):379–385, 2016. ISSN 19327420. doi: 10.1016/j.cmet.2015.11.014.

[61] Erwin Neher and Bert Sakmann. Single-channel currents recorded from membrane of denervated frog muscle fibres. *Nature*, 260(5554):799–802, 1976. ISSN 00280836. doi: 10.1038/260799a0.

[62] Yasunobu Okada. *Patch Clamp Techniques*. Springer, Okasaki, Japan, 2012. ISBN 978-4-431-53992-6.

[63] Daniel A. Kane and Evgeny V. Pavlov. Calculation of ion currents across the inner membrane of functionally intact mitochondria. *Channels*, 7(6), 2013. ISSN 19336969. doi: 10.4161/chan.26290.

[64] Kyoungwon Park, Yung Kuo, Volodymyr Shvadchak, Antonino Ingargiola, Xinghong Dai, Lawrence Hsiung, Wookyeom Kim, Hong Zhou, Peng Zou, Alex J. Levine, Jack Li, and Shimon Weiss. Membrane insertion of - and membrane potential sensing by - semiconductor voltage nanosensors: Feasibility demonstration. *Science Advances*, 4(1):e1601453, 2018. ISSN 2375-2548. doi: 10.1126/sciadv.1601453. URL http://advances.sciencemag.org/lookup/doi/10.1126/sciadv.1601453.

[65] Katherine M Tyner, Raoul Kopelman, and Martin Philbert. "Nanosized voltmeter" enables cellular-wide electric field mapping. *Biophysical journal*, 93(4):1163–1174,

2007. ISSN 00063495. doi: 10.1529/biophysj.106.092452. URL http://dx.doi.org/10.1529/biophysj.106.092452.

[66] Wesley Wei-Wen Hsiao, Yuen Yung Hui, Pei-Chang Tsai, and Huan-Cheng Chang. Fluorescent Nanodiamond: A Versatile Tool for Long-Term Cell Tracking, Super-Resolution Imaging, and Nanoscale Temperature Sensing. *Accounts of Chemical Research*, page acs.accounts.5b00484, 2016. ISSN 0001-4842. doi: 10.1021/acs.accounts.5b00484. URL http://pubs.acs.org/doi/abs/10.1021/acs.accounts.5b00484.

[67] Anke Krueger and Daniel Lang. Functionality is Key: Recent Progress in the Surface Modification of Nanodiamond. *Advanced Functional Materials*, 22(5):890–906, 3 2012. ISSN 1616301X. doi: 10.1002/adfm.201102670. URL http://doi.wiley.com/10.1002/adfm.201102670.

[68] V. V. Danilenko. On the history of the discovery of nanodiamond synthesis. *Physics of the Solid State*, 46(4):595–599, 2004. ISSN 1063-7834. doi: 10.1134/1.1711431. URL http://link.springer.com/10.1134/1.1711431.

[69] Valerii Yu Dolmatov. Detonation-synthesis nanodiamonds: synthesis, structure, properties and applications. *Russian Chemical Reviews*, 76(4):339–360, 2007. ISSN 0036-021X. doi: 10.1070/RC2007v076n04ABEH003643. URL http://stacks.iop.org/0036-021X/76/i=4/a=R04?key=crossref.20319d9f722eee84434718e8d616c4ff.

[70] Olga a. Shenderova and Gary E. McGuire. Science and engineering of nanodiamond particle surfaces for biological applications (Review). *Biointerphases*, 10(3):030802, 2015. ISSN 1934-8630. doi: 10.1116/1.4927679. URL http://scitation.aip.org/content/avs/journal/bip/10/3/10.1116/1.4927679.

[71] E. Neu, C. Arend, E. Gross, F. Guldner, C. Hepp, D. Steinmetz, E. Zscherpel, S. Ghodbane, H. Sternschulte, D. Steinmüller-Nethl, Y. Liang, A. Krueger, and C. Becher. Narrowband fluorescent nanodiamonds produced from chemical vapor deposition films. *Applied Physics Letters*, 98(24):98–100, 2011. ISSN 00036951. doi: 10.1063/1.3599608. URL https://doi.org/10.1063/1.3599608.

[72] Leiming Fang, Hiroaki Ohfuji, and Tetsuo Irifune. A novel technique for the synthesis of nanodiamond powder. *Journal of Nanomaterials*, 2013, 2013. ISSN 16874110. doi: 10.1155/2013/201845.

[73] Julia Tisler, Gopalakrishnan Balasubramanian, Boris Naydenov, Roman Kolesov, Bernhard Grotz, Rolf Reuter, Jean-Paul Paul Boudou, Patrick A. Curmi, Mohamed Sennour, Alain Thorel, Michael Börsch, Kurt Aulenbacher, Rainer Erdmann, Philip R. Hemmer, Fedor Jelezko, and Jörg Wrachtrup. Fluorescence and spin properties of defects in single digit nanodiamonds. *ACS Nano*, 3(7):1959–1965, 7 2009. ISSN 19360851. doi: 10.1021/nn9003617. URL http://dx.doi.org/10.1021/nn9003617.

[74] Helena S Knowles, Dhiren M Kara, and Mete Atatüre. Observing bulk diamond spin coherence in high-purity nanodiamonds. *Nature Materials*, 13(1):21–5, 1 2014. ISSN 1476-1122. doi: 10.1038/nmat3805. URL http://dx.doi.org/10.1038/nmat3805.

[75] Laura Moore, Valéria Grobárová, Helen Shen, Han Bin Man, Júlia Míčová, Miroslav Ledvina, Jan Štursa, Milos Nesladek, Anna Fišerová, and Dean Ho. Comprehensive interrogation of the cellular response to fluorescent, detonation and functionalized nanodiamonds. *Nanoscale*, 6(20):11712–21, 10 2014. ISSN 2040-3372. doi: 10.1039/c4nr02570a. URL http://www.ncbi.nlm.nih.gov/pubmed/25037888.

[76] Meng Si Wu, Der Shan Sun, Yu Chung Lin, Chia Liang Cheng, Shih Che Hung, Po Kong Chen, Jen Hung Yang, and Hsin Hou Chang. Nanodiamonds protect skin from ultraviolet B-induced damage in mice. *Journal of Nanobiotechnology*, 13(1): 1–12, 2015. ISSN 14773155. doi: 10.1186/s12951-015-0094-4. URL ???

[77] C. J H Wort and Richard S. Balmer. Diamond as an electronic material. *Materials Today*, 11(1-2):22–28, 2008. ISSN 13697021. doi: 10.1016/S1369-7021(07)70349-8. URL http://dx.doi.org/10.1016/S1369-7021(07)70349-8.

[78] N. Aslam, G. Waldherr, P. Neumann, F. Jelezko, and J. Wrachtrup. Photo-induced ionization dynamics of the nitrogen vacancy defect in diamond investigated by single-shot charge state detection. *New Journal of Physics*, 15:1–9, 2013. ISSN 13672630. doi: 10.1088/1367-2630/15/1/013064.

[79] Eisuke Abe and Kento Sasaki. Tutorial: Magnetic resonance with nitrogen-vacancy centers in diamond—microwave engineering, materials science, and magnetometry. *Journal of Applied Physics*, 123(161101):3–14, 2018. ISSN 0021-8979. doi: 10.1063/1.5011231. URL http://arxiv.org/abs/1802.07857.

[80] X. D. Chen, C. H. Dong, F. W. Sun, C. L. Zou, J. M. Cui, Z. F. Han, and G. C. Guo. Temperature dependent energy level shifts of nitrogen-vacancy centers in diamond. *Applied Physics Letters*, 99(16):1–3, 2011. ISSN 00036951. doi: 10.1063/1.3652910. URL http://aip.scitation.org/doi/full/10.1063/1.3652910https://doi.org/10.1063/1.3652910.

[81] Marcus W. Doherty, Neil B. Manson, Paul Delaney, Fedor Jelezko, Jörg Wrachtrup, and Lloyd C.L. Hollenberg. The nitrogen-vacancy colour centre in diamond. *Physics Reports*, 528(1):1–45, 7 2013. ISSN 03701573. doi: 10.1016/j.physrep.2013.02.001. URL http://www.scopus.com/inward/record.url?eid=2-s2.0-84878600144&partnerID=tZOtx3y1.

[82] Florian Dolde, Marcus W. Doherty, Julia Michl, Ingmar Jakobi, Boris Naydenov, Sebastien Pezzagna, Jan Meijer, Philipp Neumann, Fedor Jelezko, Neil B. Manson, and Jörg Wrachtrup. Nanoscale Detection of a Single Fundamental Charge in Ambient Conditions Using the NV- Center in Diamond. *Physical Review Letters*, 112(9): 097603, 3 2014. ISSN 0031-9007. doi: 10.1103/PhysRevLett.112.097603. URL http://link.aps.org/doi/10.1103/PhysRevLett.112.097603.

[83] M. W. Doherty, F. Dolde, H. Fedder, F. Jelezko, J. Wrachtrup, N. B. Manson, and L. C.L. Hollenberg. Theory of the ground-state spin of the NV - center in diamond. *Physical Review B - Condensed Matter and Materials Physics*, 85(20):1–21, 2012. ISSN 10980121. doi: 10.1103/PhysRevB.85.205203.

[84] Edward H. Chen, Hannah A. Clevenson, Kerry A. Johnson, Linh M. Pham, Dirk R. Englund, Philip R. Hemmer, and Danielle A. Braje. High-sensitivity, spin-based

electrometry with an ensemble of nitrogen-vacancy centers in diamond. *Physical Review A*, 053417:1–7, 2017. ISSN 2469-9926. doi: 10.1103/PhysRevA.95.053417. URL http://arxiv.org/abs/1703.07517.

[85] David R. Glenn, Dominik B. Bucher, Junghyun Lee, Mikhail D. Lukin, Hongkun Park, and Ronald L. Walsworth. High-resolution magnetic resonance spectroscopy using a solid-state spin sensor. *Nature*, 555(7696):351–354, 2018. ISSN 0028-0836. doi: 10.1038/nature25781. URL http://www.nature.com/doifinder/10.1038/nature25781.

[86] J. R. Maze, P. L. Stanwix, J. S. Hodges, S. Hong, J. M. Taylor, P. Cappellaro, L. Jiang, M. V. Gurudev Dutt, E. Togan, A. S. Zibrov, A. Yacoby, R. L. Walsworth, and M. D. Lukin. Nanoscale magnetic sensing with an individual electronic spin in diamond. *Nature*, 455(7213):644–647, 2008. ISSN 0028-0836. doi: 10.1038/nature07279. URL http://www.nature.com/doifinder/10.1038/nature07279.

[87] T Staudacher, F Shi, S Pezzagna, J Meijer, J Du, C A Meriles, F Reinhard, and J Wrachtrup. Nuclear magnetic resonance spectroscopy on a (5-nanometer)3 sample volume. *Science (New York, N.Y.)*, 339(6119):561–563, 2013. ISSN 1095-9203. doi: 10.1126/science.1231675. URL http://www.ncbi.nlm.nih.gov/pubmed/23372009.

[88] Nabeel Aslam, Matthias Pfender, Philipp Neumann, Rolf Reuter, Andrea Zappe, Felipe Fávaro de Oliveira, Andrej Denisenko, Hitoshi Sumiya, Shinobu Onoda, Junichi Isoya, and Jörg Wrachtrup. Nanoscale nuclear magnetic resonance with chemical resolution. *Science*, 357(July):67–71, 2017. ISSN 1095-9203. doi: 10.1126/science.aam8697. URL http://science.sciencemag.org/content/early/2017/05/31/science.aam8697%5Cninternal-pdf://0.0.17.168/tab-pdf.html.

[89] Yuen Yung Hui, Chia-Liang Cheng, and Huan-Cheng Chang. Nanodiamonds for optical bioimaging. *Journal of Physics D: Applied Physics*, 43(37): 374021, 9 2010. ISSN 0022-3727. doi: 10.1088/0022-3727/43/37/374021. URL http://www.scopus.com/inward/record.url?eid=2-s2.0-78249244758&partnerID=tZOtx3y1http://stacks.iop.org/0022-3727/43/i=37/a=374021http://apps.webofknowledge.com/full_record.do?product=WOS&search_mode=CombineSearches&qid=24&SID=X2WjzM5ryRnKucMQdbY&page=7&.

[90] V. Paget, J. A. Sergent, R. Grall, S. Altmeyer-Morel, H. A. Girard, T. Petit, C. Gesset, M. Mermoux, P. Bergonzo, J. C. Arnault, and S. Chevillard. Carboxylated nanodiamonds are neither cytotoxic nor genotoxic on liver, kidney, intestine and lung human cell lines. *Nanotoxicology*, 8(1):46–56, 2014. ISSN 1743-5390. doi: 10.3109/17435390.2013.855828. URL http://www.tandfonline.com/doi/abs/10.3109/17435390.2013.855828?journalCode=inan20.

[91] Amanda M Schrand, Houjin Huang, Cataleya Carlson, John J Schlager, Eiji Omacr Sawa, Saber M Hussain, and Liming Dai. Are diamond nanoparticles cytotoxic? *Journal of Physical Chemistry B*, 111(1):2–7, 1 2007. ISSN 1520-6106. doi: 10.1021/jp066387v. URL http://www.ncbi.nlm.nih.gov/pubmed/17201422.

[92] Dae Gon Lim, Ki Hyun Kim, and Si Kwon Sung. Comprehensive evaluation of carboxylated nanodiamond as a topical drug delivery system. *International Journal of Nanomedicine*, 11:2381–2395, 2016. URL https://www.dovepress.com/comprehensive-evaluation-of-carboxylated-nanodiamond-as-a-topical-drug-peer-reviewed-article-IJN.

[93] Masanori Horie, Lilian Kaede Komaba, Haruhisa Kato, Ayako Nakamura, Kazuhiro Yamamoto, Shigehisa Endoh, Katsuhide Fujita, Shinichi Kinugasa, Kohei Mizuno, Yoshihisa Hagihara, Yasukazu Yoshida, and Hitoshi Iwahashi. Evaluation of cellular influences induced by stable nanodiamond dispersion; The cellular influences of nanodiamond are small. *Diamond and Related Materials*, 24:15–24, 2012. ISSN 09259635. doi: 10.1016/j.diamond.2012.01.037. URL http://dx.doi.org/10.1016/j.diamond.2012.01.037.

[94] Yuan Yuan, Xiang Wang, Guang Jia, Jia Hui Liu, Tiancheng Wang, Yiqun Gu, Sheng Tao Yang, Sen Zhen, Haifang Wang, and Yuanfang Liu. Pulmonary toxicity and translocation of nanodiamonds in mice. *Diamond and Related Materials*, 19(4):291–299, 2010. ISSN 09259635. doi: 10.1016/j.diamond.2009.11.022. URL http://dx.doi.org/10.1016/j.diamond.2009.11.022.

[95] Laura Moore, Junyu Yang, Thanh T Ha Lan, Eiji Osawa, Dong Keun Lee, William D. Johnson, Jianzhong Xi, Edward Kai Hua Chow, and Dean Ho. Biocompatibility Assessment of Detonation Nanodiamond in Non-Human Primates and Rats Using Histological, Hematologic, and Urine Analysis. *ACS Nano*, 10(8):7385–7400, 2016. ISSN 1936086X. doi: 10.1021/acsnano.6b00839.

[96] A.P. Puzyr, A.V. Baron, K.V. Purtov, E.V. Bortnikov, N.N. Skobelev, O.A. Mogilnaya, and V.S. Bondar. Nanodiamonds with novel properties: A biological study. *Diamond and Related Materials*, 16(12):2124–2128, 12 2007. ISSN 09259635. doi: 10.1016/j.diamond.2007.07.025. URL http://linkinghub.elsevier.com/retrieve/pii/S0925963507003160http://www.sciencedirect.com/science/article/pii/S0925963507003160.

[97] Xiaoyong Zhang, Jilei Yin, Cheng Kang, Jing Li, Ying Zhu, Wenxin Li, Qing Huang, and Zhiyong Zhu. Biodistribution and toxicity of nanodiamonds in mice after intratracheal instillation. *Toxicology letters*, 198(2):237–43, 10 2010. ISSN 1879-3169. doi: 10.1016/j.toxlet.2010.07.001. URL http://www.sciencedirect.com/science/article/pii/S0378427410015833.

[98] Yuan Yuan, Yuanwei Chen, Jia-Hui Liu, Haifang Wang, and Yuanfang Liu. Biodistribution and fate of nanodiamonds in vivo. *Diamond and Related Materials*, 18 (1):95–100, 1 2009. ISSN 09259635. doi: 10.1016/j.diamond.2008.10.031. URL http://www.sciencedirect.com/science/article/pii/S0925963508005153.

[99] T. Burleson, N. Yusuf, and A. Stanishevsky. Surface modification of nanodiamonds for biomedical application and analysis by infrared spectroscopy. *Journal of Achievements in Materials and Manufacturing Engineering*, 37(2):258–263, 2009. URL http://ww.journalamme.org/papers_vol37_2/3725.pdf.

[100] Lionel Marcon, Franck Riquet, Dorothée Vicogne, Sabine Szunerits, Jean-François Bodart, and Rabah Boukherroub. Cellular and in vivo toxicity of functionalized nanodiamond in Xenopus embryos. *Journal of Materials Chemistry*, 20(37):8064, 9 2010. ISSN 0959-9428. doi: 10.1039/c0jm01570a. URL http://apps.webofknowledge.com/full_record.do?product=UA&search_mode=GeneralSearch&qid=2&SID=W2gpbMyx3kAm8dnJujq&page=1&doc=20http://pubs.rsc.org/en/content/articlehtml/2010/jm/c0jm01570ahttp://xlink.rsc.org/?DOI=c0jm01570a.

[101] V Vaijayanthimala, Po-Yun Cheng, Shih-Hua Yeh, Kuang-Kai Liu, Cheng-Hsiang Hsiao, Jui-I Chao, and Huan-Cheng Chang. The long-term stability and biocompatibility of fluorescent nanodiamond as an in vivo contrast agent. *Biomaterials*, 33(31): 7794–802, 11 2012. ISSN 1878-5905. doi: 10.1016/j.biomaterials.2012.06.084. URL http://www.ncbi.nlm.nih.gov/pubmed/22863379.

[102] D. MacLaurin, L. T. Hall, A. M. Martin, and L. C L Hollenberg. Nanoscale magnetometry through quantum control of nitrogen-vacancy centres in rotationally diffusing nanodiamonds. *New Journal of Physics*, 15, 2013. ISSN 13672630. doi: 10.1088/1367-2630/15/1/013041.

[103] Pei-Chang Tsai, Oliver Y Chen, Yan-Kai Tzeng, Yuen Yung Hui, Jiun You Guo, Chih-Che Wu, Ming-Shien Chang, and Huan-Cheng Chang. Gold/diamond nanohybrids for quantum sensing applications. *EPJ Quantum Technology*, 2(1): 19, 2015. ISSN 2196-0763. doi: 10.1140/epjqt/s40507-015-0031-3. URL http://www.epjquantumtechnology.com/content/2/1/19.

[104] Pei Chang Tsai, Chandra P. Epperla, Jo Shan Huang, Oliver Y. Chen, Chih Che Wu, and Huan Cheng Chang. Measuring Nanoscale Thermostability of Cell Membranes with Single Gold-Diamond Nanohybrids. *Angewandte Chemie - International Edition*, 56(11):3025–3030, 2017. ISSN 15213773. doi: 10.1002/anie.201700357.

[105] David A. Simpson, Emma Morrisroe, Julia M. McCoey, Alain H. Lombard, Dulini C. Mendis, François Treussart, Liam T. Hall, Steven Petrou, and Lloyd C.L. Hollenberg. Non-Neurotoxic Nanodiamond Probes for Intraneuronal Temperature Mapping. *ACS Nano*, 11(12):12077–12086, 2017. ISSN 1936086X. doi: 10.1021/acsnano.7b04850.

[106] David R Glenn, Kyungheon Lee, Hongkun Park, Ralph Weissleder, Amir Yacoby, Mikhail D Lukin, Hakho Lee, Ronald L Walsworth, and Colin B Connolly. Single-cell magnetic imaging using a quantum diamond microscope. *Nature Methods*, 12(May): 1–5, 2015. ISSN 1548-7091. doi: 10.1038/nmeth.3449. URL http://www.nature.com/doifinder/10.1038/nmeth.3449.

[107] John F. Barry, Matthew J. Turner, Jennifer M. Schloss, David R. Glenn, Yuyu Song, Mikhail D. Lukin, Hongkun Park, and Ronald L. Walsworth. Optical magnetic detection of single-neuron action potentials using quantum defects in diamond. *Proceedings of the National Academy of Sciences*, 113(49):14133–14138, 11 2016. ISSN 0027-8424. doi: 10.1073/pnas.1601513113. URL http://arxiv.org/abs/1602.01056http://www.pnas.org/content/113/49/14133.abstract.

[108] Victor S Perunicic, C D Hill, L T Hall, and L C L Hollenberg. A quantum spin-probe molecular microscope. *Nature communications*, 7:12667, 10 2016. ISSN 2041-1723. doi: 10.1038/ncomms12667. URL https://www.nature.com/articles/ncomms12667.

[109] Fazhan Shi, Qi Zhang, Pengfei Wang, Hongbin Sun, Junfeng Jiarong Wang, Xing Rong, Ming Chen, Chenyong Ju, Friedemann Reinhard, Junfeng Jiarong Wang, and Jiangfeng Du. Single-protein spin resonance spectroscopy under ambient conditions. *Science Research Reports*, 347(6226):1135–1138, 2015. ISSN 0036-8075, 1095-9203. doi: 10.1126/science.aaa2253. URL http://science.sciencemag.org/content/347/6226/1135.full.pdf+html.

[110] T Häberle, D Schmid-Lorch, F Reinhard, and J Wrachtrup. Nanoscale nuclear magnetic imaging with chemical contrast. *Nature nanotechnology*, 10(2):125–8, 2015. ISSN 1748-3395. doi: 10.1038/nnano.2014.299. URL http://www.ncbi.nlm.nih.gov/pubmed/25559711.

[111] Hunter C. Davis, Pradeep Ramesh, Aadyot Bhatnagar, Audrey Lee-Gosselin, John F. Barry, David R. Glenn, Ronald L. Walsworth, and Mikhail G. Shapiro. Mapping the Microscale Origins of MRI Contrast with Subcellular NV Diamond Magnetometry. *Nature Communications*, 9(131):1–9, 2018. ISSN 2041-1723. doi: 10.1038/s41467-017-02471-7. URL http://arxiv.org/abs/1610.01924.

[112] Tsai-Jung Wu, Yan-Kai Tzeng, Wei-Wei Chang, Chi-An Cheng, Yung Kuo, Chin-Hsiang Chien, Huan-Cheng Chang, and John Yu. Tracking the engraftment and regenerative capabilities of transplanted lung stem cells using fluorescent nanodiamonds. *Nature nanotechnology*, 8(9):682–689, 8 2013. ISSN 1748-3387. doi: 10.1038/nnano.2013.147. URL http://www.nature.com/doifinder/10.1038/nmeth.2666%5Cnhttp://www.ncbi.nlm.nih.gov/pubmed/24161977http://dx.doi.org/10.1038/nnano.2013.147http://www.ncbi.nlm.nih.gov/pubmed/23912062.

[113] Hsin Hung Lin, Hsiao Wen Lee, Ruey Jen Lin, Chih Wei Huang, Yi Chun Liao, Yit Tsong Chen, Jim Min Fang, Te Chang Lee, Alice L. Yu, and Huan Cheng Chang. Tracking and Finding Slow-Proliferating/Quiescent Cancer Stem Cells with Fluorescent Nanodiamonds. *Small*, 11(34):4394–4402, 2015. URL http://onlinelibrary.wiley.com/doi/10.1002/smll.201500878/abstract;jsessionid=370FE9DD50167A25138573095766DEC8.f03t02.

[114] Weixin Hou, Tan Boon Toh, Lissa Nurrul Abdullah, Tay Wei Zheng Yvonne, Kuan J. Lee, Ilonka Guenther, and Edward Kai Hua Chow. Nanodiamond–Manganese dual mode MRI contrast agents for enhanced liver tumor detection. *Nanomedicine: Nanotechnology, Biology, and Medicine*, 13(3):783–793, 2017. ISSN 15499642. doi: 10.1016/j.nano.2016.12.013. URL http://dx.doi.org/10.1016/j.nano.2016.12.013.

[115] Feng Jen Hsieh, Yen Wei Chen, Yao Kuan Huang, Hsien Ming Lee, Chun Hung Lin, and Huan Cheng Chang. Correlative Light-Electron Microscopy of Lipid-Encapsulated Fluorescent Nanodiamonds for Nanometric Localization of Cell Surface Antigens. *Analytical Chemistry*, 90(3):1566–1571, 2018. ISSN 15206882. doi: 10.1021/acs.analchem.7b04549.

[116] Michael P. Lake and Louis S. Bouchard. Targeted nanodiamonds for identification of subcellular protein assemblies in mammalian cells. *PLoS ONE*, 12(6):1–18, 2017. ISSN 19326203. doi: 10.1371/journal.pone.0179295.

[117] Shingo Sotoma, Ryuji Igarashi, Jun Iimura, Yuta Kumiya, Hidehito Tochio, Yoshie Harada, and Masahiro Shirakawa. Suppression of Nonspecific Protein-Nanodiamond Adsorption Enabling Specific Targeting of Nanodiamonds to Biomolecules of Interest. *Chemistry Letters*, 44(3):354–356, 2015. ISSN 0366-7022. doi: 10.1246/cl.141036. URL https://www.jstage.jst.go.jp/article/cl/44/3/44_141036/_article.

[118] Wenliang Liu, Fenglei Yu, Jianbo Yang, Bo Xiang, Peng Xiao, and Li Wang. 3D Single-Molecule Imaging of Transmembrane Signaling by Targeting Nanodiamonds.

Advanced Functional Materials, 26(3):365–375, 2016. ISSN 16163028. doi: 10.1002/adfm.201502883.

[119] Miu Shan Chan, Ling Sum Liu, Hoi Man Leung, and Pik Kwan Lo. Cancer-Cell-Specific Mitochondria-Targeted Drug Delivery by Dual-Ligand-Functionalized Nanodiamonds Circumvent Drug Resistance. *ACS Applied Materials and Interfaces*, 9 (13):11780–11789, 2017. ISSN 19448252. doi: 10.1021/acsami.6b15954.

[120] Han B. Man, Hansung Kim, Ho Joong Kim, Erik Robinson, Wing Kam Liu, Edward Kai Hua Chow, and Dean Ho. Synthesis of nanodiamond-daunorubicin conjugates to overcome multidrug chemoresistance in leukemia. *Nanomedicine: Nanotechnology, Biology, and Medicine*, 10(2):359–369, 2014. ISSN 15499634. doi: 10.1016/j.nano.2013.07.014. URL http://dx.doi.org/10.1016/j.nano.2013.07.014.

[121] Jing Li, Ying Zhu, Wenxin Li, Xiaoyong Zhang, Yan Peng, and Qing Huang. Nanodiamonds as intracellular transporters of chemotherapeutic drug. *Biomaterials*, 31(32): 8410–8, 11 2010. ISSN 1878-5905. doi: 10.1016/j.biomaterials.2010.07.058. URL http://www.sciencedirect.com/science/article/pii/S0142961210009014.

[122] Tae Kyung Ryu, Gyoung Ja Lee, Chang Kyu Rhee, and Sung Wook Choi. Cellular Uptake Behavior of Doxorubicin-Conjugated Nanodiamond Clusters for Efficient Cancer Therapy. *Macromolecular Bioscience*, 15(10):1469–1475, 2015. ISSN 16165195. doi: 10.1002/mabi.201500176.

[123] Robert Lam, Mark Chen, Erik Pierstorff, Houjin Huang, Eiji Osawa, and Dean Ho. Nanodiamond-Embedded Microfilm Devices for Localized Chemotherapeutic Elution. *ACS nano*, 2(10):2095–2102, 2008. doi: 10.1021/nn800465x.

[124] Zhiqin Chu, Kaikei Miu, Pingsai Lung, Silu Zhang, Saisai Zhao, Huan-Cheng Chang, Ge Lin, and Quan Li. Rapid endosomal escape of prickly nanodiamonds: implications for gene delivery. *Scientific reports*, 5:11661, 2015. ISSN 2045-2322. doi: 10.1038/srep11661. URL http://www.pubmedcentral.nih.gov/articlerender.fcgi?artid=4485068&tool=pmcentrez&rendertype=abstract.

[125] Amanda M. Schrand, Suzanne A. Ciftan Hens, and Olga A. Shenderova. Nanodiamond Particles: Properties and Perspectives for Bioapplications. *Critical Reviews in Solid State and Materials Sciences*, 34(1):18–74, 1 2009. ISSN 1040-8436. doi: 10.1080/10408430902831987. URL http://apps.webofknowledge.com/full_record.do?product=WOS&search_mode=CombineSearches&qid=24&SID=X2WjzM5ryRnKucMQdbY&page=9&doc=89.

[126] Ewen Smith and Geoffrey Dent. *Modern Raman Spectrocopy: A Practical Approach*, volume 5. John Wiley & Sons, Ltd, 2005. ISBN 9780471497943. doi: 10.1002/0470011831.

[127] Dustin W. Shipp, Faris Sinjab, and Ioan Notingher. Raman spectroscopy: techniques and applications in the life sciences. *Advances in Optics and Photonics*, 9(2):315, 2017. ISSN 1943-8206. doi: 10.1364/AOP.9.000315. URL https://www.osapublishing.org/abstract.cfm?URI=aop-9-2-315.

[128] Graeme Clemens, James R. Hands, Konrad M. Dorling, and Matthew J. Baker. Vibrational spectroscopic methods for cytology and cellular research. *The Analyst*, 139(18):4411–4444, 2014. ISSN 0003-2654. doi: 10.1039/C4AN00636D. URL http://xlink.rsc.org/?DOI=C4AN00636D.

[129] N. Uzunbajakava, A. Lenferink, Y. Kraan, B. Willekens, G. Vrensen, J. Greve, and C. Otto. Nonresonant Raman imaging of protein distribution in single human cells. *Biopolymers - Biospectroscopy Section*, 72(1):1–9, 2003. ISSN 00063525. doi: 10.1002/bip.10246. URL https://onlinelibrary.wiley.com/doi/abs/10.1002/bip.10246.

[130] N. Uzunbajakava, A. Lenferink, Y. Kraan, E. Volokhina, G. Vrensen, J. Greve, and C. Otto. Nonresonant confocal Raman imaging of DNA and protein distribution in apoptotic cells. *Biophysical Journal*, 84(6):3968–3981, 2003. ISSN 00063495. doi: 10.1016/S0006-3495(03)75124-8. URL http://dx.doi.org/10.1016/S0006-3495(03)75124-8.

[131] Christoph Krafft, Thomas Knetschke, Richard H W Funk, and Reiner Salzer. Identification of organelles and vesicles in single cells by Raman microspectroscopic mapping. *Vibrational Spectroscopy*, 38(1-2):85–93, 2005. ISSN 09242031. doi: 10.1016/j.vibspec.2005.02.008.

[132] Christian Matthäus, Tatyana Chernenko, Judith a Newmark, Carol M Warner, and Max Diem. Label-free detection of mitochondrial distribution in cells by nonresonant Raman microspectroscopy. *Biophysical journal*, 93(2):668–673, 2007. ISSN 00063495. doi: 10.1529/biophysj.106.102061. URL https://www.sciencedirect.com/science/article/pii/S0006349507713188?via%3Dihub.

[133] Keisaku Hamada, Katsumasa Fujita, Nicholas Isaac Smith, Minoru Kobayashi, Yasushi Inouye, and Satoshi Kawata. Raman microscopy for dynamic molecular imaging of living cells. *Journal of biomedical optics*, 13(4):044027, 1 2008. ISSN 1083-3668. doi: 10.1117/1.2952192. URL http://biomedicaloptics.spiedigitallibrary.org/article.aspx?doi=10.1117/1.2952192http://biomedicaloptics.spiedigitallibrary.org/article.aspx?articleid=1102744.

[134] A. R. Boyd, L. L. McManus, G. A. Burke, and B. J. Meenan. Raman spectroscopy of primary bovine aortic endothelial cells: A comparison of single cell and cell cluster analysis. *Journal of Materials Science: Materials in Medicine*, 22(8):1923–1930, 2011. ISSN 09574530. doi: 10.1007/s10856-011-4371-y.

[135] Alina Bogumila Zoladek, Ramneek Kaur Johal, Samuel Garcia-Nieto, Flavius Pascut, Kevin M. Shakesheff, Amir M. Ghaemmaghami, and Ioan Notingher. Label-free molecular imaging of immunological synapses between dendritic and T cells by Raman micro-spectroscopy. *The Analyst*, 135(12):3205, 12 2010. ISSN 0003-2654. doi: 10.1039/c0an00508h. URL http://xlink.rsc.org/?DOI=c0an00508hhttp://pubs.rsc.org/en/content/articlehtml/2010/an/c0an00508h.

[136] Claudia Scalfi-Happ, Martin Udart, Carmen Hauser, and Angelika Rück. Investigation of lipid bodies in a colon carcinoma cell line by confocal Raman microscopy. *Medical Laser Application*, 26(4):152–157, 2011. ISSN 16151615. doi: 10.1016/j.mla.2011.08.002. URL http://dx.doi.org/10.1016/j.mla.2011.08.002.

[137] H Abramczyk, J Surmacki, M Kopec, A K Olejnik, K Lubecka-Pietruszewska, and K Fabianowska-Majewska. The role of lipid droplets and adipocytes in cancer. Raman imaging of cell cultures: MCF10A, MCF7, and MDA-MB-231 compared to adipocytes in cancerous human breast tissue. *Analyst*, 140(7):2224–2235, 2015. ISSN 0003-2654. doi: 10.1039/c4an01875c. URL http://www.ncbi.nlm.nih.gov/pubmed/25730442%5Cnhttp://www.ncbi.nlm.nih.gov/entrez/query.fcgi?cmd=Retrieve&db=PubMed&dopt=Citation&list_uids=25730442.

[138] Andrew C. Terentis, Sara A. Fox, Samantha J. Friedman, and Emily S. Spencer. Confocal Raman microspectroscopy discriminates live human metastatic melanoma and skin fibroblast cells. *Journal of Raman Spectroscopy*, 44(9):1205–1216, 9 2013. ISSN 03770486. doi: 10.1002/jrs.4363. URL http://onlinelibrary.wiley.com/doi/10.1002/jrs.4363/abstract.

[139] Nadezda A. Brazhe, Marek Treiman, Alexey R. Brazhe, Ninett L. Find, Georgy V. Maksimov, and Olga V. Sosnovtseva. Mapping of Redox State of Mitochondrial Cytochromes in Live Cardiomyocytes Using Raman Microspectroscopy. *PLoS ONE*, 7(9):1–8, 2012. ISSN 19326203. doi: 10.1371/journal.pone.0041990.

[140] Mitsugu Ogawa, Yoshinori Harada, Yoshihisa Yamaoka, Katsumasa Fujita, Hitoshi Yaku, and Tetsuro Takamatsu. Label-free biochemical imaging of heart tissue with high-speed spontaneous Raman microscopy. *Biochemical and Biophysical Research Communications*, 382(2):370–374, 2009. ISSN 0006291X. doi: 10.1016/j.bbrc.2009.03.028. URL http://dx.doi.org/10.1016/j.bbrc.2009.03.028.

[141] Almar F. Palonpon, Mikiko Sodeoka, and Katsumasa Fujita. Molecular imaging of live cells by Raman microscopy. *Current Opinion in Chemical Biology*, 17(4):708–715, 2013. ISSN 13675931. doi: 10.1016/j.cbpa.2013.05.021. URL http://dx.doi.org/10.1016/j.cbpa.2013.05.021.

[142] Robin J. Swain, Sarah J. Kemp, Peter Goldstraw, Teresa D. Tetley, and Molly M. Stevens. Assessment of Cell Line Models of Primary Human Cells by Raman Spectral Phenotyping. *Biophysical Journal*, 98(8):1703–1711, 2010. ISSN 15420086. doi: 10.1016/j.bpj.2009.12.4289. URL http://dx.doi.org/10.1016/j.bpj.2009.12.4289.

[143] Ioan Notingher, Isabelle Bisson, Julia M. Polak, and Larry L. Hench. In situ spectroscopic study of nucleic acids in differentiating embryonic stem cells. *Vibrational Spectroscopy*, 35(1-2):199–203, 2004. ISSN 09242031. doi: 10.1016/j.vibspec.2004.01.014.

[144] Christian Matthäus, Susie Boydston-White, Milos Miljković, Melissa Romeo, and Max Diem. Raman and infrared microspectral imaging of mitotic cells. *Applied spectroscopy*, 60(1):1–8, 1 2006. ISSN 0003-7028. doi: 10.1366/000370206775382758. URL http://journals.sagepub.com/doi/abs/10.1366/000370206775382758?url_ver=Z39.88-2003&rfr_id=ori%3Arid%3Acrossref.org&rfr_dat=cr_pub%3Dpubmed&.

[145] Robin J. Swain, Gavin Jell, and Molly M. Stevens. Non-invasive analysis of cell cycle dynamics in single living cells with Raman micro-spectroscopy. *Journal of Cellular Biochemistry*, 104(4):1427–1438, 2008. ISSN 07302312. doi: 10.1002/jcb.21720.

[146] Quinn Matthews, Andrew Jirasek, Julian Lum, Xiaobo Duan, and Alexandre G Brolo. Variability in Raman Spectra of Single Human Tumor Cells Cultured in Vitro: Correlation with Cell Cycle and Culture Confluency. *Applied Spectroscopy*, 64(8):871–887, 2010. ISSN 1943-3530. doi: 10.1366/000370210792080966. URL http://journals.sagepub.com/doi/abs/10.1366/000370210792080966?url_ver=Z39.88-2003&rfr_id=ori:rid:crossref.org&rfr_dat=cr_pub%3Dpubmed.

[147] Flavius C. Pascut, Spandan Kalra, Vinoj George, Nathan Welch, Chris Denning, and Ioan Notingher. Non-invasive label free monitoring the cardiac differentiation of human embryonic stem cells in-vitro by Raman spectroscopy. *Biochimica et biophysica acta*, 1830(6):3517–24, 2013. ISSN 0006-3002. doi: 10.1016/j.bbagen.2013.01.030. URL http://www.ncbi.nlm.nih.gov/pubmed/23403134.

[148] Taro Ichimura, Liang Da Chiu, Katsumasa Fujita, Satoshi Kawata, Tomonobu M. Watanabe, Toshio Yanagida, and Hideaki Fujita. Visualizing cell state transition using raman spectroscopy. *PLoS ONE*, 9(1), 2014. ISSN 19326203. doi: 10.1371/journal.pone.0084478.

[149] Surekha Barkur, Aseefhali Bankapur, Madhura Pradhan, Santhosh Chidangil, Deepak Mathur, and Uma Ladiwala. Probing differentiation in cancer cell lines by single-cell micro-Raman spectroscopy. *Journal of Biomedical Optics*, 20(8):085001, 2015. ISSN 1083-3668. doi: 10.1117/1.JBO.20.8.085001. URL http://biomedicaloptics.spiedigitallibrary.org/article.aspx?doi=10.1117/1.JBO.20.8.085001.

[150] James W. Chan, Douglas S. Taylor, and Deanna L. Thompson. The effect of cell fixation on the discrimination of normal and leukemia cells with laser tweezers Raman spectroscopy. *Biopolymers*, 91(2):132–139, 2 2009. ISSN 00063525. doi: 10.1002/bip.21094. URL http://www.ncbi.nlm.nih.gov/pubmed/18825777.

[151] M. Isabelle, J. Dorney, A. Lewis, G. R. Lloyd, O. Old, N. Shepherd, M. Rodriguez-Justo, H. Barr, K. Lau, I. Bell, S. Ohrel, G. Thomas, N. Stone, and C. Kendall. Multi-centre Raman spectral mapping of oesophageal cancer tissues: A study to assess system transferability. *Faraday Discussions*, 187:87–103, 2016. ISSN 13645498. doi: 10.1039/c5fd00183h. URL http://pubs.rsc.org/en/Content/ArticleLanding/2016/FD/C5FD00183H#!divAbstract.

[152] I Notingher, S Verrier, S Haque, J M Polak, and L L Hench. Spectroscopic study of human lung epithelial cells (A549) in culture: living cells versus dead cells. *Biopolymers*, 72(4):230–40, 1 2003. ISSN 0006-3525. doi: 10.1002/bip.10378. URL http://www.ncbi.nlm.nih.gov/pubmed/12833477.

[153] Abhaya Dutta, Rekha Gautam, Sreejata Chatterjee, Freek Ariese, Sujit Kumar Sikdar, and Siva Umapathy. Ascorbate Protects Neurons against Oxidative Stress: A Raman Microspectroscopic Study. *ACS Chemical Neuroscience*, 6(11):1794–1801, 2015. ISSN 19487193. doi: 10.1021/acschemneuro.5b00106.

[154] S. Verrier, I. Notingher, J. M. Polak, and L. L. Hench. In Situ Monitoring of Cell Death Using Raman Microspectroscopy. *Biopolymers*, 74(1-2):157–162, 2004. ISSN 00063525. doi: 10.1002/bip.20063.

[155] Ioan Notingher, Jamuna Selvakumaran, and Larry L. Hench. New detection system for toxic agents based on continuous spectroscopic monitoring of living cells. *Biosensors and Bioelectronics*, 20(4):780–789, 2004. ISSN 09565663. doi: 10.1016/j.bios.2004.04.008.

[156] I Notingher, C Green, C Dyer, E Perkins, N Hopkins, C Lindsay, and L L Hench. Discrimination between ricin and sulphur mustard toxicity in vitro using Raman spectroscopy. *Journal of the Royal Society, Interface / the Royal Society*, 1(1):79–90, 11 2004. ISSN 1742-5689. doi: 10.1098/rsif.2004.0008. URL http://rsif.royalsocietypublishing.org/content/1/1/79.

[157] Silvia Caponi, Lavinia Liguori, Alessandra Giugliarelli, Maurizio Mattarelli, Assunta Morresi, Paola Sassi, Lorena Urbanelli, and Carlo Musio. Raman micro-spectroscopy: A powerful tool for the monitoring of dynamic supramolecular changes in living cells. *Biophysical Chemistry*, 182:58–63, 2013. ISSN 03014622. doi: 10.1016/j.bpc.2013.06.013.

[158] Stanislav O. Konorov, Mario A. Jardon, James M. Piret, Michael W. Blades, and Robin F. B. Turner. Raman microspectroscopy of live cells under autophagy-inducing conditions. *The Analyst*, 137(20):4662, 2012. ISSN 0003-2654. doi: 10.1039/c2an35477b. URL http://xlink.rsc.org/?DOI=c2an35477b.

[159] Yasuaki Naito, Akio Toh-e, and Hiro O. Hamaguchi. In vivo time-resolved Raman imaging of a spontaneous death process of a single budding yeast cell. *Journal of Raman Spectroscopy*, 36(9):837–839, 2005. ISSN 03770486. doi: 10.1002/jrs.1397.

[160] Vishnu Vardhan Pully and Cees Otto. The intensity of the 1602 cm-1 band in human cells is related to mitochondrial activity. *Journal of Raman Spectroscopy*, 40(5):473–475, 2009. ISSN 03770486. doi: 10.1002/jrs.2269.

[161] Jie Yang, Xuesong Liu, Kapil Bhalla, Caryn Naekyung Kim, Ana Maria Ibrado, Jiyang Cai, Tsung-i Peng, Dean P Jones, and Xiaodong Wang. Prevention of Apoptosis by Bcl-2 : Release of Cytochrome c from Mitochondria Blocked Prevention of Apoptosis by Bcl-2 : Release of Cytochrome c from Mitochondria Blocked. *Science*, 1129(1997), 2006. doi: 10.1126/science.275.5303.1129.

[162] R. M. Kluck. The Release of Cytochrome c from Mitochondria: A Primary Site for Bcl-2 Regulation of Apoptosis. *Science*, 275(5303):1132–1136, 1997. ISSN 00368075. doi: 10.1126/science.275.5303.1132. URL http://www.sciencemag.org/cgi/doi/10.1126/science.275.5303.1132.

[163] M Okada and NI Smith. Label-free Raman observation of cytochrome c dynamics during apoptosis. *Proceedings of the National Academy of Sciences*, 109(1):28–32, 2012.

[164] Almar F Palonpon, Jun Ando, Hiroyuki Yamakoshi, Kosuke Dodo, Mikiko Sodeoka, Satoshi Kawata, and Katsumasa Fujita. Raman and SERS microscopy for molecular imaging of live cells. *Nature protocols*, 8(4):677–92, 2013. ISSN 1750-2799. doi: 10.1038/nprot.2013.030. URL http://www.ncbi.nlm.nih.gov/pubmed/23471112.

[165] N Yadav, A Pliss, A Kuzmin, P Rapali, L Sun, P Prasad, and D Chandra. Transformations of the macromolecular landscape at mitochondria during DNA-damage-induced apoptotic cell death. *Cell Death and Disease*, 5(10):1453–12, 1 2014. ISSN 2041-4889. doi: 10.1038/cddis.2014.405. URL http://dx.doi.org/10.1038/cddis.2014.405.

[166] G. J. Puppels, J H Olminkhof, G M Segers-Nolten, C Otto, F F de Mul, and J Greve. Laser irradiation and Raman spectroscopy of single living cells and chromosomes: Sample degradation occurs with 514.5 nm but not with 660 nm laser light. *Experimental Cell Research*, 195(2):361–367, 8 1991. ISSN 00144827. doi: 10.1016/0014-4827(91)90385-8. URL http://www.ncbi.nlm.nih.gov/pubmed/2070819http://www.sciencedirect.com/science/article/pii/0014482791903858.

[167] Victoria Sánchez, Klaus Redmann, Joachim Wistuba, Frank Wübbeling, Martin Burger, Harriette Oldenhof, Willem F. Wolkers, Sabine Kliesch, Stefan Schlatt, and Con Mallidis. Oxidative DNA damage in human sperm can be detected by Raman microspectroscopy. *Fertility and Sterility*, 98(5), 2012. ISSN 00150282. doi: 10.1016/j.fertnstert.2012.07.1059.

[168] Abdullah Chandra Sekhar Talari, Ahtasham Raza, Shazza Rehman, and Ihtesham U Rehman. Analyzing normal proliferating, hypoxic and necrotic regions of T-47D human breast cancer spheroids using Raman spectroscopy. *Applied Spectroscopy Reviews*, 52(10):909–924, 11 2017. ISSN 0570-4928. doi: 10.1080/05704928.2017.1363053. URL https://www.tandfonline.com/doi/full/10.1080/05704928.2017.1363053.

[169] Fran Adar and Maria Erecinska. Spectral evidence for interactions between membrane-bound hemes. *FEBS Letters*, 80(1):195–200, 1977.

[170] Minoru Kakita, Masanari Okuno, and Hiro O. Hamaguchi. Quantitative analysis of the redox states of cytochromes in a living L929 (NCTC) cell by resonance Raman microspectroscopy. *Journal of Biophotonics*, 6(3):256–259, 2013. ISSN 1864063X. doi: 10.1002/jbio.201200042.

[171] Masaharu Akao, Brian O'Rourke, Yasushi Teshima, Jegatheesan Seharaseyon, and Eduardo Marbán. Mechanistically distinct steps in the mitochondrial death pathway triggered by oxidative stress in cardiac myocytes. *Circulation Research*, 92(2):186–194, 2003. ISSN 00097330. doi: 10.1161/01.RES.0000051861.21316.E9.

[172] A. Almohammedi, S. M. Kapetanaki, B. R. Wood, E. L. Raven, N. M. Storey, and A. J. Hudson. Spectroscopic analysis of myoglobin and cytochrome c dynamics in isolated cardiomyocytes during hypoxia and reoxygenation. *Journal of The Royal Society Interface*, 12(105):20141339–20141339, 2015. ISSN 1742-5689. doi: 10.1098/rsif.2014.1339. URL http://rsif.royalsocietypublishing.org/cgi/doi/10.1098/rsif.2014.1339.

[173] Philippe Pasdois, Joanne E. Parker, Elinor J. Griffiths, and Andrew P. Halestrap. The role of oxidized cytochrome c in regulating mitochondrial reactive oxygen species production and its perturbation in ischaemia. *Biochemical Journal*, 436(2):493–505, 2011. ISSN 0264-6021. doi: 10.1042/BJ20101957. URL http://biochemj.org/lookup/doi/10.1042/BJ20101957.

[174] Konstantin A. Okotrub and Nikolay V. Surovtsev. Photobleaching of the resonance Raman lines of cytochromes in living yeast cells. *Journal of Photochemistry and Photobiology B: Biology*, 141:269–274, 2014. ISSN 18732682. doi: 10.1016/j.jphotobiol.2014.10.008. URL http://dx.doi.org/10.1016/j.jphotobiol.2014.10.008.

[175] Xiaofei Yuan, Yizhi Yanqing Song, Yizhi Yanqing Song, Jiabao Xu, Yinhu Wu, Andrew Glidle, Maggie Cusack, Umer Z Ijaz, Jonathan M Cooper, Wei E Huang, and Huabing Yin. Effect of laser irradiation on cell function and its implications in Raman spectroscopy. *Applied and environmental microbiology*, 84(8):1–12, 4 2018. ISSN 1098-5336. doi: 10.1128/AEM.02508-17. URL http://www.ncbi.nlm.nih.gov/pubmed/29427427.

[176] Vitaly I. Korepanov, Hiro o. Hamaguchi, Eiji Osawa, Vladimir Ermolenkov, Igor K. Lednev, Bastian J.M. Etzold, Olga Levinson, Boris Zousman, Chandra Prakash Epperla, and Huan Cheng Chang. Carbon structure in nanodiamonds elucidated from Raman spectroscopy. *Carbon*, 121:322–329, 2017. ISSN 00086223. doi: 10.1016/j.carbon.2017.06.012. URL http://dx.doi.org/10.1016/j.carbon.2017.06.012.

[177] Gerwin Jan Puppels, F F de Mul, Cees Otto, J Greve, M Robert-Nicoud, D J Arndt-Jovin, and T M Jovin. Studying single living cells and chromosomes by confocal Raman microspectroscopy. *Nature*, 347(6290):301–303, 9 1990. ISSN 0028-0836. doi: 10.1038/347301a0. URL http://dx.doi.org/10.1038/347301a0.

[178] Jianwei Qin, Moon S. Kim, Walter F. Schmidt, Byoung Kwan Cho, Yankun Peng, and Kuanglin Chao. A line-scan hyperspectral Raman system for spatially offset Raman spectroscopy. *Journal of Raman Spectroscopy*, 47(4):437–443, 2016. ISSN 10974555. doi: 10.1002/jrs.4825.

[179] Sarah E Bohndiek, Ashwin Wagadarikar, Cristina L Zavaleta, Dominique Van de Sompel, Ellis Garai, Jesse V Jokerst, Siavash Yazdanfar, and Sanjiv S Gambhir. A small animal Raman instrument for rapid, wide-area, spectroscopic imaging. *Proceedings of the National Academy of Sciences of the United States of America*, 110:12408–13, 2013. ISSN 1091-6490. doi: 10.1073/pnas.1301379110. URL http://www.pubmedcentral.nih.gov/articlerender.fcgi?artid=3725059&tool=pmcentrez&rendertype=abstract.

[180] Adrian Ghita, Pavel Matousek, and Nick Stone. High sensitivity non-invasive detection of calcifications deep inside biological tissue using Transmission Raman Spectroscopy. *Journal of Biophotonics*, 8:1–9, 2017. ISSN 18640648. doi: 10.1002/jbio.201600260.

[181] Perry Edwards, Chenji Zhang, Baigang Zhang, Xiangqian Hong, Vivek K. Nagarajan, Bing Yu, and Zhiwen Liu. Smartphone based optical spectrometer for diffusive reflectance spectroscopic measurement of hemoglobin. *Scientific Reports*, 7(1):1–7, 2017. ISSN 20452322. doi: 10.1038/s41598-017-12482-5. URL http://dx.doi.org/10.1038/s41598-017-12482-5.

[182] J. Jehlička, P. Vítek, H. G M Edwards, M. Heagraves, and T. Čapoun. Application of portable Raman instruments for fast and non-destructive detection of minerals on outcrops. *Spectrochimica Acta - Part A: Molecular and Biomolecular Spectroscopy*, 73(3):410–419, 2009. ISSN 13861425. doi: 10.1016/j.saa.2008.09.004.

[183] Anastasia Rousaki, Cristina Vázquez, Verónica Aldazábal, Cristina Bellelli, Mariana Carballido Calatayud, Adam Hajduk, Emmanuel Vargas, Oscar Palacios, Peter Vandenabeele, and Luc Moens. The first use of portable Raman instrumentation for the in situ study of prehistoric rock paintings in Patagonian sites. *Journal of Raman Spectroscopy*, 48(11):1459–1467, 2017. ISSN 10974555. doi: 10.1002/jrs.5107.

[184] Scott D Bergeson, Justin B Peatross, N Jay Eyring, John F Fralick, Douglas N Stevenson, and Scott B Ferguson. Resonance Raman measurements of carotenoids using light-emitting diodes. *Journal of biomedical optics*, 13(4):044026, 2007. ISSN 10833668. doi: 10.1117/1.2952075.

[185] Samy Andrea Strola, Jean-Charles Baritaux, Emmanuelle Schultz, Anne Catherine Simon, Cédric Allier, Isabelle Espagnon, Dorothée Jary, and Jean-Marc Dinten. Single bacteria identification by Raman spectroscopy. *Journal of Biomedical Optics*, 19(11):111610, 2014. ISSN 1083-3668. doi: 10.1117/1.JBO.19.11.111610. URL http://biomedicaloptics.spiedigitallibrary.org/article.aspx?doi=10.1117/1.JBO.19.11.111610.

[186] Clare E. Harvey, Evelien M. van Schrojenstein Lantman, Arjan J. G. Mank, and Bert M. Weckhuysen. An integrated AFM-Raman instrument for studying heterogeneous catalytic systems: a first showcase. *Chemical Communications*, 48(12):1742, 2012. ISSN 1359-7345. doi: 10.1039/c2cc15939b. URL http://xlink.rsc.org/?DOI=c2cc15939b.

[187] V.N. Lednev, S.M. Pershin, P.A. Sdvizhenskii, M.Y. Grishin, A.N. Fedorov, V.V. Bukin, V.B. Oshurko, and A.N. Shchegolikhin. Combining Raman and laser induced breakdown spectroscopy by double pulse lasing. *Analytical and Bioanalytical Chemistry*, pages 277–286, 2017. ISSN 16182650. doi: 10.1007/s00216-017-0719-6.

[188] Ute Neugebauer, Stefan H. Heinemann, Michael Schmitt, and Jürgen Popp. Combination of patch clamp and raman spectroscopy for single-cell analysis. *Analytical Chemistry*, 83(1):344–350, 2011. ISSN 00032700. doi: 10.1021/ac1024667.

[189] Kokila D Egodage, Sebastian Dochow, Thomas W Bocklitz, Olga Chernavskaia, Christian Matthäus, Michael Schmitt, and Juergen Popp. The combination of optical coherence tomography and Raman spectroscopy for tissue characterization. *Journal of Biomedical Photonics & Engineering*, 1(2):169–177, 2015. URL http://jbpe.ssau.ru/index.php/JBPE/article/view/2503/2632.

[190] Walter Müller, Martin Kielhorn, Michael Schmitt, Jürgen Popp, and Rainer Heintzmann. Light sheet Raman micro-spectroscopy. *Optica*, 3(4):452, 2016. ISSN 2334-2536. doi: 10.1364/OPTICA.3.000452. URL https://www.osapublishing.org/abstract.cfm?URI=optica-3-4-452.

[191] I. V. Zhukov, S. V. Anishchik, and Yu N. Molin. ODMR Spectroscopy of NV Centers in Diamond Under High MW Power. *Applied Magnetic Resonance*, 48(11-12):1461–1469, 2017. ISSN 09379347. doi: 10.1007/s00723-017-0933-6.

[192] Zhen Yu Wang, Jian Ming Cai, Alex Retzker, and Martin B. Plenio. All-optical magnetic resonance of high spectral resolution using a nitrogen-vacancy spin in diamond. *New Journal of Physics*, 16, 2014. ISSN 13672630. doi: 10.1088/1367-2630/16/8/083033.

[193] Yan-Kai Kai Tzeng, Orestis Faklaris, Be-Ming Ming Chang, Yung Kuo, Jui-Hung Hung Hsu, and Huan-Cheng Cheng Chang. Superresolution imaging of albumin-conjugated fluorescent nanodiamonds in cells by stimulated emission depletion. *Angewandte Chemie - International Edition*, 50(10):2262–2265, 3 2011. ISSN 14337851. doi: 10.1002/anie.201007215. URL http://www.ncbi.nlm.nih.gov/pubmed/21351332http://onlinelibrary.wiley.com/doi/10.1002/anie.201007215/abstract;jsessionid=441555781890CF70A41377557891754B.f02t01.

[194] S M B Lakley, A B F Edotov, J B Ecker, N A Ltangerel, I V F Edotov, P H Emmer, M O S Cully, and A M Z Heltikov. Stimulated fluorescence quenching in nitrogen – vacancy centers of diamond : temperature effects. *Optics Letters*, 41(9):2077–2080, 2016. doi: 10.1364/ol.41.002077. URL https://www.osapublishing.org/ol/abstract.cfm?uri=ol-41-9-2077.

[195] Eva Rittweger, Kyu Young Han, Scott E. Irvine, Christian Eggeling, and Stefan W. Hell. STED microscopy reveals crystal colour centres with nanometric resolution. *Nature Photonics*, 3(3):144–147, 2 2009. ISSN 1749-4885. doi: 10.1038/nphoton.2009.2. URL http://www.scopus.com/inward/record.url?eid=2-s2.0-61449201752&partnerID=tZOtx3y1.

[196] Shen Li, Xiang-dong Chen, Bo-Wen Zhao, Yang Dong, Chong-Wen Zou, Guang-Can Guo, and Fang-Wen Sun. Optical far-field super-resolution microscopy using nitrogen vacancy center ensemble in bulk diamond. *Applied Physics Letters*, pages 2–6, 2016. URL http://arxiv.org/abs/1609.01827.

[197] Jacopo Forneris, Laura Guarina, Federico Picollo, Paolo Olivero, Marco Genovese, Ekaterina Moreva, Paolo Traina, Sviatoslav Ditalia Tchernij, Claudio Franchino, Ivano Ruo Berchera, Giorgio Brida, Ivo P. Degiovanni, and Valentina Carabelli. Super-resolution from single photon emission: toward biological application. *Quantum Photonic Devices*, 10358 (August 2017):1, 2017. ISSN 1996756X. doi: 10.1117/12.2275040. URL https://www.spiedigitallibrary.org/conference-proceedings-of-spie/10358/2275040/Super-resolution-from-single-photon-emission-toward-biological-application/10.1117/12.2275040.full.

[198] Kiho Kim, Jiwon Yun, Donghyuck Lee, and Dohun Kim. An efficient fluorescent single-particle position tracking system for long-term pulsed measurements of nitrogen-vacancy centers in diamond. *Review of Scientific Instruments*, 89(2):1–6, 2018. ISSN 10897623. doi: 10.1063/1.5003707. URL https://doi.org/10.1063/1.5003707.

[199] D. R. Glenn, R. R. Fu, P. Kehayias, D. Le Sage, E. A. Lima, B. P. Weiss, and R. L. Walsworth. Micrometer-scale magnetic imaging of geological samples using a quantum diamond microscope. *Geochemistry, Geophysics, Geosystems*, 18(8):3254–3267, 2017. ISSN 15252027. doi: 10.1002/2017GC006946. URL https://arxiv.org/ftp/arxiv/papers/1707/1707.06714.pdf.

[200] Gopalakrishnan Balasubramanian, Andrii Lazariev, Sri Ranjini Arumugam, and De-Wen Duan. Nitrogen-Vacancy color center in diamond-emerging nanoscale applications in bioimaging and biosensing. *Current opinion in chemical biology*,

20(1):69–77, 6 2014. ISSN 1879-0402. doi: 10.1016/j.cbpa.2014.04.014. URL http://www.sciencedirect.com/science/article/pii/S1367593114000593http://www.scopus.com/inward/record.url?eid=2-s2.0-84901392265&partnerID=tZOtx3y1.

[201] Thomas Häberle, Thomas Oeckinghaus, Dominik Schmid-Lorch, Matthias Pfender, Felipe Fávaro de Oliveira, Seyed Ali Momenzadeh, Amit Finkler, and Jörg Wrachtrup. Nuclear quantum-assisted magnetometer. *Review of Scientific Instruments*, 88(1): 013702, 1 2017. ISSN 0034-6748. doi: 10.1063/1.4973449. URL http://aip.scitation.org/doi/10.1063/1.4973449.

[202] Patrick Appel, Marc Ganzhorn, Elke Neu, and Patrick Maletinsky. Nanoscale microwave imaging with a single electron spin in diamond. *New Journal of Physics*, 17 (11):112001, 2015. ISSN 13672630. doi: 10.1088/1367-2630/17/11/112001. URL http://dx.doi.org/10.1088/1367-2630/17/11/112001.

[203] L. Thiel, D. Rohner, M. Ganzhorn, P. Appel, E. Neu, B. Müller, R. Kleiner, D. Koelle, and P. Maletinsky. Quantitative nanoscale vortex imaging using a cryogenic quantum magnetometer. *Nature Nanotechnology*, 11(8):677–681, 2016. ISSN 17483395. doi: 10.1038/nnano.2016.63. URL http://dx.doi.org/10.1038/nnano.2016.63.

[204] Matthew Pelliccione, Alec Jenkins, Preeti Ovartchaiyapong, Christopher Reetz, Eve Emmanouilidou, Ni Ni, and Ania C. Bleszynski Jayich. Scanned probe imaging of nanoscale magnetism at cryogenic temperatures with a single-spin quantum sensor. *Nature Nanotechnology*, 11(8):700–705, 2016. ISSN 17483395. doi: 10.1038/nnano.2016.68.

[205] P. Maletinsky, S. Hong, M. S. Grinolds, B. Hausmann, M. D. Lukin, R. L. Walsworth, M. Loncar, and A. Yacoby. A robust scanning diamond sensor for nanoscale imaging with single nitrogen-vacancy centres. *Nature Nanotechnology*, 7(5):320–324, 2012. ISSN 17483395. doi: 10.1038/nnano.2012.50. URL http://dx.doi.org/10.1038/nnano.2012.50.

[206] M. S. Grinolds, S. Hong, P. Maletinsky, L. Luan, M. D. Lukin, R. L. Walsworth, and A. Yacoby. Nanoscale magnetic imaging of a single electron spin under ambient conditions. *Nature Physics*, 9(4):215–219, 2013. ISSN 17452473. doi: 10.1038/nphys2543. URL http://dx.doi.org/10.1038/nphys2543.

[207] Tony X. Zhou, Rainer J. Stöhr, and Amir Yacoby. Scanning diamond NV center probes compatible with conventional AFM technology. *Applied Physics Letters*, 111 (16):1–5, 2017. ISSN 00036951. doi: 10.1063/1.4995813.

[208] Weina Liu, Boris Naydenov, Sabyasachi Chakrabortty, Bettina Wuensch, Kristina Hübner, Sandra Ritz, Helmut Cölfen, Holger Barth, Kaloian Koynov, Haoyuan Qi, Robert Leiter, Rolf Reuter, Jörg Wrachtrup, Felix Boldt, Jonas Scheuer, Ute Kaiser, Miguel Sison, Theo Lasser, Philip Tinnefeld, Fedor Jelezko, Paul Walther, Yuzhou Wu, and Tanja Weil. Fluorescent Nanodiamond–Gold Hybrid Particles for Multimodal Optical and Electron Microscopy Cellular Imaging. *Nano Letters*, page acs.nanolett.6b02456, 2016. ISSN 1530-6984. doi: 10.1021/acs.nanolett.6b02456. URL http://pubs.acs.org/doi/abs/10.1021/acs.nanolett.6b02456.

[209] Mark a Zurbuchen, Michael P Lake, Sirus a Kohan, Belinda Leung, and Louis-S Bouchard. Nanodiamond landmarks for subcellular multimodal optical and electron imaging. *Scientific reports*, 3:2668, 1 2013. ISSN 2045-2322. doi: 10.1038/srep02668. URL http://www.nature.com/srep/2013/130916/srep02668/full/srep02668.htmlhttp://www.pubmedcentral.nih.gov/articlerender.fcgi?artid=3773618&tool=pmcentrez&rendertype=abstract.

[210] P. a. Janmey and P. K J Kinnunen. Biophysical properties of lipids and dynamic membranes. *Trends in Cell Biology*, 16(10):538–546, 2006. ISSN 09628924. doi: 10.1016/j.tcb.2006.08.009.

[211] Neeraj Prabhakar, Tuomas Näreoja, Eva von Haartman, Didem Şen Karaman, Hua Jiang, Sami Koho, Tatiana a Dolenko, Pekka E Hänninen, Denis I Vlasov, Victor G Ralchenko, Satoru Hosomi, Igor I Vlasov, Cecilia Sahlgren, and Jessica M Rosenholm. Core-shell designs of photoluminescent nanodiamonds with porous silica coatings for bioimaging and drug delivery II: application. *Nanoscale*, 5(9):3713–22, 5 2013. ISSN 2040-3372. doi: 10.1039/c3nr33926b. URL http://www.ncbi.nlm.nih.gov/pubmed/23493921http://pubs.rsc.org/en/Content/ArticleHTML/2013/NR/C3NR33926B.

[212] Min Gu, Yaoyu Cao, Stefania Castelletto, Betty Kouskousis, and Xiangping Li. Super-resolving single nitrogen vacancy centers within single nanodiamonds using a localization microscope. *Optics express*, 21(15):17639–46, 7 2013. ISSN 1094-4087. doi: 10.1364/OE.21.017639. URL http://www.osapublishing.org/viewmedia.cfm?uri=oe-21-15-17639&seq=0&html=true.

[213] K. Beha, A. Batalov, N. B. Manson, R. Bratschitsch, and A. Leitenstorfer. Optimum photoluminescence excitation and recharging cycle of single nitrogen-vacancy centers in ultrapure diamond. *Physical Review Letters*, 109(9):1–5, 2012. ISSN 00319007. doi: 10.1103/PhysRevLett.109.097404.

[214] Gregory W. Faris and Richard A. Copeland. Wavelength dependence of the Raman cross section for liquid water. *Applied Optics*, 36(12):2686, 1997. ISSN 0003-6935. doi: 10.1364/AO.36.002686. URL https://www.osapublishing.org/abstract.cfm?URI=ao-36-12-2686.

[215] Dimitri Pappas, Benjamin W. Smith, and James D. Winefordner. Raman spectroscopy in bioanalysis. *Talanta*, 51(1):131–144, 2000. ISSN 00399140. doi: 10.1016/S0039-9140(99)00254-4.

[216] Sunuk Choe, Jungbae Yoon, Myeongwon Lee, Jooeon Oh, Dongkwon Lee, Heeseong Kang, Chul Ho Lee, and Donghun Lee. Precise temperature sensing with nanoscale thermal sensors based on diamond NV centers. *Current Applied Physics*, 18(9):1066–1070, 2018. ISSN 15671739. doi: 10.1016/j.cap.2018.06.002. URL https://doi.org/10.1016/j.cap.2018.06.002.

[217] Margaret E Robinson, James D Ng, Huilong Zhang, Joseph T. Buchman, Olga A. Shenderova, Christy L. Haynes, Zhenqiang Ma, Randall H. Goldsmith, and Robert J Hamers. Optically detected magnetic resonance for selective imaging of diamond nanoparticles. *Analytical Chemistry*, page acs.analchem.7b03157, 2017. ISSN 0003-2700. doi: 10.1021/acs.analchem.7b03157. URL http://pubs.acs.org/doi/10.1021/acs.analchem.7b03157.

[218] Eva Brauchle, Sibylle Thude, Sara Y. Brucker, and Katja Schenke-Layland. Cell death stages in single apoptotic and necrotic cells monitored by Raman microspectroscopy. *Scientific Reports*, 4:1–9, 2014. ISSN 20452322. doi: 10.1038/srep04698.

[219] Iwan W. Schie, Jan Rüger, Abdullah S. Mondol, Anuradha Ramoji, Ute Neugebauer, Christoph Krafft, and Jürgen Popp. High-Throughput Screening Raman Spectroscopy Platform for Label-Free Cellomics. *Analytical Chemistry*, 90(3):2023–2030, 2018. ISSN 15206882. doi: 10.1021/acs.analchem.7b04127.

[220] Max Diem, Antonella Mazur, Kathleen Lenau, Jen Schubert, Ben Bird, Milo Miljković, Christoph Krafft, and Jürgen Popp. Molecular pathology via IR and Raman spectral imaging. *Journal of Biophotonics*, 6(11-12):855–886, 2013. ISSN 1864063X. doi: 10.1002/jbio.201300131.

[221] Lingbo Kong, Pengfei Zhang, Jing Yu, Peter Setlow, and Yong Qing Li. Rapid confocal Raman imaging using a synchro multifoci-scan scheme for dynamic monitoring of single living cells. *Applied Physics Letters*, 98(21):20–22, 2011. ISSN 00036951. doi: 10.1063/1.3595482. URL https://doi.org/10.1063/1.3595482.

[222] Sebastian Schlücker, Michael D. Schaeberle, Scott W. Huffman, and Ira W. Levin. Raman microspectroscopy: A comparison of point, line, and wide-field imaging methodologies. *Analytical Chemistry*, 75(16):4312–4318, 2003. ISSN 00032700. doi: 10.1021/ac034169h.

[223] Christian T. Nguyen, Ruffin E. Evans, Alp Sipahigil, Mihir K. Bhaskar, Denis D. Sukachev, Viatcheslav N. Agafonov, Valery A. Davydov, Liudmila F. Kulikova, Fedor Jelezko, and Mikhail D. Lukin. All-optical nanoscale thermometry with silicon-vacancy centers in diamond. *Applied Physics Letters*, 112(20):3–7, 2018. ISSN 00036951. doi: 10.1063/1.5029904.

[224] Adam M. Wojciechowski, Mürsel Karadas, Alexander Huck, Christian Osterkamp, Steffen Jankuhn, Jan Meijer, Fedor Jelezko, and Ulrik L. Andersen. Contributed Review: Camera-limits for wide-field magnetic resonance imaging with a nitrogen-vacancy spin sensor. *Review of Scientific Instruments*, 89(3):1–8, 2018. ISSN 10897623. doi: 10.1063/1.5010282.

[225] Jeremy M Lerner. Imaging Spectrometer Fundamentals for Researchers in the Biosciences—A Tutorial. *Journal of the International Society for Analytical Cytology*, 69 (A):659–676, 2006. ISSN 1552-4922. doi: 10.1002/cyto.a.

[226] Shoji Kawahito. CMOS Image Sensors. *IEEJ Transactions on Sensors and Micromachines*, 134(7):199–205, 2014. ISSN 1341-8939. doi: 10.1541/ieejsmas.134.199. URL http://jlc.jst.go.jp/DN/JST.JSTAGE/ieejsmas/134.199?lang=en&from=CrossRef&type=abstract.

[227] Roy Esplin. Use of Curved Slits to Increase the Throughput of a Hadamard Spectrometer. *Optical Engineering*, 19(4):623–627, 1980. doi: 10.1117/12.7972570.increase. URL https://digitalcommons.usu.edu/sdl_pubs/44/.

[228] N M Larson, R Crosmun, and Y Talmi. Theoretical comparison of singly multiplexed hadamard transform spectrometers and scanning spectrometers. *Applied optics*, 13 (11):2662–8, 1974. ISSN 0003-6935. doi: 10.1364/AO.13.002662. URL http://www.ncbi.nlm.nih.gov/pubmed/20134751.

[229] S D Feller, Haojun Chen, David J Brady, Michael E Gehm, Chaoray Hsieh, Omid Momtahan, and Ali Adibi. Multiple order coded aperture spectrometer. *Optics express*, 15(9):5625–30, 2007. ISSN 1094-4087. doi: 10.1364/OE.15.005625. URL http://www.ncbi.nlm.nih.gov/pubmed/19532820.

[230] David Kittle, Kerkil Choi, Ashwin Wagadarikar, and David J. Brady. Multiframe image estimation for coded aperture snapshot spectral imagers. *Applied Optics*, 49(36):6824, 2010. ISSN 0003-6935. doi: 10.1364/AO.49.006824. URL https://www.osapublishing.org/abstract.cfm?URI=ao-49-36-6824.

[231] Xiangyun Ma, Huijie Wang, Yang Wang, Da Chen, Wenliang Chen, and Qifeng Li. Improving the resolution and the throughput of spectrometers by a digital projection slit. *Opt. Express*, 25(19):23045–23050, 2017. ISSN 10944087. doi: 10.1364/OE.25.023045. URL http://www.opticsexpress.org/abstract.cfm?URI=oe-25-19-23045.

[232] A Ermakova, G Pramanik, J-M Cai, G Algara-Siller, U Kaiser, T Weil, Y-K Tzeng, H C Chang, L P McGuinness, M B Plenio, B Naydenov, and F Jelezko. Detection of a few metallo-protein molecules using color centers in nanodiamonds. *Nano letters*, 13(7):3305–9, 7 2013. ISSN 1530-6992. doi: 10.1021/nl4015233. URL http://www.ncbi.nlm.nih.gov/pubmed/23738579.

[233] Orestis Faklaris, Jacques Botsoa, Thierry Sauvage, Jean-François Roch, and François Treussart. Photoluminescent nanodiamonds: Comparison of the photoluminescence saturation properties of the NV color center and a cyanine dye at the single emitter level, and study of the color center concentration under different preparation conditions. *Diamond and Related Materials*, 19(7-9):988–995, 7 2010. ISSN 09259635. doi: 10.1016/j.diamond.2010.03.002. URL http://www.sciencedirect.com/science/article/pii/S0925963510001287.

[234] Orestis Faklaris, Vandana Joshi, Theano Irinopoulou, Patrick Tauc, Mohamed Sennour, Hugues Girard, Céline Gesset, Jean-Charles Arnault, Alain Thorel, Jean-Paul Boudou, Patrick A. Curmi, and François Treussart. Photoluminescent diamond nanoparticles for cell labeling: study of the uptake mechanism in mammalian cells. *ACS nano*, 3(12):3955–3962, 12 2009. ISSN 19360851. doi: 10.1021/nn901014j. URL http://www.ncbi.nlm.nih.gov/pubmed/19863087http://pubs.acs.org/doi/abs/10.1021/nn901014j.

[235] Yuen Yung Hui, Yi-Ren Chang, Nitin Mohan, Tsong-shin Lim, Yi-ying Chen, and Huan-Cheng Chang. Polarization modulation spectroscopy of single fluorescent nanodiamonds with multiple nitrogen vacancy centers. *The journal of physical chemistry. A*, 115(10):1878–84, 3 2011. ISSN 1520-5215. doi: 10.1021/jp110761u. URL http://dx.doi.org/10.1021/jp110761u.

[236] L. Rondin, G. Dantelle, a. Slablab, F. Grosshans, F. Treussart, P. Bergonzo, S. Perruchas, T. Gacoin, M. Chaigneau, H. C. Chang, V. Jacques, and J. F. Roch. Surface-induced charge state conversion of nitrogen-vacancy defects in nanodiamonds. *Physical Review B - Condensed Matter and Materials Physics*, 82(11):

115449, 9 2010. ISSN 10980121. doi: 10.1103/PhysRevB.82.115449. URL http://link.aps.org/doi/10.1103/PhysRevB.82.115449.

[237] Richelle M. Teeling-Smith, Young Woo Jung, Nicolas Scozzaro, Jeremy Cardellino, Isaac Rampersaud, Justin A. North, Marek Šimon, Vidya P. Bhallamudi, Arfaan Rampersaud, Ezekiel Johnston-Halperin, Michael G. Poirier, P. Chris Hammel, and P. Chris Hammel. NV Center Electron Paramagnetic Resonance of a Single Nanodiamond Attached to an Individual Biomolecule. *arXiv:1511.06831 [cond-mat, physics:physics]*, 110(9):2044–2052, 2016. ISSN 15420086. doi: 10.1016/j.bpj.2016.03.022. URL http://arxiv.org/abs/1511.06831%5Cnhttp://www.arxiv.org/pdf/1511.06831.pdf.

[238] Sebastian Zaiser, Torsten Rendler, Ingmar Jakobi, Thomas Wolf, Sang-yun Lee, Samuel Wagner, Philipp Neumann, Ville Bergholm, Thomas Schulte-Herbrüggen, Philipp Neumann, and Jörg Wrachtrup. Enhancing quantum sensing sensitivity by a quantum memory. *Nature Communications*, 7:12279, 2016. ISSN 2041-1723. doi: 10.1038/ncomms12279. URL http://www.nature.com/doifinder/10.1038/ncomms12279.

[239] Remi Mahfouz, Daniel L. Floyd, Wei Peng, Jennifer T. Choy, Marko Loncar, and Osman M. Bakr. Size-controlled fluorescent nanodiamonds: a facile method of fabrication and color-center counting. *Nanoscale*, 5(23):11776, 2013. ISSN 2040-3364. doi: 10.1039/c3nr03320a. URL http://xlink.rsc.org/?DOI=c3nr03320a.

[240] Huiliang Zhang, David R. Glenn, Richard Schalek, Jeff W. Lichtman, and Ronald L. Walsworth. Efficiency of Cathodoluminescence Emission by Nitrogen-Vacancy Color Centers in Nanodiamonds. *Small*, 1700543:1–9, 2017. ISSN 16136829. doi: 10.1002/smll.201700543.

[241] Sinan Karaveli, Ophir Gaathon, Abraham Wolcott, Reyu Sakakibara, Darcy Peterka, Jonathan S. Owen, Rafael Yuste, and Dirk R. Englund. Modulation of nitrogen vacancy charge state and fluorescence in nanodiamonds using electrochemical potential. *PNAS*, 113(15):3938–3943, 2015. ISSN 0027-8424. doi: 10.1364/CLEO{_}QELS.2015.FTh3B.6. URL http://www.scopus.com/inward/record.url?eid=2-s2.0-84935116466&partnerID=tZOtx3y1http://www.pnas.org/content/early/2016/03/23/1504451113.

[242] S. V. Anishchik and K. L. Ivanov. Sensitive detection of level anticrossing spectra of nitrogen vacancy centers in diamond. *Physical Review B*, 96(11):1–10, 2017. ISSN 24699969. doi: 10.1103/PhysRevB.96.115142.

[243] S. Kühn, C. Hettich, C. Schmitt, J. P.H. Poizat, and V. Sandoghdar. Diamond colour centres as a nanoscopic light source for scanning near-field optical microscopy. *Journal of Microscopy*, 202(1):2–6, 2001. ISSN 00222720. doi: 10.1046/j.1365-2818.2001.00829.x.

[244] C. Schreyvogel, V. Polyakov, R. Wunderlich, J. Meijer, and C. E. Nebel. Active charge state control of single NV centres in diamond by in-plane Al-Schottky junctions. *Scientific Reports*, 5:1–12, 2015. ISSN 20452322. doi: 10.1038/srep12160. URL http://dx.doi.org/10.1038/srep12160.

[245] Xiang-Cui Lei, Yue-Kun Heng, Sen Qian, Jing-Kai Xia, Shu-Lin Liu, Zhi Wu, Bao-Jun Yan, Mei-Hang Xu, Zheng Wang, Xiao-Nan Li, Xiang-Dong Ruan, Xiao-Zhuang

Wang, Yu-Zhen Yang, Wen-Wen Wang, Can Fang, Feng-Jiao Luo, Jing-Jing Liang, Lu-Ping Yang, and Biao Yang. Evaluation of new large area PMT with high quantum efficiency. *Chinese Physics C*, 40(2):026002, 2016. ISSN 1674-1137. doi: 10.1088/1674-1137/40/2/026002. URL http://stacks.iop.org/1674-1137/40/i=2/a=026002?key=crossref.17a31df0aebff92a0989dab5eaccdbeb.

[246] Hammamatsu. Hammamatsu - Guide to detector selection, 2018. URL http://www.hamamatsu.com/jp/en/community/optical_sensors/articles/guide_to_detector_selection/index.html.

[247] Arne Wickenbrock, Huijie Zheng, Lykourgos Bougas, Nathan Leefer, Samer Afach, Andrey Jarmola, Victor M. Acosta, and Dmitry Budker. Microwave-free magnetometry with nitrogen-vacancy centers in diamond. *Applied Physics Letters*, 109(053505): 1–4, 6 2016. doi: 10.1063/1.4960171. URL http://arxiv.org/abs/1606.03070http://dx.doi.org/10.1063/1.4960171.

[248] Jae Sung Park, Chang Kyoung Choi, and Kenneth D. Kihm. Optically sliced micro-PIV using confocal laser scanning microscopy (CLSM). *Experiments in Fluids*, 37(1): 105–119, 2004. ISSN 07234864. doi: 10.1007/s00348-004-0790-6.

[249] V. V. Pully, A. T M Lenferink, and C. Otto. Time-lapse Raman imaging of single live lymphocytes. *Journal of Raman Spectroscopy*, 42(2):167–173, 2011. ISSN 03770486. doi: 10.1002/jrs.2683. URL https://onlinelibrary.wiley.com/doi/abs/10.1002/jrs.2683.

[250] Jacob Filik. Raman spectroscopy: a simple, non-destructive way to characterise diamond and diamond-like materials. *Spectroscopy Europe*, 17(5): 10–16, 2005. URL http://www.spectroscopyeurope.com/articles/55-articles/1570-raman-spectroscopy-a-simple-non-destructive-way-to-characterise-diamond-and-diamond-like-ma//www.chm.bristol.ac.uk/pt/diamond/pdf/se17.pdf.

[251] C H Liu, Y Zhou, Y Sun, J Y Li, L X Zhou, S Boydston-White, V Masilamani, K Zhu, Y Pu, and R R Alfano. Resonance Raman and Raman Spectroscopy for Breast Cancer Detection. *Technology in Cancer Research & Treatment*, 12(4):371–382, 2013. ISSN 15330346. doi: 10.7785/tcrt.2012.500325. URL http://journals.sagepub.com/doi/abs/10.7785/tcrt.2012.500325.

[252] Christoph Krafft, Michael Schmitt, Iwan W. Schie, Dana Cialla-May, Christian Matthï¿½us, Thomas Bocklitz, and Jï¿½rgen Popp. Label-Free Molecular Imaging of Biological Cells and Tissues by Linear and Nonlinear Raman Spectroscopic Approaches. *Angewandte Chemie - International Edition*, 56(16):4392–4430, 2017. ISSN 15213773. doi: 10.1002/anie.201607604. URL https://onlinelibrary.wiley.com/doi/full/10.1002/anie.201607604#.

[253] Travis W. Sawyer, Kyle S. Hawkins, and Michael Damento. Using confidence intervals to evaluate the focus alignment of spectrograph detector arrays. *App. Opt.*, 56(18): 5295–5300, 2017. ISSN 0003-6935. doi: 10.1364/AO.56.005295. URL https://www.osapublishing.org/abstract.cfm?URI=ao-56-18-5295.

[254] Ji-Xin Cheng, Y Kevin Jia, Gengfeng Zheng, and X Sunney Xie. Laser-scanning coherent anti-Stokes Raman scattering microscopy and applications to cell biology. *Biophysical journal*, 83(1):502–9, 7 2002. ISSN 0006-3495. doi: 10.1016/S0006-3495(02)75186-2. URL http://www.sciencedirect.com/science/article/pii/S0006349502751862.

[255] Alina Zoladek, Flavius C. Pascut, Poulam Patel, and Ioan Notingher. Non-invasive time-course imaging of apoptotic cells by confocal Raman micro-spectroscopy. *Journal of Raman Spectroscopy*, 42(3):251–258, 3 2011. ISSN 03770486. doi: 10.1002/jrs.2707. URL http://doi.wiley.com/10.1002/jrs.2707http://onlinelibrary.wiley.com/doi/10.1002/jrs.2707/full.

[256] Jagadeesh Babu Nanubolu and Jonathan C Burley. Investigating the recrystallisation behaviour of amorphous paracetamol by variable temperature Raman studies and surface Raman mapping . *Molecular Pharmaceutics*, 9:1544–1558, 2012. URL http://pubs.acs.org/doi/full/10.1021/mp300035g.

[257] ThermoFisher Scientific. Imaging live cells through time and space, 2018. URL https://www.thermofisher.com/uk/en/home/references/newsletters-and-journals/bioprobes-journal-of-cell-biology-applications/bioprobes-70/time-lapse-fluorescence-microscopy.html.

[258] Chia-Yi Fang, V Vaijayanthimala, Chi-An Cheng, Shih-Hua Yeh, Ching-Fang Chang, Chung-Leung Li, and Huan-Cheng Chang. The exocytosis of fluorescent nanodiamond and its use as a long-term cell tracker. *Small (Weinheim an der Bergstrasse, Germany)*, 7(23):3363–70, 12 2011. ISSN 1613-6829. doi: 10.1002/smll.201101233. URL http://www.ncbi.nlm.nih.gov/pubmed/21997958.

[259] Florence Draux, Pierre Jeannesson, Abdelilah Beljebbar, Ali Tfayli, Nicolas Fourre, Michel Manfait, Josep Sulé-Suso, and Ganesh D Sockalingum. Raman spectral imaging of single living cancer cells: a preliminary study. *The Analyst*, 134(3):542–548, 3 2009. ISSN 0003-2654. doi: 10.1039/b812610k. URL http://www.ncbi.nlm.nih.gov/pubmed/19238292.

[260] F. Bonnier, P. Knief, B. Lim, A. D. Meade, J. Dorney, K. Bhattacharya, F. M. Lyng, and H. J. Byrne. Imaging live cells grown on a three dimensional collagen matrix using Raman microspectroscopy. *The Analyst*, 135(12):3169, 12 2010. ISSN 0003-2654. doi: 10.1039/c0an00539h. URL http://pubs.rsc.org/en/content/articlehtml/2010/an/c0an00539hhttp://xlink.rsc.org/?DOI=c0an00539h.

[261] Tobias J. Moritz, Douglas S. Taylor, Denise M. Krol, John Fritch, and James W. Chan. Detection of doxorubicin-induced apoptosis of leukemic T-lymphocytes by laser tweezers Raman spectroscopy. *Biomedical Optics Express*, 1(4):1138, 2010. ISSN 2156-7085. doi: 10.1364/BOE.1.001138. URL https://www.osapublishing.org/boe/abstract.cfm?uri=boe-1-4-1138.

[262] Alison J. Hobro, Nicolas Pavillon, Katsumasa Fujita, Muge Ozkan, Cevayir Coban, and Nicholas I. Smith. Label-free Raman imaging of the macrophage response to the malaria pigment hemozoin. *The Analyst*, 140(7):2350–2359, 2015. ISSN 0003-2654. doi: 10.1039/C4AN01850H. URL http://xlink.rsc.org/?DOI=C4AN01850H.

[263] Nwe-Nwe Aye-Han and Jin Zhang. A Multiparameter Live Cell Imaging Approach to Monitor Cyclic AMP and Protein Kinase A Dynamics in Parallel. In Robert H Newman and Qiang Ni, editors, *Fluorescent Protein-Based Biosensors*, chapter 16, pages 207–217. Springer, 2013. ISBN 9781627036214. URL https://link.springer.com/protocol/10.1007%2F978-1-62703-622-1_16https://www.ncbi.nlm.nih.gov/pmc/articles/PMC4112587/.

[264] J. M. Hyser, B. Utama, S. E. Crawford, J. R. Broughman, and M. K. Estes. Activation of the Endoplasmic Reticulum Calcium Sensor STIM1 and Store-Operated Calcium Entry by Rotavirus Requires NSP4 Viroporin Activity. *Journal of Virology*, 87 (24):13579–13588, 2013. ISSN 0022-538X. doi: 10.1128/JVI.02629-13. URL http://jvi.asm.org/cgi/doi/10.1128/JVI.02629-13.

[265] Xiangduo Kong, Samarendra K. Mohanty, Jared Stephens, Jason T. Heale, Veronica Gomez-Godinez, Linda Z. Shi, Jong Soo Kim, Kyoko Yokomori, and Michael W. Berns. Comparative analysis of different laser systems to study cellular responses to DNA damage in mammalian cells. *Nucleic Acids Research*, 37(9):1–14, 2009. ISSN 03051048. doi: 10.1093/nar/gkp221.

[266] Melanie M Frigault, Judith Lacoste, Jody L Swift, and Claire M Brown. Live-cell microscopy - tips and tools. *Journal of cell science*, 122(Pt 6):753–767, 2009. ISSN 0021-9533. doi: 10.1242/jcs.033837.

[267] F. Ehrentreich and L. Summchen. Spike removal and denoising of Raman spectra by wavelet transform methods. *Analytical Chemistry*, 73(17):4364–4373, 2001. ISSN 00032700. doi: 10.1021/ac0013756.

[268] Sara Mattana, Maurizio Mattarelli, Lorena Urbanelli, Krizia Sagini, Carla Emiliani, Mauro Dalla Serra, Daniele Fioretto, and Silvia Caponi. Non-contact mechanical and chemical analysis of single living cells by microspectroscopic techniques. *Light: Science & Applications*, 7(17139):1–9, 2018. doi: 10.1038/lsa.2017.139. URL https://www.nature.com/articles/lsa2017139.pdf?origin=ppubhttp://pubs.rsc.org/en/content/articlelanding/2018/an/c7an01043e#!divAbstract.

[269] Maider Vidal and José Manuel Amigo. Pre-processing of hyperspectral images. Essential steps before image analysis. *Chemometrics and Intelligent Laboratory Systems*, 117:138–148, 2012. ISSN 01697439. doi: 10.1016/j.chemolab.2012.05.009. URL http://dx.doi.org/10.1016/j.chemolab.2012.05.009.

[270] Stanislav O. Konorov, H. Georg Schulze, James M. Piret, Robin F.B. Turner, and Michael W. Blades. Evidence of marked glycogen variations in the characteristic Raman signatures of human embryonic stem cells. *Journal of Raman Spectroscopy*, 42(5):1135–1141, 2011. ISSN 03770486. doi: 10.1002/jrs.2829.

[271] Caleb J. Behrend, Catherine P. Tarnowski, and Michael D. Morris. Identification of outliers in hyperspectral Raman image data by nearest neighbor comparison. *Applied Spectroscopy*, 56(11):1458–1461, 2002. ISSN 00037028. doi: 10.1366/00037020260377760.

[272] Peter Lasch. Spectral pre-processing for biomedical vibrational spectroscopy and microspectroscopic imaging. *Chemometrics and Intelligent Laboratory Systems*, 117:100–114, 2012. ISSN 01697439. doi: 10.1016/j.chemolab.2012.03.011. URL http://dx.doi.org/10.1016/j.chemolab.2012.03.011.

[273] Carlo V. Cannistraci, Franco M. Montevecchi, and Massimo Alessio. Median-modified Wiener filter provides efficient denoising, preserving spot edge and morphology in 2-DE image processing. *Proteomics*, 9(21):4908–4919, 2009. ISSN 16159853. doi: 10.1002/pmic.200800538.

[274] Delphine Feuerstein, Kim H. Parker, and Martyn G. Boutelle. Practical methods for noise removal: Applications to spikes, nonstationary quasi-periodic noise, and baseline drift. *Analytical Chemistry*, 81(12):4987–4994, 2009. ISSN 00032700. doi: 10.1021/ac900161x.

[275] Daisuke Kato. Improvement of Raman spectroscopy by quenching the fluorescence. *Journal of Applied Physics*, 45(5):2281–2282, 1974. ISSN 00218979. doi: 10.1063/1.1663576.

[276] Tatu Rojalin, Lauri Kurki, Timo Laaksonen, Tapani Viitala, Juha Kostamovaara, Keith C. Gordon, Leonardo Galvis, Sebastian Wachsmann-Hogiu, Clare J. Strachan, and Marjo Yliperttula. Fluorescence-suppressed time-resolved Raman spectroscopy of pharmaceuticals using complementary metal-oxide semiconductor (CMOS) single-photon avalanche diode (SPAD) detector. *Analytical and Bioanalytical Chemistry*, 408(3):761–774, 2016. ISSN 16182650. doi: 10.1007/s00216-015-9156-6.

[277] Stefan Wolf and Heinz Döring. Application of cheap lasers in shifted excitation Raman difference spectroscopy. *Proceedings of SPIE*, 8427, 2012. doi: 10.1117/12.922372. URL http://dx.doi.org/10.1117/12.922372.

[278] Xin Su, Shaoyin Fang, Daosen Zhang, Qinnan Zhang, Xiaoxu Lu, Jindong Tian, Jinping Fan, and LiyunZhong. Raman spectrum reveals Mesenchymal stem cells inhibiting HL60 cells growth. *Spectrochimica Acta - Part A: Molecular and Biomolecular Spectroscopy*, 177:15–19, 2017. ISSN 13861425. doi: 10.1016/j.saa.2017.01.021. URL http://dx.doi.org/10.1016/j.saa.2017.01.021.

[279] Takeshi Hasegawa, Jujiro Nishijo, and Junzo Umemura. Separation of Raman spectra from fluorescence emission background by principal component analysis. *Chemical Physics Letters*, 317(6):642–646, 2000. ISSN 00092614. doi: 10.1016/S0009-2614(99)01427-X.

[280] Peter Gerald Moore. *Principles of statistical techniques: a first course from the beginnings for schools and universities, with many examples and solutions,*. Cambridge University Press, 1969. ISBN 0521290554. URL https://books.google.co.uk/books?id=FU44AAAAIAAJ&pg=PA238&lpg=PA238&dq=moving+average+oscillations&source=bl&ots=YnH_nTTagW&sig=KFA562_Bb3ykP3SBEPotTRFmH8Q&hl=en&sa=X&ved=0ahUKEwjhrZTuku_bAhWEvRQKHbmyB6I4ChDoAQgoMAA#v=onepage&q=movingaverageoscillations.

[281] Abraham Savitzky and Marcel J.E. Golay. Smoothing and Differentiation of Data by Simplified Least Squares Procedures. *Analytical Chemistry*, 36(8):1627–1639, 1964. ISSN 15206882. doi: 10.1021/ac60214a047.

[282] Paul H.C. Eilers. A perfect smoother. *Analytical Chemistry*, 75(14):3631–3636, 2003. ISSN 00032700. doi: 10.1021/ac034173t.

[283] Katarzyna Majzner, Kamila Kochan, Neli Kachamakova-Trojanowska, Edyta Maslak, Stefan Chlopicki, and Malgorzata Baranska. Raman imaging providing insights into chemical composition of lipid droplets of different size and origin: In hepatocytes and endothelium. *Analytical Chemistry*, 86(13):6666–6674, 2014. ISSN 15206882. doi: 10.1021/ac501395g.

[284] Víctor Olmos, Carmen Bedia, Romà Tauler, and Anna de Juan. Preprocessing Tools Applied to Improve the Assessment of Aldrin Effects on Prostate Cancer Cells Using Raman Spectroscopy. *Applied Spectroscopy*, 72(3):489–500, 2018. ISSN 19433530. doi: 10.1177/0003702817746947.

[285] Max Diem, Miloš Miljković, Benjamin Bird, Tatyana Chernenko, Jen Schubert, Ellen Marcsisin, Antonella Mazur, Erin Kingston, Evgenia Zuser, Kostas Papamarkakis, and Nora Laver. Applications of Infrared and Raman Microspectroscopy of Cells and Tissue in Medical Diagnostics: Present Status and Future Promises. *Spectroscopy: An International Journal*, 27 (5-6):463–496, 2012. ISSN 0712-4813. doi: 10.1155/2012/848360. URL http://apps.webofknowledge.com/full_record.do?product=WOS&search_mode=CitingArticles&qid=4&SID=Q2YLZht949sQbGSYf2K&page=3&doc=30.

[286] Thomas Dieing, Olaf Hollricher, and Jan Toporski, editors. *Confocal Raman Microscopy*, volume 158 of *Springer Series in Optical Sciences*. Springer, Berlin, Heidelberg, 2011. ISBN 978-3-642-12521-8. doi: 10.1007/978-3-642-12522-5. URL http://link.springer.com/10.1007/978-3-642-12522-5.

[287] F.a. Kruse, a.B. Lefkoff, J.W. Boardman, K.B. Heidebrecht, a.T. Shapiro, P.J. Barloon, and a.F.H. Goetz. The spectral image processing system (SIPS)—interactive visualization and analysis of imaging spectrometer data. *Remote Sensing of Environment*, 44(2-3):145–163, 1993. ISSN 00344257. doi: 10.1016/0034-4257(93)90013-N.

[288] Jing Wang and Chein-I Chang. Independent component analysis-based dimensionality reduction with applications in hyperspectral image analysis. *IEEE Transactions on Geoscience and Remote Sensing*, 44(6):1586–1600, 6 2006. ISSN 0196-2892. doi: 10.1109/TGRS.2005.863297. URL http://ieeexplore.ieee.org/lpdocs/epic03/wrapper.htm?arnumber=1634722.

[289] Aoife A Gowen, Yaoze Feng, Edurne Gaston, and Vasilis Valdramidis. Recent applications of hyperspectral imaging in microbiology. *Talanta*, 137:43–54, 5 2015. ISSN 1873-3573. doi: 10.1016/j.talanta.2015.01.012. URL http://www.sciencedirect.com/science/article/pii/S0039914015000260.

[290] S. P. Singh and C. Murali Krishna. Raman spectroscopy of oral tissues: correlation of spectral and biochemical markers. *Analytical Methods*, 6(21):8613–8620, 9 2014. ISSN 1759-9660. doi: 10.1117/12.2052797. URL http://pubs.rsc.org/en/content/articlehtml/2014/ay/c4ay01615ghttp://proceedings.spiedigitallibrary.org/proceeding.aspx?articleid=1840634.

[291] Martin Hedegaard, Christian Matthäus, Søren Hassing, Christoph Krafft, Max Diem, and Jürgen Popp. Spectral unmixing and clustering algorithms for assessment of single cells by Raman microscopic imaging. *Theoretical Chemistry Accounts*, 130 (4-6):1249–1260, 6 2011. ISSN 1432881X. doi: 10.1007/s00214-011-0957-1. URL http://link.springer.com/10.1007/s00214-011-0957-1.

[292] Václav Ranc, Josef Srovnal, Libor Kvítek, and Marian Hajduch. Discrimination of circulating tumor cells of breast cancer and colorectal cancer from normal human mononuclear cells using Raman spectroscopy. *The Analyst*, 138(20):5983, 2013. ISSN 0003-2654. doi: 10.1039/c3an00855j. URL http://xlink.rsc.org/?DOI=c3an00855j.

[293] Z. Farhane, F. Bonnier, A. Casey, A. Maguire, L. O'Neill, and H. J. Byrne. Cellular discrimination using in vitro Raman micro spectroscopy: the role of the nucleolus. *The Analyst*, 140(17):5908–5919, 2015. ISSN 0003-2654. doi: 10.1039/C5AN01157D. URL http://xlink.rsc.org/?DOI=C5AN01157D.

[294] Sota Takanezawa, Shin-ichi Morita, Yukihiro Ozaki, and Yasushi Sako. Raman Spectral Dynamics of Single Cells in the Early Stages of Growth Factor Stimulation. *Biophysical Journal*, 108(9):2148–2157, 2015. ISSN 00063495. doi: 10.1016/j.bpj.2015.03.037. URL http://linkinghub.elsevier.com/retrieve/pii/S0006349515002982.

[295] J B MacQueen. Kmeans Some Methods for classification and Analysis of Multivariate Observations. *5th Berkeley Symposium on Mathematical Statistics and Probability 1967*, 1(233):281–297, 1967. ISSN 00970433. doi: citeulike-article-id:6083430. URL http://projecteuclid.org/euclid.bsmsp/1200512992.

[296] Batirtze Prats Mateu, Eva Harreither, Markus Schosserer, Verena Puxbaum, Elisabeth Gludovacz, Nicole Borth, Notburga Gierlinger, and Johannes Grillari. Label-free live cell imaging by Confocal Raman Microscopy identifies CHO host and producer cell lines. *Biotechnology Journal*, 12(1), 2017. ISSN 18607314. doi: 10.1002/biot.201600037.

[297] G W Zack, W E Rogers, and S A Latt. Automatic measurement of sister chromatid exchange frequency. *Journal of Histochemistry & Cytochemistry*, 25(7):741–753, 7 1977. ISSN 0022-1554. doi: 10.1177/25.7.70454. URL http://www.ncbi.nlm.nih.gov/pubmed/70454http://journals.sagepub.com/doi/10.1177/25.7.70454.

[298] Nobuyuki Otsu. A Threshold Selection Method from Gray-Level Histograms. *IEEE Transactions on Systems, Man, and Cybernetics*, 9(1):62–66, 1979. ISSN 0018-9472. doi: 10.1109/TSMC.1979.4310076. URL http://ieeexplore.ieee.org/document/4310076/.

[299] Andrey N. Kuzmin, Artem Pliss, and Paras N. Prasad. Ramanomics: New omics disciplines using micro raman spectrometry with biomolecular component analysis for molecular profiling of biological structures. *Biosensors*, 7(4), 2017. ISSN 20796374. doi: 10.3390/bios7040052.

[300] Zeineb Farhane, Franck Bonnier, and Hugh J. Byrne. Monitoring doxorubicin cellular uptake and trafficking using in vitro Raman microspectroscopy: short and long time exposure effects on lung cancer cell lines. *Analytical and Bioanalytical Chemistry*, 409(5):1333–1346, 2017. ISSN 16182650. doi: 10.1007/s00216-016-0065-0. URL http://dx.doi.org/10.1007/s00216-016-0065-0.

[301] Joke De Gelder, Kris De Gussem, Peter Vandenabeele, and Luc Moens. Reference database of Raman spectra of biological molecules. *Journal of Raman Spectroscopy*, 38(9):1133–1147, 9 2007. ISSN 03770486. doi: 10.1002/jrs.1734. URL http://doi.wiley.com/10.1002/jrs.1734.

[302] Fabian Pedregosa, Gaël Varoquaux, Alexandre Gramfort, Vincent Michel, Bertrand Thirion, Olivier Grisel, Mathieu Blondel, Peter Prettenhofer, Ron Weiss, Vincent Dubourg, Jake Vanderplas, Alexandre Passos, David Cournapeau, Matthieu Brucher,

Matthieu Perrot, and Édouard Duchesnay. Scikit-learn: Machine Learning in Python. *Journal of Machine Learning Research*, 12:2825–2830, 2012. ISSN 15324435. doi: 10.1007/s13398-014-0173-7.2. URL http://dl.acm.org/citation.cfm?id=2078195%5Cnhttp://arxiv.org/abs/1201.0490.

[303] Thomas Bocklitz, Angela Walter, Katharina Hartmann, Petra Rösch, and Jürgen Popp. How to pre-process Raman spectra for reliable and stable models? *Analytica Chimica Acta*, 704(1-2):47–56, 2011. ISSN 00032670. doi: 10.1016/j.aca.2011.06.043. URL http://dx.doi.org/10.1016/j.aca.2011.06.043.

[304] Bradley R. Smith, Daniel Gruber, and Taras Plakhotnik. The effects of surface oxidation on luminescence of nano diamonds. *Diamond and Related Materials*, 19(4):314–318, 2010. ISSN 09259635. doi: 10.1016/j.diamond.2009.12.009. URL http://dx.doi.org/10.1016/j.diamond.2009.12.009http://www.sciencedirect.com/science/article/pii/S0925963509003690.

[305] Robert Silbajoris, William Linak, Olga Shenderova, Christopher Winterrowd, Huan-Cheng Chang, Jay L. Zweier, Anirudh Kota, Lisa A. Dailey, Nicholas Nunn, Philip A. Bromberg, and James M. Samet. Detonation nanodiamond toxicity in human airway epithelial cells is modulated by air oxidation. *Diamond and Related Materials*, 58:16–23, 9 2015. ISSN 09259635. doi: 10.1016/j.diamond.2015.05.007. URL http://www.sciencedirect.com/science/article/pii/S0925963515000941.

[306] Giacomo Reina, Emanuela Tamburri, Silvia Orlanducci, Stefano Gay, Roberto Matassa, Valeria Guglielmotti, Teresa Lavecchia, Maria Letizia Terranova, and Marco Rossi. Nanocarbon surfaces for biomedicine. *BioMatter*, 4(3):3–6, 2014. ISSN 21592535. doi: 10.4161/biom.28537.

[307] Jan Havlik, Vladimira Petrakova, Ivan Rehor, Vaclav Petrak, Michal Gulka, Jan Stursa, Jan Kucka, Jan Ralis, Torsten Rendler, San-Yung Lee, Rolf Reuter, Joerg Wrachtrup, Miroslav Ledvina, Milos Nesladek, and Petr Cigler. Boosting nanodiamond fluorescence: towards development of brighter probes. *Nanoscale*, 5(8):3208–3211, 2013. ISSN 2040-3364. doi: 10.1039/c2nr32778c.

[308] Msaukiranji Mkandawire, Andrea Pohl, Tatiana Gubarevich, Victoria Lapina, Dietmar Appelhans, Gerhard Rödel, Wolfgang Pompe, Jürgen Schreiber, and Jörg Opitz. Selective targeting of green fluorescent nanodiamond conjugates to mitochondria in HeLa cells. *Journal of Biophotonics*, 2(10):596–606, 2009. ISSN 1864063X. doi: 10.1002/jbio.200910002. URL http://onlinelibrary.wiley.com/doi/10.1002/jbio.200910002/abstract.

[309] Zhiqin Chu, Silu Zhang, Bokai Zhang, Chunyuan Zhang, Chia-Yi Fang, Ivan Rehor, Petr Cigler, Huan-Cheng Chang, Ge Lin, Renbao Liu, and Quan Li. Unambiguous observation of shape effects on cellular fate of nanoparticles. *Scientific reports*, 4:4495, 2014. ISSN 2045-2322. doi: 10.1038/srep04495. URL http://www.pubmedcentral.nih.gov/articlerender.fcgi?artid=3968459&tool=pmcentrez&rendertype=abstract.

[310] Katarzyna Solarska-Ściuk, Agnieszka Gajewska, Sława Glińska, Maciej Studzian, Sylwia Michlewska, Łucja Balcerzak, Janusz Skolimowski, Bogumiła Kolago, and

Grzegorz Bartosz. Intracellular transport of nanodiamond particles in human endothelial and epithelial cells. *Chemico-Biological Interactions*, 219:90–100, 5 2014. ISSN 18727786. doi: 10.1016/j.cbi.2014.05.013. URL http://www.sciencedirect.com/science/article/pii/S0009279714001719.

[311] Kuang-Kai Liu, Chia-Liang Cheng, Chia-Ching Chang, and Jui-I Chao. Biocompatible and detectable carboxylated nanodiamond on human cell. *Nanotechnology*, 18(32):325102, 8 2007. ISSN 0957-4484. doi: 10.1088/0957-4484/18/32/325102. URL http://stacks.iop.org/0957-4484/18/i=32/a=325102?key=crossref.1b07d9cb855fca508e9124515cc604b9.

[312] Kinga Adach, Mateusz Fijalkowski, Gabriela Gajek, Janusz Skolimowski, Renata Kontek, and Alina Blaszczyk. Chemico-Biological Interactions Studies on the cytotoxicity of diamond nanoparticles against human cancer cells and lymphocytes. *Chemico-Biological Interactions*, 254:156–166, 2016. ISSN 0009-2797. doi: 10.1016/j.cbi.2016.06.004. URL http://dx.doi.org/10.1016/j.cbi.2016.06.004.

[313] Milena Keremidarska, Aneliya Ganeva, Dimitar Mitev, Todor Hikov, Radina Presker, Lilyana Pramatarova, and Natalia Krasteva. Comparative study of cytotoxicity of detonation nanodiamond particles with an osteosarcoma cell line and primary mesenchymal stem cells. *Biotechnology and Biotechnological Equipment*, 28(4):733–739, 2014. ISSN 13102818. doi: 10.1080/13102818.2014.947704. URL http://dx.doi.org/10.1080/13102818.2014.947704.

[314] Reem Eldawud, Manuela Reitzig, Jörg Opitz, Yon Rojansakul, Wenjuan Jiang, Shikha Nangia, and Cerasela Zoica Dinu. Combinatorial approaches to evaluate nanodiamond uptake and induced cellular fate. *Nanotechnology*, 27(8):085107, 2016. ISSN 0957-4484. doi: 10.1088/0957-4484/27/8/085107. URL http://stacks.iop.org/0957-4484/27/i=8/a=085107?key=crossref.2f12bfdc9a109cb02d239a3a24c8ddd9.

[315] Julia Wehling, Ralf Dringen, Richard N. Zare, Michael Maas, and Kurosch Rezwan. Bactericidal activity of partially oxidized nanodiamonds. *ACS Nano*, 8(6):6475–6483, 2014. ISSN 1936086X. doi: 10.1021/nn502230m. URL http://pubs.acs.org/doi/full/10.1021/nn502230m.

[316] Kuang Kai Liu, Chi Ching Wang, Chia Liang Cheng, and Jui I. Chao. Endocytic carboxylated nanodiamond for the labeling and tracking of cell division and differentiation in cancer and stem cells. *Biomaterials*, 30(26):4249–4259, 2009. ISSN 01429612. doi: 10.1016/j.biomaterials.2009.04.056. URL http://dx.doi.org/10.1016/j.biomaterials.2009.04.056.

[317] Uche C. Anozie and Paul Dalhaimer. Molecular links among non-biodegradable nanoparticles, reactive oxygen species, and autophagy. *Advanced Drug Delivery Reviews*, 122:65–73, 12 2017. ISSN 0169409X. doi: 10.1016/j.addr.2017.01.001. URL http://linkinghub.elsevier.com/retrieve/pii/S0169409X17300017.

[318] Henry Lujan and Christie M. Sayes. Cytotoxicological pathways induced after nanoparticle exposure: studies of oxidative stress at the 'nano–bio' interface. *Toxicology Research*, 6(5):580–594, 8 2017. ISSN 2045-452X. doi: 10.1039/C7TX00119C. URL http://xlink.rsc.org/?DOI=C7TX00119C.

[319] Volodymyr I. Lushchak. Free radicals, reactive oxygen species, oxidative stress and its classification. *Chemico-Biological Interactions*, 224:164–175, 2014. ISSN 18727786. doi: 10.1016/j.cbi.2014.10.016. URL http://dx.doi.org/10.1016/j.cbi.2014.10.016.

[320] Sheetal Korde Choudhari, Minal Chaudhary, Amol R. Gadbail, Aparna Sharma, and Satyajit Tekade. Oxidative and antioxidative mechanisms in oral cancer and precancer: A review. *Oral Oncology*, 50(1):10–18, 1 2014. ISSN 13688375. doi: 10.1016/j.oraloncology.2013.09.011. URL http://dx.doi.org/10.1016/j.oraloncology.2013.09.011http://www.sciencedirect.com/science/article/pii/S1368837513006945.

[321] Kinga Adach, Mateusz Fijalkowski, and Janusz Skolimowski. Antioxidant Effect of Hydroxylated Diamond Nanoparticles Measured in Soybean Oil Antioxidant Effect of Hydroxylated Diamond Nanoparticles Measured in Soybean Oil. *Fullerenes, Nanotubes and Carbon Nanostructures*, 4046(July 2017):1024–1032, 2015. doi: 10.1080/1536383X.2015.1057701. URL http://www.tandfonline.com/doi/full/10.1080/1536383X.2015.1057701?instName=University+of+Cambridge.

[322] Shawqi H. Alawdi, Ezzeldin S. El-Denshary, Marwa M. Safar, Housam Eidi, Marie Odile David, and Mosaad A. Abdel-Wahhab. Neuroprotective Effect of Nanodiamond in Alzheimer's Disease Rat Model: a Pivotal Role for Modulating NF-kappaB and STAT3 Signaling. *Molecular Neurobiology*, 54(3):1906–1918, 2017. ISSN 15591182. doi: 10.1007/s12035-016-9762-0.

[323] Q Zhao, J Yang, and J Liu. Purification method dependent fluorescence from nitrogen-vacancy (NV) centers of nano-diamonds. *RSC Advances*, 6:47164–47173, 2014. ISSN 2046-2069. doi: 10.1039/c6ra01510g. URL http://pubs.rsc.org/en/Content/ArticleLanding/2016/RA/C6RA01510G#!divAbstract.

[324] S. Sotoma, K. Akagi, S. Hosokawa, R. Igarashi, H. Tochio, Y. Harada, and M. Shirakawa. Comprehensive and quantitative analysis for controlling the physical/chemical states and particle properties of nanodiamonds for biological applications. *RSC Adv.*, 5(18):13818–13827, 2015. ISSN 2046-2069. doi: 10.1039/C4RA16482B. URL http://xlink.rsc.org/?DOI=C4RA16482B.

[325] Jonathan Cebik, John K McDonough, Filipe Peerally, Rene Medrano, Ioannis Neitzel, Yury Gogotsi, and Sebastian Osswald. Raman spectroscopy study of the nanodiamond-to-carbon onion transformation. *Nanotechnology*, 24(20):205703, 2013. ISSN 1361-6528. doi: 10.1088/0957-4484/24/20/205703. URL http://www.ncbi.nlm.nih.gov/pubmed/23598775.

[326] M. Aramesh, O. Shimoni, K. Ostrikov, S. Prawer, and J. Cervenka. Surface charge effects in protein adsorption on nanodiamonds. *Nanoscale*, 7(13):5726–5736, 2015. ISSN 2040-3372. doi: 10.1039/C5NR00250H. URL http://pubs.rsc.org/en/Content/ArticleLanding/2015/NR/C5NR00250H#!divAbstract.

[327] Bastian J. M. Etzold, Ioannis Neitzel, Manfred Kett, Florian Strobl, Vadym N. Mochalin, and Yury Gogotsi. Layer-by-Layer Oxidation for Decreasing the Size of Detonation Nanodiamond. *Chemistry of Materials*, 26(11):3479–3484, 6 2014. ISSN 0897-4756. doi: 10.1021/cm500937r. URL http://dx.doi.org/10.1021/cm500937r.

[328] Sebastian Osswald, Gleb Yushin, Vadym Mochalin, Sergei O Kucheyev, and Yury Gogotsi. Control of sp / sp Carbon Ratio and Surface Chemistry of Nanodiamond Powders by Selective Oxidation in Air Control of sp 2 / sp 3 Carbon Ratio and Surface Chemistry of Nanodiamond Powders by Selective Oxidation in Air. *Synthesis*, 128 (35):11635–11642, 2006. doi: 10.1021/ja063303n. URL http://pubs.acs.org/doi/abs/10.1021/ja063303n.

[329] Nitin Mohan, Chao-Sheng Chen, Hsiao-Han Hsieh, Yi-Chun Wu, and Huan-Cheng Chang. In vivo imaging and toxicity assessments of fluorescent nanodiamonds in Caenorhabditis elegans. *Nano Letters*, 10(9):3692–3699, 9 2010. ISSN 1530-6992. doi: 10.1021/nl1021909. URL http://www.ncbi.nlm.nih.gov/pubmed/20677785.

[330] Stanley R. Sternberg. Biomedical Image Processing. *Computer*, 16(1):22–34, 1983. ISSN 00189162. doi: 10.1109/MC.1983.1654163. URL https://ieeexplore.ieee.org/document/1654163/.

[331] Isabelle Fakhoury, Walid Saad, Kamal Bouhadir, Peter Nygren, Regine Schneider-Stock, and Hala Gali-Muhtasib. Uptake, delivery, and anticancer activity of thymoquinone nanoparticles in breast cancer cells. *Journal of Nanoparticle Research*, 18(7): 1–16, 2016. ISSN 1572896X. doi: 10.1007/s11051-016-3517-8.

[332] Kislay Roy, Yogesh S. Patel, Rupinder K. Kanwar, Rangam Rajkhowa, Xungai Wang, and Jagat R. Kanwar. Biodegradable Eri silk nanoparticles as a delivery vehicle for bovine lactoferrin against MDA-MB-231 and MCF-7 breast cancer cells. *International Journal of Nanomedicine*, 11:25–44, 2015. ISSN 11782013. doi: 10.2147/IJN.S91810.

[333] Yuling Liu, Yingqi Xu, Minghui Wu, Lijiao Fan, Chengwei He, Jian Bo Wan, Peng Li, Meiwan Chen, and Hui Li. Vitamin E succinate-conjugated F68 micelles for mitoxantrone delivery in enhancing anticancer activity. *International Journal of Nanomedicine*, 11:3167–3178, 2016. ISSN 11782013. doi: 10.2147/IJN.S103556.

[334] Vaishnavi M. Kulkarni, Dhananjay Bodas, Deepa Dhoble, Vandana Ghormade, and Kishore Paknikar. Radio-frequency triggered heating and drug release using doxorubicin-loaded LSMO nanoparticles for bimodal treatment of breast cancer. *Colloids and Surfaces B: Biointerfaces*, 145:878–890, 2016. ISSN 18734367. doi: 10.1016/j.colsurfb.2016.06.010. URL http://dx.doi.org/10.1016/j.colsurfb.2016.06.010.

[335] Chandran Murugan, Kathirvel Rayappan, Ramar Thangam, Ramasamy Bhanumathi, Krishnamurthy Shanthi, Raju Vivek, Ramasamy Thirumurugan, Atanu Bhattacharyya, Srinivasan Sivasubramanian, Palani Gunasekaran, and Soundarapandian Kannan. Combinatorial nanocarrier based drug delivery approach for amalgamation of anti-tumor agents in bresat cancer cells: an improved nanomedicine strategies. *Scientific reports*, 6(October):34053, 2016. ISSN 2045-2322 (Electronic). doi: 10.1038/srep34053. URL http://dx.doi.org/10.1038/srep34053.

[336] Danrong Hu, Omar Mezghrani, Lei Zhang, Yi Chen, Xue Ke, and Tianyuan Ci. GE1 I peptide modified and reduction-responsive hyaluronic acid-based nanoparticles induced higher efficacy of doxorubicin for breast carcinoma therapy. *International Journal of Nanomedicine*, 11:5125–5147, 2016. ISSN 11782013. doi: 10.2147/IJN.S113469.

[337] Yuan Chiang Chung, Jang Fang Kuo, Wan Chen Wei, King Jen Chang, Wei Ting Chao, and Ming Tan. Caveolin-1 dependent endocytosis enhances the chemosensitivity of HER-2 positive breast cancer cells to trastuzumab emtansine (T-DM1). *PLoS ONE*, 10(7):1–15, 2015. ISSN 19326203. doi: 10.1371/journal.pone.0133072.

[338] Helena S. Knowles, Dhiren M. Kara, and Mete Atatüre. Controlling a nuclear spin in a nanodiamond. *Physical Review B*, 115206(June):1–6, 2016. ISSN 2469-9950. doi: 10.1103/PhysRevB.96.115206. URL http://arxiv.org/abs/1611.06898.

[339] I. Petrov, O. Shenderova, V. Grishko, V. Grichko, T. Tyler, G. Cunningham, and G. McGuire. Detonation nanodiamonds simultaneously purified and modified by gas treatment. *Diamond and Related Materials*, 16(12):2098–2103, 12 2007. ISSN 09259635. doi: 10.1016/j.diamond.2007.05.013. URL http://www.sciencedirect.com/science/article/pii/S0925963507002877.

[340] Weijia Ma, Xiaoyan Yu, Xiongwei Qu, and Qingxin Zhang. Functionalization of agglomerating nanodiamonds with biodegradable poly(epsilon-caprolactone) through surface-initiated polymerization. *Diamond and Related Materials*, 62:14–21, 2016. ISSN 09259635. doi: 10.1016/j.diamond.2015.12.011. URL http://dx.doi.org/10.1016/j.diamond.2015.12.011http://linkinghub.elsevier.com/retrieve/pii/S0925963515301084.

[341] Vadym N Mochalin, Amanda Pentecost, Xue-Mei Li, Ioannis Neitzel, Matthew Nelson, Chongyang Wei, Tao He, Fang Guo, and Yury Gogotsi. Adsorption of Drugs on Nanodiamond: Toward Development of a Drug Delivery Platform. *Molecular Pharmaceutics*, 10:3728–3735, 2013. doi: 10.1021/mp400213z. URL http://pubs.acs.org/doi/abs/10.1021/mp400213z.

[342] Jianli Cheng, Junpo He, Changxi Li, and Yuliang Yang. Facile Approach to Functionalize Nanodiamond Particles with V-Shaped Polymer Brushes. *Chemistry of Materials*, 20(13):4224–4230, 7 2008. ISSN 0897-4756. doi: 10.1021/cm800357g. URL http://dx.doi.org/10.1021/cm800357g.

[343] J. P. Tetienne, T. Hingant, L. Rondin, A. Cavaillès, L. Mayer, G. Dantelle, T. Gacoin, J. Wrachtrup, J. F. Roch, and V. Jacques. Spin relaxometry of single nitrogen-vacancy defects in diamond nanocrystals for magnetic noise sensing. *Physical Review B - Condensed Matter and Materials Physics*, 87(23):1–12, 2013. ISSN 10980121. doi: 10.1103/PhysRevB.87.235436.

[344] L. Guarina, C. Calorio, D. Gavello, E. Moreva, P. Traina, A. Battiato, S. Ditalia Tchernij, J. Forneris, M. Gai, F. Picollo, P. Olivero, M. Genovese, E. Carbone, A. Marcantoni, and V. Carabelli. Nanodiamonds-induced effects on neuronal firing of mouse hippocampal microcircuits. *Scientific Reports*, 8(1):2221, 2018. ISSN 2045-2322. doi: 10.1038/s41598-018-20528-5. URL http://www.nature.com/articles/s41598-018-20528-5.

[345] Kostiantyn Turcheniuk Mochalin and Vadym. Biomedical Applications of Nanodiamond (Review). *Nanotechnology*, 2017. ISSN 1361-6528. doi: 10.1088/1361-6528/aa6ae4. URL http://iopscience.iop.org/article/10.1088/1361-6528/aa6ae4%0Ahttp://iopscience.iop.org/10.1088/1361-6528/aa6ae4.

[346] Haruhisa Kato, Ayako Nakamura, Masanori Horie, and Shigehisa Endoh. Preparation and characterization of stable dispersions of carbon black and nanodiamond in culture medium for in vitro toxicity assessment. *Carbon*, 49(12):3989–3997, 2011. ISSN 0008-6223. doi: 10.1016/j.carbon.2011.05.039. URL http://dx.doi.org/10.1016/j.carbon.2011.05.039.

[347] Simon R. Hemelaar, Andreas Nagl, François Bigot, Melissa M. Rodríguez-García, Marcel P. de Vries, Mayeul Chipaux, and Romana Schirhagl. The interaction of fluorescent nanodiamond probes with cellular media. *Microchimica Acta*, 184(4), 2017. ISSN 14365073. doi: 10.1007/s00604-017-2086-6. URL https://link.springer.com/article/10.1007%2Fs00604-017-2086-6.

[348] Xiaoyong Zhang, ShiQi Wang, Meiying Liu, Junfeng Hui, Bin Yang, Lei Tao, and Yen Wei. Surfactant-dispersed nanodiamond: biocompatibility evaluation and drug delivery applications. *Toxicology Research*, 2(5):335, 2013. ISSN 2045-452X. doi: 10.1039/c3tx50021g. URL http://xlink.rsc.org/?DOI=c3tx50021g.

[349] Saniya Alwani, Randeep Kaur, Deborah Michel, Jackson M Chitanda, Ronald E Verrall, Chithra Karunakaran, and Ildiko Badea. Lysine-functionalized nanodiamonds as gene carriers: development of stable colloidal dispersion for in vitro cellular uptake studies and siRNA delivery application. *International Journal of Nanomedicine*, 2016 (Issue 1):687–702, 2016. ISSN 1178-2013.

[350] Shingo Sotoma and Masahiro Shirakawa. Monodispersed Colloidal Solutions of Surface-modified Detonation-synthesized Nanodiamonds and Their Aggregation Resistance. *Chemistry Letters*, 45(6):697–699, 2016. ISSN 0366-7022. doi: 10.1246/cl.160250. URL https://www.jstage.jst.go.jp/article/cl/45/6/45_160250/_article.

[351] Cristina Resetco, Daniel Frank, N. Ugur Kaya, Nezha Badi, and Filip Du Prez. Precisely alternating functionalized polyampholytes prepared in a single pot from sustainable thiolactone building blocks. *ACS Macro Letters*, 6(3):277–280, 2017. ISSN 21611653. doi: 10.1021/acsmacrolett.7b00079.

[352] Jong Woo Lee, Seonju Lee, Sangmok Jang, Kyu Young Han, Younggyu Kim, Jaekyung Hyun, Seong Keun Kim, and Yan Lee. Preparation of non-aggregated fluorescent nanodiamonds (FNDs) by non-covalent coating with a block copolymer and proteins for enhancement of intracellular uptake. *Molecular bioSystems*, 9(5):1004–11, 5 2013. ISSN 1742-2051. doi: 10.1039/c2mb25431j. URL http://apps.webofknowledge.com/full_record.do?product=WOS&search_mode=CombineSearches&qid=24&SID=X2WjzM5ryRnKucMQdbY&page=13&doc=122.

[353] Wentao Wang, Xin Ji, Liang Du, and Hedi Mattoussi. Enhanced Colloidal Stability of Various Gold Nanostructures Using a Multicoordinating Polymer Coating. *Journal of Physical Chemistry C*, 121(41):22901–22913, 2017. ISSN 19327455. doi: 10.1021/acs.jpcc.7b07732.

[354] Yuzhou Wu, Anna Ermakova, Weina Liu, Goutam Pramanik, Tran Minh Vu, Andrea Kurz, Liam McGuinness, Boris Naydenov, Susanne Hafner, Rolf Reuter, Joerg Wrachtrup, Junichi Isoya, Christina Förtsch, Holger Barth, Thomas Simmet, Fedor

Jelezko, and Tanja Weil. Programmable Biopolymers for Advancing Biomedical Applications of Fluorescent Nanodiamonds. *Advanced Functional Materials*, 25(42): 6576–6585, 2015. ISSN 16163028. doi: 10.1002/adfm.201502704.

[355] Soheyla Honary and Foruhe Zahir. Effect of Zeta Potential on the Properties of Nano-Drug Delivery Systems - A Review (Part 1). *Tropical Journal of Pharmaceutical Research*, 12(2):255–264, 2013.

[356] Eleonore Fröhlich. The role of surface charge in cellular uptake and cytotoxicity of medical nanoparticles. *International Journal of Nanomedicine*, 7:5577–5591, 2012. URL https://doi.org/10.2147/IJN.S36111.

[357] Laia Gines, Soumen Mandal, Ashek-I Ahmed, Chia-Liang Cheng, Maabur Sow, and Oliver Williams. Positive Zeta Potential of Nanodiamonds. *Nanoscale*, pages 12549–12555, 2017. ISSN 2040-3364. doi: 10.1039/C7NR03200E. URL http://pubs.rsc.org/en/Content/ArticleLanding/2017/NR/C7NR03200E.

[358] Anke Krueger, Masaki Ozawa, Gerald Jarre, Yuejiang Liang, Jochen Stegk, and Li Lu. Deagglomeration and functionalisation of detonation diamond. *Physica Status Solidi (A) Applications and Materials Science*, 204(9):2881–2887, 2007. ISSN 18626300. doi: 10.1002/pssa.200776330.

[359] Jui-I Chao, Elena Perevedentseva, Pei-Hua Chung, Kuang-Kai Liu, Chia-Liang Chih-Yuan Cheng, Chia-Ching Chang, and Chia-Liang Chih-Yuan Cheng. Nanometer-sized diamond particle as a probe for biolabeling. *Biophysical Journal*, 93(6):2199–2208, 9 2007. ISSN 0006-3495. doi: 10.1529/biophysj.107.108134. URL http://www.pubmedcentral.nih.gov/articlerender.fcgi?artid=1959542&tool=pmcentrez&rendertype=abstract.

[360] Amanda M. Schrand, Liming Dai, John J. Schlager, Saber M. Hussain, and Eiji Osawa. Differential biocompatibility of carbon nanotubes and nanodiamonds. *Diamond and Related Materials*, 16(12):2118–2123, 12 2007. ISSN 09259635. doi: 10.1016/j.diamond.2007.07.020. URL http://www.sciencedirect.com/science/article/pii/S0925963507003111http://linkinghub.elsevier.com/retrieve/pii/S0925963507003111.

[361] Jitka Slegerova, Miroslav Hajek, Ivan Rehor, Frantisek Sedlak, Jan Stursa, Martin Hruby, and Petr Cigler. Designing the nanobiointerface of fluorescent nanodiamonds: highly selective targeting of glioma cancer cells. *Nanoscale*, 7(2):415–420, 2015. ISSN 2040-3364. doi: 10.1039/C4NR02776K. URL http://xlink.rsc.org/?DOI=C4NR02776K.

[362] Shu-Jung Yu, Ming-Wei Kang, Huan-Cheng Chang, Kuan-Ming Chen, and Yueh-Chung Yu. Bright fluorescent nanodiamonds: no photobleaching and low cytotoxicity. *Journal of the American Chemical Society*, 127(50):17604–5, 12 2005. ISSN 0002-7863. doi: 10.1021/ja0567081. URL http://www.ncbi.nlm.nih.gov/pubmed/16351080.

[363] Zhi-Yi Lien, Tzu-Chia Hsu, Kuang-Kai Liu, Wei-Siang Liao, Kuo-Chu Hwang, and Jui-I. Chao. Cancer cell labeling and tracking using fluorescent and magnetic nanodiamond. *Biomaterials*, 33(26):6172–6185, 2012. ISSN 01429612. doi:

10.1016/j.biomaterials.2012.05.009. URL http://linkinghub.elsevier.com/retrieve/pii/S0142961212005261.

[364] Mao Feng Weng, Bo Jui Chang, Su Yu Chiang, Niann Shiah Wang, and Huan Niu. Cellular uptake and phototoxicity of surface-modified fluorescent nanodiamonds. *Diamond and Related Materials*, 22:96–104, 2012. ISSN 09259635. doi: 10.1016/j.diamond.2011.12.035. URL http://dx.doi.org/10.1016/j.diamond.2011.12.035.

[365] Natalia Dworak, Maciej Wnuk, Jacek Zebrowski, Grzegorz Bartosz, and Anna Lewinska. Genotoxic and mutagenic activity of diamond nanoparticles in human peripheral lymphocytes in vitro. *Carbon*, 68:763–776, 2014. ISSN 00086223. doi: 10.1016/j.carbon.2013.11.067. URL http://dx.doi.org/10.1016/j.carbon.2013.11.067.

[366] Jennifer Mytych, Anna Lewinska, Jacek Zebrowski, and Maciej Wnuk. Nanodiamond-induced increase in ROS and RNS levels activates NF-κB and augments thiol pools in human hepatocytes. *Diamond and Related Materials*, 55:95–101, 5 2015. ISSN 09259635. doi: 10.1016/j.diamond.2015.03.014. URL http://www.sciencedirect.com/science/article/pii/S0925963515000527.

[367] Vanesa C. Sanchez, Ashish Jachak, Robert H. Hurt, and Agnes B. Kane. Biological interactions of graphene-family nanomaterials: An interdisciplinary review. *Chemical Research in Toxicology*, 25(1):15–34, 2012. ISSN 0893228X. doi: 10.1021/tx200339h.

[368] Yanli Chang, Sheng Tao Yang, Jia Hui Liu, Erya Dong, Yanwen Wang, Aoneng Cao, Yuanfang Liu, and Haifang Wang. In vitro toxicity evaluation of graphene oxide on A549 cells. *Toxicology Letters*, 200(3):201–210, 2011. ISSN 03784274. doi: 10.1016/j.toxlet.2010.11.016. URL http://dx.doi.org/10.1016/j.toxlet.2010.11.016.

[369] Yongbin Zhang, Syed F Ali, Enkeleda Dervishi, Yang Xu, Zhongrui Li, Daniel Casciano, and Alexandru S Biris. Cytotoxicity Effects of Graphene and Single-Wall Carbon Nanotubes in Neural Phaeochromocytoma-Derived PC12 Cells. *American Chemcial Society*, 4(6):3181–3186, 2010. doi: Doi10.1021/Nn1007176.

[370] Lin-Song Wang, Lin Wang, Li Wang, Ge Wang, Zhao-Hu Li, and Jian-Ji Wang. Effect of 1-butyl-3-methylimidazolium tetrafluoroborate on the wheat (Triticum aestivum L.) seedlings. *Environmental toxicology*, 24(3):296–303, 2009. ISSN 1522-7278. doi: 10.1002/tox.

[371] U Sydlik, M Bierhals, J Abel, R P F Schins, and K Unfried. Ultrafine carbon particles induce apoptosis and proliferation in rat lung epithelial cells via specific signalling pathways both using EGF-R. *American Journal of Physiology: Lung Cellular and Molecular Physiology*, 291:L725 – L733, 2006. doi: 10.1152/ajplung.00131.2006. URL http://ajplung.physiology.org/content/ajplung/291/4/L725.full.pdf.

[372] Sonja Boland, Salik Hussain, and Armelle Baeza-Squiban. Carbon black and titanium dioxide nanoparticles induce distinct molecular mechanisms of toxicity. *Wiley Interdisciplinary Reviews: Nanomedicine and Nanobiotechnology*, 6(6):641–652, 2014. ISSN 19390041. doi: 10.1002/wnan.1302.

[373] Jiacheng Zhao and Martina Heide Stenzel. Entry of Nanoparticles into Cells: the Importance of Nanoparticle Properties. *Polymer Chemistry*, 9:259–272, 2018. ISSN 1759-9954. doi: 10.1039/C7PY01603D. URL http://pubs.rsc.org/en/Content/ArticleLanding/2017/PY/C7PY01603D.

[374] Y Colpin, A Swan, A V Zvyagin, and T Plakhotnik. Imaging and sizing of diamond nanoparticles. *Optics Letters*, 31(5):625–627, 2006. ISSN 0146-9592. doi: 10.1364/OL.31.000625. URL Size;Scattering;Nanodiamonds;Diamonds;Fluorescence;Smallest;.

[375] Florian Dolde, H. Fedder, M. W. Doherty, T Noebauer, F. Rempp, G. Balasubramanian, T. Wolf, F. Reinhard, L. C. L. Hollenberg, F. Jelezko, J. Wrachtrup, and T. Nöbauer. Electric-field sensing using single diamond spins. *Nature Physics*, 7(6):459–463, 6 2011. ISSN 1745-2473. doi: 10.1038/NPHYS1969. URL http://www.nature.com/doifinder/10.1038/nphys1969.

[376] N J Cherepy, a R Holzwarth, and R a Mathies. Near-infrared resonance Raman spectra of Chloroflexus aurantiacus photosynthetic reaction centers. *Biochemistry*, 34(15):5288–5293, 1995. ISSN 0006-2960.

[377] Medhanie Tesfay Gebrekidan, Christian Knipfer, Florian Stelzle, Juergen Popp, Stefan Will, and Andreas Braeuer. A shifted-excitation Raman difference spectroscopy (SERDS) evaluation strategy for the efficient isolation of Raman spectra from extreme fluorescence interference. *Journal of Raman Spectroscopy*, pages 1–8, 2015. ISSN 03770486. doi: 10.1002/jrs.4775. URL http://doi.wiley.com/10.1002/jrs.4775.

[378] Andrey N. Kuzmin, Artem Pliss, and Aliaksandr V. Kachynski. Biomolecular component analysis of cultured cell nucleoli by Raman microspectrometry. *Journal of Raman Spectroscopy*, 44(2):198–204, 2013. ISSN 03770486. doi: 10.1002/jrs.4173.

[379] Abigail S Haka, Karen E Shafer-Peltier, Maryann Fitzmaurice, Joseph Crowe, Ramachandra R Dasari, and Michael S Feld. Diagnosing breast cancer by using Raman spectroscopy. *Proceedings of the National Academy of Sciences of the United States of America*, 102(35):12371–6, 2005. ISSN 0027-8424. doi: 10.1073/pnas.0501390102. URL http://www.pnas.org/content/102/35/12371.full.

[380] Rekha Gautam, Sandeep Vanga, Freek Ariese, and Siva Umapathy. Review of multidimensional data processing approaches for Raman and infrared spectroscopy. *EPJ Techniques and Instrumentation*, 2(1):8, 2015. ISSN 2195-7045. doi: 10.1140/epjti/s40485-015-0018-6. URL http://www.epjtechniquesandinstrumentation.com/content/2/1/8.

[381] Gabriela Figueroa-González and Carlos Pérez-Plasencia. Strategies for the evaluation of DNA damage and repair mechanisms in cancer. *Oncology Letters*, 13(6):3982–3988, 2017. ISSN 17921082. doi: 10.3892/ol.2017.6002.

[382] Cheng Chen, Ishtiaq Ahmed, and Ljiljana Fruk. Reactive oxygen species production by catechol stabilized copper nanoparticles. *Nanoscale*, 5(23):11610–11614, 2013. ISSN 20403364. doi: 10.1039/c3nr03563h.

[383] Bianca Geiseler, Marko Miljevic, Philipp Müller, and Ljiljana Fruk. Phototriggered Production of Reactive Oxygen Species by TIO 2 Nanospheres and Rods. *Journal of Nanomaterials*, 2012:1–9, 2012. ISSN 1687-4110. doi: 10.1155/2012/708519. URL http://www.hindawi.com/journals/jnm/2012/708519/.

[384] Alexandre Barras, Joël Lyskawa, Sabine Szunerits, Patrice Woisel, and Rabah Boukherroub. Direct Functionalization of Nanodiamond Particles Using Dopamine Derivatives. *Langmuir*, 27(20):12451–12457, 10 2011. ISSN 0743-7463. doi: 10.1021/la202571d. URL http://pubs.acs.org/doi/abs/10.1021/la202571d.

[385] Lan Bo Chen. Mitochondrial membrane potential in living cells. *Annual review of cell biology*, 4:155–81, 1 1988. ISSN 0743-4634. doi: 10.1146/annurev.cb.04.110188.001103. URL http://www.annualreviews.org/doi/abs/10.1146/annurev.cb.04.110188.001103.

[386] Anne Heller, Gero Brockhoff, and Achim Goepferich. Targeting drugs to mitochondria. *European Journal of Pharmaceutics and Biopharmaceutics*, 82(1):1–18, 2012. ISSN 09396411. doi: 10.1016/j.ejpb.2012.05.014. URL http://dx.doi.org/10.1016/j.ejpb.2012.05.014.

[387] Kilian N. R. Wuest, Vanessa Trouillet, Anja S. Goldmann, Martina H. Stenzel, and Christopher Barner-Kowollik. Polymer Functional Nanodiamonds by Light-Induced Ligation. *Macromolecules*, 49(5):1712–1721, 3 2016. ISSN 0024-9297. doi: 10.1021/acs.macromol.5b02607. URL http://pubs.acs.org/doi/abs/10.1021/acs.macromol.5b02607.

[388] Hazel H Szeto. Cell-permeable, Mitochondrial-targeted, Peptide Antioxidants. *American Association of Pharmaceutical Scientists*, 8(2):277–283, 2006.

[389] Dominique Chretien, Paule Benit, Hyung-Ho Ha, Susanne Keipert, Riyad El-Khoury, Young-Tae Chang, Martin Jastroch, Howard Jacobs, Pierre Rustin, and Malgorzata Rak. Mitochondria Are Physiologically Maintained At Close To 50 °C. *PLOS Biology*, page 133223, 2017. ISSN 1545-7885. doi: 10.1101/133223. URL https://www.biorxiv.org/content/early/2017/05/02/133223http://journals.plos.org/plosbiology/article?id=10.1371/journal.pbio.2003992.

[390] Nick Lane. Hot mitochondria? *PLOS Biology*, 16(1):1–6, 2018. ISSN 1545-7885. doi: 10.1371/journal.pbio.2005113. URL http://journals.plos.org/plosbiology/article/file?id=10.1371/journal.pbio.2005113&type=printablehttps://journals.plos.org/plosbiology/article?id=10.1371/journal.pbio.2005113.

[391] Xiao-Qun Ye, Qi Li, Guang-Hui Wang, Fen-Fen Sun, Gui-Jun Huang, Xiu-Wu Bian, Shi-Cang Yu, and Gui-Sheng Qian. Mitochondrial and energy metabolism-related properties as novel indicators of lung cancer stem cells. *International Journal of Cancer*, 129(4):820–831, 2011. ISSN 00207136. doi: 10.1002/ijc.25944. URL http://doi.wiley.com/10.1002/ijc.25944.